UNIVERSITY OF SOUTHAMPTON

FACULTY OF ENGINEERING, SCIENCE & MATHEMATICS

School of Chemistry

High-Throughput Discovery of Lithium Battery Materials

by

Alan Daniel Spong BSc (Hons), AMRSC

Thesis for the degree of Doctor of Philosophy

April 2005

To Pop Pop Ron

With love

UNIVERSITY OF SOUTHAMPTON

ABSTRACT

FACULTY OF ENGINEERING, SCIENCE AND MATHEMATICS

SCHOOL OF CHEMISTRY

Doctor of Philosophy

High-Throughput Discovery of Lithium Battery Materials

By Alan Daniel Spong

This thesis outlines the application of high-throughput methodologies to the discovery of potential lithium battery materials. Arrays of positive electrode materials of varying composition were prepared using automated techniques from ink suspensions and aqueous media. These materials were deposited directly onto an electrode substrate and were tested electrochemically using slow-scan cyclic voltammetry. In addition, the materials were characterised using high-throughput X-ray diffraction and SEM techniques.

A study to determine the validity of the experimental method was undertaken for $LiMn_2O_4$, carbon black and PVDF-HFP materials. During the study, the effect of the percolation of electronic conductivity due to the amount of carbon in the materials was investigated by preparing composite electrodes with varying carbon loading and observing the difference in capacity at a given sweep rate.

A new solution synthesis route was developed for lithium iron phosphate ($LiFePO_4$), which was utilised for combinatorial synthesis. The solution route was used to prepare substituted olivines of the type $LiMPO_4$ (where M = Co, Ni, Fe and Mn) These were investigated and evaluated for use as positive electrode materials. An investigation of the effect of sucrose content in the precursor was conducted and the method showed clear differences in performance between materials with high and low residual carbon content. The effect of zirconium doping in lithium iron phosphates was studied and the screening method showed elevated peak current and capacity values as the carbon loading was increased. However, a corresponding increase in the capacity and current was not observed as the zirconium doping level was increased.

Table of Contents

Abstract i

Table of Contents ii

Authors Declaration vii

Acknowledgements viii

Symbols ix

Abbreviations xii

Chapter 1: Introduction

1.1 Overview of Battery Systems 2

1.1.1 Historical Background 2

1.1.2 The Need for New Power Sources 3

1.2 Theoretical Background 5

1.2.1 Energy Density 5

1.2.2 Theoretical Capacity 6

1.2.3 Specific Power 6

1.2.4 Specific Capacity 7

1.3 Non-Lithium Battery Systems 7

1.3.1 Primary Cells 7

1.3.2 Secondary Cells 9

1.4 Lithium Cells 9

1.4.1 Chemical Potential 10

1.4.2 Cell Potential 10

1.4.3 Lithium Primary Cells 11

1.4.4 Secondary Lithium Cells 12

1.4.5 Positive Electrodes 14

1.4.6 Negative Electrodes 19

1.4.7 Electrolytes 20

1.5 Preparation Techniques 21

1.5.1 Solid State Synthesis 21

1.5.2 Sol-gel and Solution Techniques 23

1.6 Power Density and Percolation Effects **26**
1.7 Combinatorial Techniques **30**
1.7.1 The Combinatorial Principle *31*
1.7.2 Combinatorial Methods in Organic Chemistry *32*
1.7.3 Combinatorial Methods in Materials Science *32*
1.7.4 High Throughput vs. Combinatorial Screening *39*
1.8 Thesis Overview **40**
1.9 References **42**

Chapter 2: Validation of the Combinatorial Technique

2.1 Background and Objectives **50**
2.2 Experimental **52**
2.2.1 Conventional Electrode Preparation of $LiMn_2O_4$ *52*
2.2.1.1 Cell Preparation 54
2.2.1.2 Electrochemical Testing 57
2.2.1.3 Scanning Electron Microscopy 58
2.2.2 Combinatorial Electrode Preparation *59*
2.2.2.1 Ink Preparation 60
2.2.2.2 Robotic Liquid Handling 62
2.2.2.3 Electrode Preparation 67
2.2.2.4 Electrochemical Testing Array 70
2.2.2.5 High-Throughput Instrumentation and Software 74
2.2.2.6 Instrumentation Testing Experiments 75
2.2.2.7 Electrochemical Screening Software 77
2.2.2.8 Screening Experiments 79
2.2.3 Electrode Film Conductivity Using the Four-Point Probe Method *80*
2.3 Results and Discussion **83**
2.31 Conventional Electrode Characterisation *83*

2.3.1.1 Micro-structural Properties of $LiMn_2O_4$/AB/PDVF. 83
2.3.1.2 Conductivity Measurements..... 85
2.3.1.3 Electrochemical Testing..... 89
2.3.2 Combinatorial Screening.....*93*
2.3.2.1 Scanning Electron Microscopy..... 93
2.3.2.2 Initial Electrochemical Testing.....98
2.3.2.3 Electrochemical Testing..... 100
2.3.2.4 Randomisation of Sample Locations.....106
2.3.2.5 Effect of Scan Rate on the Electrochemical Response..... 111
2.3.2.6 Reproducibility..... 113
2.3.2.7 Conductivity Measurements of High-Throughput samples. 115

2.4 Conclusion..... 116
2.4.1 Further Work..... *117*
2.5 References.....119

Chapter 3: Solution Based Synthesis of $LiFePO_4$: A Prerequisite to Combinatorial Synthesis

3.1 Background and Objectives.....121

3.2 Experimental.....123
3.2.1 Solid-State Synthesis of $LiFePO_4$..... *123*
3.2.1.1 The Role of Sucrose.....124
3.2.2 Solution Synthesis of $LiFePO_4$.....*124*
3.2.2.1 Two Step Preparation of $LiFePO_4$.....125
3.2.2.2 Preparation of Substituted $LiMPO_4$ by Solution Synthesis... 126
3.2.3 X-ray Powder Diffraction..... *126*
3.2.4 Scanning Electron Microscopy and EDX Mapping..... *129*
3.2.5 Optical Microscopy.....*129*
3.2.6 Electrochemical Testing..... *130*

3.2.7 Analysis for Iron Content by TGA *130*
3.2.8 Analysis of Iron Content in $LiFePO_4$ Samples by AAS *132*
3.2.9 Composite Conductivity Measurements *134*

3.3 Results and Discussion **135**
3.3.1 X-ray Diffraction *135*
3.3.2 Optical Microscopy *141*
3.3.3 Scanning Electron Microscopy *143*
3.3.4 EDX Spot Analysis *146*
3.3.5 Electronic Conductivity *154*
3.3.6 Electrochemical Testing *155*
3.3.6.1 One Step Synthesis of $LiFePO_4$ *155*
3.3.6.2 Two Step Syntheses of $LiFePO_4$ *168*

3.4 Conclusion **171**
3.4.1 Further Work *172*
3.5 References **173**

Chapter 4: Combinatorial Screening of $LiMPO_4$ compounds

4.1 Background and Objectives **175**
4.2 Experimental **178**
4.2.1 Array Synthesis *178*
4.2.2 Electrochemical Screening *183*
4.2.2.1 Calculation of Electrode Mass 184
4.2.3 Optimisation of XRD and SEM Array Deposition Techniques *185*
4.2.4 X-Ray Diffraction of $LiMPO_4$ Arrays *194*
4.2.5 Scanning Electron Microscopy 195

4.3 Results and Discussion **196**

4.3.1 Electrochemical Testing of LiMPO4 Arrays.....196
4.3.1.1 $LiFe_{0.8}Mg_{0.2}PO_4$ and $LiFePO_4$..... 196
4.3.1.2 LiFePO4 and Sucrose..... 204
4.1.3.3 $Li_{1-x}Zr_xFePO_4$ Arrays..... 207
4.3.1.4 Ternary Mixed Metal Phosphate – $LiCo_xNi_yFe_{1-x-y}PO_4$... 212
4.3.2 Combinatorial X-ray Diffraction.....219
4.33 Combinatorial SEM of $LiMPO_4$ Arrays.....*223*

4.5 Conclusion..... **234**
4.5.1 Further Work..... *235*

4.6 References.....**236**

Chapter 5: Conclusions and Further Work

5.1 Conclusion.....**339**

5.2 Further Work..... **242**

Appendices.....**244**

Acknowledgements

I would particularly like to thank my supervisor Dr John Owen for his support and guidance throughout my studies. My thanks also go to Dr Girts Vitins who helped me greatly with both experimental work and the data analysis portion of the project.

I gratefully acknowledge the help of my family for their ongoing encouragement especially to my mum, dad, my grandmother and my sister Hayley for their love and support and constant faith that I was on the right path. My great thanks go to Michelle for her continuing love and guidance over the past two years.

I would like to dedicate this thesis to the memory of my grandfather, for his unwavering belief in me and for his love and support, thank you Pop.

In addition I would like to acknowledge many other people who have given me help and advice over the last few years, most notably the members of the Solid State Electrochemistry Group, Thierry Le Gall, Ken Reiman and Matt Roberts, for ensuring the social side of group life was maintained. I am also grateful to the many former members of the SSE group in particular Phil Nelson, Ailsa Leck, Karen Brace and Toby Gordon-Smith. I would also like to thank all the other members of the Southampton Electrochemistry Group who gave me so much help and advice. Finally I give thanks to some close friends who have been there for me over the years, Karl, Alice, Matt, Lai, John and Pete and the many others who have given me invaluable assistance during the last three years.

Without all of your support, writing this thesis would have been a much more difficult process, thank you.

Symbols

2Θ	X-ray glancing angle	° or deg
a	A variable	-
b	A variable	-
c	A variable	-
C	Concentration	mol dm^{-3} or ppm
C/t	Cycling rate	$hours^{-1}$
$C_{Fe(NO3)3}$	Concentration of $Fe(NO_3)_3$	mol dm^{-3}
C_{Sp}	Specific capacity	mA h g^{-1}
C_{Th}	Theoretical capacity	mA h g^{-1}
$d_{AM,I}$	Density of the active material ink	g cm^{-3}
E	Cell potential	V
F	Faraday number (96485)	C mol^{-1}
$f_{AM,I}$	Fraction of active material in solid contents	-
$f_{s,I}$	Fraction of solids in active material ink	-
I	Current	A
I	Intensity	-
j	Current density	mA cm^{-2}
l	Sample thickness	cm
m	Mass	g
M	A transition metal (Mn, Co, Ni, Fe)	-
m_{AM}	Mass of active material	g
M_{AM}	Molar mass of active material	g mol^{-1}
$m_{AM,Electrode}$	Mass of active material on the electrode	g
m_{el}	Mass of electrode material	g
$m_{LiFePO4}$	Mass of pure $LiFePO_4$ in a sample	g
$M_{LiFePO4}$	Molecular mass of $LiFePO_4$	g mol^{-1}
$M_{LiFePO4.5}$	Molecular mass of $LiFePO_{4.5}$	g mol^{-1}
n	Number of moles	mol

n_e	Number of electrons	-
n_{el}	Number of moles of active material on the electrode surface	mol
$n_{LiFePO4}$	Number of moles of $LiFePO_4$	mol
$\emptyset$	Diameter	cm
p	Probability	-
P_{Den}	Power density	W kg^{-1}
R	Resistance	Ω
R_s	Sheet resistance	Ω/□
t	Time	s or h
V	Volume	cm^{-3} or mL
$V_{AM,\,I}$	Volume of active material ink in vial	mL
V_e	Volume of ink deposited on electrode	mL
$V_{tot,\,I}$	Total volume of ink in vial	mL
V_c	Percolation threshold (critical concentration)	-
V_{el}	Volume of material transferred to the electrode	L
$V_{Fe(NO3)3}$	Volume of $Fe(NO_3)_3$	L
V_{Prec}	Precursor sample volume in well	L
$W_{C,\,AM}$	Weight concentration of active material	g cm^{-3}
W_m	Gravimetric energy density	W h g^{-1}
W_V	Volumetric energy density	W h cm^{-3}
w_{carbon}	Weigh Fraction of carbon	-
$w_{LiFePO4}$	Weight Fraction of $LiFePO_4$	-
x	Variable – number of moles of lithium	-
x	A variable	-
X	A non-metal element	-
y	A variable	-
z	A variable	-
$\Delta\,\overline{G}$	Gibbs free energy change for a system	kJ mol^{-1}
μ_{Li}^{Neg}	Chemical potential of the negative electrode in a lithium cell	-

μ_{Li}^{Pos}	Chemical potential of the positive electrode in a lithium cell	-
μ	Chemical potential	-
ρ_s	Sheet resistively	Ω m
σ_s	Specific conductivity	S cm^{-1}
υ	Scan rate	mV s^{-1}

Abbreviations

AAS	Atomic absorption spectroscopy
AB	Acetylene black
At.%	Atomic percentage
CCD	Charge coupled device
CCS	Continuous composition spread
CE	Counter electrode
CP	Cyclopentanone
CSV	Comma separated variable
DMC	Di-methyl carbonate
DMFC	Direct methanol fuel cell
DNA	Deoxyribonucleic acid
EC	Ethylene carbonate
EDX	Energy dispersive X-ray (spectroscopy)
ESEM	Environmental scanning electron microscopy
FOM	Figure of merit
GADDS	General area detector diffraction system
HFP	Hexafluoro-propylene
IMLB	International Meeting on Lithium Batteries
M	Molar concentration
MGC	Machineable glass ceramic
NHE	Normal hydrogen electrode
NiMH	Nickel metal hydride battery
NiCd	Nickel cadmium battery
OCP	Open circuit potential
PCB	Printed circuit board
PEO	Polyethylene oxide
PLION	Polymer lithium ion battery
PTFE	Polytetrafluoroethylene

PVA	Polyvinyl alcohol
PVDF	Polyvinylidene fluoride
RE	Reference electrode
RF	Radio frequency
SEM	Scanning electron microscope
TGA	Thermogravimetric analysis
VMP	Variable multi-channel potentiostat
Vol.%	Volume percentage
WE	Working electrode
Wt.%	Weight percentage
XRD	X-ray diffraction

Chapter 1:
Introduction

The history of materials science is replete with examples of slow and time-consuming approaches to the discovery of novel materials. It has generally been accepted that the principle of automating the synthesis and screening of materials is advantageous in terms of increasing the number of materials that can be processed, while reducing the screening costs and production time [1, 2]. This new approach to discovery is known as high-throughput or combinatorial materials science. It is a multidisciplinary field covering aspects of chemistry, engineering and physics. It has been applied to many areas of materials science, and it is the aim of this project to apply these new methods to the area of lithium battery discovery. The following sections outline the work conducted to date in the study of lithium battery materials and explore new advances in combinatorial methodologies in the area of materials synthesis and screening.

1.1 Overview of Battery Systems

An electrochemical power source (or battery) is a means of storing electronic charge in the form of chemical potential energy. The energy supplied by a chemical energy store can be released as a flow of electrons between the positive and negative terminals of a cell by means of an electrochemical oxidation-reduction reaction [3]. It is this conversion of chemical to electrical energy that has enabled the development of the new mobile technologies of the last century.

1.1.1 Historical Background

The development of the electrochemical cells used today as batteries can be traced back to the work of Alessandro Volta (1745-1827) [4]. His experiments produced the first device capable of supplying a continuous electric current. The 'Volta Pile' (first demonstrated in 1800) consisted of two electrodes of different metals separated by a layer of non-metallic material. This simple arrangement is still used in advanced battery systems today in which a negative and positive electrode are separated by a non metallic membrane [5]. The development of the battery began an electrochemical revolution in science enabling Humphrey Davy (in 1807) to discover the new elements of potassium and sodium and their isolation by electrolysis [6]. The development of the technology to store electrical energy has

allowed chemical reactions to be studied at different potentials, giving rise to the discipline of electrochemistry.

The commercialisation of the first battery systems began in the 1870s with the invention of the telegraph and electrically powered torches, and growth continued into the twentieth century with the widespread use of domestic radio receivers. The rapid developments in the microelectronics sector over the last 30 years have led to parallel demand for new power sources to supply these emerging technologies [7].

By 1997, it was estimated that total annual battery production totalled 8-15 units per head of population and, in the year 2000 the total world battery market exceeded US$ 40 billion per annum. Of these commercial systems, over half were lead-acid type batteries mainly used in vehicle starting, lighting and ignition (SLI) applications [8]. The remaining half was made up of cells used for a wide range of applications. Examples of these are primary alkaline cells used in personal electronics. This is an area that has seen continual growth of between 6-12 % per annum over the last 25 years [9]. During the last decade the growth in mobile electronic communications has led to a huge demand for high power and high-energy cells. Until recently, these devices have utilised rechargeable (secondary) cells based on nickel cadmium (NiCd) and nickel metal hydride (NiMH) technology, which were used in early video cameras and mobile phones. During the past decade several types of lithium secondary cells have been commercialised [10] and are in widespread use (*e.g.,* power sources in laptop computers and mobile phones), replacing the older lower energy and voltage NiCd and NiMH secondary cells .

1.1.2 The Need for New Power Sources

The miniaturisation of mobile electronic devices over the last three decades has been matched in scale by the systems used to power them. However, the power source is still generally the heaviest component in most modern devices and so the performance is restricted by the battery storage capacity and the number of cells required to deliver the desired potential [11]. Advances have been made in the area of two older materials: alkaline-manganese dioxide and lead acid systems, which have been optimised using new advanced materials and processing techniques to give a many-fold improvement in their performance [7]. However, these materials

do not provide the necessary high voltage and high capacity in a lightweight material required by new devices. Emerging technologies require the development of advanced battery systems that are capable of supplying high specific energy (> 180 W h kg^{-1}) and volumetric energy density (> 360 W h dm^{-3}) and long cycle life (> 500 cycles) [11]; these requirements can only be met by high voltage lightweight lithium batteries.

Lightweight battery materials have become increasingly more prevalent in the last decade for use in traction applications mainly as a direct result of the environmental effects of burning fossil fuels for automotive use. Many vehicle manufactures such as Toyota have invested heavily in the production of prototype hybrid cars. The Toyota Prius [12] was one of the first production electric hybrid vehicles on the market. It runs on an array of 28 NiMH rechargeable batteries providing a total voltage of 201 V to an electric motor. The battery system is recharged using a generator powered by the internal combustion engine. This provides many benefits over battery powered electric vehicles, but the efficiency of electric and hybrid vehicles could be greatly enhanced using more lightweight, but equally powerful battery materials. The needs of today will be small in comparison to the future use of mobile power sources. Mobile phone and laptop computer use are growing exponentially and, with the doubling of computer processing power every eighteen months; the need for lightweight high-energy batteries is expected to grow even faster, as the advent of even newer technologies requires the development higher energy materials. The development of new more powerful battery materials is expected to grow in parallel with this increased demand, with a two-fold increase in volumetric and gravimetric specific energy densities expected between 1996 and 2006 (see Figure 1.1) [13].

The discovery of new lithium battery materials is often a process of trial and error. In fact, it is difficult to predict the suitability of new battery materials by theory alone. The discovery and optimisation of a given system commonly involves many experiments, which is a time consuming process involving many variables in synthesis. Thus, combinatorial screening methodologies would greatly enhance the rate of materials discovery in this area. The application of a combinatorial strategy to lithium battery materials discovery is quite appropriate, as the electrochemical testing of these materials requires several hours per charge and discharge.

Combinatorial methods would allow many systems to be studied simultaneously, greatly reducing the experimental time and cost of testing.

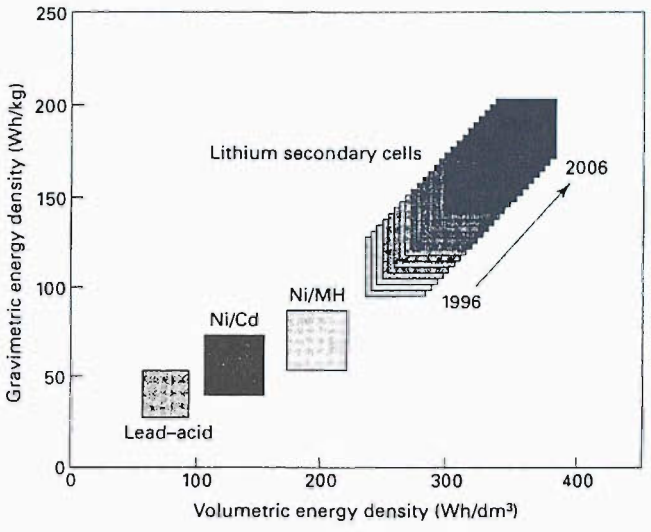

Figure 1.1 - Gravimetric and volumetric energy densities of some common battery technologies [13].

1.2 Theoretical Background

Battery materials and cell designs are compared using parameters that describe aspects of their performance. New battery materials can be categorised by theoretical values for specific energy density, specific capacity and cell voltage. New cell designs can be evaluated in a similar way for commercial cells. Generally the most important factor is the amount of energy that can be gained from a given weight or volume of reactants or a typical cell design.

1.2.1 Energy Density

Specific energy can be expressed for a given cell reaction as a function of mass W_m or volume W_v in the following ways [14]:

$$W_m = \frac{-\Delta G}{m} \quad \text{(Gravimetric energy density)} \qquad \textbf{Equation 1.1}$$

or $$W_v = \frac{-\Delta G}{V} \quad \text{(Volumetric energy density)} \qquad \textbf{Equation 1.2}$$

Where, V is the volume and m is the mass of reactants.

The value $\Delta\overline{G}$ is the Gibbs free energy change for the given reaction and is related to the cell potential (E) by [14]:

$$E = \frac{-\Delta\overline{G}}{nF} \qquad \textbf{Equation 1.3}$$

Where n is the number of moles and F is the Faraday Constant (96485 C mol^{-1}).

1.2.2 Theoretical Capacity

Theoretical capacity (C_{Th}) is usually quoted in units of mA h g^{-1}; it gives the total theoretical charge stored per gram of active material, or total composite mass, given by:

$$C_{Th} = n_e \frac{m_{AM}}{M_{AM} \times 3.6} \times F \qquad \textbf{Equation 1.4}$$

Where m_{AM} is the mass of active material present in the electrode and M_{AM} is the molar mass of the active material. The value of 3.6 is included in order to convert the capacity in coulombs into mA h, a common way of quoting the charge stored in a battery material.

1.2.3 Specific Power

Specific power is related to the energy density at a given discharge rate and indicates how rapidly the cell can be discharged and how much power is generated. It is usually measured in watts per unit mass. Materials with a high energy density may also exhibit a high voltage and capacity drop at high discharge rate, and hence, have a low power density.

Specific power is given by:

$$P_{Sp} = \frac{IE}{m}$$ **Equation 1.5**

Where, I is the current.

1.2.4 Specific Capacity

The capacity of a cell is normalised to the quantity of active mass present and as with theoretical capacity it is commonly measured in mA h g^{-1}. The specific capacity C_{Sp} is related to the current by the following equation,

$$C_{Sp} = \frac{1}{3.6 \times m} \int_0^t I.dt$$ **Equation 1.6**

1.3 Non-Lithium Battery Systems

Battery systems based on chemistries other than lithium intercalation have been in development and production for many decades and were used in the new emerging technologies of the twentieth century. There are many different types of cell. Some are based on chemistry that is irreversible, and are thus, one-use (primary) cells (e.g., alkaline-manganese dioxide cells) and others are rechargeable (secondary) cells. Examples of these include lead-acid and nickel cadmium cells. Examples are summarised in Table 1.1. The practical energy density is defined as the amount of useful energy that can be extracted from the system.

1.3.1 Primary Cells

A primary battery is a cell that undergoes only one discharge. Once the active reagents have been consumed, the useful life of the cell is exceeded and cannot be recharged. Thus, the active component cannot be regenerated after discharging. One of the first primary cells to be developed was the Leclanché cell. This was

based on zinc and manganese dioxide with an aqueous electrolyte [15]. Variations on these types of cells are still in large-scale production today. In the Leclanché cell, the anode is composed of zinc and manganese dioxide (MnO_2) serves as the cathode with ammonium chloride and zinc chloride dissolved in water as the electrolyte. These cells provide an open circuit potential (OCP) between 1.55 and 1.74 V. The electrochemical system of the Leclanché cell is shown in Equation 1.7 [16].

$$Zn(s)|ZnCl_2(aq),NH_4Cl(aq)|MnO_2(s),C(s) \qquad \textbf{Equation 1.7}$$

During the discharge process in a Leclanché cell, oxidation of zinc occurs at the anode to form zinc ions in solution. A corresponding reduction of Mn^{4+} to a Mn^{3+} state occurs at the cathode. Variations on the Leclanché cell have been developed to optimise the system, for example the use of different electrolytes such as potassium hydroxide in the alkaline manganese cell. This results in a constant capacity output over a wide range of current drains. Another example of a variation on the Leclanché cell is the zinc chloride cell, in which the electrolyte consists mainly of zinc chloride electrolyte. This modification was found to result in better service capacity at high current drain, at low temperatures and on continuous discharge [17].

Table 1.1 - Some common battery types.

System	Example Cell Reaction	OCP / V	$\Delta \overline{G}$ / kJ mol^{-1}	n_e	Energy density / W h kg^{-1}
Leclanche [18]	$Zn\ (s) + 2MnO_2\ (s) + 2NH_4Cl\ (aq) \xrightarrow{e} 2MnOOH\ (s) + Zn(NH_3)_2Cl_2\ (aq)$	1.50	144	1	50-75
Primary Alkaline [19]	$Zn\ (s) + 2MnO_2\ (s) + H_2O\ (l) \xrightarrow{2e} 2MnO.OH\ (s) + ZnO\ (s)$	1.50	289	2	120
Lead Acid [20]	$Pb\ (s) + PbO_2 + 2H_2SO_4\ (aq) \xleftrightarrow{2e} 2PbSO_4(s) + 2H_2O(l)$	2.15	415	2	30-40
Lithium Primary [21]	$nx\text{Li}\ (s) + (CF_x)_n\ (s) \xrightarrow{e} nx\text{LiF}(s) + n\text{C}\ (s)$	3.10	299	1	515-2180
Lithium Secondary [22]	*General:* $yLi + Li_x(HOST) \xleftrightarrow{e} Li_{x+y}(HOST)$ $Li_{1-x}FePO_4 \xleftrightarrow{e} Li_{1-x}FePO_4 + x\text{Li} + e^-$	2 to 5 3.5	193-482	1	260-400

The values for ΔG quoted in Table 1.1 for the above relations were calculated from the cell potential. These values reflect the free energy of the reactions in the cell and are therefore non-standard. The cell potential is the most accurate method for the calculation ΔG.

1.3.2 Secondary Cells

Secondary cells have the benefit of being based on reversible chemical processes. Therefore, they can be charged, discharged and then recharged many times. Lead acid cells currently account for the largest market share of all battery systems (> 50 %) because of their low cost and excellent reversibility of cycling [23]. However, lead acid cells are large and heavy and have a specific capacity much lower than that of lithium systems (~ 30 mA h g^{-1}) [20].

Other secondary battery systems include those used in portable electronic devices, such as in early mobile phones and camcorders. These systems are based on nickel cadmium oxide (NiCd) and nickel metal hydride (NiMH) chemistries. Such systems involve the oxidation and reduction of transition metal oxides by the movement of hydrogen [24].

1.4 Lithium Cells

Research in the area of lithium batteries has seen rapid growth due to a large demand for battery systems with high specific capacity, energy and power density. Battery systems based on lithium redox chemistry provide many benefits over existing systems mainly due to the large negative electrode potential of lithium metal (-3.04 V *vs.* NHE [25]) and the high energy storage capability of lithium transition metal oxide materials.

When lithium metal is combined with suitable positive electrode materials, such as $LiCoO_2$ or $LiMnO_2$, in a cell, systems with high cell voltages, commonly of OCP and working voltages around 3 - 4 V *vs.* Li are produced. Some systems exhibit cell potentials as high as 5.0 V *vs.* Li, such as $LiCoPO_4$ with a structure based on the olivine type mineral [26]. A benefit of this high cell potential is that the number of cells in a battery required to provide a useful potential can be reduced by a factor of two or three. This is particularly useful for microelectronics

applications, such as mobile phones, laptop computers and digital cameras and the developments of new on-chip battery technologies to power small microchip-sized devices; all of which operate at high potentials [27].

1.4.1 Chemical Potential

The rationale for the interest in battery systems lies in thermodynamics. The high voltage of lithium systems relative to other battery chemistries can be explained by the free energy of the insertion reaction, in which lithium guest ions are inserted or removed from host materials. As a guest ion is incorporated into the host, the Gibbs free energy G changes with number of moles of guest atoms (n_g). Such changes are described by the chemical potential μ. This refers to the potential of a single species, (Li), given by Equation 1.8. More generally, n refers to a change in the composition of the system, and changing the value of $\Delta G/n$ will change the electrochemical potential at which the insertion reaction occurs. The value of μ can be directly measured from the cell potential E.

$$\mu = \Delta G / \Delta n_{Li} \qquad \textbf{Equation 1.8}$$

A cell with a lithium negative electrode and a host inorganic positive electrode has chemical potentials μ and μ_0 respectively. If the guest has a charge ze in the solution of the cell (z = 1 for Li), one lithium ion is intercalated for every z electrons passed though the potential difference E. The word done on the cell by each intercalated ion is $-zeE$. This work is equal to the change in free energy of the two electrodes, which is ΔG, the Gibbs free energy.

1.4.2 Cell Potential

The cell voltage can be calculated from the maximum energy available from a reaction (ΔG). The value of ΔG can be maximised using electrode materials that have a large difference in chemical potential.

$$E = \frac{(\mu_{Li}^{Neg} - \mu_{Li}^{Pos})}{F} \qquad \textbf{Equation 1.9}$$

And the average cell potential is also related to the Gibbs free energy change for a system by [14],

$$E = \frac{-\Delta G}{F}$$ **Equation 1.10**

In the case of a lithium battery, the lithium metal negative electrode is zero on this scale and cathode materials are chosen with a large negative value of chemical potential to maximise the cell voltage. During the reaction, the chemical potential of the lithium electrode remains constant (as it is metallic) and undergoes no phase change on cycling. The chemical potential of the positive electrode however, can vary during the intercalation reactions.

1.4.3 Lithium Primary Cells

Primary cells based on lithium were first commercialised by SAFT in 1973 after nearly two decades of research [28]. Cells based on lithium metal anodes are of interest as commercial cells, because lithium metal provides favourable thermodynamic electrode potentials with very high specific capacity. It is also lightweight and its oxidised form is non-toxic. Primary cells have been developed with voltages of around 3 V *vs.* Li and with energy densities in excess of 300 Wh kg^{-1} [7]. Another benefit is the long shelf life offered by lithium primary cells due to the formation of a passivating layer on lithium metal anode inhibiting self-discharge, known as the SEI (Solid-Electrolyte Interface). This process allows cells to be stored for 5-10 years at ambient temperature with little loss in cell capacity [29].

Lithium cells are capable of operating over a wide range of temperatures, due to the low freezing point of non-aqueous solvents. Therefore, lithium cells can operate practically at temperatures as low as -40 °C, and cell construction allows operations as high as 60 °C [30]. These properties make them favourable for use in low-rate devices, such as watches and calculators, where they are capable of long operating times.

Lithium primary cells utilise non-aqueous electrolytes composed of aprotic organic solvents containing a dissolved lithium salt such as $LiPF_6$. In most lithium primary cells, the negative electrode is lithium metal and the positive electrode must

be a material that can undergo an electrochemical reaction with lithium metal, providing a high cell voltage and energy density in comparison to other primary cells, an example is shown in Table 1.1.

1.4.4 Secondary Lithium Cells

Rechargeable (secondary) lithium cells used for electrochemical testing are traditionally composed of a lithium metal negative electrode, non-aqueous electrolytes and a positive electrode material capable of undergoing a reversible electrochemical reaction. These materials are generally composed of rigid inorganic materials that are open structures to enable the insertion or de-insertion of lithium ions on cycling. They are known as intercalation hosts or staged structures in which ionic species can be reversibly inserted or removed electrochemically with only minor changes to the structure of the host lattice, an example is $LiMn_2O_4$ spinel [31]. During charging, the lithium ions are removed from the active material leaving Mn_2O_4 with manganese in a + 4 oxidation state. During discharge, lithium is inserted into the structure and manganese is reduced effectively to + 3.5; or more accurately Mn^{3+} and Mn^{4+} co-exist in the structure [32].

Figure 1.2 is a representation of a simple lithium cell, which on charging, lithium is removed from the host structure and plated through the electrolyte on to lithium metal. During discharge, lithium ions flow from the negative electrode and are incorporated into the host structure of the positive electrode material. The reverse of this occurs during charge, when lithium is removed from the host and plated on the surface of lithium metal.

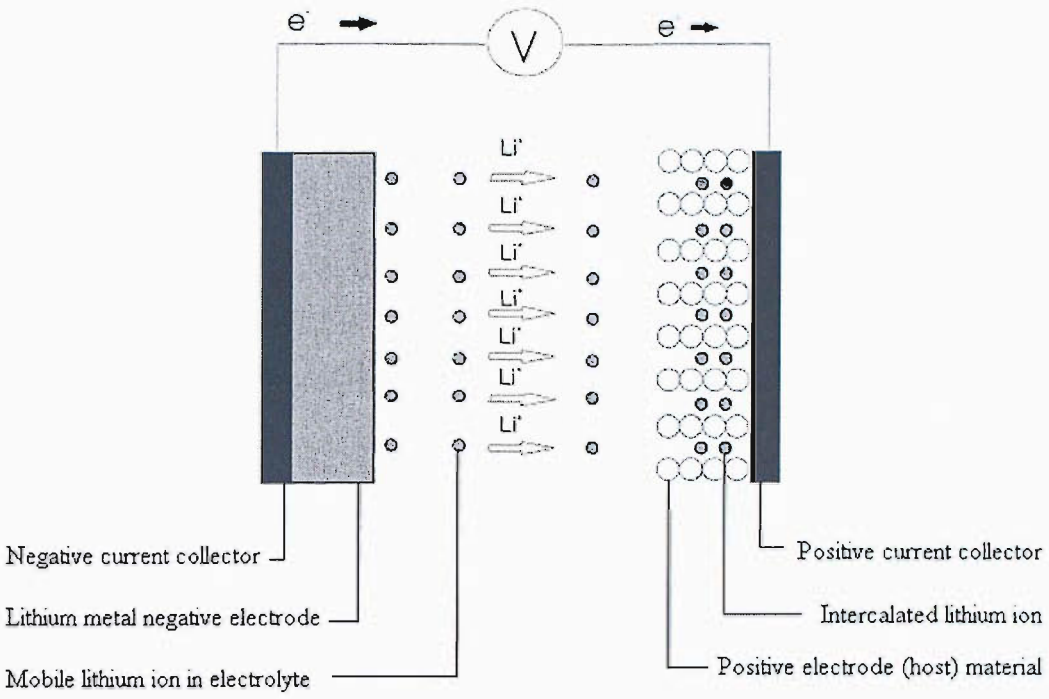

Figure 1.2 - A schematic diagram of a lithium cell under discharge conditions [11].

This reaction yields a flow of electrons through a circuit due to the difference in chemical potential between the negative and positive electrodes and determines the cell voltage (*E* in V *vs.* Li). Due to the difference in electrode potentials between the positive inorganic materials and lithium, cell voltages between 2 and 5 V can be achieved [33], making these cells attractive for use in high power applications (see Figure 1.3).

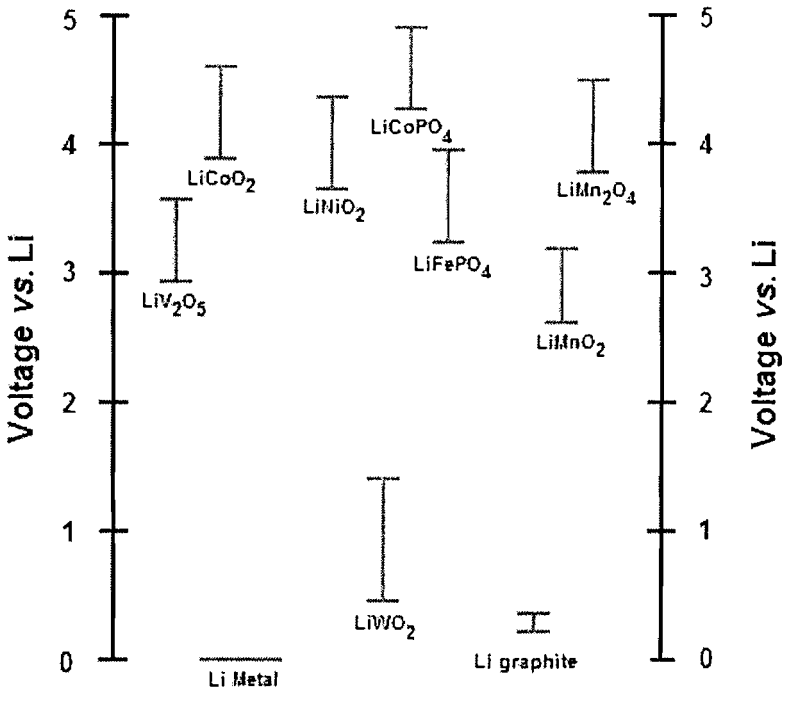

Figure 1.3 - Electrochemical potential of some lithium intercalation compounds *vs.* metallic lithium [34, 35].

1.4.5 Positive Electrodes

Positive electrodes used in lithium rechargeable batteries generally consist of the inorganic transition metal containing compounds described above. Many materials have been investigated as potential positive electrode materials and a few have reached the commercial stage, most notably lithium cobalt oxide ($LiCoO_2$) [36].

When choosing a positive electrode material, one must aim to maximise the specific capacity, conductivity, optimise the operational voltage range and minimise the amount of non-redox active additives, such as binder and conductivity additive. Table 1.2 shows some common positive electrode materials and their properties.

Table 1.2 - Common positive electrode materials used in lithium batteries.

Material	Voltage *vs.* Li / V	Specific capacity/ mA h g^{-1}	Disadvantages	Advantages
V_2O_5	3.3	182	Poor cyclability	Inexpensive
MnO_2	3.0	115	Poor cyclability	Inexpensive, Environmentally benign
$LiMn_2O_4$	4.0	120	Low capacity	Non-toxic, inexpensive, environmentally benign
$LiFePO_4$	3.5	170	Low density	Non-toxic, inexpensive, environmentally benign, safe
$LiNiPO_4$	5.0	170	Low conductivity	High voltage
$LiCoPO_4$	4.8	170	Toxic, expensive	High voltage
$LiNiO_2$	3.8	220	Unsafe	Less expensive than Cobalt
$LiCoO_2$	3.9	180	Toxic, expensive	Good rate capability, high conductivity

The first commercial lithium cell to be sold in large numbers was the 'lithium-ion' cell or rocking chair cell based on lithium cobalt oxide ($LiCoO_2$) positive electrode material, which was commercialised by *Sony* in 1991 [36]. $LiCoO_2$ was chosen because of its high rate capability, high voltage and good conductivity. However, other potential positive electrode materials have been studied in recent years most notably $LiMn_2O_4$ [31, 37] and $LiFePO_4$ [38]. Both have been examined extensively due to their low cost, environmental benignity and high capacity.

The feasibility of $LiFePO_4$ as a positive electrode material was first demonstrated in 1997 by Padhi *et al.*, in which the material was synthesised by solid-state reaction. Their initial electrochemical tests achieved a specific capacity value of between 100 and 110 mA h g^{-1} less than the 170 mA h g^{-1} theoretical value. However, this material has since been regarded as the most promising material for use in future applications. $LiFePO_4$ shares the general structure of olivine type materials that are based on $(Mg,Fe)_2SiO_4$, which is commonly found throughout the earths crust [39].

$LiFePO_4$ is a crystalline solid material of ordered olivine structure (orthorhombic) in which phosphorus atoms occupy tetrahedral sites with iron and lithium occupying the octahedral sites. FeO_6 octahedra are linked through common corners in the *bc*-plane and LiO_6 octahedra form edge-sharing chains along the *b*-axis (see structure Figure 1.4) [40]. The cell reaction is shown below in Equation 1.11.

$$LiFePO_4 - xLi^+ - xe^- \leftrightarrow Li_{1-x}FePO_4 \quad [38] \qquad \textbf{Equation 1.11}$$

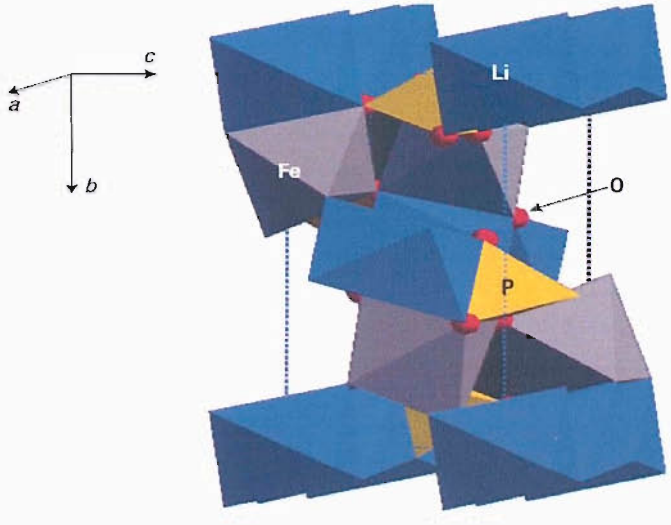

Figure 1.4 - The structure of olivine phase $LiFePO_4$, structural arrangement of atoms is identical to that of the mineral $(Mg,Fe)_2SiO_4$ consisting of interconnected edge sharing octahedra of Fe and Li with phosphorus occupying the tetrahedral sites [41].

New synthesis routes have been developed for $LiFePO_4$ as a means to obtain almost full theoretical capacity of 170 mA h g^{-1}. Many groups have used traditional solid-state synthesis routes to produce materials which give up to 95% theoretical capacity [42]. These routes involve using solid powders of transition metal containing oxides and hydroxides and grinding them using a pestle and mortar to form a somewhat homogeneous precursor. This precursor is then calcined in a furnace for typically ten hours or more until the material has reacted. The material that is obtained is generally of low purity and must undergo successive grinding and

calcination steps to obtain a pure single-phase product. An example of such a route is the oxalate route suggested by Andersson *et al.* [43].

To prepare a sufficiently pure phase material using this type of route, high temperatures in excess of 800 °C must be used for several days. This is due to the large distances (> 1 μm) between diffusing species (see section 1.5).

On electrochemical cycling, $LiFePO_4$ materials demonstrate two-phase behaviour in which the lithium electrochemically is removed from the host structure $FePO_4$ and deposited on the negative electrode. Table 1.3 summarises the main synthesis routes for $LiFePO_4$ reported to date.

Table 1.3 - Synthesis routes reported for the preparation of $LiFePO_4$ consist mainly of solid-state preparation routes. The development of sol-gel or solution based routes would greatly reduce the calcination temperature and reaction time.

Synthesis type	Precursors	Preparation conditions	Specific capacity / mA h g^{-1}	Cycling conditions	Ref.
Solid-state	$Fe(CH_3COO)_2$, $(NH_4)_3PO_4$, Li_2CO_3	300-350 °C, re-grinding, treatment at 800 °C, 24 h	122	RT, 2.0/4.5 V	[38]
Solid-state	Li_2CO_3, $FeC_2O_4 \cdot H_2O$, $(NH_4)_2HPO_4$	300 °C in vacuum, 450 °C for 10 h, 800 °C for 36 h	65	23 °C	[44]
Solid-state	CH_3COOLi, $Fe(CH_3COO)_2$, $NH_4H_2PO_4$	Mixed in carbon gel (15 wt.% C), 350 °C 5 h, 700 °C 10 h	155	RT C/5 2.8/4.0 V	[42]
Solid-state	$FeC_2O_4 \cdot 2H_2O$, $(NH_4)_2HPO_4$, $LiOH \cdot H_2O$	350 °C 5 h, regrinding, 675 °C 24 h, cooled to 70 °C, 14 h	100-110	20 °C 3.0/4.0 V	[45]
Solid-state	$Fe(CH_3CO_2)$, $NH_4H_2PO_4$, Li_2CO_3	320 °C 10 h, regrinding, 400-800 °C, 24 h	160	23 °C C/38	[46]
Hydrothermal synthesis	$Fe_3(PO_4)_2 \cdot 5H_2O$, Li_3PO_4, sucrose 5 wt.%	Hydrothermal synthesis: 220 °C, 24 bar, 1 h, milling for 24 h; 550 °C 0.25 h	155-160	RT C/50 2.0/4.5 V	[47]
Hydro-Quebec Synthesis	$Fe(CO_2CH_3)_2$, $NH_4H_2PO_4$, $LiCO_3$, Sucrose	700 °C, 4h, 8 % H_2 in Ar, second treatment with sucrose 0.1-10 % of mass	160	20 mV h^{-1}, 80 °C	[48]
Sol-gel	$Fe(NO_3)_3.9H2O$, $Li(CH_3CO_2)$, H_3PO_4, $HOCH_2COOH$	600-700°C, 5-15h	100	RT	[48]

1.4.6 Negative Electrodes

Lithium metal was used as a negative electrode in early lithium rechargeable batteries due to its high specific capacity and high electrode potential. However, its electropositive nature makes it unstable in a wide variety of electrolyte systems leading to the formation of a passivating layer on the negative electrode enabling long storage times with little loss in capacity. This property is advantageous for primary cells, but can cause problems when it is used in secondary cells, especially on discharge. During the charging process lithium is removed from the positive host material and plated on the surface of the metallic lithium, which plates with almost 100% efficiency. However, on discharge the stripping is not 100% efficient because some deposited lithium grains become undercut and others become completely isolated from the bulk material upon repeated charging and discharging. This process produces a more porous electrode surface than in the original case. The increase in surface area increases its reactivity and reactions with components in the electrolyte lead to high cell temperature and eventually thermal runaway.

The commercial lithium cells of today use carbon-based negative electrodes in which lithium is removed and inserted via an intercalation reaction. Perhaps the most widely used negative electrode is graphite that has a layered, staged structure that can easily accommodate one lithium atom per six carbon atoms (LiC_6, see Figure 1.5). Upon cycling graphite, the observed potential decreases in a series of plateaux eventually reaching a value of 0.02 V *vs.* Li for the composition LiC_6 [49].

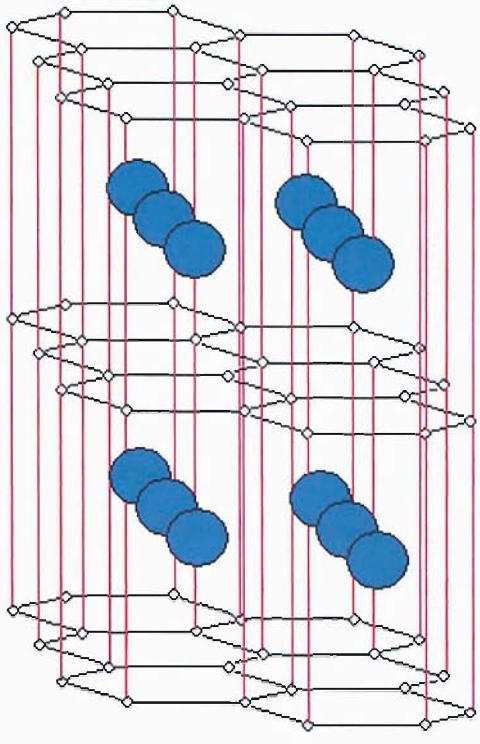

Figure 1.5 - Lithium intercalation in graphite to form the AAA structure of graphite. Intercalation reactions result in the production of staged structures, which exist at different voltages. The structure reaches its maximum stoichiomentry when six carbon atoms surround one lithium ion. The intercalated lithium ions are shown as blue spheres.

1.4.7 Electrolytes

Lithium battery materials require the use of non-aqueous electrolytes due to the reactivity of lithium with water. These solvents are usually aprotic organic solvents containing a lithium salt to provide high conductivity. Recent work has also focused on the development of polymer electrolytes that have led to the polymer lithium ion battery or *Plion* battery [50]. Polymer electrolytes are composed of lithium salts such as $LiPF_6$ dissolved in high molecular weight polymers such as poly(ethelene oxide) (PEO). An electrolyte must employ a solvent that has a high solubility for lithium ions; it must also be safe and non-toxic [51]. The electrolyte salt must be of high ionic mobility for the lithium ion and thermally, electrochemically and chemically stable. To reduce thermal runaway in lithium

cells, electrolytes contain additives that are active at high potentials, which act as overcharge protection for the cells [52, 53]. These additives undergo electrochemical reactions at potentials above that of the active materials and around the potential at which the decomposition of the electrolyte solvent occurs. These reactions are either electro-polymerisation or redox shuttle reactions that inhibit the decomposition of the electrolyte. This stops the build up of hydrogen in the cell casing and reduces the risk of units catching fire [54, 55].

1.5 Preparation Techniques

There are many possible techniques that can be used to prepare inorganic materials. These include chemical vapour deposition, sputtering techniques and traditional solid-state synthesis methods. In addition, sol-gel methods are useful, as they require all reagents to be in the solution phase, this makes these methods suitable for use with combinatorial synthesis methodologies. In this research both solid state and sol-gel methods were used for materials preparation.

1.5.1 Solid State Synthesis

Solid-state reactions involve the heating of solid reagents at high temperatures for many hours to yield crystalline materials. This method of synthesis is most widely used for the preparation of many useful inorganic materials including battery materials. In these reactions, the precursor materials are mixed together using a pestle and mortar to produce a mixture of solid precursor. The materials are usually poorly mixed and, therefore, temperature and calcination times must be high to yield a pure product. The reason for these high temperature conditions is due to the overall energy of the process of bond-making and bond-breaking in a solid material. The reaction of two crystalline phases to form a product occurs by the migration of ions between the interfaces two phases by diffusion. In the case of an organic reaction, typically only one bond is broken or formed. Therefore, these reactions can proceed at low temperatures. However, in a solid-state reaction, the bonding in the whole structure may be affected [56] and hence, these reactions occur at high temperatures.

1.5.2 Sol-gel and Solution Techniques

Sol-gel and solution routes are an ideal type of procedure to adapt for combinatorial synthesis because in a combinatorial experiment, there is an emphasis on a rapid one-step approach to simplify the process or rapid preparation on an array. Because sol-gel-type reactions generally proceed by a one step calcination step they are very suitable for use in conjunction with parallel preparation methods. In sol-gel/solution synthesis techniques, diffusion distances are low, and hence, only short heating times or a low-temperature heating period is required. Because inorganic materials prepared using combinatorial techniques cannot easily be reground and re-calcined many times on the array, it is important to complete the desired reaction in one step with no disruption to the sample. It is also advantageous to have all reagents in solution to enable compositional changes to be made using existing commercial liquid handling systems. A general scheme for a sol-gel reaction is shown in Figure 1.6.

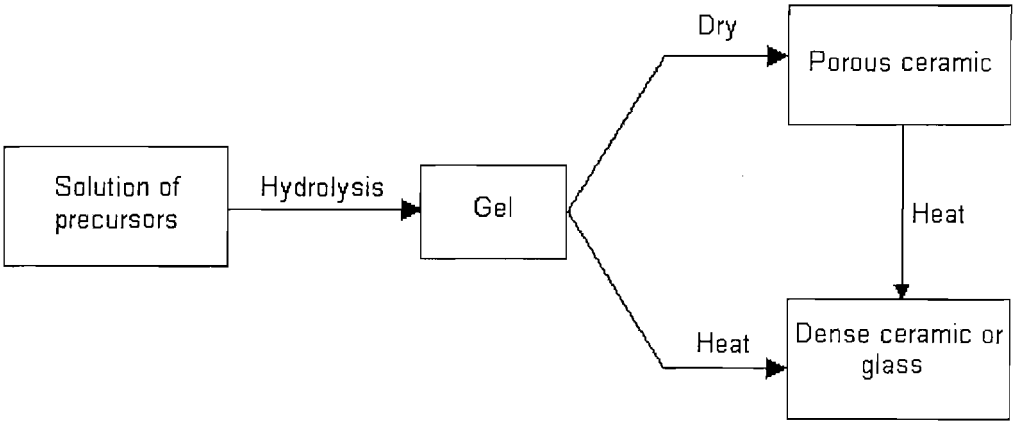

Figure 1.6 - The sol-gel process. When the gel is dried at high temperature dense ceramics or glasses are formed. Drying at low temperatures above the critical pressure of water produces microporous solids known as xero-gels or aero-gels [57].

Reactions to produce inorganic materials proceed mainly by diffusion of ionic species within a precursor material in which bonds are made and broken. This often requires high temperatures and long heating times. It is, therefore, favourable to decrease the distance between the reacting particles or the overall particle size to reduce these diffusion distances and hence reaction temperatures.

Solution and sol-gel routes were first developed to prepare glasses and ceramic materials [58], but many solution and sol-gel routes to other inorganic materials including battery materials have been reported. Sol-gel routes exist for the preparation of $LiCoO_2$ [59], $LiCo_{1-x}Ni_xO_2$ [60], $LiMn_2O_4$ [61] and recently a sol-gel route to $LiFePO_4$ has been reported using citric acid as a chelating agent [62].

A sol-gel reaction (see Figures 1.7 and 1.8) has the benefit of reducing the particle size and hence the reaction rate using chemical bonding, to link reacting particles together forming a gel. A chelating agent is introduced to the precursors, such as a molecule with two or more carboxylic acid functionalities. These acid functions react to form bonds with the precursor components in a type of polymerisation reaction that leads to the formation of a xero-gel as the solvent is removed (see Figure 1.6). This gel is then heated in a tube furnace, often at lower temperatures than are required in a standard solid-state reaction yielding a product that should require little further heat treatment.

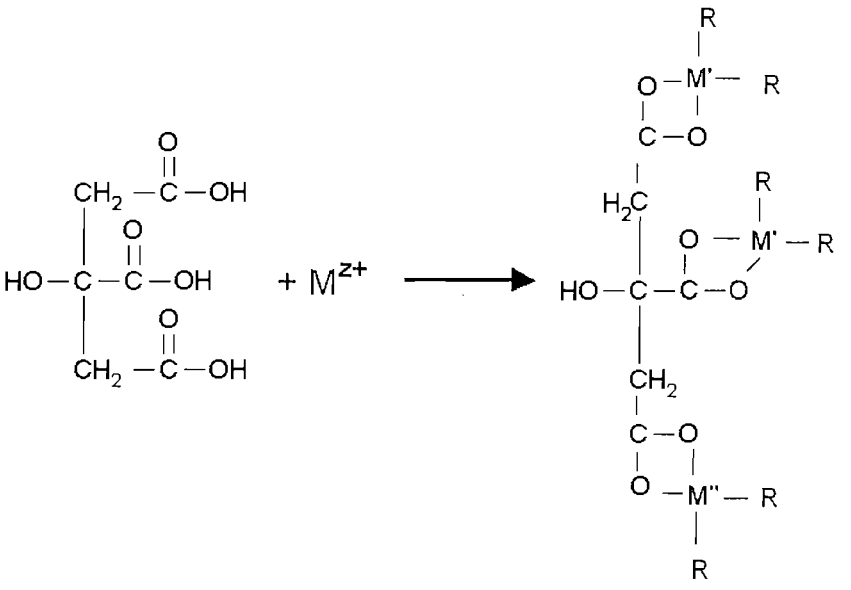

Figure 1.7 - An example of a sol-gel reaction, in which the inorganic components are bonded together via a chelating agent, in this case citric acid. The carboxylate ligands bond to the metal centre in several ways, for example they can be bridging, monodentate, or bridging-chelating.

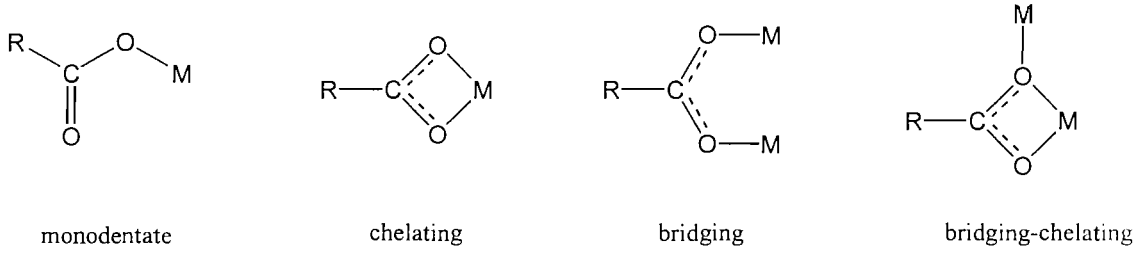

Figure 1.8 - Types of ligand bonding for carboxylate groups with metal ions.

Solution routes have been developed which rely on the decomposition of species at moderate temperatures, such as metal carbonates, hydroxides and nitrates. When these crystallites decompose, they lose gaseous species that yield small very reactive particles thus, resulting in increased reaction rates. Homogenous mixtures can be prepared from solutions of reactant ions dispersed on the atomic scale. However, when the solvent is removed, it is important to ensure that the dry precipitate is of the correct stoichiometry. As the precursor materials are dried, the different components must be confined in close proximity. If not, components will

separate from one another and crystallise at different locations in the dried materials leading to non-stoiciometric precursor, which may not produce the desired product after calcination.

Therefore, a technique must be developed to enable the components to crystallise in the same region or to inhibit crystallisation. This can be achieved by adding a gelling or fixing agent, such as a long chain polymer or possibly a sugar. Studies by Nguyen *et al.* have produced a route to the synthesis of oxide powders by polymeric steric entrapment in which transition metal precursors are confined in the correct stoichiometry within polymer chains of PVA [63].

1.6 Power Density and Percolation Effects

Lithium battery materials are useful because the redox reactions that occur at a given potential yield a flow of electrons or current. The electrical energy from the reactions is stored, as chemical energy is associated with the oxidation state of the host structure. The amount of current that can flow is related to the external load resistance of the cell and can depend on resistance of the electrode materials and electrolyte. The power of a cell is calculated from the product of cell potential and the current. This is important because it is a measure of the ability of a cell to sustain a large current drain without premature polarisation. Polarisation of the cell occurs when the applied current causes depletion of the active material species (*e.g.*, Li) at the electrode surface. This leads to large overvoltages and eventual polarisation.

The ability of a cell to sustain large current drains depends on the ease of electron transfer from the current collector to the active material, and hence the conductivity. However, such redox active materials are often poor conductors, and therefore, the full capacity associated with the redox reactions is inaccessible in their pure form. It is often necessary to add a conducting component to the electrode material; this is added to the pristine material usually as carbon black or graphite. The addition of a large amount this conductor results in the formation of a percolation network, which introduces conducting pathways between the poorly conducting active particles. At low carbon loadings, a poorly defined network exists which is not sufficiently developed to facilitate the utilisation of the capacity of the active component. At high values of carbon loading, a well-defined network exists

in which all the particles of active material are sufficiently connected. The point at which the addition of further carbon causes no significant increase in the composite conductivity is known as the percolation threshold.

The critical value of the percolation threshold is referred to on many occasions in the results and discussion sections of this thesis. There are many mathematical relationships and models in the literature to describe the effects of percolation and the percolation threshold (V_c) [64-66] providing a variety of definitions and theories.

Broadbent and Hammersley [67, 68] were the first to study percolation behaviour and developed lattice models for the flow of fluid through a static medium. They successfully showed that the flow of fluid did not occur if the concentration of the static medium was smaller than some nonzero value. In addition, they introduced the theory of percolation probability, which describes the likelihood that a given region is sufficiently well connected to the other regions to facilitate conduction [69]. Numerical studies of percolation within lattices have been carried out by Dean and Bird [70], in which they used the site percolation model to study *2D* and *3D* lattices. From this and other studies [71] emerged the understanding of the topological aspects of percolation threshold, which describes the stages of site percolation within a lattice (see Figure 1.9).

Last and Thouless explored this type of lattice model experimentally using a sheet of conducting graphite paper with 2500 possible conduction sites with a random arrangement of punched 'holes'. In the experiment, a hole represented a non-conducting site, whereas the un-punched material was considered closed. The holes were punched randomly using a random numbers to generate the x and y co-ordinate values and the conductivity of the sheets was measured after every 25 pairs of numbers were punched into the sheet [72]. They found that the conductivity as a function of the amount of paper remaining approached zero at the critical concentration for *2D* site percolation (V_c).

The most prominent model is the statistical percolation model developed by Kirkpatrick [69] and Zallen [73] with which geometric and electrical quantities can be forecasted. This model is based on the assumption that the conducting (filler) components do not interact with one another and are therefore randomly dispersed in the matrix. The statistical percolation model allows the forecasting of the behaviour of a completely unconnected set of objects. By varying the number of connections,

the model allows the description of the transition from a local to an infinite 'communication state'. In this model, the percolation threshold is described as the critical volume fraction separating these two states [66]. Close to the percolation threshold the statistical model predicts a power-law variation for the measurable quantities with the volume fraction of fillers.

This theory can been related to the dc electrical conductivity (σ), which shows a power-law dependency close to the percolation threshold such that when $V > V_c$.

$$\sigma \propto (V - V_c)^t \qquad \textbf{Equation 1.12}$$

Where, V is the fraction (or concentration) of conducting additive and t is the exponent characterising the transition. This is assumed to be universal and therefore depends only on the dimensionality of the system, $t \approx 2$ for a three dimensional system.

Percolation theory has been used in many areas of science to describe the effects in disordered systems, its derivations lie in the probabilities of site occupancy. An example is a square lattice where each site is occupied randomly with probability *(p)* or empty with probability *(1-p)*. Occupied and empty sites denote very different physical characteristics, as in the example of battery materials. If the occupied sites are conductors and the empty sites are insulators and electrical current can only flow between the nearest neighbour sites. At low concentration, the conductor sites are isolated and are found in small clusters. Two conductor sites are part of the same cluster if a path of nearest neighbour conductor sites connects them. At low values of *p,* the mixture is an insulator since a conducting path between each sides of the lattice does not exist, as in Figure 1.9 (a)]. At high p values, a large number of conduction sites exist, and hence, many conducting pathways exist between both sides of the lattice. This makes the mixture conducting as in Figure 1.9 (c). At a value between these two extremes, a point exists at which the mixture first becomes conducting; this is defined as the conduction threshold [see Figure 1.9 (b)] as described by Seager and Pike [74].

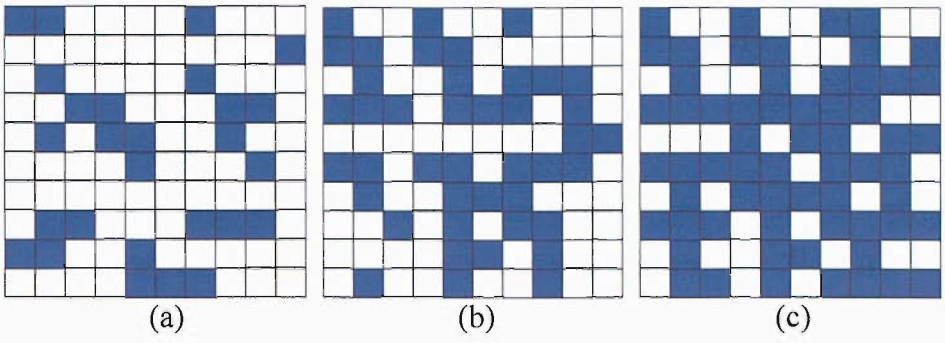

Figure 1.9 - Percolation network formation in a binary mixture, (a) below the conduction threshold, (b) at the conduction threshold, (c) above the conduction threshold.

In the area of lithium battery materials, ternary composites of active material, a conducting additive (*e.g.*, CB) and a polymer (*e.g.*, PTFE) are prepared and used as electrode materials. The active materials are often poor electronic conductors that require the addition of conducting carbon to enable full utilisation of their capacity. The manner in which the carbon interacts with the active material and polymer gives rise to percolation phenomenon as described in Figure 1.10

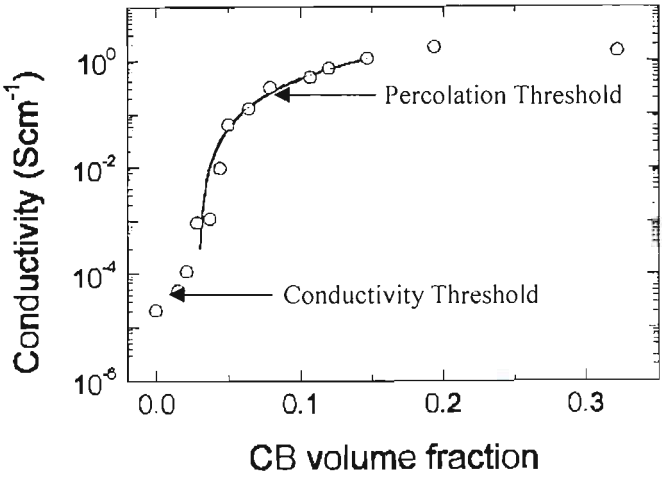

Figure 1.10 - Conductivity *vs.* CB volume fraction. The solid line gives the best fit for the equation $\sigma = \sigma_0(V - V_c)^t$. $\sigma_0 = 41$ S cm^{-1}, $V_c = 0.03$ and $t = 1.7$. Reproduced from [75].

In this thesis, the percolation threshold referred to in the results and discussion sections for lithium battery electrode compositions. It is defined as the point at which the increase in the amount of conducting additive does not significantly increase the conductivity of the composite. It is the critical point at which the conducting components increase in mass fraction no longer results in a significant increase in conductivity. The percolation threshold can therefore be defined as the point at which the further addition of the conductive component to the mixture does not significantly increase the conductivity of the composite.

1.7 Combinatorial Techniques

The development of a strategy to rapidly prepare and screen samples for useful properties has become an important tool in chemistry, crossing a multitude of disciplines and has seen the largest growth in organic synthesis in the area of drug discovery. Recently, this methodology has been applied to other areas of chemistry and is an emerging tool for use in the discovery and optimisation of materials. The area of combinatorial chemistry grew rapidly in the late 1980s and early 1990s and is now represented by many books and a journal [76, 77].

Combinatorial research projects are common in organic chemistry laboratories in both academia and in industry. Pharmaceutical companies now consider the combinatorial techniques developed in the late eighties as tools for the development of new marketable products. With the arrival of the discipline of combinatorial chemistry has come the commercialisation of laboratory equipment particularly suited for high-throughput experimentation and extensive patent applications by companies such as Symyx [78]. The development of computer-controlled apparatus such as robotic liquid handlers and characterisation tools has enabled large numbers of experiments to be performed simultaneously in a rapid, routine and reproducible manner. For example, the sequencing of the human genome made extensive use of robotic laboratory equipment designed for combinatorial chemistry and the undertaking of such a project would not have been possible had DNA sequencing equipment not been developed with high-throughput experimentation in mind [79].

1.7.1 The Combinatorial Principle

The combinatorial strategy in its general sense comprises the treatment of a given starting material with many successive alternative processing steps, such as treatment with a different type of precursor or different sequence of precursors as in the case of solid phase synthesis. Additional alternative parameters may include the processing temperature or the type of solvent used (see Figure 1.11).

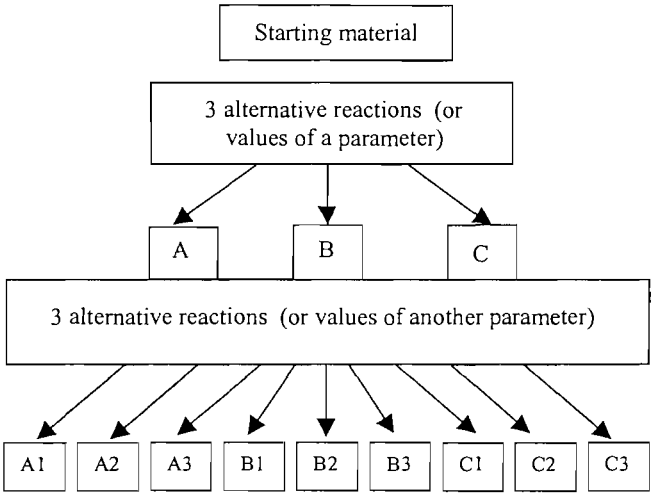

Figure 1.11 - The combinatorial principle.

1.7.2 Combinatorial Methods in Organic Chemistry

Combinatorial chemistry has its roots in the development of the process of solid phase synthesis that was first demonstrated for a tetrapeptide by Merrifield in 1963 [80]. This new approach to peptide synthesis involved the sequential attachment of amino acids to an insoluble polymer (a chloromethylated copolymer of styrene and divinylbenzene). Each step involved the addition of a new amino acid group to the peptide resulting in the formation of large peptide chains that could not be prepared easily using conventional methods due to technical difficulties with solubility and purification. The method allowed ease of separation of precursors and products by filtration and the polymer was easily removed once the desired peptide had been prepared. Merrifield also stated that this type of reaction was conducive to automation, allowing any number of different peptides to be prepared.

The work of H. M. Geysen helped to initiate a combinatorial revolution in chemistry, which began with the publication of his first paper in combinatorial chemistry [81]. He was the first to demonstrate the power of combinatorial or high-throughput experimentation to find useful compounds [82]. In his 1986 paper, it was suggested that small peptide chains may illicit antibody responses in animals and neutralise the infectivity of a protein-bearing microorganism. It was hoped that synthetic vaccines could be developed based on this effect. In order to accomplish this, a complete set of epitropes had to be produced. These would then need to be screened to determine the correct member for a target antibody. Geysen and co-workers achieved the parallel preparation of hundreds of peptides in the form of reusable libraries, thus validating the combinatorial method [81, 82].

Since this pioneering work hundreds of papers have been published and combinatorial chemistry has developed into an invaluable tool used in many disciplines in chemistry and biological sciences. In fact, the large number of papers reporting new developments in the field led to the commission of the Journal of Combinatorial Chemistry in 1999.

1.7.3 Combinatorial Methods in Materials Science

The discovery of new materials is often a process of trial and error involving many experiments; this is often expensive and time consuming. Advanced materials are

often composed of a multitude of components all of which need to be optimised to obtain useful functional materials. Ultimately materials science is not concerned with the screening of materials but screening for useful properties.

The combinatorial techniques developed for organic chemistry made use of molecular diversity by changing the quantity of staring materials and processing parameters to produce potentially billions of compounds. This was possible because the variables in synthesis of a large molecule are almost infinite. Because many materials exist as multi-component systems or composites, many variables in their synthesis may be changed giving rise to a large number of materials from only several precursors.

Combinatorial methods have been successfully applied to many areas of materials science, such as electrocatalyst screening, superconducting materials and thin film dielectric materials. The idea of preparing a large number of samples simultaneously in materials science was first outlined by Kennedy *et al.* in 1965. In this work, composition spreads of ternary-alloys were prepared on stainless steel and molybdenum foil substrates [83]. The substrate was divided up into 200 equally sized samples and characterised by X-ray fluorescence.

The work of Hanak introduced the new concept of high-throughput experimentation in materials science in 1970 [84]. The paper outlined a new approach to synthesis by preparing all possible compositions of three-component superconducting materials using a co-sputtering method. The main problem faced by Hanak and co-workers was the characterisation of the arrays, but it was recognised that the characterisation should be rapid and non-invasive. It was decided to measure the transition temperature (T_c), as it was known to be very sensitive to compositional changes and was easily measured for all compositions simultaneously. This approach to high throughput screening is outlined in Figure 1.12.

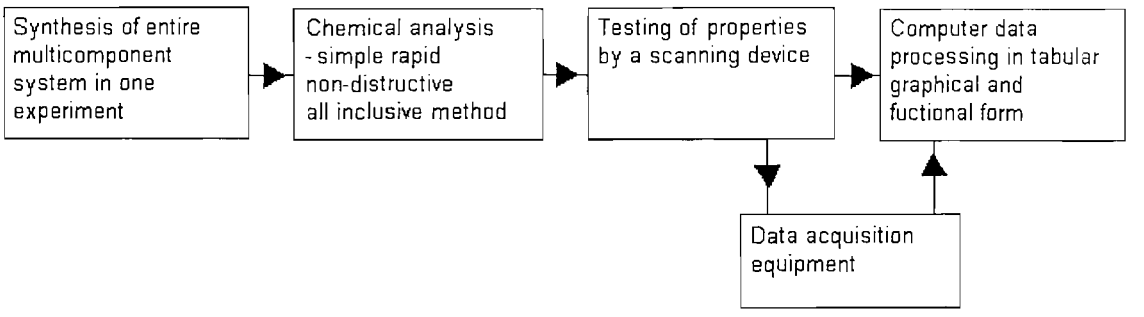

Figure 1.12 - Flow chart of processes needed for the study of entire multicomponent systems in single steps [84].

Reddington *et al.* [85] reported of the use of parallel screening methodologies applied to electro-functional materials. In this study, optical screening for fluorescent materials was used to determine the activity of arrays of electrochemical catalyst materials for use in direct methanol fuel cells (DMFC). The ions generated in the electrochemical reaction were converted to a fluorescence signal using a fluorescent acid-base indicator. The H^+ ions generated by the electro-oxidation of methanol were imaged and a 645-member electrode arrays containing five elements (palladium, ruthenium, osmium, iridium and rhodium) were screened. This resulted in the discovery of a catalyst of optimum performance with the following atomic percentage proportions (palladium [44%], ruthenium [41%], osmium [10%], and iridium [5%]).

Van Dover *et al.* [86, 87] reported a technique to prepare and screen electronic materials in the form of thin-film dielectrics, for use in integrated circuit applications. A continuous composition spread (CCS) was produced by RF magnetron sputtering from three targets containing transition metals on silicon wafer substrates. These materials were then screened for a useful figure of merit (FOM), in this case the product of the permittivity of free space and the breakdown field. Ternary phase diagrams were produced indicating the 'hot spots' at which the highest FOM values were obtained (see Figure 1.13).

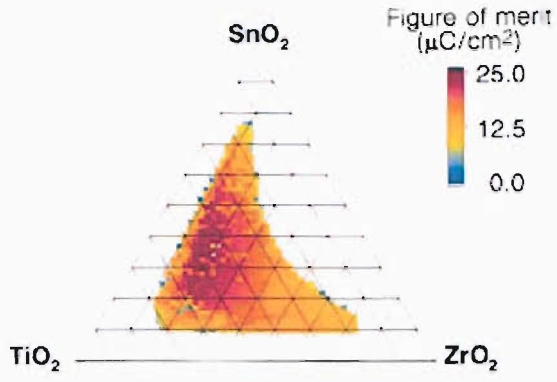

Figure 1.13 - Ternary phase diagram produced for a composition spread of thin-film dielectric materials. The scale bar indicates the magnitude of the figure of merit, in this case the product of the permittivity of free space and the breakdown field [86].

To date, most combinatorial electrochemistry research has been based on the screening of electrocatalysts. The first example of combinatorial electrochemistry appeared in 1998 and was focused on an automated method for generating large libraries of metal alloy catalysts for methanol oxidation for use in fuel cells. Other approaches have utilised modified ink jet printers, which were used to print metal 'salt inks' on conducting paper. The subsequent inks were later screened for catalytic activity [1].

More recently work has been undertaken at Southampton University to electrochemically screen electrocatalysts for use in fuel cell electrodes. Sixty-four element arrays of carbon supported platinum catalysts of varying platinum loading (which results in a change in the particle size) to demonstrate the speed and sensitivity of the screening methodology. The results of the screening revealed that specific activity for steady-state methanol oxidation and oxygen reduction at room temperature in H_2SO_4 electrolyte was found to be at a maximum for the largest particle sizes, in agreement with the literature [88].

More recently, there has been interest in the development of a combinatorial method for the screening of lithium battery materials and several research groups have undertaken different projects. There have been two main approaches to the problem of preparing a large number of samples of lithium battery materials (see Figure 1.14). Firstly, one can prepare a composition spread of electrode materials by multi-target RF sputtering. This has been the approach of the Dahn group, for the study of negative electrodes. In this approach, 75x75 mm wafer substrates were

rotated within a commercially available 3-target sputtering machine and films of systematic compositional variation were produced. The rotating substrate table was under continuous rotation and produces intimately mixed compositions or artificial layered structures. Characterisation of the films was carried out by *X-ray* diffraction and electrochemical testing using high-throughput screening methodologies. In this way large regions of ternary phase diagrams can be explored. The effectiveness of this method was demonstrated for $SiSn_xAl_y$ compositions (where, $0 < x, y < 1$) [89]. The composition spreads of materials were characterised using in-house designed 64-channel pseudopotentiostat. The effectiveness of the electrochemical technique was compared to the commercially available *Scribner MMA* instrument [90]. The wafer substrates containing a composition spread of materials were placed within a hermetically sealed 64-channel combinatorial cell [91]. The results obtained using the combinatorial technique were found to compare well with the results obtained using conventional cells (2325 coin-type cells). This technique has been used to study Ni/Pt superlattice structures [92], Thin films of varying $Mo_{1-x}Sn_x$ composition [93] and Si-Sn alloys [94]. Copper-zinc and copper-tin alloys were prepared by electrodeposition using a Hull Cell [95, 96]. XRD was then performed on the samples prepared on Ni foil and samples of these compositions were characterised using SEM and conventional electrochemical techniques. The electrochemical performance of SiAlSn [97]and SiAlMn [98] compositions and were also studied using this combinatorial method to determine their suitability as potential negative electrode materials for lithium batteries. Sputtering techniques have also been developed by Whitacre *et al.* to study $Li_yMn_xNi_{2-x}O_4$ positive electrode materials [99], in which hundreds of micro-cells were fabricated on a single silicon wafer substrate.

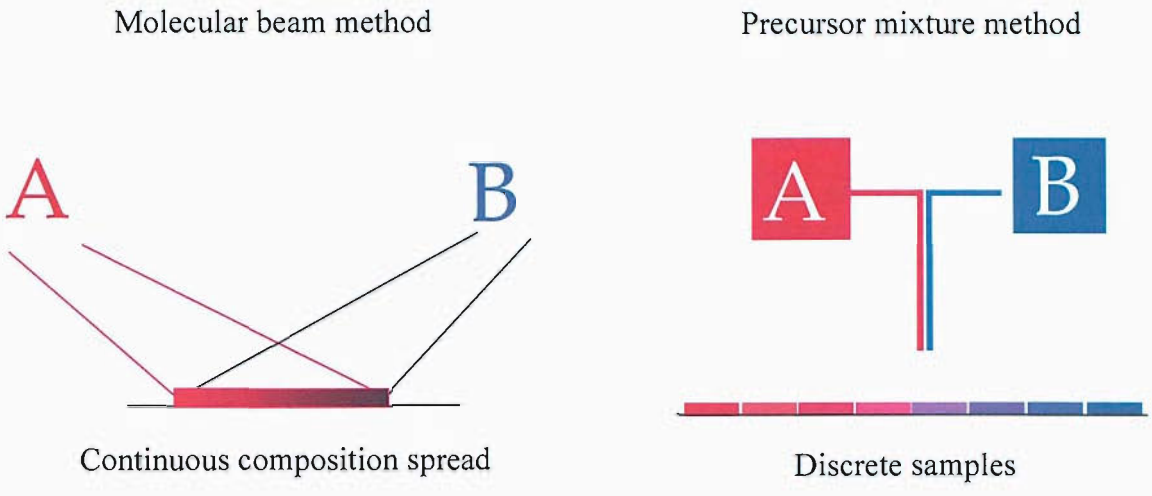

Figure 1.14 - Methods of preparation of multiple sample arrays.

Another possible approach is direct synthesis of materials using sol-gel or solution techniques. Takada *et al.* have used this method to prepare $LiCoO_2$ electrodes by automated synthesis using existing sol-gel methods [100]. They prepared a 4x4 array of electrode material precursors on platinum electrodes and were heat treated at 900 °C. These were then characterised by X-ray diffraction and electrochemical testing. However, no composition spreads were prepared.

Given the large number of possible materials and permutations in the synthesis of lithium battery materials, it is important to determine the most attractive material and synthesis route that will lead to the greatest improvement in performance. It has already been demonstrated that substitution for Mn within $LiMn_2O_4$ have led to preparation of materials with better cycling performance, but with reduced capacity [101]. The manganese oxide spinel has the attractive advantage of being non-toxic and inexpensive, but with the disadvantage of lower capacity [31]. It is unlikely that these materials will be able to compete with lithium cobalt oxide, which is the active material in most commercial lithium cells because of their lower capacity and poor retention of capacity on cycling.

In contrast, lithium iron phosphate is superior to $LiCoO_2$ in terms of theoretical specific capacity, density, safety and environmental benignity [38]. It does however suffer from low conductivity, and thus, a large amount of supporting conductor (> 5 wt. %) must be added to provide acceptable capacity levels, reducing the overall capacity of the electrodes away from theoretical values [39]. However,

$LiFePO_4$ remains the most attractive new material for development of commercial cells. The substitution of other elements into the structure of the $LiFePO_4$ can allow the optimisation of the material with may result in novel superior materials. Chaing *et al.* has recently reported the doping of $LiFePO_4$ with zirconium, niobium, and other transition metals, which is reported to have the effect of increasing the intrinsic conductivity by 10^8 [41].

Figure 1.15 shows the elements on the periodic table that could be incorporated into the structure of $LiFePO_4$, thus, producing a multi-component material as a solid solution. Some substitutions have already been reported for this material, such as Mn [102] and Ni [103] substitution for Fe. However, to carry out such a large study with the substitution of many elements, conventional techniques must be replaced by high-throughput experimentation. It is the aim of chapter two to demonstrate the validity of the method of combinatorial screening applied to lithium battery material synthesis and to show that results achieved using multiple sample preparation and screening give reliable data when compared to that of conventional methods.

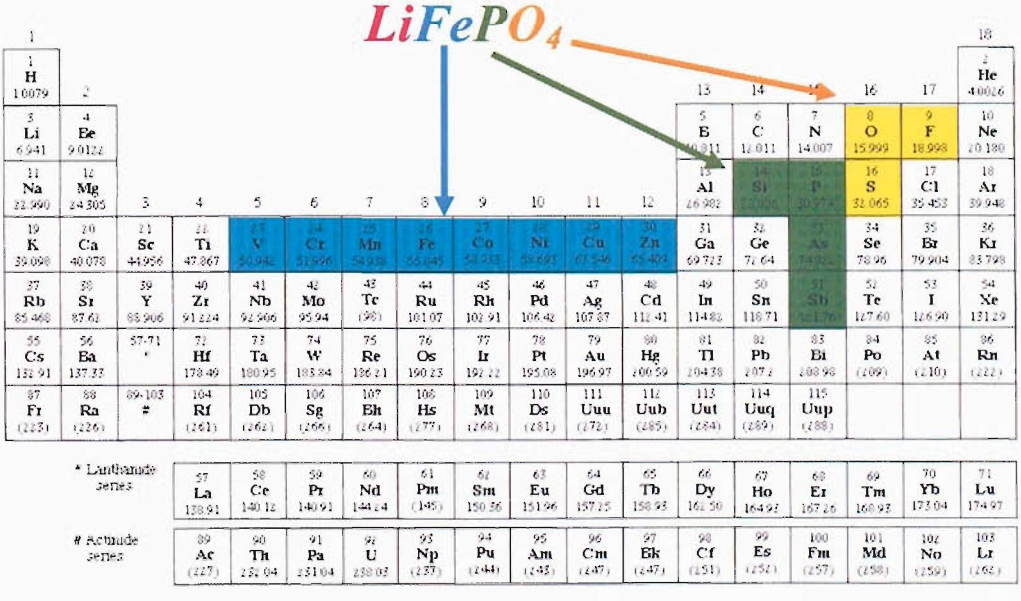

Figure 1.15 - Possible substitutions for $LiFePO_4$ in a combinatorial experiment.

1.7.4 High Throughput vs. Combinatorial Screening

The terms combinatorial and high-throughput screening are often used interchangeably in the literature. However, there are differences between these two approaches (see Figure 1.16). Organic chemists initially introduced the phrase combinatorial screening in the late eighties to describe the process of treating samples with a series of combinatorial steps to efficiently generate diversity in the samples. These samples can then be subjected to a series of parallel operations to screen the compounds for useful activity. The advantage of this method is that a large number of samples can be prepared using a limited number steps (*i.e.* 'Split and pooled' approach. High-throughput (parallel-based) screening has the goal of maximising the number of experiments carried out simultaneously with the majority of operations being carried out in parallel. It allows the diversity of experimental space to be explored in terms of sample composition or variation in experimental conditions [104].

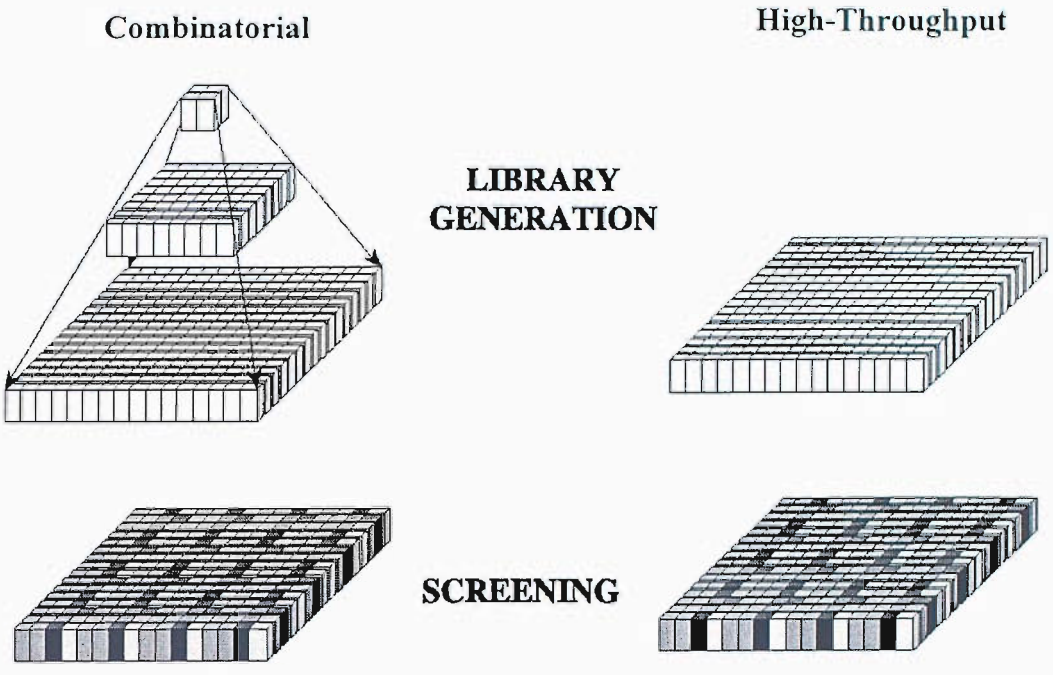

Figure 1.16 - Combinatorial and high-throughput techniques [104].

1.8 Thesis Overview

The aim of the work presented in this thesis is to apply these high-throughput techniques to the area of lithium battery positive electrodes and to determine the validity of such a method. These techniques require the development of solution-based routes to the synthesis of battery materials and their application to combinatorial synthesis. The objective is to prepare composition spreads of positive electrode candidates in the form of libraries of discrete samples. These will then be tested using electrochemical cycling and characterisation techniques including scanning electron microscopy (SEM) and X-ray diffraction. The electrochemical testing and X-ray powder diffraction will be undertaken using small sized samples each of different composition and will aim to accurately reproduce the performance of large scale samples prepared using conventional techniques.

Studying such a large number of compounds with the $LiMPO_4$ formula requires the synthesis of a number of cells on a scale outside the experimental capacity of a standard multi-channel potentiostat. The study of each of these compounds could be conducted in an array of many small cells. This would be of the order of 64 different cells cycled simultaneously with the cells being synthesised

on the working electrodes on the array possibly using an ink jet printer or solution deposition techniques. This should provide an accurate screen for many different compounds in a relatively short time period. Techniques need to be developed for the preparation of electrode libraries with sufficient electronic and ionic conductivity to facilitate electrochemical screening using a high-throughput approach.

1.9 References

1. Evans, J.R.G., Edirisinghe, M.J., Coveney, P.V., and Eames, J., *Journal of the European Ceramic Society*, 2001, **21**, (13), p. 2291-2299.
2. Cawse, J.N., *Accounts of Chemical Research*, 2001, **34**, (3), p. 213-221.
3. Linden, D., *Handbook of Batteries*. 1995, New York: McGraw-Hill. 1.3.
4. Crump, T., *A Brief History of Science*. 2001, Robinson: London. p. 153-160.
5. Scrosati, B. and Vincent, C.A., *Modern Batteries: An Introduction to Electrochemical Power Sources*. 1997, London: Arnold. 200-201.
6. Stock, J.T. and Orna, M.V., *Electrochemistry Past and Present*. 1989, Washington DC: ACS.
7. Brodd, R.J., Bullock, K.R., Leising, R.A., Middaugh, R.L., Miller, J.R., and Takeuchi, E., *Journal of the Electrochemical Society*, 2004, **151**, (3), p. K1-K11.
8. Scrosati, B. and Vincent, C.A., *Modern Batteries: An Introduction to Electrochemical Power Sources*. 1997, London: Arnold. 1-5.
9. Scrosati, B. and Vincent, C.A., *Modern Batteries: An Introduction to Electrochemical Power Systems*. 1997, London: Arnold. 65-97.
10. Scrosati, B. and Vincent, C.A., *Modern Batteries: An Introduction to Electrochemical Power Sources*. 1997, London: Arnold. 228.
11. Owen, J.R., *Chemical Society Reviews*, 1997, **26**, (4), p. 259-267.
12. Toyota Motor Corporation, 1 Toyota-Cho, Toyota City, Aichi Prefecture 471-8571, Japan
13. Scrosati, B. and Vincent, C.A., *Modern Batteries: An Introduction to Electrochemical Power Systems*. 1997, London: Arnold. 199.
14. Gabano, J.P., *Lithium batteries*. 1983, London: Academic Press. 2-3.
15. Linden, D., *Handbook of Batteries*. 1995: McGraw-Hill. 7.4 - 7.5.
16. Scrosati, B. and Vincent, C.A., *Modern Batteries: An Introduction to Electrochemical Power Sources*. 1997, London: Arnold. 66.
17. Scrosati, B. and Vincent, C.A., *Modern Battreies: An Introduction to Electrochemical Power Systems*. 1997, London: Arnold. 84.
18. Scrosati, B. and Vincent, C.A., *Modern Batteries: An Introduction to Electrochemical Power Sources*. 1997, London: Arnold. 66-67.

19. Scrosati, B. and Vincent, C.A., *Modern Batteries: An Introduction to Electrochemical Power Sources*. 1997, London: Arnold. 163-164.
20. Linden, D., *Handbook of Batteries*. 1995: McGraw-Hill. 24.4.
21. Scrosati, B. and Vincent, C.A., *Modern Batteries: An Introduction to Electrocehmical Power Sources*. 1997: McGraw-Hill. 118-119.
22. Linden, D., *Handbook of Batteries*. 1995: McGraw-Hill. 36.10.
23. Scrosati, B. and Vincent, C.A., *Modern Battreies: An Introduction to Electrochemical Power Sources*. 1997, London: Arnold. 142-143.
24. Song, M.Y., Ahn, D., Kwon, I., Lee, R., and Rim, H., *Journal of Alloys and Compounds*, 2000, **298**, (1-2), p. 254-260.
25. Weast, R.C., *CRC Handbook of Chemistry and Physics*. 1989, CRC Publishing Company. p. D-152.
26. Lloris, J.M., Vicente, C.P., and Tirado, J.L., *Electrochemical and Solid State Letters*, 2002, **5**, (10), p. A234-A237.
27. Ilic, D., et al., *IBA 2004 Abstract No: 30, Graz Austria*, 2004, p. 59.
28. SAFT, Lithium Division, 12 rue Sadi Carnot, 93170- BAGNOLET, France.
29. Chu, Y.H., Shul, Y.G., Choi, W.C., Woo, S.I., and Han, H.S., *Journal of Power Sources*, 2003, **118**, (1-2), p. 334-341.
30. Plichta, E.J., Hendrickson, M., Thompson, R., Au, G., Behl, W.K., Smart, M.C., Ratnakumar, B.V., and Surampudi, S., *Journal of Power Sources*, 2001, **94**, (2), p. 160-162.
31. Thackeray, M.M., David, W.I.F., Bruce, P.G., and Goodenough, J.B., *Materials Research Bulletin*, 1983, **18**, (4), p. 461-472.
32. Amatucci, G. and Tarascon, J.M., *Journal of the Electrochemical Society*, 2002, **149**, (12), p. K31-K46.
33. Kawai, H., Nagata, M., Kageyama, H., Tukamoto, H., and West, A.R., *Electrochimica Acta*, 1999, **45**, (1-2), p. 315-327.
34. Linden, D., *Handbook of Batteries*. 1995, New York: McGraw Hill. 36.6.
35. Okada, S., Sawa, S., Egashira, M., Yamaki, J., Tabuchi, M., Kageyama, H., Konishi, T., and Yoshino, A., *Journal of Power Sources*, 2001, **97-8**, p. 430-432.
36. Armstrong, A.R. and Bruce, P.G., *Nature*, 1996, **381**, (6582), p. 499-500.
37. David, W.I.F., Goodenough, J.B., Thackeray, M.M., and Thomas, M., *Revue De Chimie Minerale*, 1983, **20**, (4-5), p. 636-642.

38. Padhi, A.K., Nanjundaswamy, K.S., and Goodenough, J.B., *Journal of the Electrochemical Society*, 1997, **144**, (4), p. 1188-1194.

39. Ravet, N., Chouinard, Y., Magnan, J.F., Besner, S., Gauthier, M., and Armand, M., *Journal of Power Sources*, 2001, **97-8**, p. 503-507.

40. Andersson, A.S., Kalska, B., Haggstrom, L., and Thomas, J.O., *Solid State Ionics*, 2000, **130**, (1-2), p. 41-52.

41. Chung, S.Y., Bloking, J.T., and Chiang, Y.M., *Nature Materials*, 2002, **1**, (2), p. 123-128.

42. Huang, H., Yin, S.C., and Nazar, L.F., *Electrochemical and Solid State Letters*, 2001, **4**, (10), p. A170-A172.

43. Andersson, A.S., Kalska, B., Jonsson, P., Haggstrom, L., Nordblad, P., Tellgren, R., and Thomas, J.O., *Journal of Materials Chemistry*, 2000, **10**, (11), p. 2542-2547.

44. Andersson, A.S., Thomas, J.O., Kalska, B., and Haggstrom, L., *Electrochemical and Solid State Letters*, 2000, **3**, (2), p. 66-68.

45. Takahashi, M., Tobishima, S., Takei, K., and Sakurai, Y., *Journal of Power Sources*, 2001, **97-8**, p. 508-511.

46. Yamada, A., Kudo, Y., and Liu, K.Y., *Journal of the Electrochemical Society*, 2001, **148**, (7), p. A747-A754.

47. Franger, S., Le Cras, F., Bourbon, C., and Rouault, H., *Electrochemical and Solid State Letters*, 2002, **5**, (10), p. A231-A233.

48. Doeff, M.M., Hu, Y.Q., McLarnon, F., and Kostecki, R., *Electrochemical and Solid State Letters*, 2003, **6**, (10), p. A207-A209.

49. Scrosati, B. and Vincent, C.A., *Modern Batteries: An Introduction to Electrochemical Power Sources*. 1997, London: Arnold. 204.

50. Tarascon, J.M. *Rechargable Li Batteries: An Ocean of Excitment and Challenges*. in *Paper presented at Electrochem 2002*. September 2002. Preston, UK.

51. Salomon, M., *Pure and Applied Chemistry*, 1998, **70**, (10), p. 1905-1912.

52. Chen, G.Y. and Richardson, T.J., *Electrochemical and Solid State Letters*, 2004, **7**, (2), p. A23-A26.

53. Adachi, M., Tanaka, K., and Sekai, K., *Journal of the Electrochemical Society*, 1999, **146**, (4), p. 1256-1261.

54. Behl, W.K. and Chin, D.T., *Journal of the Electrochemical Society*, 1988, **135**, (1), p. 21-25.

55. Narayanan, S.R., Surampudi, S., Attia, A.I., and Bankston, C.P., *Journal of the Electrochemical Society*, 1991, **138**, (8), p. 2224-2229.

56. Weller, M.T., *Inorganic Materials Chemistry*. 1994, Oxford: OUP. 26-27.

57. Shriver, D.F., Atkins, P.W., and Langford, C.H., *Inorganic Chemistry: Second Edition*. 1998, Oxford: Oxford University Press. 771.

58. Wen, J.Y. and Wilkes, G.L., *Chemistry of Materials*, 1996, **8**, (8), p. 1667-1681.

59. Sun, Y.K., Oh, I.H., and Hong, S.A., *Journal of Materials Science*, 1996, **31**, (14), p. 3617-3621.

60. Chang, S.H., Kang, S.G., and Jang, K.H., *Bulletin of the Korean Chemical Society*, 1997, **18**, (1), p. 61-65.

61. Huang, H.T. and Bruce, P.G., *Journal of the Electrochemical Society*, 1994, **141**, (7), p. L76-L79.

62. Dominko, R., Bele, M., Gaberscek, M., Remskar, M., Hanzel, D., and Jamnik, J., *Abstract No: 62, IBA 2004, Graz, Austria.*, 2004, p. 125.

63. Nguyen, M.H., Lee, S.J., and Kriven, W.M., *Journal of Materials Research*, 1999, **14**, (8), p. 3417-3426.

64. Frisch, H.L. and Hammersley, J.M., *Journal for the Society for Industrial and Applied Mathematics*, 1963, **11**, (894).

65. Kirkpatrick, S., *Physical Review Letters*, 1971, **27**, (1722).

66. Flandin, L., Prasse, T., Schueler, R., Schulte, K., Bauhofer, W., and Cavaille, J.Y., *Physical Review B*, 1999, **59**, (22), p. 14349-14355.

67. Hammersley, J.M., *Proceedings of the Cambridge Philosophy Society*, 1957, **53**, p. 642.

68. Fisher, M.E. and Essam, J.W., *J. Math. Phys*, 1961, **2**, p. 609.

69. Kirkpatrick, S., *Reviews of Modern Physics*, 1973, **45**, (4), p. 574-587.

70. Dean, P. and Bird, N.F., *Proceedings of the Cambridge Philosophical Society*, 1967, **63**, p. 477.

71. Erdos, P. and Renyi, A., *Publications of the Mathematical Institute of the Hungarian Academy of Sciences*, 1960, **5**, p. 17.

72. Last, B.J. and Thouless, D.J., *Physical Review Letters*, 1971, **27**, (25), p. 1719-1721.

73. Zallen, R., *The Physics of Amorphous Soilds*. 1983, New York: Wiley. Chap. 4.
74. Seager, C.H. and Pike, G.E., *Physical Review B*, 1974, **10**, (4), p. 1435-1445.
75. Mandal, S., Amarilla, J.M., Ibanez, J., and Rojo, J.M., *Journal of the Electrochemical Society*, 2001, **148**, (1), p. A24-A29.
76. Fenniri, H., *Combinatorial Chemistry: A Practical Approach*. 2000, Oxford.
77. Journal of Combinatorial Chemistry.
78. Symex Technologies inc., 3100 Central Expressway, Santa Clara, CA, 95051.
79. Lander, E.S., et al., *Nature*, 2001, **409**, (6822), p. 860-921.
80. Merrifield, R.B., *J. Am. Chem. Soc*, 1963, **85**, p. 2149-2152.
81. Geysen, H.M., Meloen, R.H., and Barteling, S.J., *Proceedings of the National Academy of Sciences of the United States of America-Biological Sciences*, 1984, **81**, (13), p. 3998-4002.
82. Geysen, H.M., Rodda, S.J., and Mason, T.J., *Molecular Immunology*, 1986, **23**, (7), p. 709-715.
83. Kennedy, K., Tibor, S., Davy, G., Zackay, V.F., and Parker, E., *Journal of Applied Physics*, 1965, **36**, (12), p. 3808-3810.
84. Hanak, J.J., *Journal of Materials Science*, 1970, **5**, p. 964-971.
85. Reddington, E., Sapienza, A., Gurau, B., Viswanathan, R., Sarangapani, S., Smotkin, E.S., and Mallouk, T.E., *Science*, 1998, **280**, (5370), p. 1735-1737.
86. van Dover, R.B., Schneemeyer, L.D., and Fleming, R.M., *Nature*, 1998, **392**, (6672), p. 162-164.
87. van Dover, R.B., Schneemeyer, L.F., Flaming, R.M., and Huggins, H.A., *Biotechnology and Bioengineering*, 1999, **61**, (4), p. 217-225.
88. Guerin, S., Hayden, B.E., Lee, C.E., Mormiche, C., Owen, J.R., Russell, A.E., Theobald, B., and Thompsett, D., *Journal of Combinatorial Chemistry*, 2004, **6**, (1), p. 149-158.
89. Dahn, J.R., Trussler, S., Hatchard, T.D., Bonakdarpour, A., Mueller-Neuhaus, J.R., Hewitt, K.C., and Fleischauer, M., *Chemistry of Materials*, 2002, **14**, (8), p. 3519-3523.
90. Cumyn, V.K., Fleischauer, M.D., Hatchard, T.D., and Dahn, J.R., *Electrochemical and Solid State Letters*, 2003, **6**, (6), p. E15-E18.

91. Fleischauer, M.D., Hatchard, T.D., Rockwell, G.P., Topple, J.M., Trussler, S., Jericho, S.K., Jericho, M.H., and Dahn, J.R., *Journal of the Electrochemical Society*, 2003, **150**, (11), p. A1465-A1469.

92. Barkhouse, D.A.R., Bonakdarpour, A., Fleischauer, M., Hatchard, T.D., and Dahn, J.R., *Journal of Magnetism and Magnetic Materials*, 2003, **261**, (3), p. 399-409.

93. Bonakdarpour, A., Hewitt, K.C., Hatchard, T.D., Fleischauer, M.D., and Dahn, J.R., *Thin Solid Films*, 2003, **440**, (1-2), p. 11-18.

94. Beaulieu, L.Y., Hewitt, K.C., Turner, R.L., Bonakdarpour, A., Abdo, A.A., Christensen, L., Eberman, K.W., Krause, J.L., and Dahn, J.R., *Journal of the Electrochemical Society*, 2003, **150**, (2), p. A149-A156.

95. Beattie, S.D. and Dahn, J.R., *Journal of the Electrochemical Society*, 2003, **150**, (11), p. C802-C806.

96. Beattie, S.D. and Dahn, J.R., *Journal of the Electrochemical Society*, 2003, **150**, (7), p. C457-C460.

97. Hatchard, T.D., Topple, J.M., Fleischauer, M.D., and Dahn, J.R., *Electrochemical and Solid State Letters*, 2003, **6**, (7), p. A129-A132.

98. Fleischauer, M. and Dahn, J.R., *Journal of the Electrochemical Society*, 2004, **151**, (8), p. A1216-A1221.

99. Whitacre, J.F., West, W.C., and Ratnakumar, B.V., *Journal of the Electrochemical Society*, 2003, **150**, (12), p. A1676-A1683.

100. Takada, K., Fujimoto, K., Sasaki, T., and Watanabe, M., *Applied Surface Science*, 2004, **223**, (1-3), p. 210-213.

101. Moon, H.S. and Park, J.W., *Journal of Power Sources*, 2003, **119**, p. 717-720.

102. Li, G.H., Azuma, H., and Tohda, M., *Electrochemical and Solid State Letters*, 2002, **5**, (6), p. A135-A137.

103. Goni, A., Lezama, L., Arriortua, M.I., Barberis, G.E., and Rojo, T., *Journal of Materials Chemistry*, 2000, **10**, (2), p. 423-428.

104. Akporiaye, D., et al., *Microporous and Mesoporous Materials*, 2001, **48**, (1-3), p. 367-373.

Chapter 2:
Validation of the Combinatorial Technique

The aim of the work in this chapter is the development and validation of a combinatorial method for the synthesis and screening of positive electrode candidates for use in lithium batteries. The work undertaken in this chapter was presented at the *International Meeting on Lithium Batteries 11 in Monterey, CA (July 2002)* [1] and was the subject of a publication in the *Journal of Power Sources* [2].

2.1 Background and Objectives

The discovery of new lithium battery materials is often a process of time-consuming experimentation as a means to produce a useful material. The synthesis of the inorganic materials that are commonly used as lithium battery materials can take many hours and often involves multiple processing steps. Characterisation can also be time consuming, in particular electrochemical testing.

Conventional 'one sample at a time' preparation techniques involve synthesis of bulk material by a solid-state reaction often with many steps in the preparation, which can involve long heating times and high temperatures. Single sample characterisation can also be a time consuming process, as the electrochemical testing of the electrodes may require several weeks to obtain a large number of cycles, and thus, gain a good understanding of the long term performance of a material. The nature of the conventional approach impedes the discovery of novel materials and optimisation of existing systems. Therefore, a new method of materials discovery is currently being explored in a diverse number of areas of materials science: This new discipline is known as combinatorial and high-throughput materials science. The benefits of this approach were first recognised by J. J. Hanak in 1970.

'*The present approach to the search for new materials suffers from a chronic ailment, that of handling one sample at a time in the process of synthesis, chemical analysis and testing of properties. It is an expensive and time-consuming approach, which prevents highly trained personnel from taking full advantage of its talents and keeps the tempo of discovery of new materials at a low level.*' – J. J. Hanak (1970, p. 964) [3].

It is the objective of this chapter to implement a high-throughput strategy for the screening of lithium battery materials. This approach will encompass the automated synthesis, composite electrode preparation, high-throughput screening and characterisation of samples.

The aims of this chapter will be to:

- Review conventional preparation techniques for lithium manganese oxide spinel and use these techniques to conduct an investigation into percolation effects in composite electrode materials.

- Demonstrate a new approach to battery material preparation in which up to sixty-four different electrodes may be prepared and tested simultaneously. The same study of percolation will be used to test the method.

- Compare the results obtained using the combinatorial approach with those of conventional methods to demonstrate the validity of the screening approach.

2.2 Experimental

An initial study of the percolation of electronic conductivity in lithium manganese oxide ($LiMn_2O_4$) composite electrodes was undertaken using conventional preparation techniques. This method was initially reported by Mandal *et al.* [4]. A combinatorial study of arrays of electrode materials of similar $LiMn_2O_4$/C composition was conducted to determine if the same effects were observed using a high-throughput method [2].

2.2.1 Conventional Electrode Preparation of $LiMn_2O_4$

Electrochemical grade lithium manganese oxide spinel ($LiMn_2O_4$, *Aldrich*) was used as received in the preparation of composite electrodes. The phase purity of the commercial material was confirmed by X-ray diffraction using a *Siemens D5000* diffractometer. $LiMn_2O_4$ was also prepared by a solid-state reaction of lithium carbonate and manganese oxide in air at 800 °C (see Appendix 1). However, given the large amount of material required for the study (especially in the high-throughput screening experiments), the material was acquired from a commercial source.

Electrodes were prepared containing varying amounts of active material, conducting additive and binder, to observe the effect of percolation of electronic conductivity. Composites were prepared containing $LiMn_2O_4$ active material (*Aldrich*), PTFE (Type: 6C-N, *Dupont*) binder and acetylene black (*Shawinigan*, 100% compressed, *Chevron Phillips Chemical Company*) was used as a conductive additive. The quantity of each material in the composite was calculated as a weight percent (wt.%) and the mass of each component was measured on a *Mettler AE163* balance with an accuracy of ± 0.0001 g.

The acetylene black and $LiMn_2O_4$ were mixed together using a pestle and mortar. A small amount of acetone was added to the mixture to enhance the mixing of the two powders leading to greater homogeneity of the composite. The PTFE binder was added once the acetone had been removed by drying. This was required to provide adhesion between the particles in the composite and to give the film good mechanical strength. The mixture was compressed manually (using a pestle and mortar) into a film approximately 2 mm in thickness. The film was then placed between two sheets of

nickel foil and placed in a rolling mill (Minimill, *Durston* [5]) to form a uniform film of approximately 0.10-0.15 mm in thickness. Films were prepared containing different proportions of the three components ($LiMn_2O_4$, AB and PTFE). These compositions are summarised in Table 2.1.

Table 2.1. Table of film compositions prepared for conventional electrode testing.

Film code	Acetylene Black / wt. %	$LiMn_2O_4$ / wt. %	PTFE / wt. %
AS01	2.0	93.0	5.0
AS02	3.0	92.0	5.0
AS03	4.0	91.0	5.0
AS04	5.0	90.0	5.0
AS05	0.2	94.8	5.0
AS06	0.4	94.6	5.0
AS07	0.6	94.4	5.0
AS08	0.8	94.2	5.0
AS09	4.5	90.5	5.0
AS10	5.5	89.5	5.0
AS11	6.0	89.0	5.0
AS12	6.5	88.5	5.0
AS13	7.0	88.0	5.0
AS14	7.5	87.5	5.0
AS15	8.0	87.0	5.0
AS16	10.0	85.0	5.0
AS17	15.0	80.0	5.0
AS18	20.0	75.0	5.0

It is expected that differences in conductivity of these films should be related to the amount of carbon contained as a weight percentage [4, 6]. Initially, a two terminal resistance measurement was made using a multimeter. The resistance of each film was measured in at least four areas on the surface.

The electrode film was placed on a piece of aluminium foil (which served as one contact) and a stainless steel piston with a diameter of 1.4 cm (1.53 cm^2) was used as the second contact. A 2.6 kg weight was used to increase pressure on the piston to provide good contact during these measurements. The resistance through the film was measured using a DVM and these values were used to calculate a specific value for conductivity. In later experiments a conductivity measurement was undertaken using the four-point probe method (as described in section 2.2.3).

2.2.1.1 Cell Preparation

Several pellets (Ø = 1.25 cm; surface area = 1 cm^2) from each film were taken using a cork borer; these were used as the positive electrodes of the cells. Rolled and punched lithium metal foil (~ 0.25 mm in thickness) was used as the negative electrode material. *Panasonic CR2016* stainless steel coin cells (*Matsushita Battery Industrial Company*) or homemade stainless steel cells were used as the current collectors (see Figures 2.1 and 2.2). The coin cells were obtained as three separate components; the positive and negative current collectors and a stainless steel disc. This disc was welded onto the positive electrode plate using a spot welder and was used to provide stack pressure in the cell. This acted in a similar way to the spring-loaded current collectors employed in the stainless steel cells. Two *F-type* glass separators (*Whatman, Fisher*) of pore size 0.7 μm were used to facilitate lithium ion flow between the electrodes. The separators were soaked in a non-aqueous electrolyte composed of 1 M $LIPF_6$ in EC/DMC.

It has been found by experience that the use of one separator greatly increased the likelihood of a short circuit during cycling due to the formation of lithium dendrites across the separator. Hence, two separators were used in all experiments. The cells were assembled in a glove box in an argon atmosphere due to the sensitivity of the lithium and the electrolyte to atmospheric moisture. Before construction of the cell, the

surface of the lithium was cleaned with a spatula to remove the passivating (oxide) layer. The lithium film was rolled to reduce its thickness. A cork borer was used to produce a lithium pellet of 1.3 cm diameter. The composite film was placed on to the positive current collector under the two glass micropore separators and approximately ten drops of electrolyte (1M $LiPF_6$ in EC/DMC) were added to the separators. The lithium pellet was placed on top of the separators with the negative current collector. The cell was closed using a crimping machine or screwed down using an Allen key.

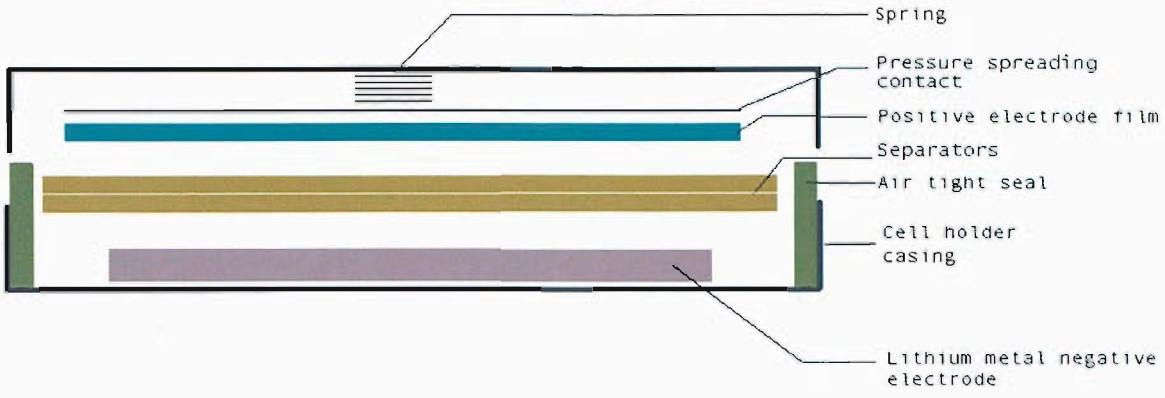

Figure 2.1 - Schematic diagram of a stainless steel coin cell used in galavanostatic cycling of electrode films.

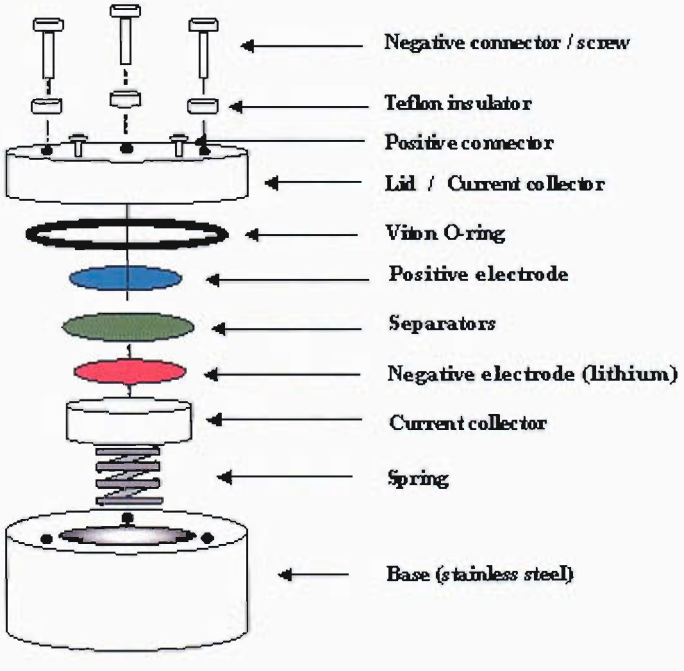

Figure 2.2 - Stainless steel cylindrical cell used for electrochemical testing [7].

2.2.1.2 Electrochemical Testing

Cells were tested using a home made six-channel galvanostat and a VMP multi-potentiostat, (*Princeton Applied Research, Biologic Science Instruments, Perkin Elmer*). In most experiments the cells were cycled using the variable multi-channel potentiostat (VMP), which is a 16-channel instrument. In both cases the cells were tested using galavanostatic cycling techniques within set potential limits (*i.e.*, the current applied to the cells was constant throughout the experiment and the voltage varied with time). The applied currents were calculated from the total theoretical capacity for the active material in the cell, using Faraday's law given in Equation 2.1:

$$Q = n_e nF \qquad \textbf{Equation 2.1}$$

Here, the charge passed (Q) is the product of the number of electrons transferred in the reaction (n_e), the number of moles of the material (n) and the Faraday constant (F = 96485 C mol^{-1}). The theoretical capacity is usually expressed in units of mA h and thus, the capacity in Coulombs should be divided by 3.6. The required current for a given cycling rate can then be found by dividing this charge by the number of hours for each charge or discharge.

The cells were cycled at three rates C/5, C/3 and C/2, between the voltage limits of 3 and 4.5 V *vs.* Li, where the redox active lithium extraction and insertion is observed. Most cells were cycled 15 times (*i.e.*, 15 charges and discharges). Different currents were applied to the cells depending on the cycling rate. As the applied current was increased, the time required for a charge and discharge was reduced. After cycling the cell, data were transferred to a software package and treated for presentation in the form of charge per cycle number and specific charge normalised by the mass of material used.

To reduce the amount of bench space required for electrode testing, a 4x4 array of coin cells was designed; this had the benefits of reducing the required space to a 20x20 cm area and allowing cycling on 16 channels to be carried out simultaneously

and accurately (see Figure 2.3). This is one of the requirements of the combinatorial method, in that it must enable an increased number of materials or compounds to be screened effectively using a small amount of bench space and capital investment.

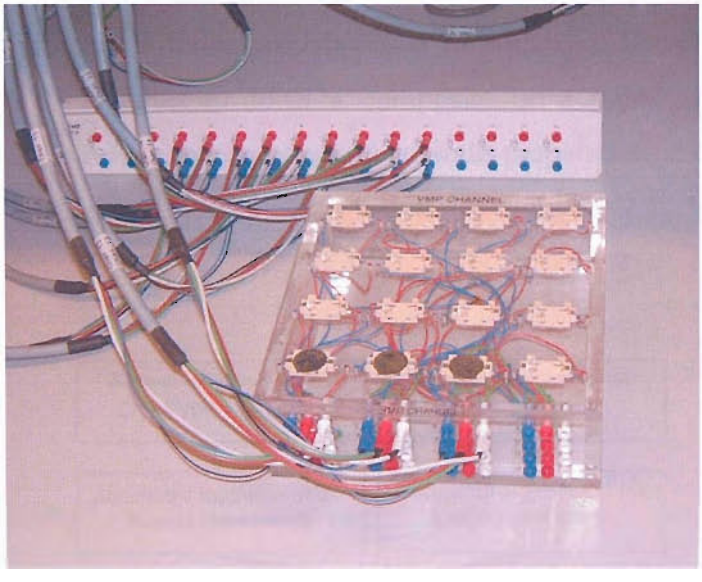

Figure 2.3 - Multi-coin cell cycling array, (dimensions 20x20x5).

2.2.1.3 Scanning Electron Microscopy

Composite electrode films were studied using SEM to observe micro-structural features and the surface topography using a *Philips XL30ESEM* in high vacuum mode. Electrode films of varying carbon content were placed in the sample chamber on aluminium sample studs. The samples were mounted to the surface of aluminium sample holders with conducting adhesive carbon disks. Typically an accelerating voltage between 15-25 kV was used. Digital images were taken of surface features using a back scattering electron and secondary electron detectors. The variation in composition was studied by energy disperse X-ray spectroscopy (EDX).

2.2.2 *Combinatorial Electrode Preparation*

The following experimental technique was developed for the high-throughput fabrication of electrode materials. The combinatorial technique described here requires all materials be in solution or as a homogeneous suspension; this constraint exists because of the type of robotic materials handling systems available. The benefit of developing and utilising solution techniques is that many different components can easily be added to together to form a composite or a precursor material. The experimental procedure for the automated electrode preparation and high-throughput screening of composite electrode materials is outlined in Figure 2.4.

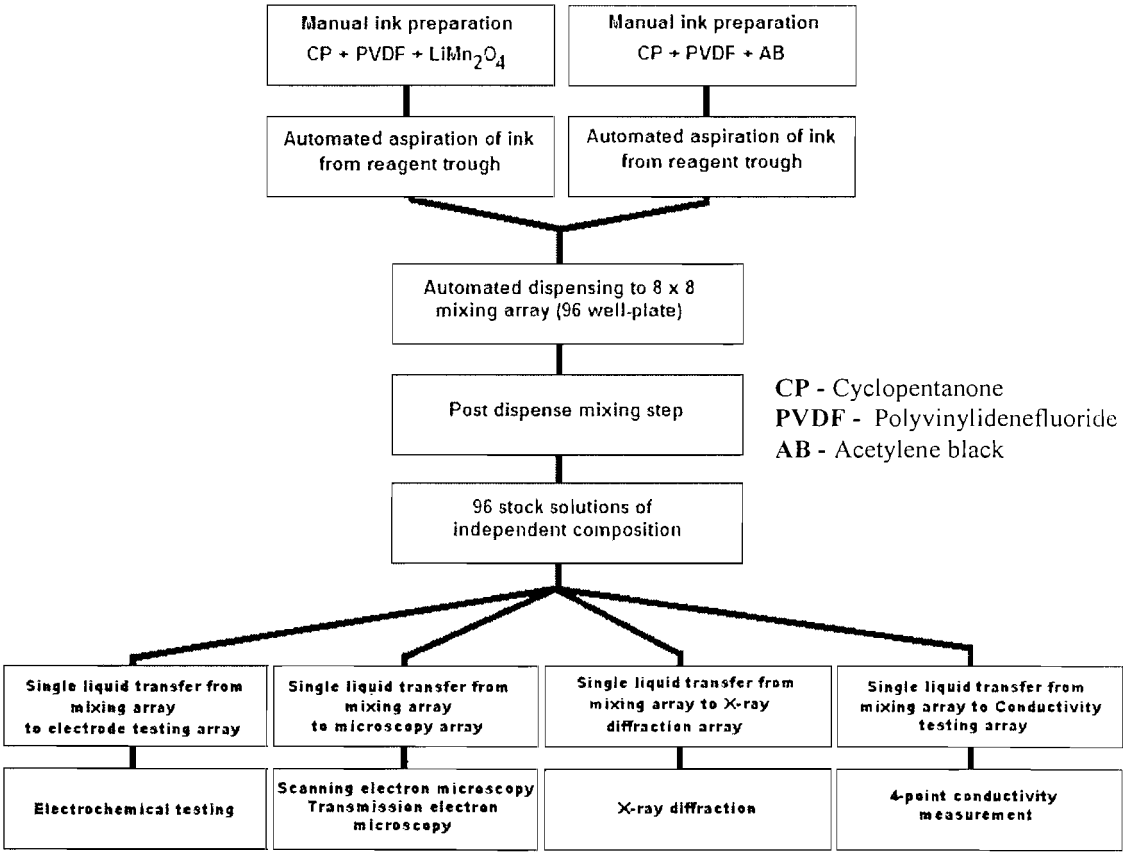

Figure 2.4 - The experimental strategy for high-throughput electrode preparation and testing.

In all of the validation experiments, a common stoichiomerty was used. The amounts of $LiMn_2O_4$ (particle size of approximately 4 μm) and carbon were changed in the electrode materials to produce composites of varying composition. Because $LiMn_2O_4$ and carbon cannot be dissolved in solution and deposited by precipitation (after evaporation of the solvent), two homogeneous ink suspensions were prepared as stock solutions for use in the automated electrode preparation.

The effect of the binder was not investigated. As an insulator it should not contribute improving the composite conductivity above that of providing adhesion between the particles of AB and $LiMn_2O_4$. The amount of binder was kept constant at 10 wt.% in both the carbon and $LiMn_2O_4$ inks. This value of 10 wt.% was determined to be the optimum amount as it provided good film adhesion and did not contribute a significant amount inactive mass to the electrode.

2.2.2.1 Ink Preparation

Two inks were prepared by suspending an optimum amount of the pure powders of $LiMn_2O_4$ (*Aldrich*) and acetylene black (AB, *Chevron Phillips Chemical Co.*), in cyclopentanone (CP, *Aldrich*), a non-toxic, low visocity solvent. CP was chosen as the solvent, as it is one of the few low-toxicity solvents capable of dissolving PVDF-HFP (polyvinylidene fluoride-hexafluoro-propylene, *Aldrich*). The PVDF/HFP was fully dissolved in CP with the aid of stirring and moderate heating (70 °C). The optimum amount of each of the three constituents was determined by preparing small samples of test inks in 10 mL vials. Samples of the inks were deposited onto aluminium foil to observe the adhesion and mechanical strength of the films. AB Inks with higher than 5 wt.% solid contents were found to be too viscous for handling with micropipettes and automated synthesis. The compositions of the inks were selected so that the sedimentive stability was as high as possible, while keeping the viscosity of the ink low enough for the desired automated processing. The optimum ink compositions for the carbon and $LiMn_2O_4$ inks are shown in Table 2.2.

The amount of the binder (PVDF-HFP) was kept constant in the solid contents for each of the inks. This was done for uniformity and to reduce the complexity of the

calculations when PVDF-HFP/AB/$LiMn_2O_4$ weight fractions and volumes were calculated. In both cases, the optimum weight fractions of the solid content (PVDF-HFP + powder) were much lower than that of CP (*i.e.*, ~3.8 wt.% solids for the AB ink and ~ 20 wt.% solids in the $LiMn_2O_4$ ink).

Table 2.2. – Optimum ink compositions.

Acetylene black ink

Constituent	Wt.% in solution	Wt.% in solid phase
PVDF-HFP	0.38	10
Acetylene black	3.39	90
Cyclopentanone	96.23	0

$LiMn_2O_4$ ink

Constituent	Wt.% in solution	Wt.% in solid phase
PVDF-HFP	2	10
$LiMn_2O_4$	18	90
Cyclopentanone	80	0

The solid content of the $LiMn_2O_4$ and AB inks were 20.0 wt.% and 3.8 wt.% respectively (see Table 2.2). The density of AB was measured as 1.25 g cm^{-3}, which is much lower than that of $LiMn_2O_4$ (4.29 g cm^{-3}). The $LiMn_2O_4$ ink has a larger fraction of solids as a proportion of the suspension than the AB ink, possibly due to acetylene black being a more porous material with a high surface area (~ 75 m^2 g^{-1}). When the solid carbon was added to cyclopentanone, the surface had to be sufficiently wetted by the CP to produce a suspension. Thus, carbon being more porous then the $LiMn_2O_4$ required more of the CP solvent to adequately wet its larger surface. For this reason it was not possible to prepare the carbon containing inks with over 4 wt. % CB, with low enough viscosity to use in conjunction with robotic liquid handling techniques. In

addition, inks containing a low mass of $LiMn_2O_4$ produced thin, inhomogeneous, poor quality dry films.

The inks were intended for use as precursors for preparation of electrode films using the robot. Therefore, a glass vessel was designed with a wide neck and a round bottom, to enable solutions to be aspirated and stirred simultaneously if needed, and at the same time minimise the solvent loss due to evaporation. The evaporation of the solvent is a major concern, as the concentration of solution aspirated directly affects the weight fraction of the constituents in the solid film. Therefore, it was important to keep all solutions sealed with parafilm while they were not required for electrode processing.

As these inks were prepared as suspensions, it was expected that some the solid contents in the inks would settle to the bottom over time. Therefore all inks were stirred for at least 24 hours before use to ensure that the components of the solid contents were well distributed within the inks. In addition the stock ink suspensions were stirred continually during the electrode preparation to reduce the number of particles settling. When the sample inks were prepared the components of each stock in were deposited in the wells. After the dispensing steps the sample vials containing the mixed ink electrode precursors were agitated in an array of vials to improve the homogeneity of the inks before deposition of the electrode samples.

2.2.2.2 Robotic Liquid Handling

The high-throughput approach to electrode film preparation relies on the ability to dispense very small volumes (1-100 μL) of reagent solutions or ink suspensions into wells of approximate volume 250-2000 μL quickly and accurately. For the preparation of electrode arrays, an automated liquid handler (*Multiprobe II, Perkin Elmer Life Sciences*) was used to mix electrode components together and deposit micro-litre quantities of robotically prepared electrode materials (see Figure 2.5). The Multiprobe II can easily handle volumes as low 1 μL (accuracy of ± 2% when aspirating 5 μL). However, to date, higher volumes (> 50 μL) have been used to increase accuracy when preparing the composite electrode inks in a well plate. The

accuracy in volume dispensing when operating with ink solutions can be improved by reducing the viscosity and by using pipette tips of larger diameter.

Figure 2.5 – The '*Perkin Elmer Multiprobe II*' robotic liquid handler, used in automated electrode preparation of composite electrodes.

The *Multiprobe II* is capable of preparing arrays on a wide variety of substrates. These included vitreous carbon, aluminium (for electrochemical screening), alumina tile and silica glass used in combinatorial X-ray diffraction instruments and SEM/EDX characterisation. Equipment used on the robot is known as *'labware'* and can be placed in set positions on the deck and can be mapped to a procedural step using the software (see Figure 2.6).

The robot was connected to a lab PC via a serial port and is controlled and programmed using commercial software called 'Winprep', available from *Perkin Elmer Life Sciences*. The commands that lead to the preparation of a sample are known collectively as a '*test*'. Tests can be broken down into '*procedures*' for different aspirating, dispensing and mixing steps. This allows the addition and manipulation of different components to be separated into individual procedures to be executed in a logical order. In this way, any number of solution libraries may be prepared from a

given number of stock solutions and can be used to prepare multiple electrode arrays. This is a useful technique for reproducing experiments to determine experimental error.

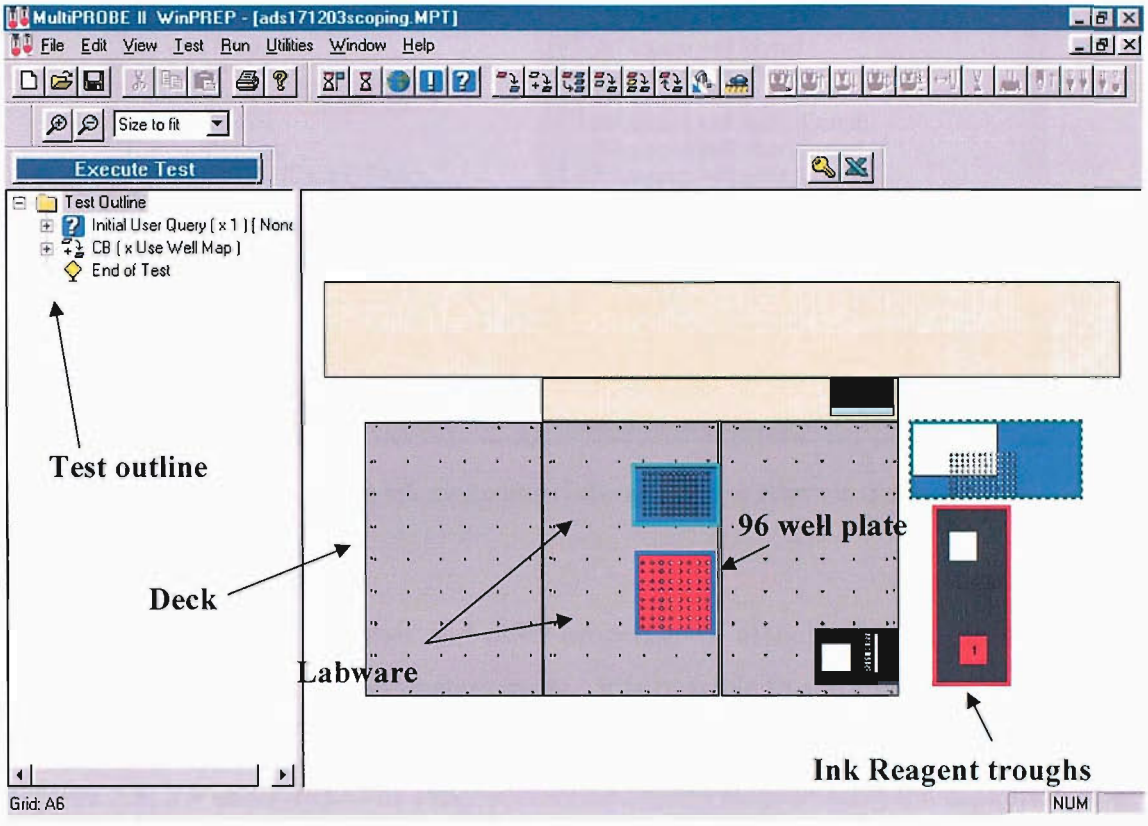

Figure 2.6 – Labware placement and experimental control using a *Multiprobe II* liquid handler.

To control the volumes of each material deposited into each well and vary the composition over 63 electrodes, an *Excel* spreadsheet was composed and uploaded to the *Multiprobe II*. This was converted to a *CSV* file that was read by the robot control software to vary the volume dispensed into each well. The volume values in the *CSV* file for the two inks were calculated from the amount of solid material required on each electrode after deposition and from the density of the inks. These amounts were calculated using formulas, which are given in section 2.2.2.3.

The 96 well plates and disposable tips have default set-ups. However custom *labware* can be included, such as the 8x8 electrode-testing array and the ink reagent vessels (see Figure 2.7).

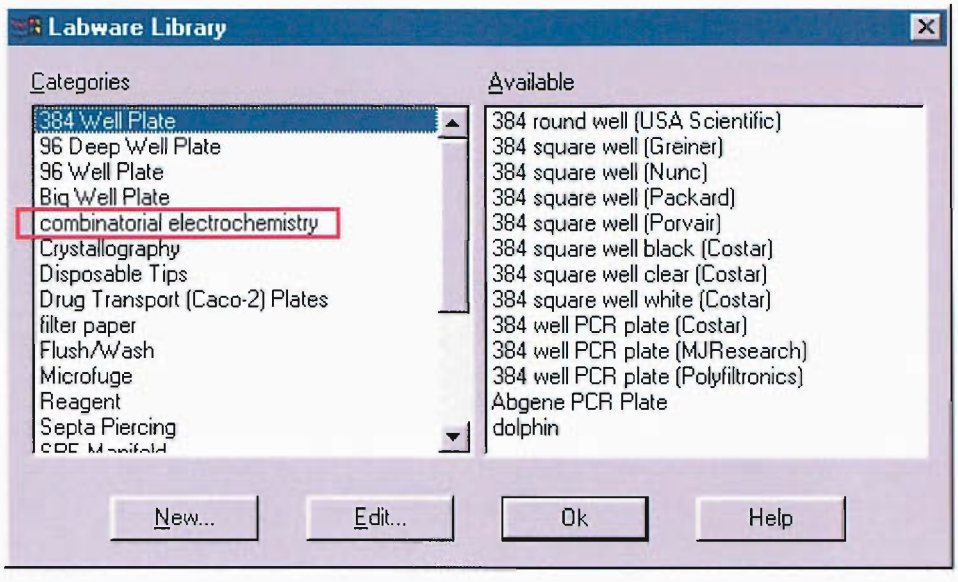

Figure 2.7 – *Labware* selection custom *labware* selection shown in the red box.

The dispensing volumes and other properties of associated with the procedure can also be changed in the parameters menu. It is possible to add mixing steps, control the number of tips in operation at anyone time and change the type of tip used (see Figures 2.8, 2.9 and 2.10). The robot controlled mixing steps involve the aspiration of a volume of the solution in the well and re-depositing it back in to the well, thus mixing the sample solution. This method was tested in early work, but is only suitable for large (> 1 mL) volumes of low viscosity solutions. Since the combinatorial method outlined in this chapter relies on the use of ink suspensions, this method of mixing was not used beyond the testing stage. It proved more reliable to use magnetic stirrers to provide stirring of the reagent inks, while mixing of the individual sample vials was achieved by hand once the components of the electrodes had been delivered to the wells from the two stock solutions. This was done by manually agitating the vials while on the array. It is expected that this form of mixing will result in some settling of the larger $LiMn_2O_4$ particles while in the sample vials, and this may potentially lead to some inaccuracies in sample mass calculations.

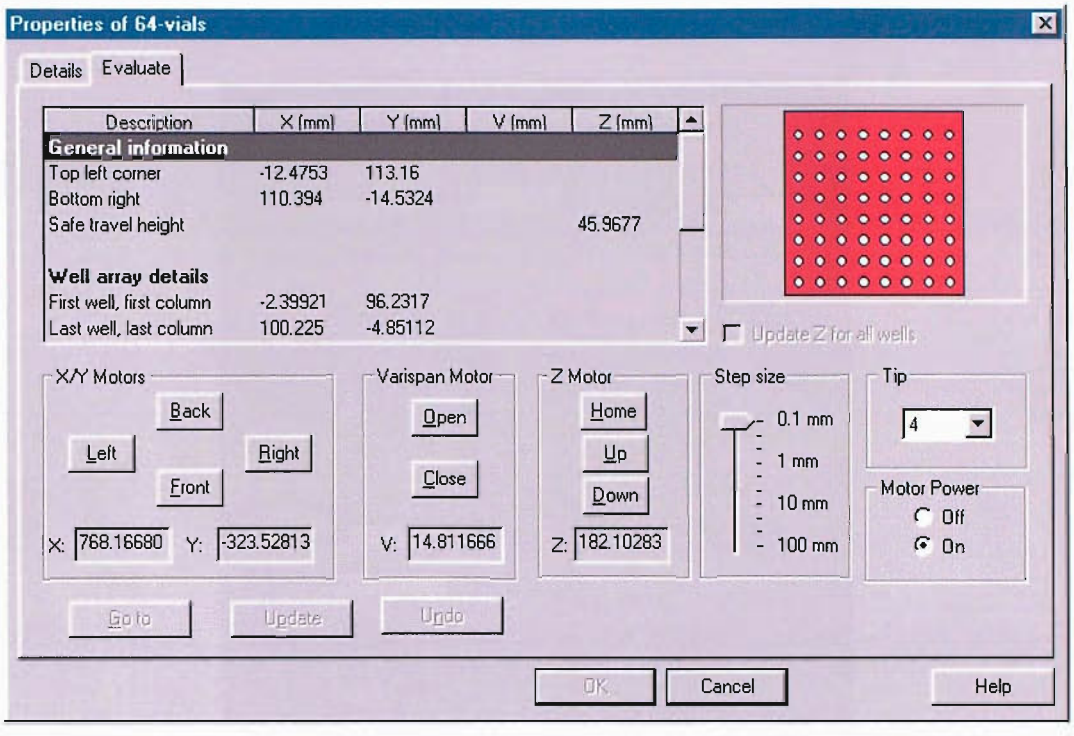

Figure 2.8 – Dimension and properties are changed in the software to allow any custom labware to be added, and existing labware to be modified.

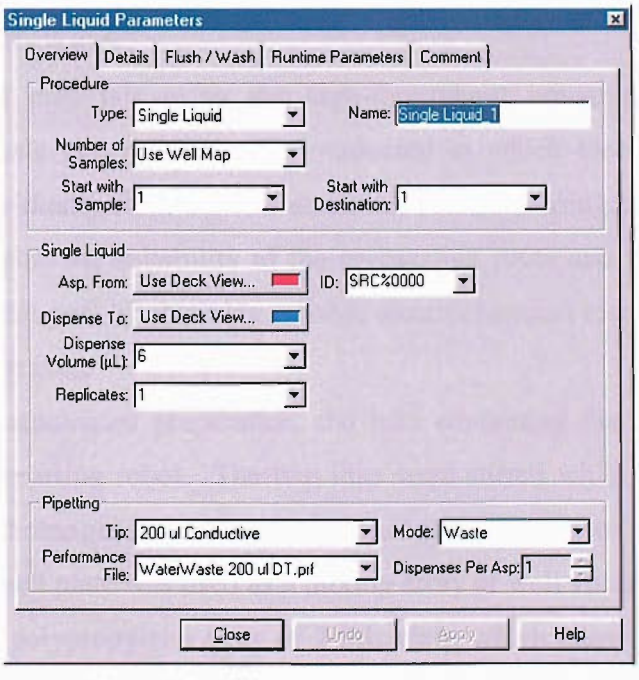

Figure 2.9 – *Winprep* test parameters menu.

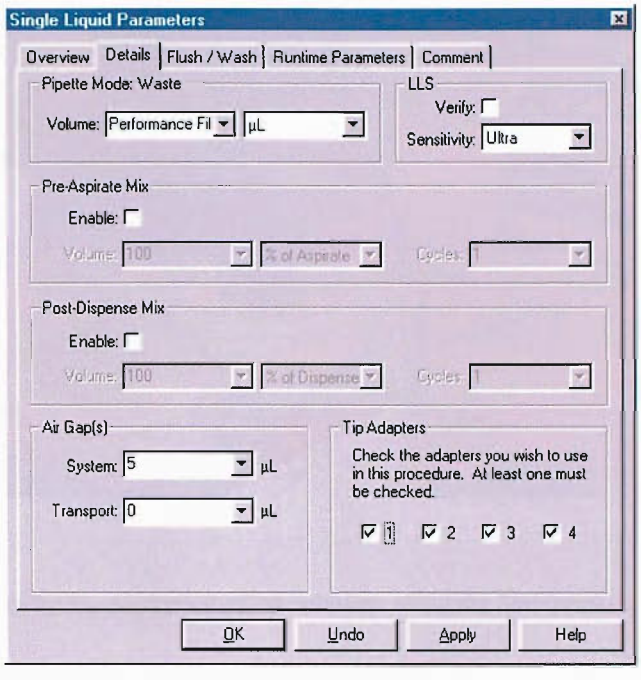

Figure 2.10 - *Winprep* test parameters menu.

2.2.2.3 Electrode Preparation

Prior to testing of materials using the high-throughput preparation and screening technique, small scale experiments were conducted in which electrode compositions were prepared individually from the two stock ink solutions using micropipettes. This was done to determine the suitability of the preparation route and the characterisation technique towards the goal of obtaining reliable electrochemical responses, before mass screening was undertaken.

During the automated preparation, the inks containing the electrode materials were mixed together using robot. The two inks were stirred while on the deck of the robot to ensure homogeneity throughout the procedure (see Figure 2.11). A polypropylene 96-well plate was used as a mixing array of well volume 250 µL, but was later replaced by a polypropylene array of 2 mL vials, which allowed greater accuracy by depositing a larger amount of material.

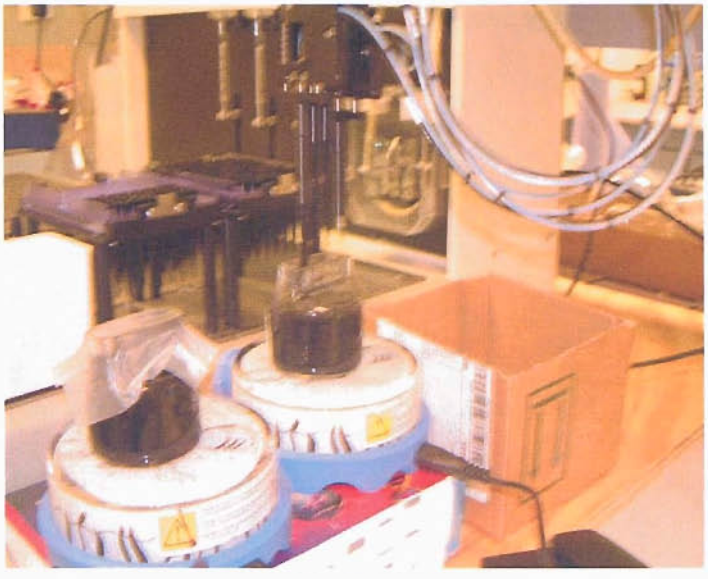

Figure 2.11 – Aspiration of ink solutions using the *Multiprobe II*.

During the mixing step the inks were aspirated from the stock solutions and dispensed into a well in a quantity that was derived from values in an *Excel* spreadsheet. When both inks were deposited in the well, the robot performed two mixing steps to ensure full mixing of the solutions known as 'post dispense mix steps' in which the robot re-aspirated the solution in the well using a disposable pipette and re-deposited it back into the well. However, in later experiments, this step was replaced by a manual-mixing step once all components were deposited in the well. This consisted of capping all the individual solutions and placing a lid on to the array. The array of suspensions was then manually agitated several times before the electrode samples were prepared. The original robotic mixing step involved the aspiration of the entire stock solution and the dispensing back into the well. However, the disposable tips easily became blocked during this original procedure leading to inaccurate deposition quantities during electrode deposition (see Figure 2.12).

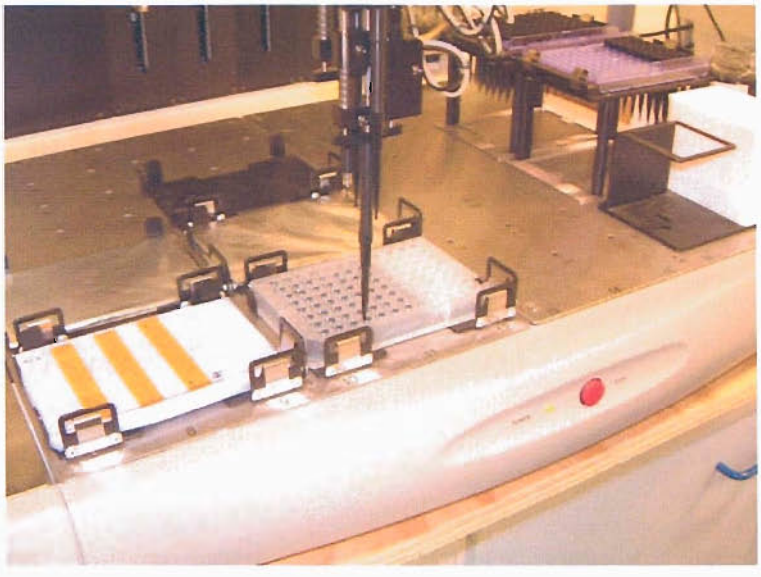

Figure 2.12. Dispensing and mixing of electrode materials into a 96 well plate.

An *in-house* designed electrode cycling array was constructed to fit into the *labware* space on the deck of the robot. This design allowed the inks containing the electrode materials to be directly dispensed by the robot to the testing array to a high accuracy ($\Delta V = \pm 2$ % while dispensing 5 μL). Typically approximately 1-5μL of ink containing electrode material was deposited on each electrode. Since the mass fractions and measured masses of the suspended material in the inks were known, the amount of active material in each electrode can be calculated, assuming that the effect of particle settling is negligible. This enabled a value of specific capacity to be obtained for each electrode. The mass of active material on the electrode surface can be calculated using the following Equations (2.2 and 2.3):

$$m_{electrode}^{AM} = V_e \times W_{AM}^{C} \frac{V_{AM,I}}{V_{TOT,I}}$$ **Equation 2.2**

$$W_{AM}^{C} = f_{s,i} \times f_{AM,s} \times d_{AM,i}$$ **Equation 2.3**

Where:

$m_{electrode}^{AM}$	=	Mass of active material on electrode surface (g)
V_e	=	Volume of ink deposited on the electrode (mL)
$V_{TOT,I}$	=	Total volume of ink in vial or well (mL)
$V_{AM,I}$	=	Volume of active material ink in vial/well (mL)
$f_{s,i}$	=	Fraction of solids in AM ink
$f_{AM,s}$	=	Fraction of AM in solid contents
$d_{AM,i}$	=	Density of AM ink (g cm^{-3})
W_{AM}^{C}	=	Weight concentration of AM (g cm^{-3})

2.2.2.4 Electrochemical Testing Array

An electrochemical cell for electrode testing based on an 8x8 square array arrangement was designed and built in house for combinatorial projects [2, 8] (see Figure 2.13). The use of this cell enabled the simultaneous study of 63 independent working electrodes of different composition. The electrodes were robotically deposited on to the polished surface of an aluminium rod ($\varnothing$ = 3 mm), which acted as the positive current collector (see Figure 2.13 A).

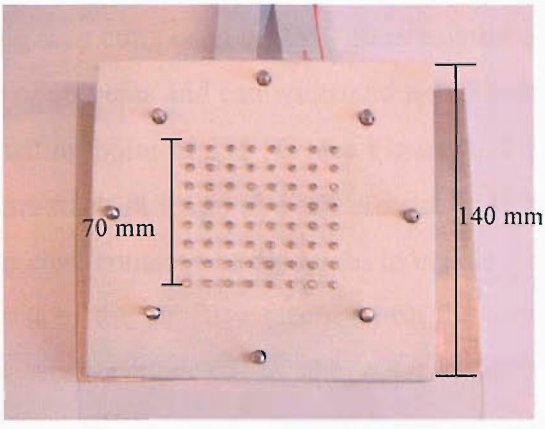

(A)

(B)

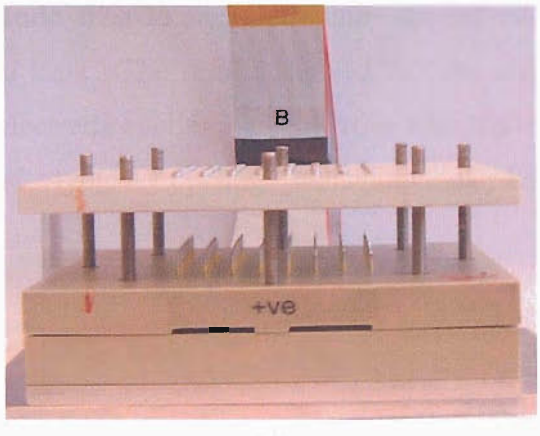

(C)

Figure 2.13 - Cell views: A - the 63 active aluminium current collectors on the combinatorial electrode testing array; B - closed view after cell construction; C - interior prior to cell construction, individual spring contacts.

The array casing was composed of 25% glass reinforced Teflon (PTFE) as it is resistant to most types of solvents and can withstand a maximum operating temperature of 260 °C and has a melting point of 335 °C (see Figure 2.13 B). Eleven springs were used to provide uniform stack pressure over all electrodes in the cell (see Figure 2.13 C). A smaller stainless steel contact was also used to enable a connection from a single channel of a potentiostat to the negative electrode on the array via a spring. The 63 aluminium electrodes were connected to the current followers (home-made) via needlepoint spring contacts (*RS Components Ltd*) that were soldered into a printed circuit board (PCB). Two 34-way ribbon cables made the final connection from the current follower unit to the PCB. Two schematic diagrams of the electrochemical cell are shown in Figures 2.14 (side elevation) and 2.15 (plan view).

In order for the array to fit into locator holes on the robot, an adapter was designed which will allow the array to be placed on the robot in exactly the same position each time. This is important, as it will allow the same 'labware' set-up to be used for each new electrode film deposition, reducing the set-up time for experiments.

The suitability of the aluminium rod as a current collector was initially tested using a film cast from the two inks. Aluminium is widely used as a current collector for positive electrodes in lithium batteries [9]. However, it was important to ascertain if the adhesion of the electrode film to the aluminium current collector was suitable for further electrochemical tests. The results showed that the aluminium rod served as a suitable substrate for electrode cycling, the electrode film showed good adhesion to the current collector and typical cycling behaviour of $LiMn_2O_4$ was observed (see section 2.3.2.1).

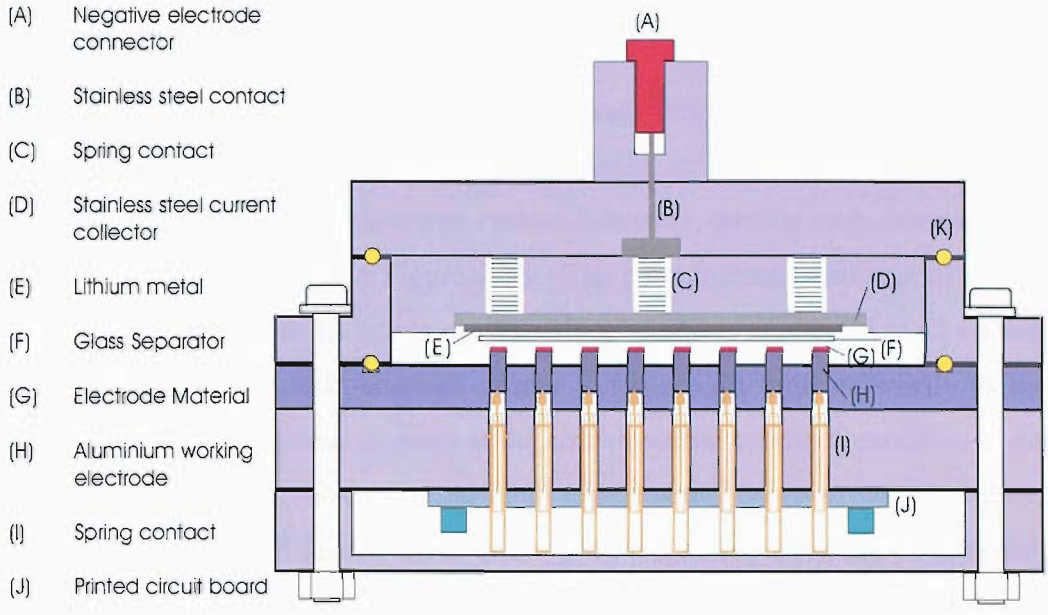

Figure 2.14 - Schematic diagram of the combinatorial electrochemical cell .

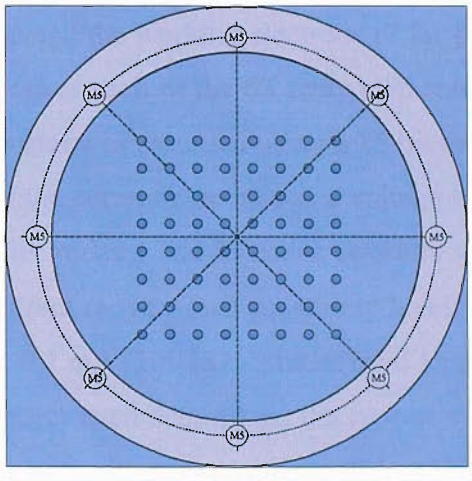

Figure 2.15 - Plan view of 8x8 array of electrodes.

2.2.2.5 High-Throughput Instrumentation and Software

The characterisation of 63-channel arrays was undertaken using in-house instrumentation and software. The current response at each of the 63 working electrodes was measured using an array of current followers, one for each channel. The circuit diagram is shown below in Figure 2.16. The combinatorial cell was of a two-electrode design. An array of 63 active positive electrodes was connected to 63 current followers housed within a multi-channel current follower unit built externally to the specifications required by several projects at the combinatorial centre of excellence. An 8x8 array of 63 active electrodes was used in all experiments; however one channel of the 16-bit card was reserved for the input of the potential sweep from the potentiostat. Therefore only 63 channels were available for testing. The voltage sweep and potential limits were set on a single channel of a multi-channel potentiostat (VMP). The cell counter and reference electrodes were connected to the negative electrode of the combinatorial cell (lithium metal electrode) and the cell potential was measured between the counter-reference electrode and the working electrode of the potentiostat, which was set at ground. The 63 working electrodes in the combinatorial cell were also at ground. Therefore the cell potential was determined by measuring the potential difference between ground and the working electrode of the potentiostat.

The current response at each of the 63 array elements, together with the voltage response form the potentiostat was recorded using a 16-bit data acquisition card (A to D converter). This recorded the current response as a voltage from 64-single ended inputs from the array working electrodes. The feedback resistors in the current followers can be replaced to tune the current range. Two sensitivity levels were used in two different instrument specifications, 0.1 mA (100 kΩ resistors) and 1 mA (10 kΩ resistors) current ranges. The choice of resistor used determined the type of system that could be studied using the system. The high sensitivity instrument (0.1 mA) was intended for the study of thin films of low active mass and the low sensitivity instrument was used for studying thicker films made from $LiMn_2O_4$/AB/PVDF inks.

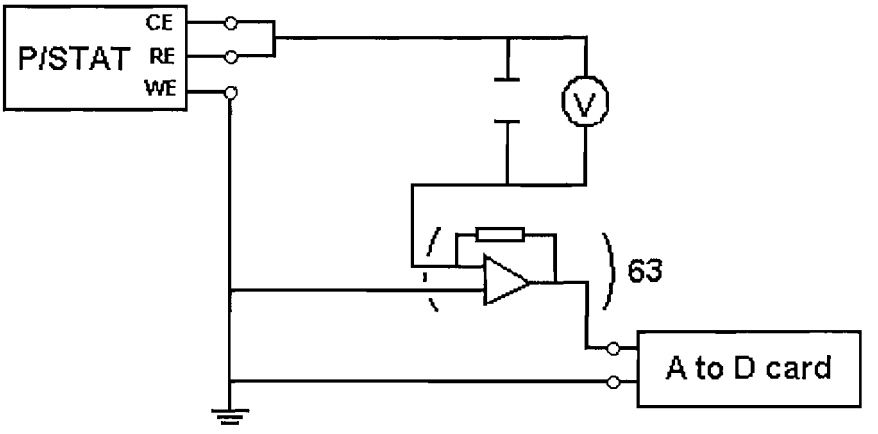

Figure 2.16 – Electrode connections between the potentiostat and current follower.

2.2.2.6 Instrumentation Testing Experiments

The electrochemical equipment was tested for suitability to perform the screening experiments (see Figure 2.17). This was undertaken to ensure a reproducible response was obtained from the individual electrodes. A 1 kΩ resistor was placed between each of the working electrodes on the combinatorial cell and the reference-counter of the VMP. A constant potential of 0.1 V was applied from the VMP to all electrodes and the observed voltage at each electrode was recorded. It was found that a variation in the range 0 to 0.5 mV was observed between the applied potential and the observed potential at the electrodes (see Table 2.3). This is the offset potential and is a measure of the amount by which the voltage at each of the 63 working electrodes varies from the applied potential. The offsets show a maximum variation of around 0.1 mV. This is acceptable for the sensitivity of the screening experiment, and therefore, does not present a problem to the experimental method.

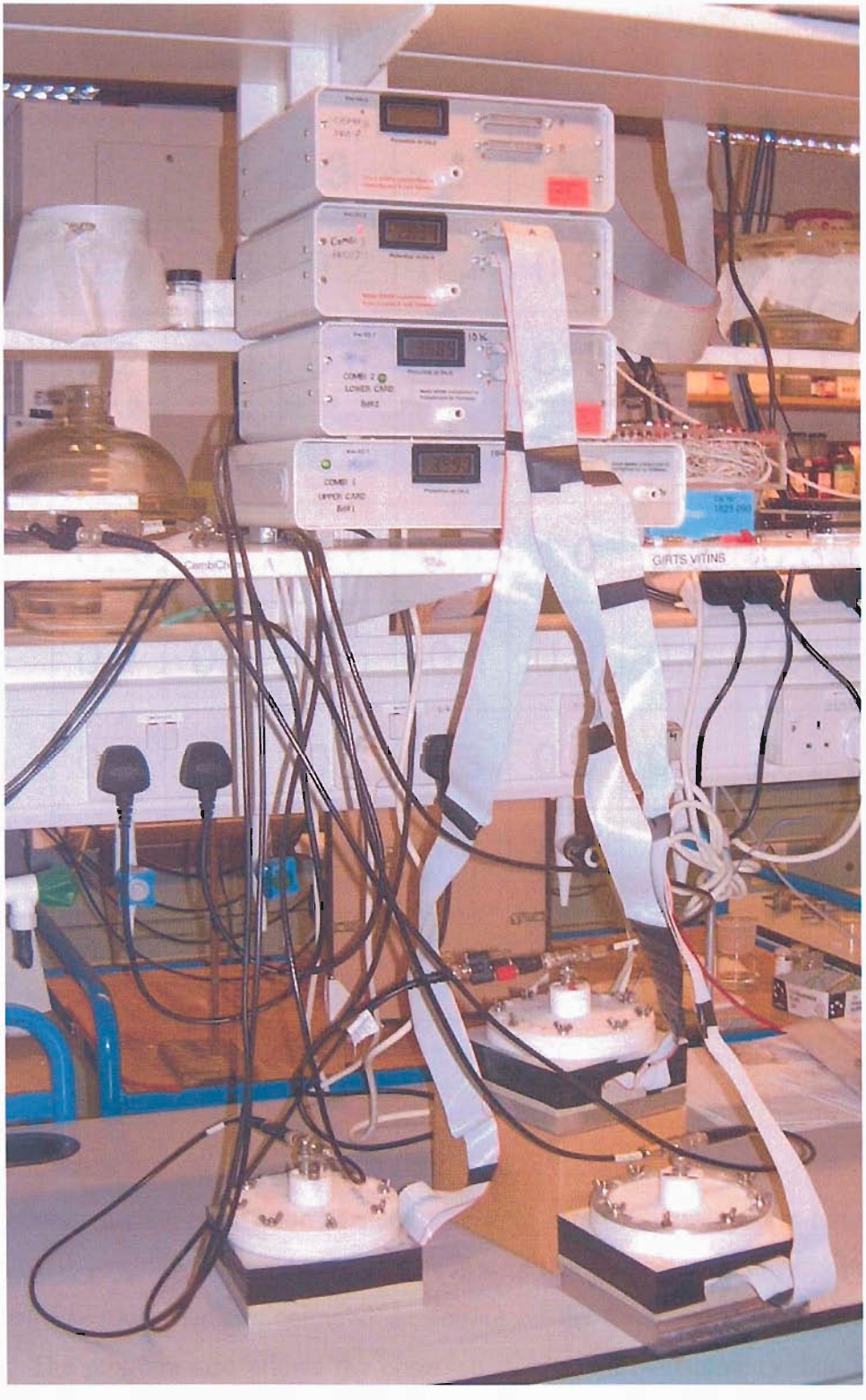

Figure 2.17 – Cycling of three combinatorial electrochemical cells, corresponding to the study of 192 individual electrode compositions.

Table 2.3 - Measured offset potentials (in mV) for current follower unit 1 when a potential of 1V was applied to electrodes in the array.

Electrode	1	2	3	4	5	6	7	8
1	0.7	0.8	0.2	0.1	0.8	0.8	0.2	*CH0*
2	0.2	0.0	0.0	0.1	0.4	0.8	-0.1	0.2
3	0.5	0.6	0.2	0.1	0.6	0.5	0.2	0.1
4	0.3	0.1	0.6	0.9	1.0	0.2	0.3	0.2
5	0.4	0.5	0.5	-0.1	0.3	0.3	0.4	0.5
6	0.2	0.5	0.3	0.3	0.5	0.5	0.1	0.3
7	0.2	0.0	0.3	0.1	0.5	0.0	0.2	0.5
8	0.5	0.5	0.2	0.2	0.1	0.3	0.6	0.3

2.2.2.7 Electrochemical Screening Software

The software for the acquisition of electrochemical data was developed in-house using visual basic programming tools [5]. The software displays the current response as an array of electrodes that are coloured depending on the measured current (see Figure 2.18). The program also allows the observation of cyclic voltammetry data for each channel (see Figure 2.19), a means of storing data and real-time observations to be made for the electrochemical response at each channel.

Screening software was also developed in addition to the acquisition program. This enabled large amounts of data, recorded over many hours to be analysed within a few minutes leading to a good understanding of the response at each channel. The current responses at each of the electrodes can be sped up by a factor of 100 allowing many hours of data to be reviewed in a few seconds. This method of data analysis has the advantage that cell data can be reviewed and analysed while the cell is running, allowing changes to the cycling regime to be made to the cell before it is discarded.

Figure 2.18 – High-throughput analysis software 'The Anaylser'. Allows rapid analysis of results obtained for the electrode array.

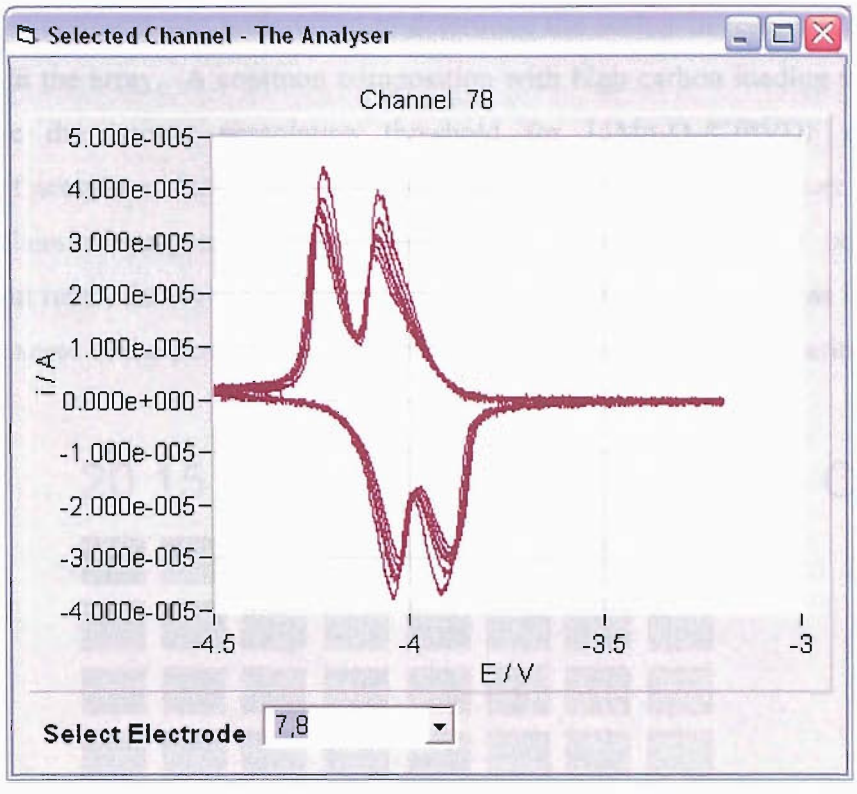

Figure 2.19 – Analysis of cyclic voltammetry data for a $LiMn_2O_4$ electrode using the combinatorial data analysis software.

2.2.2.8 Screening Experiments

The aim of these initial experiments was to evaluate and test the combinatorial methodology and equipment, to determine the level of reproducibility of results and to evaluate the method with respect to existing electrode testing methodologies. In the initial test experiments, eight different electrode compositions along the *x*-axis were repeated eight times along the *y*-axis. This gave sixty-four individual mixed ink compositions. This was undertaken to ensure there were sufficient compositions to observe a trend in the percolation curve and to determine the statistical significance of the result. Of the eight compositions chosen, some were below the expected percolation threshold while others were on or above it. The compositions chosen were 1, 2, 3, 5, 7, 10, 15 and 20 wt.% of acetylene black and the amount of binder was kept constant at 10 wt.% of the composite (see Figure 2.20).

An experiment was undertaken to determine the scatter in results across the all electrodes in the array. A common composition with high carbon loading was chosen high above the known percolation threshold for $LiMn_2O_4$/C/PVDF composites (20 wt.% of acetylene black). This high level of carbon was used to ensure the scatter in electrochemical response was not due to poor electronic contact between the particles, but rather due to the screening process, as 20 wt.% of carbon was found to be a value in excess of the percolation threshold as determined by earlier experiments.

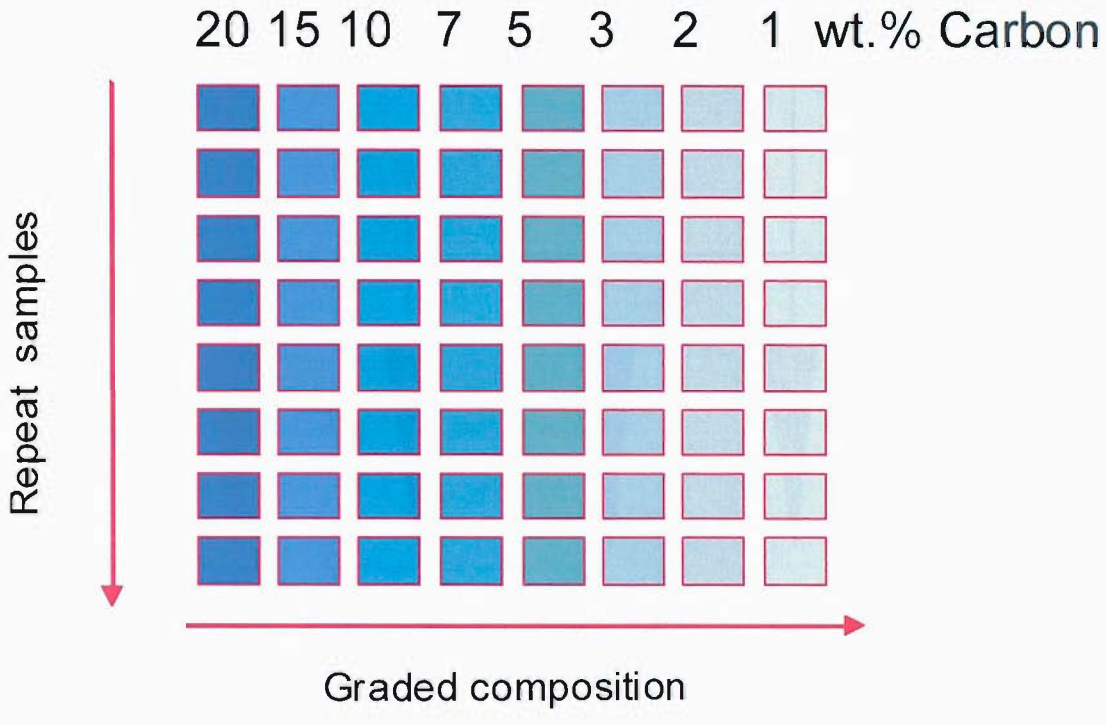

Figure 2.20 - Electrode compositions used in the validation experiment.

2.2.3 Electrode Film Conductivity Using the Four-Point Probe Method

Composite films of varying composition of conducting additive were tested using a four-point probe method (see Figure 2.21). The experimental apparatus consisted of four equally spaced tungsten metal tips of finite radius. The four tips were mounted on a spring-loaded stage that could be moved up and down to enable access to the sample. A current source was used to supply current through the two outer probes. A

multimeter was used to measure the voltage across the inner two probes to determine the sheet resistance (R) by measuring the IR drop. The thickness of the sample was measured using a micrometer *(± 0.01 mm)*. A *Solartron ECI-1287* was used to apply a constant voltage to the samples in these experiments. The use of this technique gave a value for film resistance as calculated using Ohm's law. This value for film resistance was converted to a specific conductivity value using the formula given below [10].

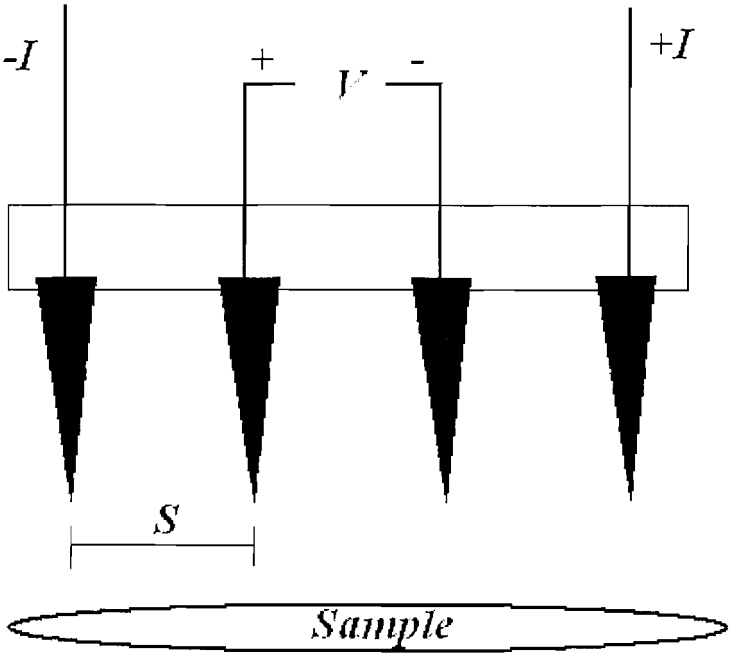

Figure 2.21 – The geometry of the four-point probe method

$$\rho_s = \frac{I}{V \times l \times 4.53}$$

Equation 2.4

Where, ρ_s is the sheet resistivity (assuming an infinite sample area), is the applied current, V is the IR drop between two reference probes, l is the film thickness and 4.53 is the value of $\pi/ln2$.

The value 4.53 was derived from equations governing the behaviour of the current paths in very thin layers *i.e.* when the film thickness (l) is much less than the probe spacing (s). These equations can be used if the film is considered as an infinitely thin film, with an infinitely large circular sample area.

Consequently the sheet resistivity for a thin sheet is:

$$\rho = \frac{\pi}{\ln 2} \times \frac{I}{V \times l} \qquad \textbf{Equation 2.5}$$

and,

$$\frac{\pi}{\ln 2} = 4.53 \qquad \textbf{Equation 2.6}$$

Therefore the sheet resistance is given by:

$$R_S = 4.53 \times \frac{V}{I} \qquad \textbf{Equation 2.7}$$

Specific conductivity is defined as:

$$\sigma_s = \frac{1}{R_s \times l} \qquad \textbf{Equation 2.8}$$

Specific conductivity values were plotted *vs.* weight fraction of conducting additive (acetylene black).

2.3 Results and Discussion

Electrode materials were prepared using conventional and combinatorial techniques and were characterised using electrochemical screening techniques, SEM and EDX. The results obtained using the different methods are compared in the following sections.

2.3.1 Conventional Electrode Characterisation

Electrode materials were prepared and screened using conventional techniques, as outlined in section 2.2. The conductivity, electrochemical cycling behaviour and film morphology were investigated using SEM.

2.3.1.1 Micro-structural Properties of $LiMn_2O_4$/AB/PDVF Films

Scanning electron microscopy was used to study the microstructure of composite electrode films of varying carbon loading. The SEM samples were prepared from the same films that were used for electrochemical testing. Films of 20, 4.5 and 0.2 wt.% were studied using a *Philips XL-30 ESEM* in high vacuum mode.

The selected SEM micrographs for three films containing 20, 4.5 and 0.2 wt.% AB show significant differences in microstructure (see Figures 2.22 –2.24). The film that contains 20 wt.% of carbon is composed of particles of the same approximate size (~ 5 μm) as the films containing 4.5 and 0.2 wt.% of carbon. However, a matrix consisting of finer particles can be seen surrounding the $LiMn_2O_4$ poly-crystals. These particles cannot be resolved using the SEM and they can be seen to fill all remaining space between the larger $LiMn_2O_4$ particles. This space-filling matrix becomes more noticeable as the carbon loading is increased from 0.2 wt.% to 20 wt.%. Small cracks in the film can also be seen in the samples containing high carbon loadings. This may indicate that at high carbon loadings the films are more fragile on the micro-scale. However these cracks which are small in number, are also small in size (~100 μm) relative to the total sample area (approximate diameter 10 mm), so should have a negligible effect on the conductivity measurement.

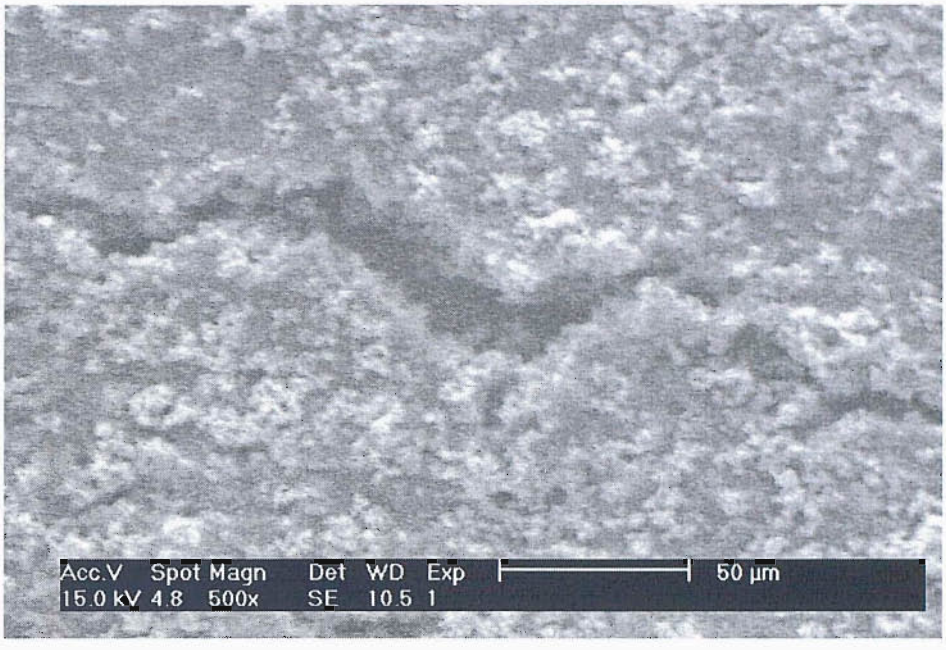

Figure 2.22 - SEM micrograph of a composite electrode containing 75 wt.% $LiMn_2O_4$, 20 wt.% AB and 5wt.% PTFE at 500x magnification.

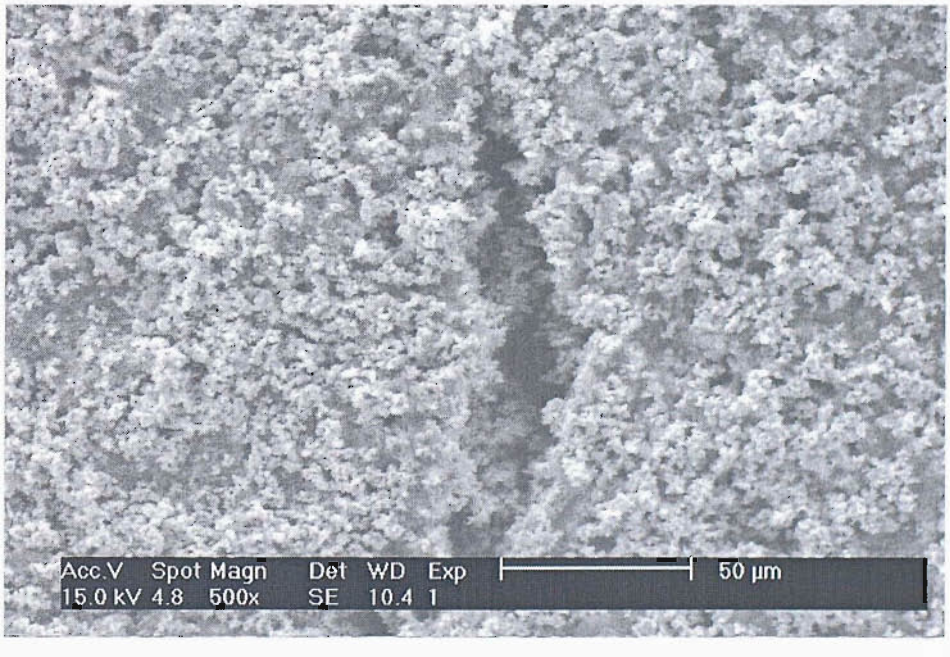

Figure 2.23 - SEM micrograph of a composite electrode containing 90.5 wt.% $LiMn_2O_4$, 4.5 wt.% AB and 5 wt.% PTFE at 500x magnification.

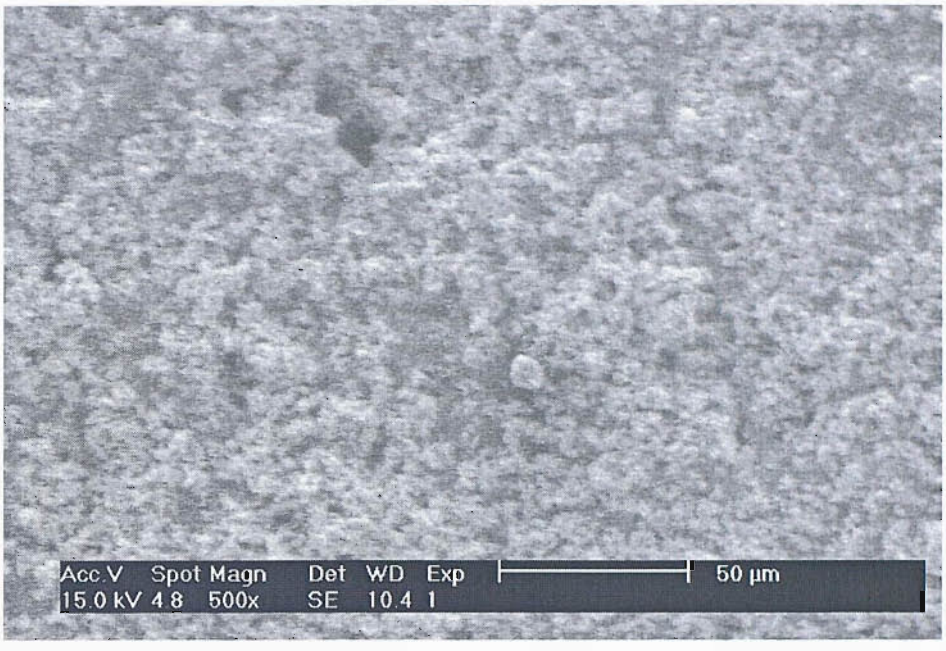

Figure 2.24 - SEM micrograph of a composite electrode containing 94.8 wt.% $LiMn_2O_4$, 0.2 wt.% AB and 5 wt.% PTFE at 500x magnification.

2.3.1.2 Conductivity Measurements

Many lithium battery materials are poor conductors and their energy storage potential can only be exploited by the formation of composite materials containing a finely divided conductor. The conductivity of the composite is therefore increased to facilitate electron flow from the current collector to the redox centres in the active material thus, increasing the rate of the insertion reaction. The mixture of insulating and conducting materials to form a composite will result in percolation behaviour, these effects can be observed in conductivity and electrochemical cycling data. A description of percolation phenomena can be found in section 1.6.

The addition of a small amount of conducting additive may have little effect on reversible cell capacity, but can result in a many-fold increase in composite conductivity if added in an amount around the percolation threshold for the active material. Experiments must be conducted to determine percolation behaviour for a new

material, by preparing composites containing varying quantities conducting additive and observing its effect on the overall composite conductivity.

The conductivity of composite electrode films containing $LiMn_2O_4$, PTFE and varying amounts of AB were investigated using two-probe and four-probe methods. The data shown in Figure 2.25 shows specific conductivity as a function of carbon weight percentage and were obtained using a two-probe measurement. It was expected that four-probe method should give similar results, but was not used in these initial experiments.

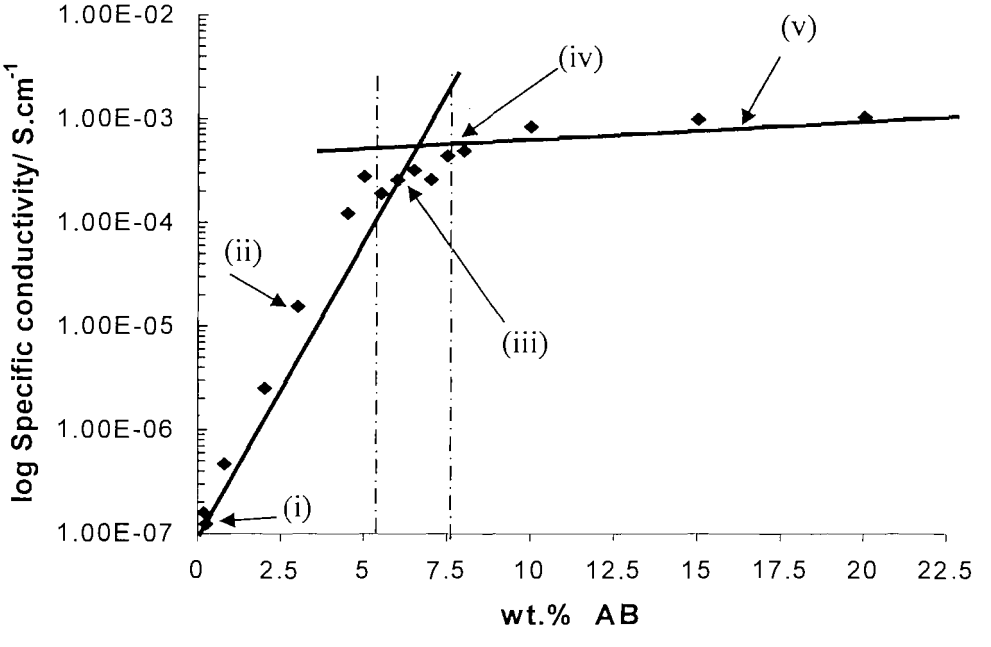

Figure 2.25 - Specific conductivity of $LiMn_2O_4$ composite films *vs.* AB weight percentage measured using a two terminal method.

Several features of the plot should be noted:

i) The lowest value for conductivity occurs when carbon is not present in the composite at 0 wt.% AB

ii) The linear region (linear on log scale) between zero and approximately 5 wt.%

iii) The gradient of the line shallows between 5 and 8 wt.%

iv) The gradient of the line approaches zero at 10 wt.%

v) The region 10 - 20 wt % has a gradient of approximately zero

Figure 2.26 is a plot of specific conductivity *vs.* wt.% carbon with the conductivity values plotted on a linear *y-axis*. The data was plotted in three groups, high (> 10 wt.%, diamonds), intermediate (5 to 8 wt.%, squares) and low (< 4 wt.%, triangles) carbon. This is the same data as is shown in Figure 2.25. This plot shows that the percolation threshold as defined as the value of wt.% carbon at which the regression lines of the intermediate and higher carbon data sets meet, this value is around 10 wt. %. However, an inspection of the log scale plot (in Figure 2.26) would suggest the percolation threshold might lie at around 7.5 wt.%, because it is clear from the data in Figure 2.26 that the conductivity of the composite increases most rapidly in the region between 0 and 4.5 wt. % of carbon. As the plot is not linear, the use of linear regression lines may not give an accurate indication of the percolation threshold. In order to gain a more accurate estimate, the data could be fitted to a relationship such as that suggested by Mandal *et al.* [4].

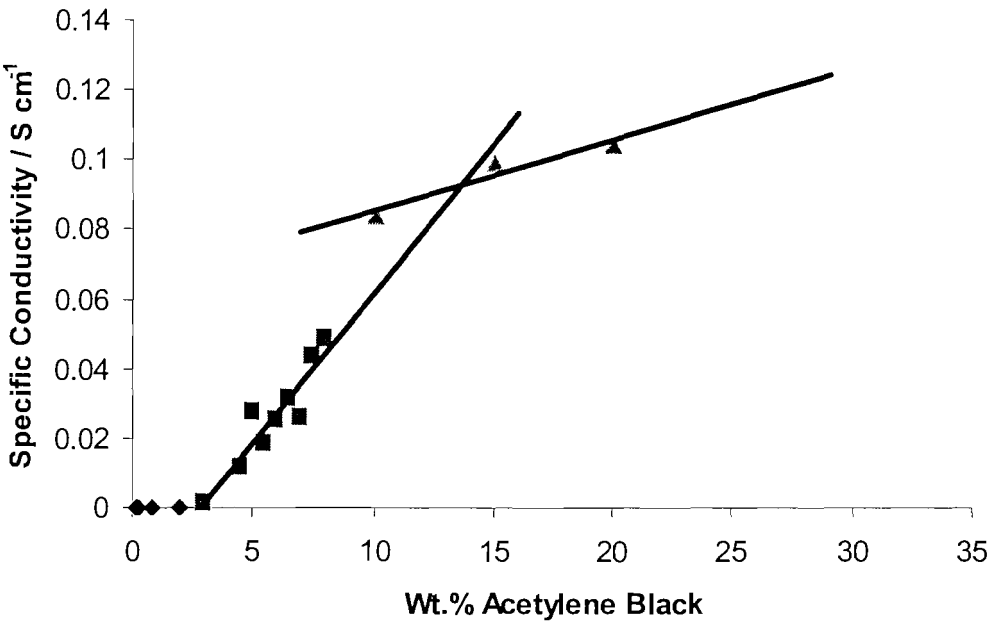

Figure 2.26 - Specific conductivity of $LiMn_2O_4$ composite films *vs.* AB weight percentage measured using a two terminal method.

The plots in Figures 2.25 and 2.26 demonstrate the theory of percolation of electronic conductivity through the composite. At 0 wt.% carbon, the composite contains only $LiMn_2O_4$, which has low conductivity (~ 1 x 10^{-3} S cm^{-1}) and PTFE, which is an insulator. Hence we observe the lowest value for conductivity. As the carbon loading increases, the carbon begins to form a conducting network through the lesser conductor ($LiMn_2O_4$) and higher values of conductivity are observed. The linear region exists up to 5 wt.% after which a lowering in the gradient occurs up to 10 wt.%. At carbon loadings greater than this value, a suitably well-developed percolation network exists, and the gradient of the line is very close to zero. In the region after 7.5 wt.%, the line becomes flat, and thus, the addition of further amounts carbon to the composite will have a negligible effect on conductivity. It can therefore be concluded that the percolation threshold for conductivity of the $LiMn_2O_4$ films containing AB occurs between 5 and 12 wt.%. An intermediate value of 7.5 wt.% will be taken as the percolation threshold. This result agrees findings reported by Mandel *et al.* [4].

2.3.1.3 Electrochemical Testing

Cells containing $LiMn_2O_4$ positive electrode material were cycled galavnostatically at three rates to observe the effect of percolation in the specific capacity data. This can be seen in Figures 2.27 and 2.28. Stainless steel and coin cells were used for these experiments. This was because the results obtained by conventional methods were required for comparison, for the purpose of determining the validity of combinatorial methods described in this section. When using very low fractions of AB the specific capacity is close to zero. However, as the AB fraction is increased, a linear region is observed between 0 and 3 wt.%. This linearity continues until a threshold is reached, after which the gradient of the line shallows and approaches zero. This behaviour is observed in cells cycled at both the C/5 and C/3 cycling rate. In both the C/5 and C/3 cases, the percolation limit can be seen to occur at approximately 5 wt.% of carbon in Figure 2.26 (log *y*-axis scale). In contrast, the threshold is seen to occur at around 7.5 wt.% in Figure 2.27 (linear *y*-axis scale).

The data in Figure 2.27 was fitted using two intersecting regression lines for two sets of data using the same method described in section 2.3.1.2. It appears from these results that the percolation limit for the specific conductivity and the specific capacity are not equal, as the threshold in the conductivity case occurs at between 7.5 and 12 wt.% depending on the graph and interpretation method. In contrast, the threshold in capacity occurs between 5 and 7.5 wt.%. This inequality in the position of the percolation limits for capacity and conductivity may be explained by the morphology of the electrode material.

The conductivity of the composites was measured vertically through the film and the value depends only on the ease of electron transport between the measuring terminals, whereas the interactions between the carbon and redox active material are not measured. However, in the case of the calculation of specific capacity, the interactions between the carbon particles and the active components give rise to the measured current. If the particles in the carbon network do not reach the active materials, a low current value will be measured. It has been reported that the surface of activated carbon carries a negative charge [6], therefore, a carbon particle is more likely to interact with the neutral active material particles than with other carbon particles. For this reason, it

is possible that the active material particles become surrounded by carbon particles, to a greater extent than the carbon network can perpetuate through the film. Hence, the redox centres of the active material can be utilised at lower carbon loadings than are required for the maximum composite conductivity to be reached using a conductivity measurement.

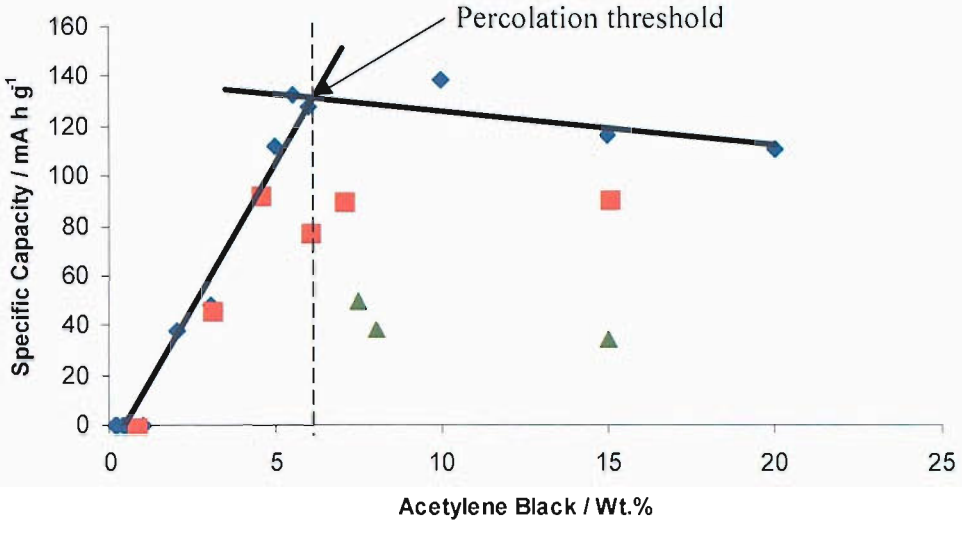

Figure 2.27 - Specific capacity for the first charge of $LiMn_2O_4$ *vs.* acetylene black wt.% at 3 cycling rates: C/5 (diamonds), C/3 (squares) and C/2 (triangles).

The cells shown in Figure 2.27 were prepared from electrode films containing a given carbon loading. The cell data above represents the first charge for different cycling rates. Therefore a different electrode was used for each data point and not all cycling rates were studied for all compositions.

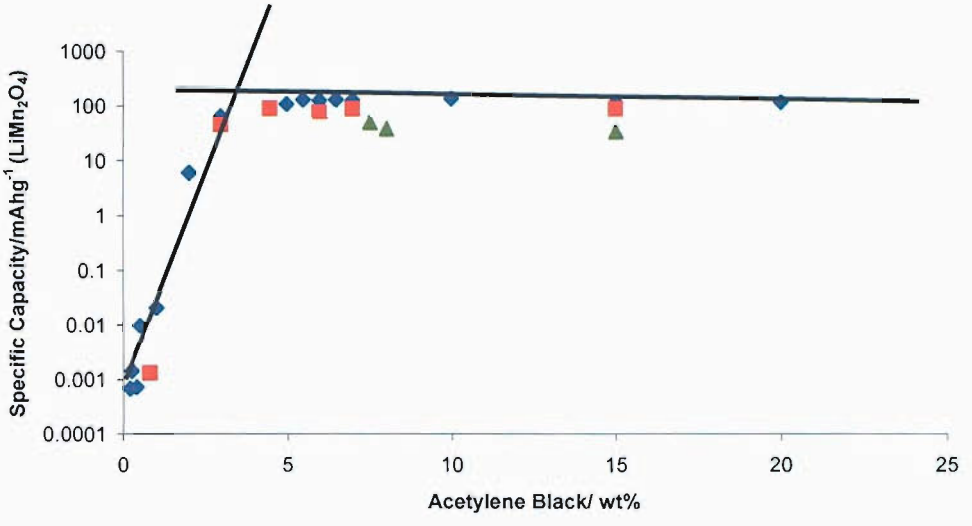

Figure 2.28- A plot of Specific capacity for the first charge (on a log scale) *vs.* AB %wt for three cycling rates: C/5 (diamonds), C/3 (squares) and C/2 (triangles). This is identical data to that shown on a non-log scale in Figure 2.27.

Cells that were cycled at the C/2 rate had a specific capacity of appoximately 40 mAh g^{-1} when containing a level of carbon above the threshold limit, whereas the cells cycled at C/5 exhibited capacity between 120-130 mAh g^{-1} above the threshold limit. This lower capacity is possibly due to the polarisation of the cells before complete discharge at higher rates. Polarisation is a term applied to processes, which causes the cell to display a potential characteristic of full discharge before the normal amount of charge has been extracted. Discharge at high rates involves higher *IR* drops and larger concentration gradients and therefore premature arrival at a set potential cut-off point. If the cells were cycled at an infinitely slow rate, the observed capacity would be equal to the theoretical capacity, as the effect of slower kinetics are overcome by the long experimental time scale (and exposure to a very small charging current), and hence, the effect of diffusion is negligible, enabling full utilisation of all redox centres.

The shown data in Figures 2.27 and 2.28 can also be supported by a theory of inhomogeneous discharge, in which the removal of lithium from the host structure is not spatially uniform. In the simple case, the lithium closest to the electrode surface is extracted before the material in the interior. A different explanation is the removal of

lithium occurs most rapidly at the interface between the carbon and the active material because the removal of the lithium from the host structure is dependent on electrons reaching the host structure. As the particles of $LiMn_2O_4$ have lower electronic conductivity than the carbon particles, most of the electron transport occurs within the carbon matrix. This leads to the de-insertion of lithium from the structure when an electron reaches the host and hence, the closer the lithium is to the carbon matrix the more readily it is removed.

Typical percolation behaviour can be seen more clearly in the log scale plot (see Figure 2.28) in which percolation in specific capacity shows a similar profile to that of conductivity. It can be seen that the specific capacity increases most rapidly in the region 0 to 3 wt.% AB. Electrodes containing 0 wt.% AB show none of the reversible capacity expected for $LiMn_2O_4$, where as carbon loadings exceeding 3 wt.% show a high percentage of expected capacity.

It can therefore be concluded that the value of the percolation threshold is not a function of the cell cycling rate and hence is an independent value for a given composite. The linear region in the specific capacity plot between 0 – 4 wt.% is offset slightly from the 0-7.5 wt. % in the conductivity plot. A possible explanation for this could be that effective maximum capacity can be achieved with a less developed percolation network than is required to deliver the maximum conductivity value for the composite. However, it is clear that the maximum capacity that can be obtained for the $LiMn_2O_4$/AB/PTFE composites is a function of the cycling rate. A high rate of cycling will result in a lower total capacity than in the case when the material is cycled infinitely slowly, assuming the composites have a carbon loading exceeding the percolation threshold.

2.3.2 *Combinatorial Screening*

2.3.2.1 Scanning Electron Microscopy

The results obtained by SEM reveal the surface features and morphology of the electrodes are dependent on the amount of carbon in the electrode. This can also be seen in the case of electrodes prepared using the conventional electrode preparation technique. In samples containing low amounts of carbon (1 and 3%), large amounts of active material particles are observed at the surface (see Figures 2.29 and 2.30 respectively). The dark areas in the micrographs of the poly-crystals of $LiMn_2O_4$ can possibly be attributed to carbon black and the lighter areas to the PVDF-HFP covering the surface of the poly-crystals. However, in the sample containing 20 wt.% of carbon (see Figure 2.32) the surface of the electrode is coated with a fine particulate material, which fills the spaces in the more porous active material poly-crystals. In this case, a smaller amount of active material is visible with a dense covering of fine particulate carbon in all the regions between the $LiMn_2O_4$ particles. An intermediate case is seen for the electrode containing 7 wt.% carbon (see Figure 2.31). A magnification of 1000x was used as the maximum magnification; this was because the instrument produced poor quality images at higher magnifications. A high magnification would have been beneficial, as it would have given an indication of the homogeneity of the samples on or around the scale of a single or group of particles.

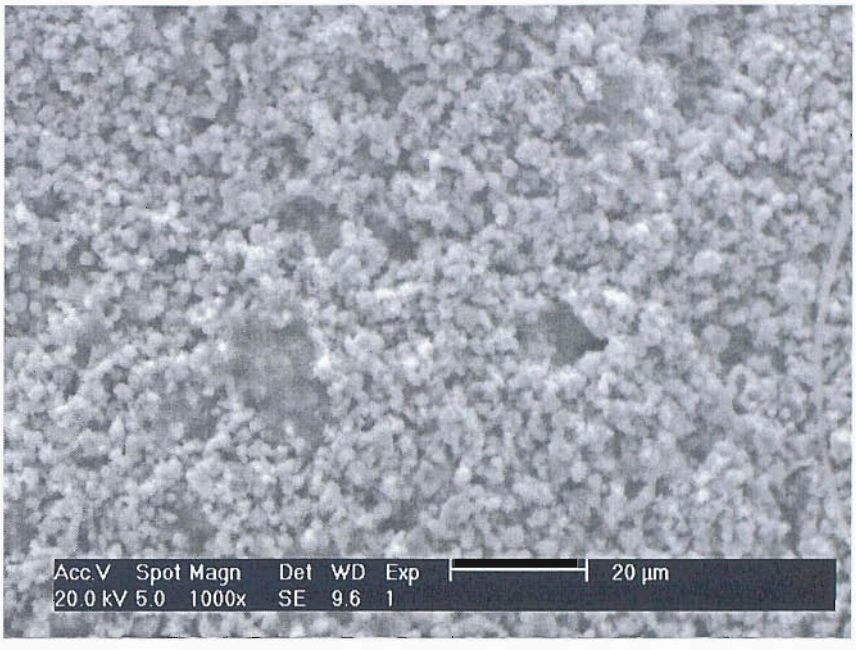

Figure 2.29 – SEM micrograph of an electrode containing $LiMn_2O_4$, 1% carbon and 10 % PVDF.

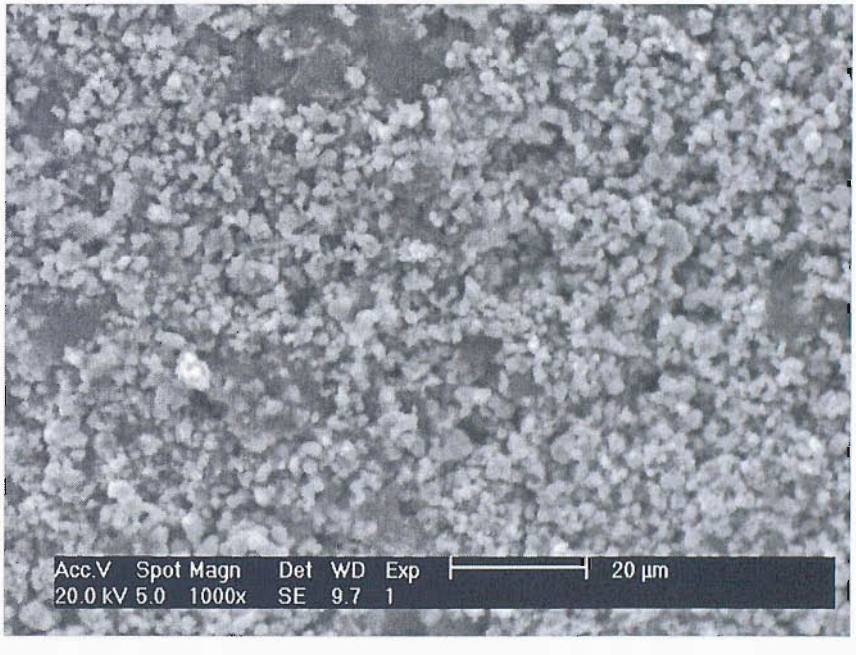

Figure 2.30 - SEM micrograph of an electrode containing $LiMn_2O_4$, 3% carbon and 10 % PVDF.

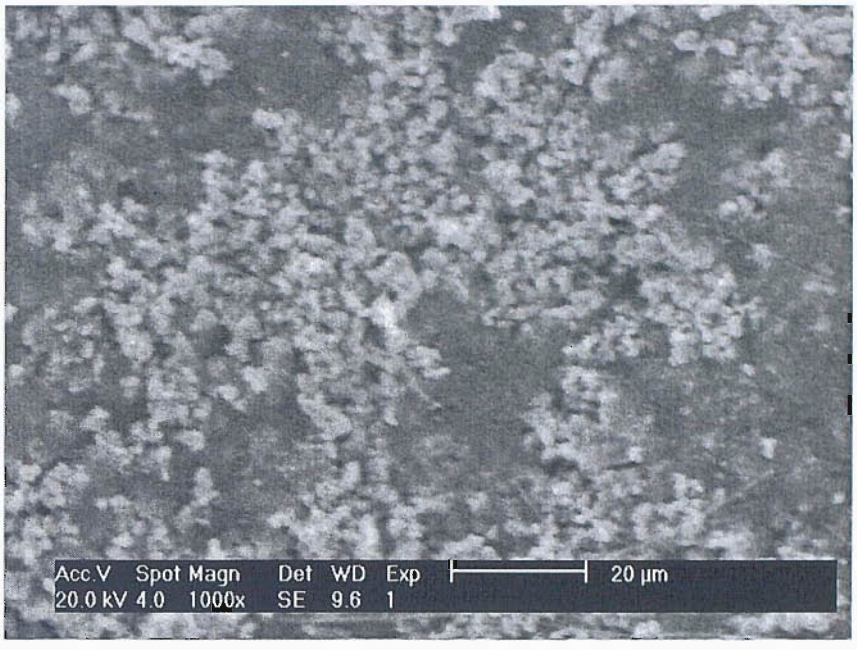

Figure 2.31 - SEM micrograph of an electrode containing $LiMn_2O_4$, 7% carbon and 10 % PVDF.

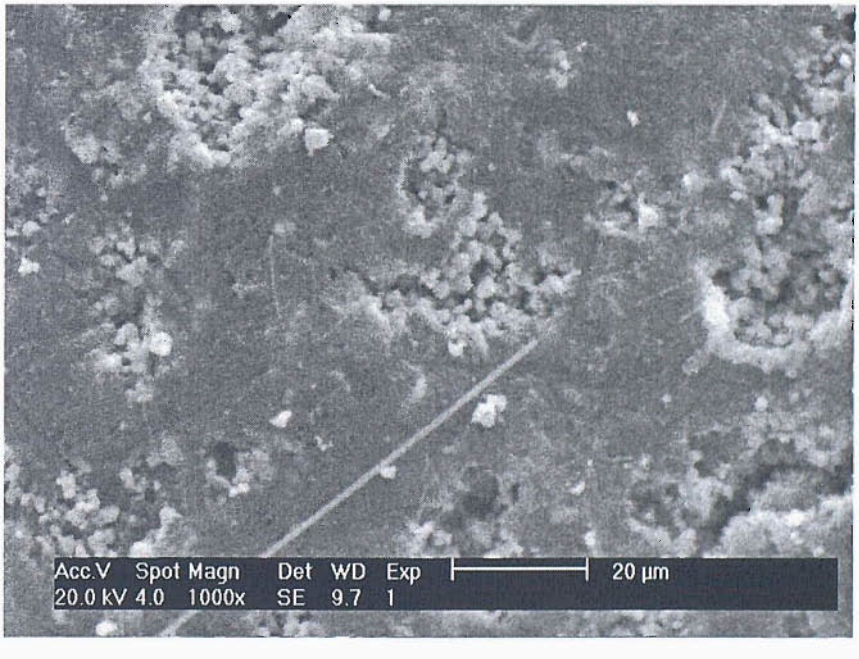

Figure 2.32 - SEM micrograph of an electrode containing $LiMn_2O_4$, 20% carbon and 10 % PVDF.

It should be noted that the carbon matrix is more pronounced in the samples prepared from ink suspensions. A possible reason for this may be that the electrode has not been sufficiently compacted. Hence the fine particles have not been displaced by larger $LiMn_2O_4$ particles that have been pushed to the surface. However gaps in the carbon coating in the 20 wt.% sample reveal the underlying $LiMn_2O_4$ poly-crystals. This result suggests the composite may not be of homogeneous composition and that the carbon particles have been pushed towards the surface of the film, while the active material has become more concentrated under the carbon layer, this may be due to sedimentation of the heavier $LiMn_2O_4$ particles after deposition but before the evaporation of the cyclopentanone solvent.

Figure 2.33 shows a comparison between two films containing 20 wt.% of carbon. The first was prepared by conventional roll milling (Figure 2.33 A) and the second, prepared from the ink suspensions (Figure 2.33 B). It is evident that the carbon matrix is more evenly distributed within the composite as the finer carbon particles are seen to fill all the space between the larger $LiMn_2O_4$ particles. In contrast, the carbon in the film prepared from the ink suspensions can be seen to form a layer on the surface of the film and smaller areas of the underlining crystalline $LiMn_2O_4$ material can be seen below the surface. One would expect from the morphology shown in the SEM micrographs below (Figure 2.23 and B) that the percolation threshold for the material shown in Figure 2.23A (conventional electrode preparation) would be lower than that of Figure 2.23B (combinatorial electrode preparation) as the carbon is mixed more effectively in the composite. Therefore a lower amount of carbon is required to obtain the expected cycling performance of $LiMn_2O_4$ in the case of the conventionally prepared electrode.

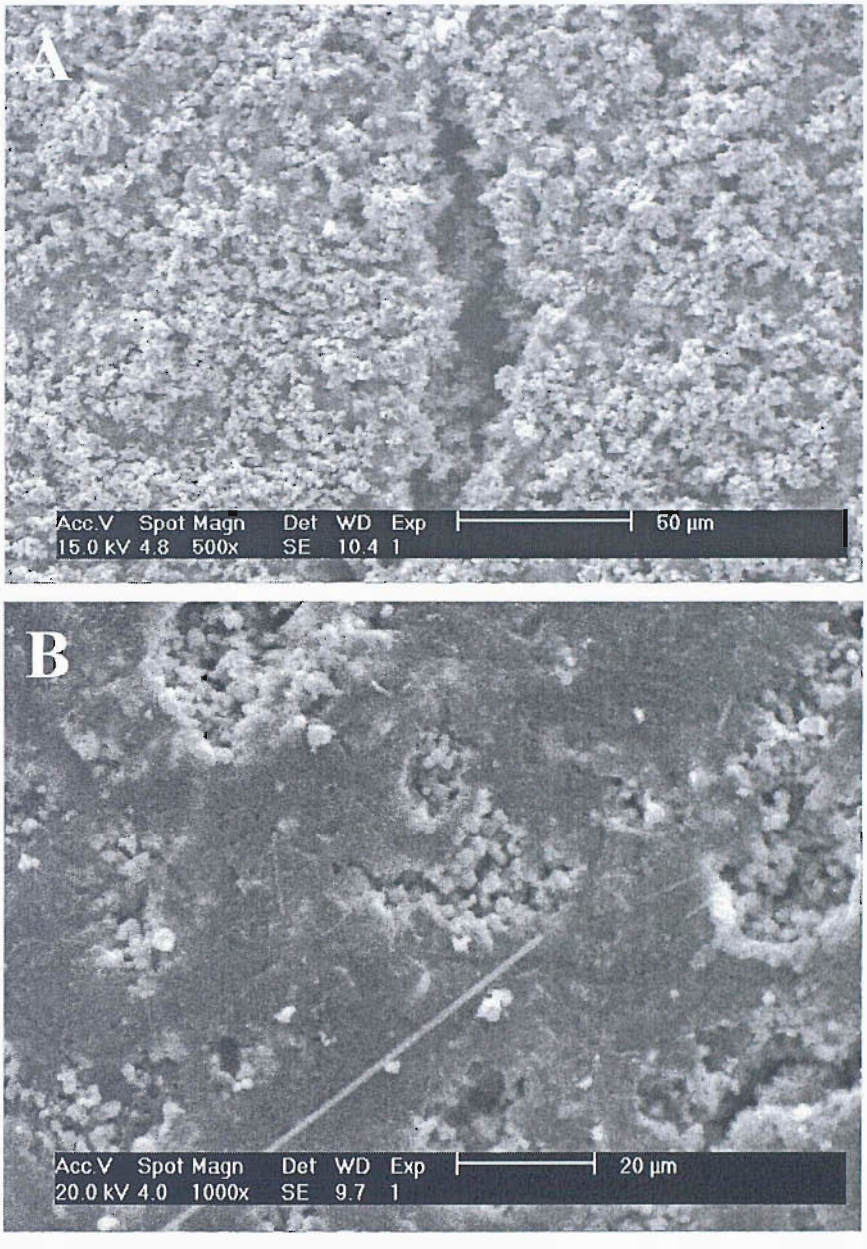

Figure 2.33 - SEM microscopy of $LiMn_2O_4$/C electrodes. (A) Containing 70 wt.% $LiMn_2O$, 20 wt.% carbon and 10 wt. % PTFE, prepared by conventional preparation techniques. (B) Containing 70 wt.% $LiMn_2O$, 20 wt.% of carbon and 10 wt.% of PVDF, prepared using high-throughput techniques.

2.3.2.2 Initial Electrochemical Testing

Initial testing of the combinatorial electrode screening method was initially carried out on a small scale using a single electrode, in order to test the effectiveness of the deposition technique and to determine the feasibility of electrochemical testing in the absence of significant stack pressure. 5 μL aliquots of ink solution were deposited onto an aluminium rod current collector $\varnothing$ = 3 mm, this produced an electrode film of approximately 150-200 μm in thickness. This rod was placed into a sealed glass vial, which served as a cell holder. The cells were constructed in a similar way to the stainless steel cells, in which lithium metal was used as the negative electrode with two *F-type* glass fibre separators soaked in 1M $LiPF_6$ in EC/DMC as the electrolyte and separating media. This technique simulated the cell arrangement on the combinatorial electrode array and allowed the cell arrangement to be tested prior to use in the 63-electrode array.

The cells were cycled galvanostatically as described in section 2.2. The cycling data shown in Figures 2.34 and 2.35 show the characteristic electrochemical behaviour of $LiMn_2O_4$. Two plateaux are observed at 3.9 V *vs.* Li, the first occurs when $x < 0.5$ and the second when $x > 0.5$ in $Li_xMn_2O_4$. The first plateau corresponds to a single-phase process and the second to two distinct cubic phases, which co-exist. The increase in potential between the two plateaux can be attributed to a change in the lithium ordering within the structure. This experiment demonstrates that electrode films can be deposited from ink suspensions directly on the electrode surface and tested electrochemically to give expected cycling characteristics using a combinatorial-type electrode arrangement.

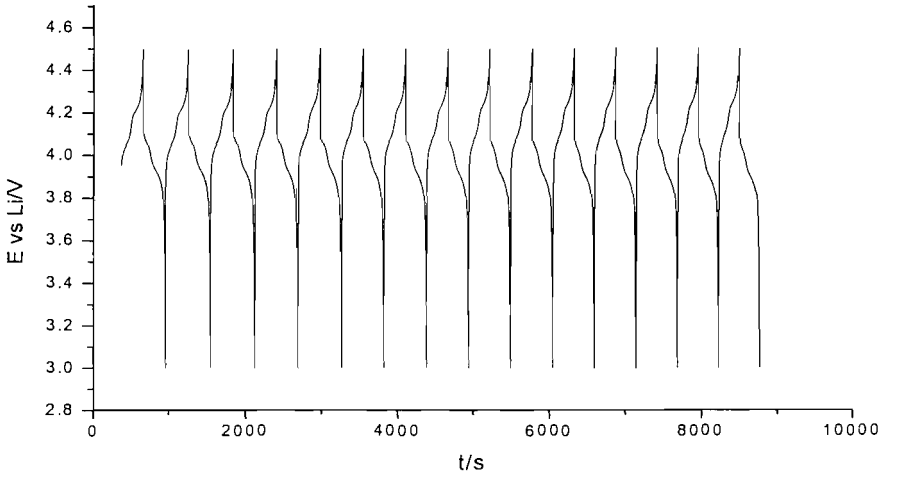

Figure 2.34 – Galvanostatic cycling data for a $LiMn_2O_4$ electrode deposited from a mixture of ink suspensions; 91 wt.% $LiMn_2O_4$ ink, 9 wt.% CB ink. Cycled at a fast charging rate 5 C (1 charge per 0.2h). Applied current = 0.085 mA for 15 cycles. Electrode capacity = 0.017 mAh.

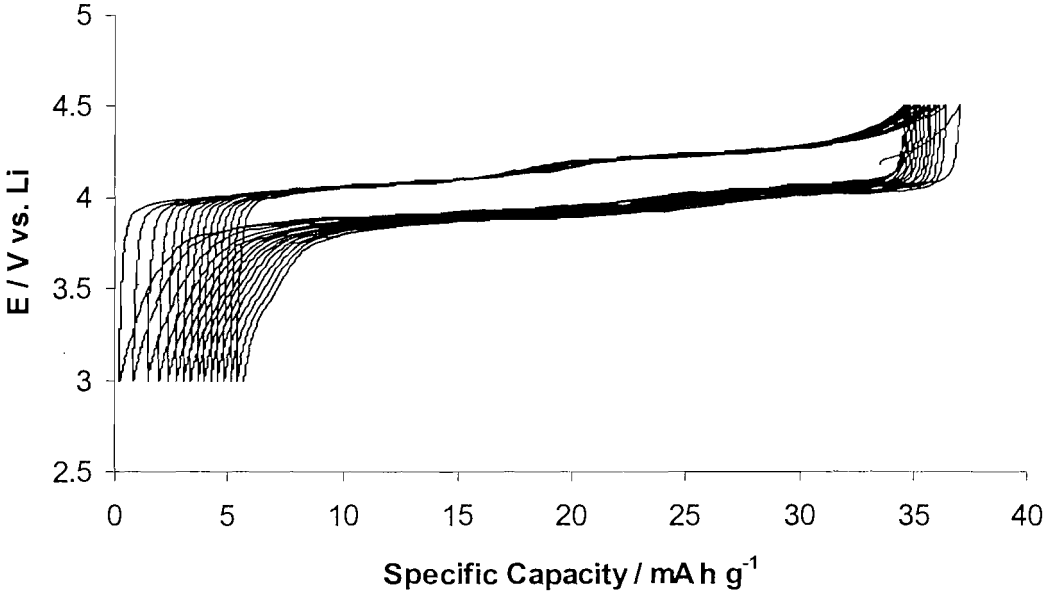

Figure 2.35 – Electrochemical cycling of a $LiMn_2O_4$/AB electrodes prepared from ink suspensions. Electrode composition: 91 wt.% $LiMn_2O_4$ ink, 9 wt.% CB ink. Cycled at a fast charging rate 5 C (1 charge per 0.2h). Applied current = 0.085 mA for 15 cycles. Electrode capacity = 0.017 mAh.

The specific capacity of the film shown in Figure 2.35 is lower than the expected practical value of ~ 110 mA h g^{-1} as seen in samples prepared using the conventional technique. In this case, a value of approximately 35 mA h g^{-1} was obtained. This difference in values was most probably a result of poor electronic contact between the electrode film, the current collector and the separators due to an absence of stack pressure. The cycling rate used in this test was 5C, faster than the C/7 rate that was used in other standard experiments. Another possible reason may be the lack of compression in the electrode film itself. As the electrodes were deposited directly from solution, they are most likely un-compacted. In the conventional preparation, electrodes were prepared from solid materials, mixed and compacted using a rolling device. The conventional electrode preparation techniques should result in increased electronic contact between the components in the electrode. This is due to the grinding and rolling processes used. These ensure greater inter-particle contact than would occur when depositing materials from solution as in the combinatorial technique. In the case of an un-compacted electrode, the reduced inter-particle contact should manifest itself as a decrease in current and hence, specific capacity.

2.3.2.3 Electrochemical Testing

Electrochemical tests were carried out on eight different compositions repeated eight times. This was to test if the system could differentiate between electrodes with high and low active material and carbon loading in terms of the kinetics of the electron transfer steps, which give rise to differences in observed specific capacity. In addition, repeating each composition eight times gave an indication of the scatter associated with the measurement technique and this was found to vary with the quantity of conducting additive in the composite.

Figure 2.36 shows a comparison between four of the eight compositions tested using the combinatorial screening system. The other four compositions are not displayed as they showed current responses above the saturation point for the current follower using 1 kΩ resistors. These data represent the intermediate case between high and low carbon levels, and thus have a larger total current response than the electrodes

containing 20 wt.% of carbon. This is because they have more active mass present, together with sufficiently high levels of carbon. The higher active mass in the electrodes resulted in a current response outside the range of the maximum current level for the instrumentation. In later experiments a lower sensitivity current follower was used to obtain data for all compositions in the range of the instrument (see Figures 2.40-2.42). The electrodes shown in the graphs in Figure 2.36 contain 1, 2, 3 and 20 percent carbon by weight, the remainder being $LiMn_2O_4$ active material with 10% PVDF-HFP binder. Electrodes containing high amounts of carbon gave a current response with less scatter than in the case of the low carbon containing electrodes, *i.e.*, the results obtained for the high carbon loaded samples were more reproducible. This result was possibly due to more of the active material in high carbon containing samples reaching its expected capacity due to the higher conductivity of the composite. In the case of the low carbon containing electrodes, more of the active material is unable to undergo the insertion/de-insertion reaction. This low capacity may be due to the poorly developed percolation network that links the particles of active material in the electrode.

In the case of the 20% carbon loaded electrodes there is an excess amount of carbon in the electrode. This is greater than the amount of carbon required to provide the particles of active material with a supply of electrons. In the low carbon loaded samples, the amount of carbon may be sufficient to facilitate limited percolation of conductivity to a small number of particles. Hence, the kinetics of the electron transfer reactions are increased in the case of high carbon loaded samples due to the presence of a larger density of conducting pathways in the composites.

The formation of agglomerates within the electrode structure may also be responsible for the scatter seen in the cycling data. Scanning electron microscopy was used to identify these agglomerates. These may exist due to the incomplete mixing of inks after deposition and drying (see section 2.3.2.1).

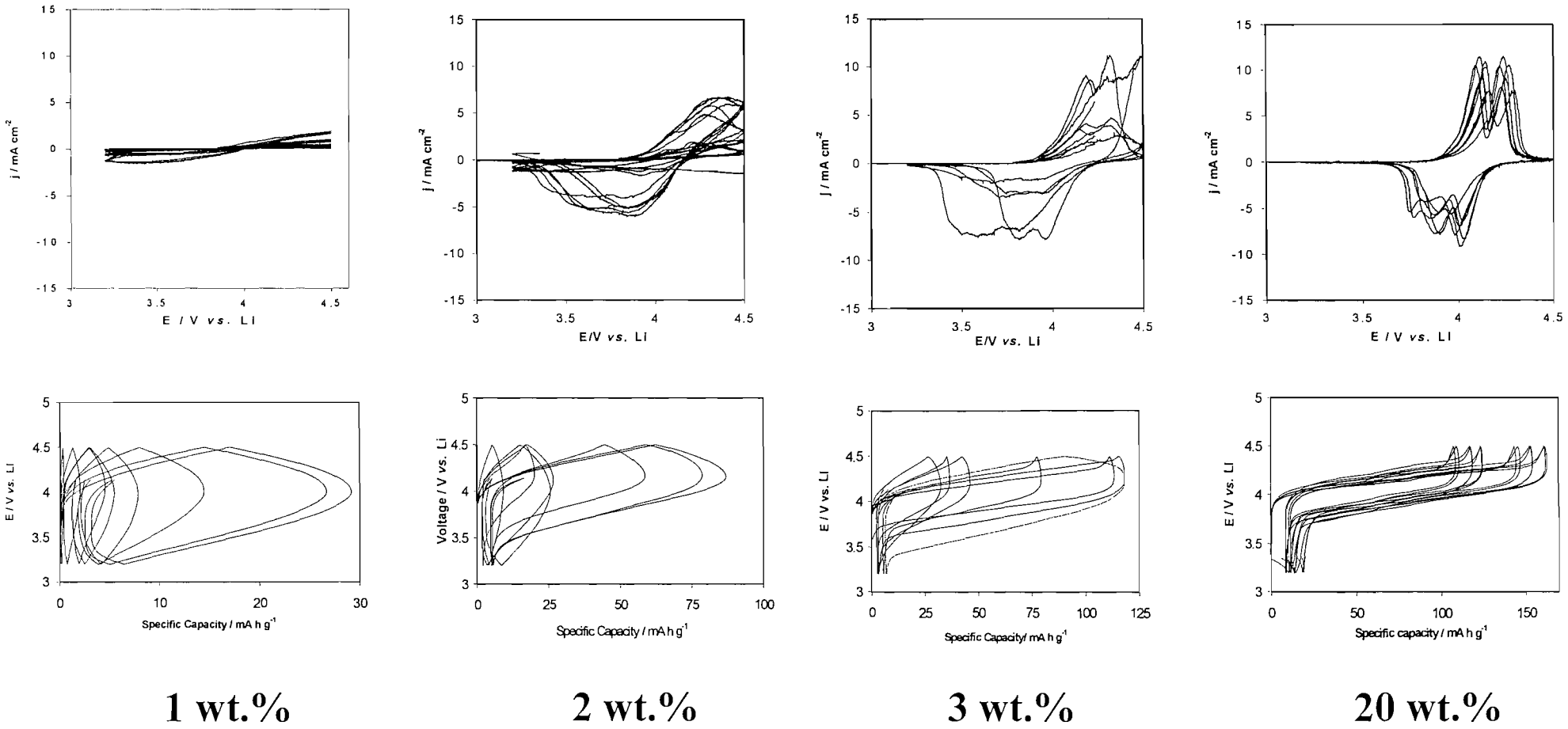

Figure 2.36 - Electrochemical cycling results for four of the eight compositions of $LiMn_2O_4$/AB/PVDF electrode in the combinatorial test cell. Slow scan cyclic voltammetry was used to study the electrode performance, $v = 0.1$ mV s^{-1}, $E = 3.2$ - 4.5 V *vs.* Li.

It was found that the results obtained for the electrodes containing 20 wt.% carbon using the combinatorial method were in good agreement with published values [4]. A value of between 110-160 mAh g^{-1} was obtained for $LiMn_2O_4$. The electrodes containing less than 3 wt.% of carbon showed specific capacities on or below the percolation threshold for lithium $LiMn_2O_4$ spinel, which lies between 5 and 10 wt.% CB.

The values of specific capacity for each of the cells in the 8x8 array were plotted against wt.% AB. This was done to determine the scatter in each measurement (see Figure 2.37). In can be noted that at low AB loadings the scatter in capacity values is at it's highest. As the amount of AB in the composite is increased over 2.5 wt. % the scatter is reduced. These results can possibly be explained by the random nature of the percolation effect. In samples containing a low level of carbon, the probability forming a continuous percolation network is much lower than at high carbon levels (~ 20 wt.%). Hence, there is a chance of forming a percolating network that adequately facilitates electron transfer to the majority of the particles, while at the same carbon level a different sample of material could exhibit a poorly developed percolation network. The type of material is formed depends on the position of the carbon in electrodes (relative to $LiMn_2O_4$) prepared using the high-throughput technique. It should be noted that the scatter observed in the early experiments was significantly reduced over time leading to a reproducible result for materials of a given composition.

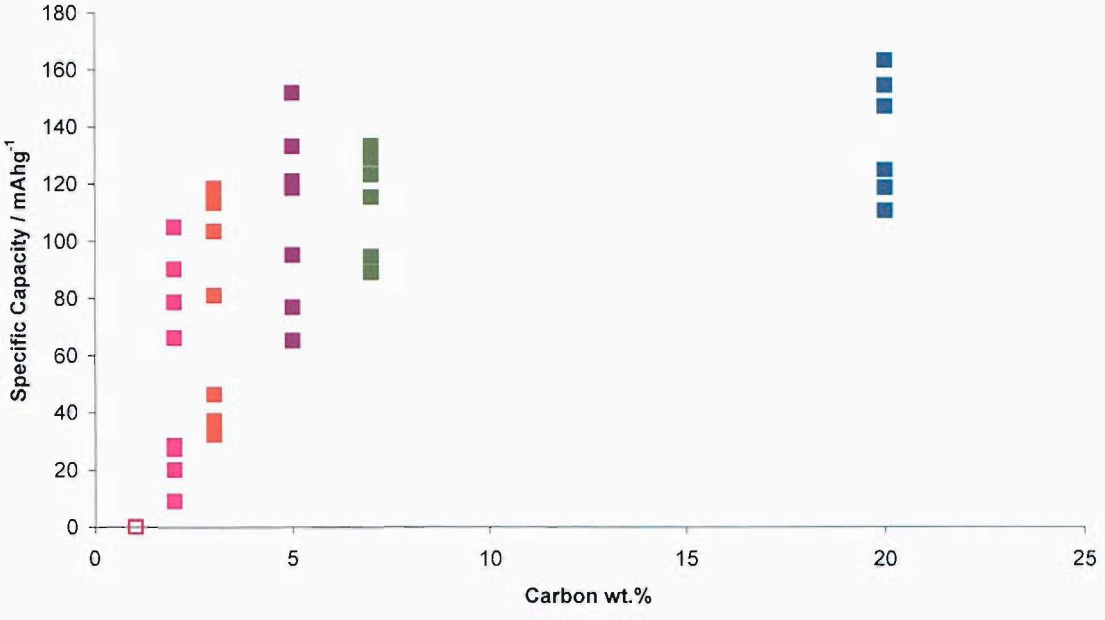

Figure 2.37 – Specific capacity *vs.* wt.% of acetylene black in the composite the composite electrode. Cycles tested using cyclic voltammetry, E = 3 - 4.5 V *vs.* Li, v = 0.01 mVs^{-1} (~ C/5).

The values for specific capacity obtained by both the combinatorial and conventional preparation techniques are compared in Figure 2.38 and 2.39. It was found that the average values for each of compositions prepared by the combinatorial technique show good agreement with data obtained from cells prepared by conventional techniques. However, it must be noted that the absolute values for the electrodes showed a large amount of scatter especially at low carbon loadings. It can be seen from the two plots that a carbon loading of approximately 3 wt.% is required to overcome the resistance limitation at 0.1 mVs^{-1} (or approximately the C/5 rate) in order to achieve the expected maximum capacity.

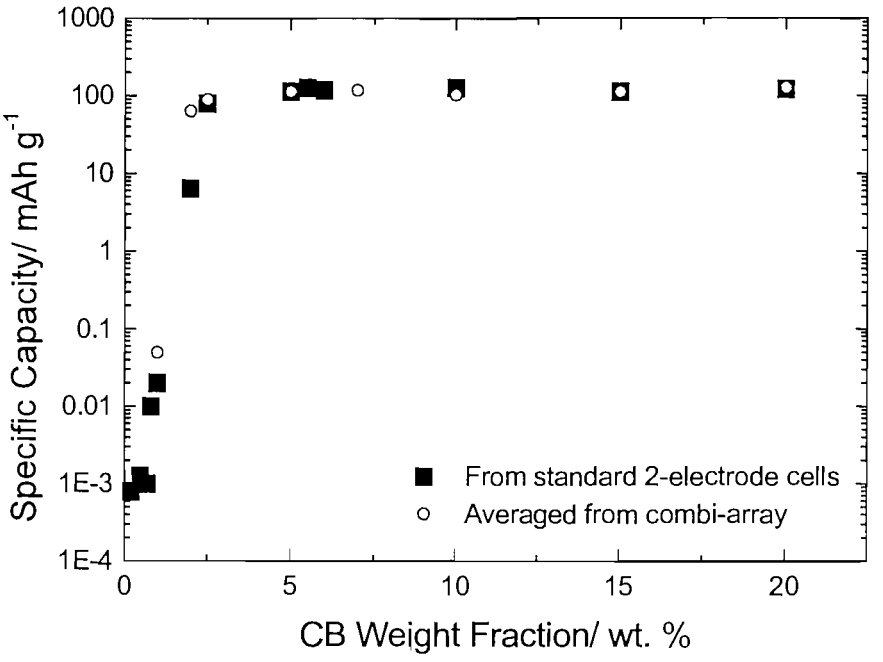

Figure 2.38 – Comparison of Specific capacity of cells prepared by conventional and combinatorial techniques.

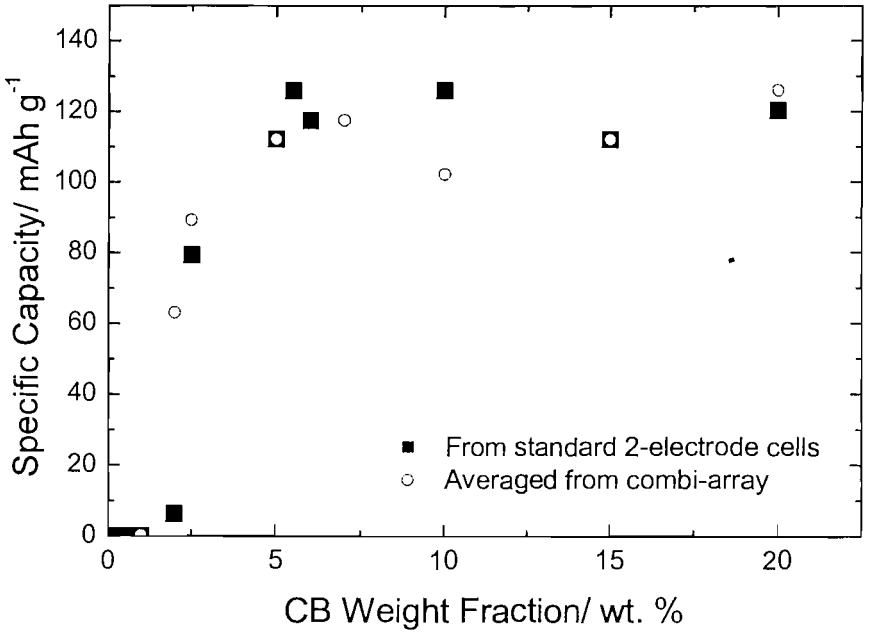

Figure 2.39 - Comparison of specific capacity of cells prepared by conventional and combinatorial techniques. *Y* data plotted on a linear scale.

An investigation into the influence of sample location on the array was undertaken. An array of samples composed of eight different compositions with eight repeat samples was prepared and the sample position were randomised using an excel spreadsheet. In previous experiments the nominally identical samples were deposited in columns with the composition changing from 0 to 20 wt.% of carbon along the rows. In the randomised experiment the samples were distributed throughout the array in no compositional order. This was undertaken to determine if the position of the sample had an influence on the electrochemical response. For example, samples closer to the edge of the array may not give such a high response as other repeat samples because the stack pressure may be lower. Samples closer to the centre may give a higher response as they may be exposed to greater stack pressure. Figure 2.40 shows the normalised (samples rearranged in order of composition) in arrangement (A) and the randomised arrangement of the electrode positions in arrangement (B) undertaken at a scan rate of 0.2 mV s^{-1}. The experiment was carried out for three scan rates, 0.2 (Figure 2.40), 0.1 (Figure 2.41) and 0.05 mV s^{-1} (Figure 2.42).

2.3.2.4 Randomisation of Sample Locations

Figures 2.40 to 2.42 show the randomised and re-organised (normalised) data sets for $LiMn_2O_4$/C/PVDF-HFP electrodes. It can be seen that the electrochemical response of the electrodes depends mainly on the composition of the samples. In Figure 2.40, electrodes showing a high electrochemical response can be seen on the edge and towards the centre of the array in an even distribution. The peak currents in the case of 15 wt.% carbon electrodes towards the edge and those in the centre of the array are approximately the same ~ 0.2 mA. It is clear there is no systematic disruption to the electrochemical response at electrodes close to the edge of the array. Likewise, the electrodes towards the centre of the array do not exhibit higher currents relative to their identical samples towards the edge of the array. However, it is clear from Figure 2.40 (B), that some electrodes showed a lower response than expected and in a few cases there was no response. This may be due to a lower amount of active material being present on the electrode (inaccuracies in materials preparation) or it may be the result of

poor electronic contact between the current collector and the active material. The complete loss of contact is probably due to a short circuit on one or more of the channels and may be due to puncturing of the separators, resulting in electronic contact between the positive and negative electrodes. However, the instances of short circuits and lower than expected performance appear to be random do not suggest that they occur as a result of sample location. It can be concluded that there is no relationship between sample location and anomalous electrochemical responses. Therefore, the randomisation of sample locations is not required to ensure that accurate results are obtained. However the variation in performance between nominally identical samples reveals a limitation of this type of method. Moreover, a reduction in the number of occurrences of short circuits and an improvement in the sample-to-sample reproducibility must be achieved in order for this method to be developed into a tool for materials screening. These problems could possibly be overcome by using a larger area current collector, ensuring that the deposited materials are well compacted and that there is sufficient stack pressure in the cell. It is also important to ensure that the electrode rods are in direct contact with the contact pins for each array element.

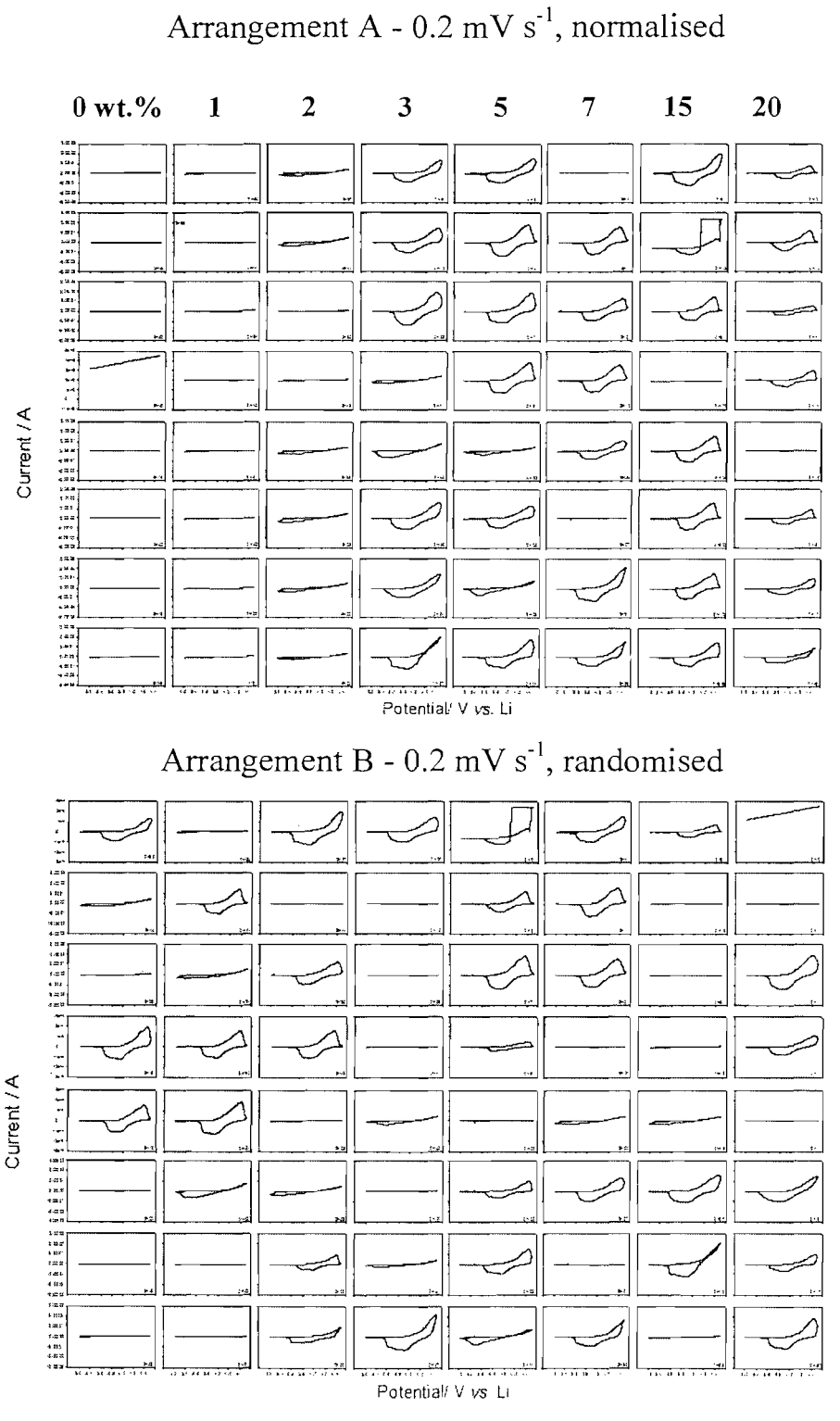

Figure 2.40 – Cyclic voltammetry obtained for an array of $LiMn_2O_4$/C/PVDF electrodes at a scan rate of 0.2 mV s^{-1}. The electrodes were cycled between 2 and 4.5 V. Electrode materials were deposited at random locations on the array to investigate the effect of sample position on electrochemical performance. The *y*-axis scale (current) in all plots is ± 0.3 mA. The *x*-axis displays values for potential between 2 and 5 V. Plot A shows the normalised data as the carbon content is increased from 0 to 20 wt.%. Plot B show the random arrangement of the samples, as they were present on the array.

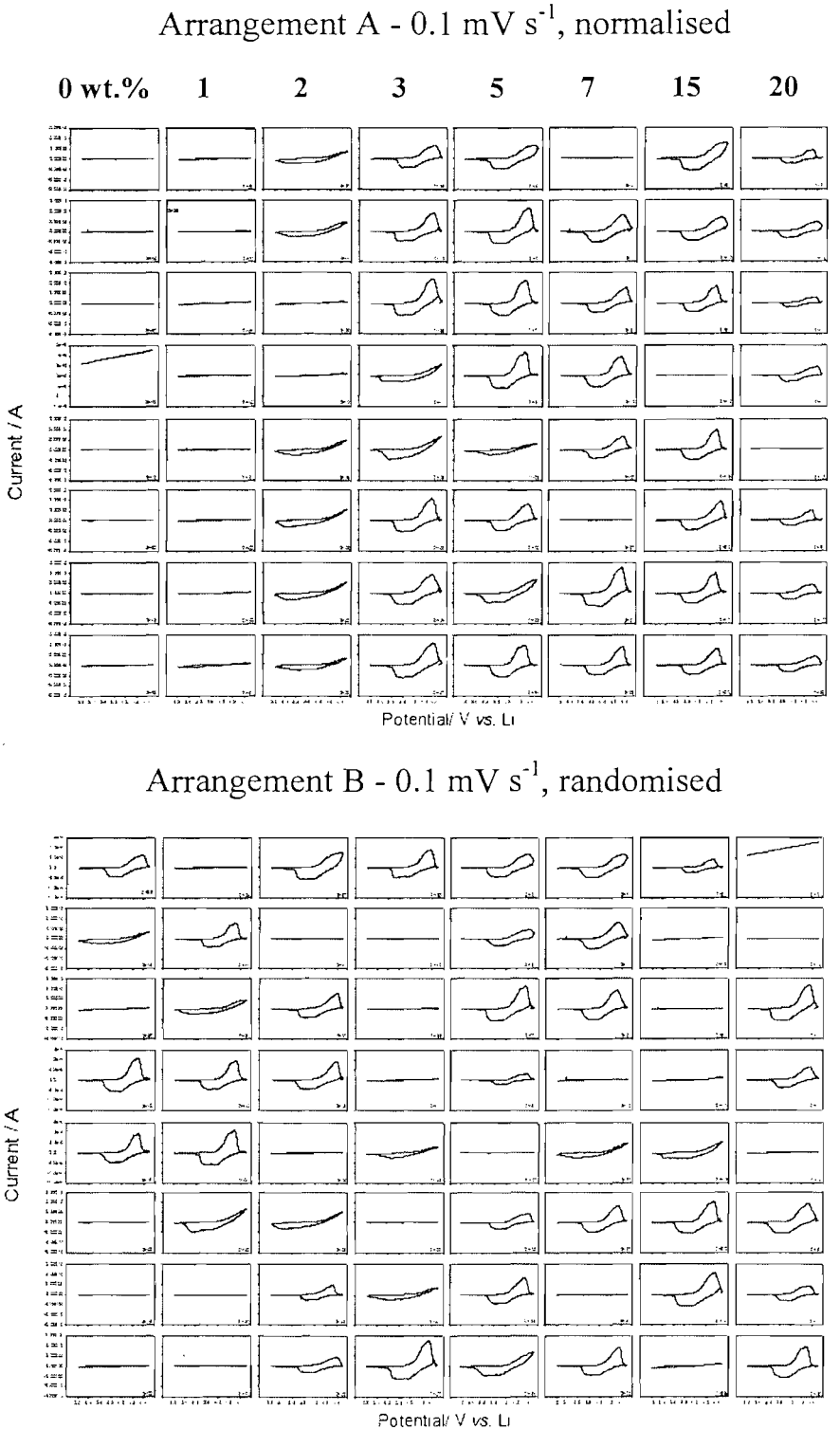

Figure 2.41 - Cyclic voltammetry obtained for an array of $LiMn_2O_4$/C/PVDF electrodes at a scan rate of 0.1 mV s^{-1}. The electrodes were cycled between 2 and 4.5 V. Electrode materials were deposited at random locations on the array to investigate the effect of sample position on electrochemical performance. The y-axis scale (current) in all plots is ± 0.15 mA. The *x*-axis displays values for potential between 2 and 5 V. Plot A shows the normalised data as the carbon content is increased from 0 to 20 wt.%. Plot B show the random arrangement of the samples, as they were present on the array.

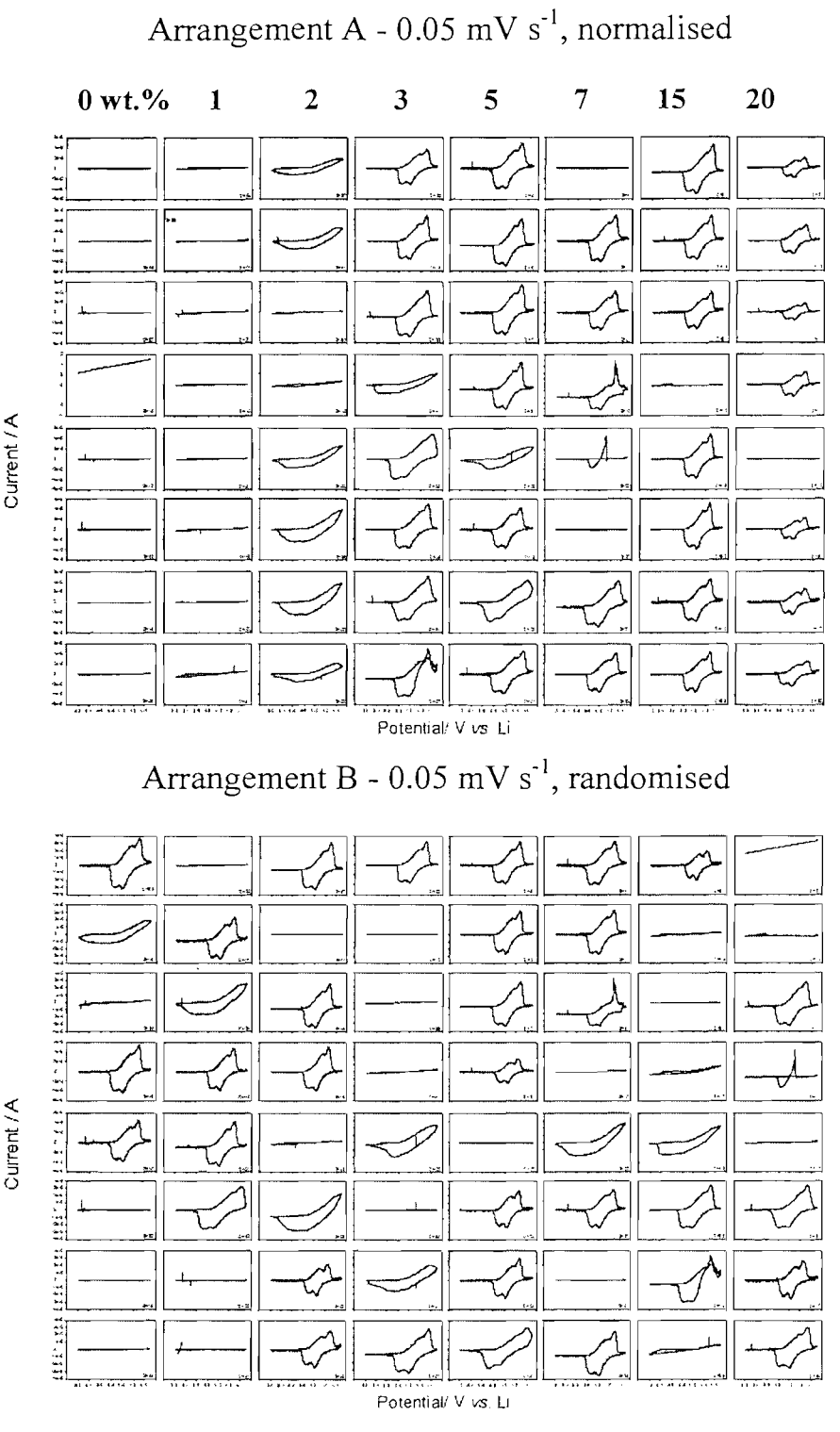

Figure 2.42 - Cyclic voltammetry obtained for an array of $LiMn_2O_4$/C/PVDF electrodes at a scan rate of 0.05 mV s^{-1}. The electrodes were cycled between 2 and 4.5 V. Electrode materials were deposited at random locations on the array to investigate the effect of sample position on electrochemical performance. The y-axis scale (current) in all plots is ± 60 μA. The *x*-axis displays values for potential between 2 and 5 V. Plot A shows the normalised data as the carbon content is increased from 0 to 20 wt.%. Plot B show the random arrangement of the samples, as they were present on the array.

2.3.2.5 Effect of Scan Rate on the Electrochemical Response

Figures 2.40-2.42 show cyclic volatmmetry data obtained at three different scan rates 0.2, 0.1 and 0.05 mV s^{-1}. A comparison of the peak current response of the electrodes in Figures 2.40 (A), 2.42 (A) and 2.42 (A) reveals that as the square root of the scan rate increases the peak current response for the majority of the electrodes increases. A plot of the average peak current for electrodes containing 15 wt.% of carbon *vs.* scan rate is shown in Figure 2.43.

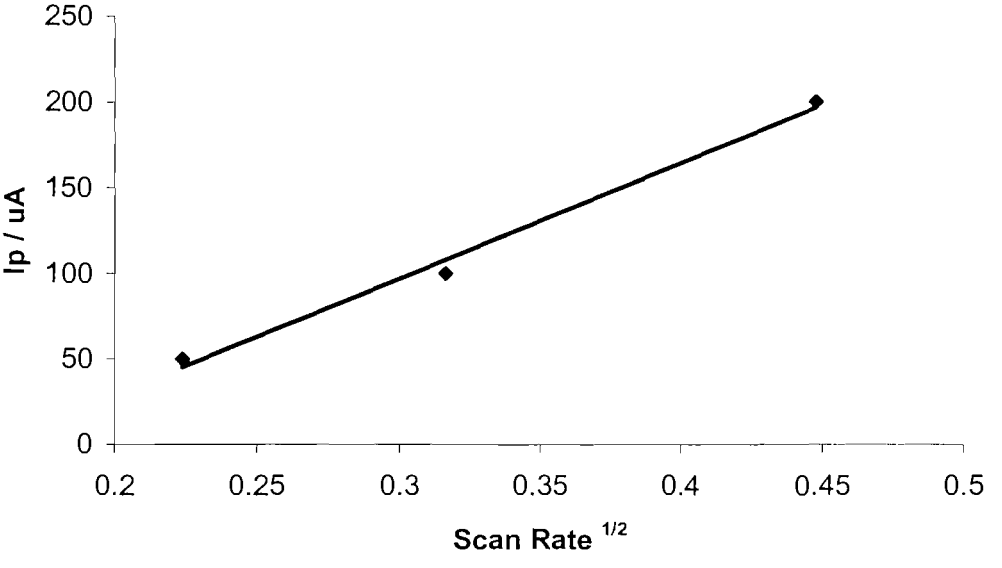

Figure 2.43 – The average peak current response for 15 wt.% carbon electrodes *vs.* the square root of the scan rate.

The values obtained at each of the scan rates clearly show an underlying trend. The electrodes containing very low carbon loadings (0 and 1 wt.%) no current response is observed. The high carbon containing samples show the largest currents at all the scan rates. It can also be seen that the total current for the 20 wt.% of carbon samples is lower than that for the 15 wt.% samples. This gives an indication that the percolation threshold has been exceeded, since the addition of an excess amount of the redox inactive carbon resulted in a decrease in the current. The samples containing 15 wt.% of carbon show the highest current response possibly because they have sufficient

conducting additive (above the percolation threshold) with an additional 5 wt.% of active mass.

A closer examination of each of the data sets reveals that at the lowest scan rate (0.05 mV s^{-1}) a significant current response is observed for electrodes containing 2 wt.% of carbon. As the scan rate is increased this response for the 2 wt.% samples diminishes. At low scan rates it is possible to resolve the two peaks in the cyclic voltammogram, which are expected for $LiMn_2O_4$. Hence, slowing down the experimental timescale allows more of the charge to be utilised within the active material. A slow rate of cycling also allows the slower kinetics of the low carbon containing electrodes to be overcome by a more prolonged cycling regime allowing the low carbon containing electrodes to register a current response.

At the outset of the experiment it was expected that at the slowest scan rate the low carbon containing samples (1-5 wt.%) would exhibit higher currents than when cycled at the highest rate (0.2 mV s^{-1}). This can be clearly seen when the response of these samples are compared in Figure 2.40 (A) and Figure 2.42 (A).

2.3.2.6 Reproducibility

An array of 63 electrodes of common composition (20 wt.% AB) was prepared to estimate the scatter associated with the combinatorial screening technique (see Figure 2.44). The high value of carbon (in excess of the percolation threshold) was chosen, as the probability of all cells reaching the required composite conductivity is greater at high carbon loadings. If this experiment were conducted at a value of 5 wt.%, one would expect to see more scatter in the data. This scatter would be due in part to the measurement technique, but also due to the effects of the probability of an electrode reaching the required conductivity for it to gain the full capacity expected from the electrode. It was important to separate these two effects; therefore a large excess of carbon was used to determine the sample-to-sample reproducibility of the method. It was found that approximately 90 % of cells performed as expected giving a specific value for capacity of around 100 mA h g^{-1} ± 15. Out of 63 cells only four showed a value close to zero. This result is most likely due to a short circuit due to film displacement or puncturing of the separator. It was found that the average capacity was 99.5 mA h g^{-1}, which rose to 107 mA h g^{-1} when the outlying points were excluded. The standard deviation from the average value was calculated to be 9.6 mA h g^{-1} when the outlying points were excluded. This demonstrates that the combinatorial method is valid for use in the screening lithium battery materials, as reproducible results have been obtained with acceptable experimental error.

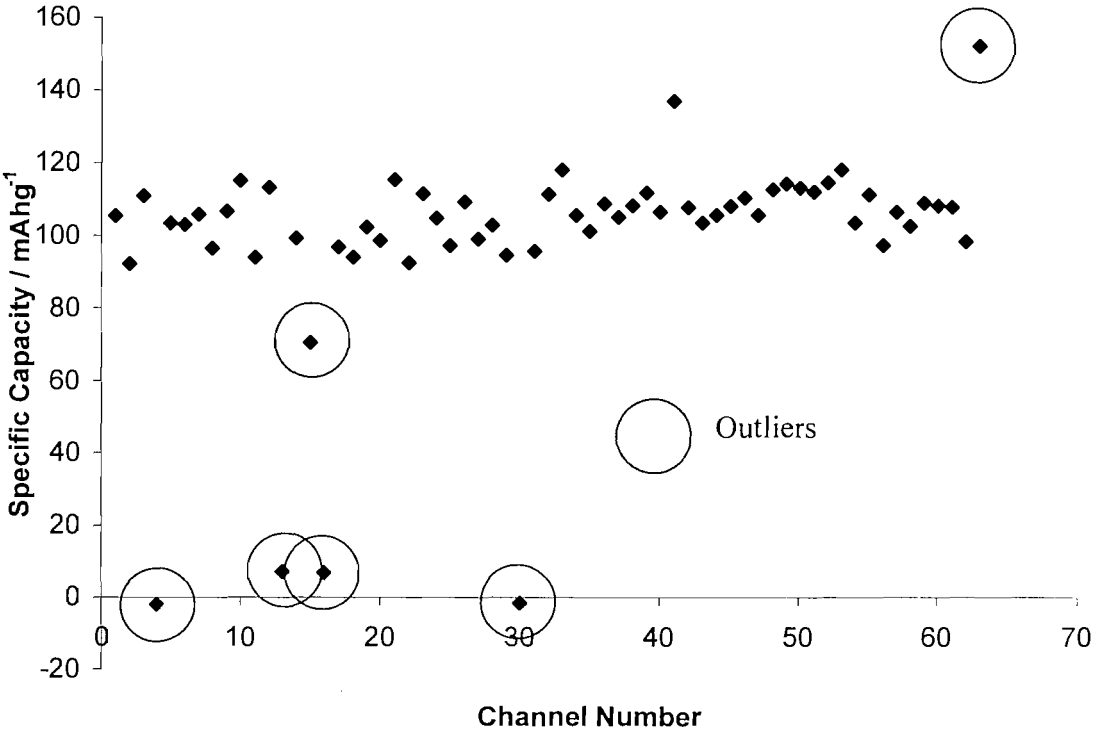

Figure 2.44 – Reproducibility of experiments using the combinatorial technique.

Average Capacity = 99.5 mA h g^{-1}
Average capacity (excluding outliers) = 106.7 mA h g^{-1}
Standard Deviation = 27.52 mA h g^{-1}
Standard Deviation (excluding outliers) = 9.86 mA h g^{-1}

2.3.2.7 Conductivity Measurements of High-throughput Samples

Conductivity measurements on samples of composites prepared from the inks suspensions were undertaken using the four-point probe technique. 6 μL aliquots of composite ink of varying carbon content were deposited on to glass microscope slides and left to dry in an oven for 30 minutes at 70 °C until all cyclopentanone had evaporated leaving a dry film. Specific values for conductivity were plotted as a function of acetylene black loading as was undertaken for the films made by conventional techniques (see Figure 2.45). Both the ink suspension and conventional prepared sample data sets were obtained using the four-point probe method.

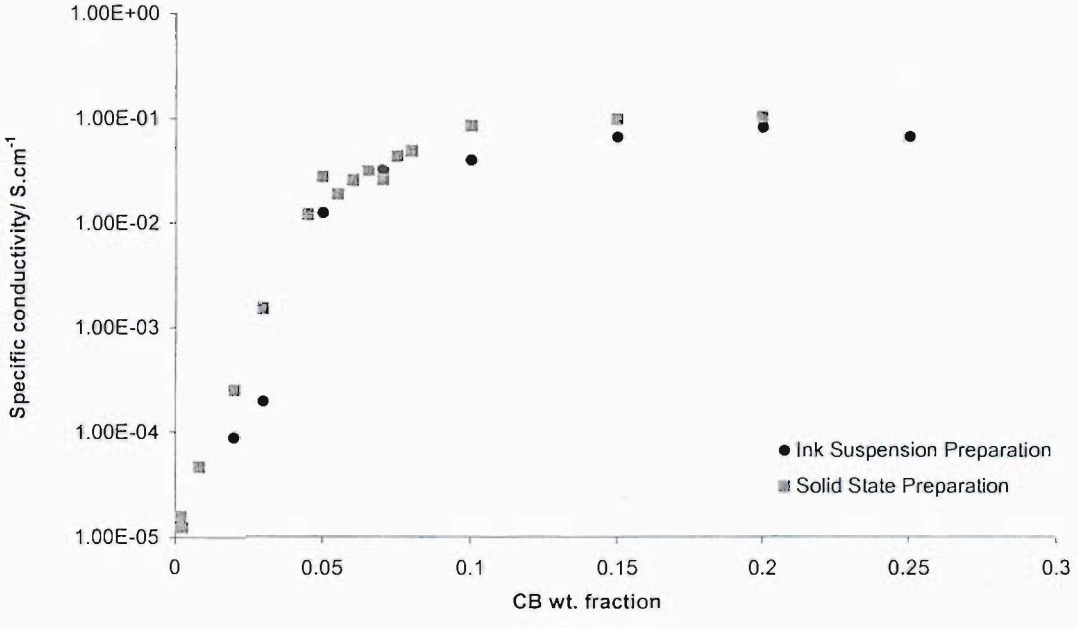

Figure 2.45 – Comparison in conductivity of samples prepared by ink deposition and conventional solid material preparation.

The conductivity of the samples prepared using conventional and ink deposition techniques show very good agreement. At high levels of carbon the maximum film conductivity observed was approximately 0.1 S cm^{-1}. The percolation threshold in conductivity was observed at around 7.5 wt. % AB for both techniques. This suggests that compaction of the electrode materials has a negligible effect on the percolation behaviour in that compressed and uncompressed electrodes reach the percolation limit at the same carbon loading and achieve almost identical value of maximum conductivity. It can be noted that the electrodes which were compressed achieved the percolation limit at around 0.5 % wt carbon less than the electrodes prepared by ink suspension, but this was within experimental errors in weight and potential measurement.

2.4 Conclusion

Results obtained from $LiMn_2O_4$ electrodes prepared using the conventional technique have led to a good understanding of the relationship between the active material and the role of the conducting additive to overall cell performance. It has been demonstrated that percolation thresholds for $LiMn_2O_4$/AB/PVDF exist and samples with carbon fractions below this threshold show lower capacity than those of cells containing a carbon level in excess of the percolation threshold. Conductivity measurements have shown behaviour, which closely follows that observed for capacity except for a shift in the percolation threshold. It has been shown that the threshold for percolation in conductivity occurs at around 10 wt. % of carbon additive and the limit in the conductivity data is around 7.5 wt. % of carbon. It is clear that both the thresholds for specific capacity and specific conductivity are manifestations of the same percolation phenomenon. The effect of the rate of cycling on the cell capacity has been demonstrated, resulting in a decreased value of specific capacity for cells cycled at a high rate. This was attributed to the effect of concentration overpotential observed in electrode materials that were cycled at a high rate. The capacity is lower than expected due to a reduction in the rate at which the active species can be removed from the electrode and occurs because the active species becomes depleted at the interface.

It has been demonstrated that the results obtained using the high-throughput method outlined in this chapter are in good agreement with those obtained using conventional methods. Cycling results showed that electronic percolation, which was effective at the C/5 rate, began at carbon black loadings from 2 to 3 wt.% in some cells. However, higher carbon loadings were required to obtain full utilisation of capacity in all of the cells. The duplication of samples gives a very useful indicator of the spread of capacity values due to non-uniform dispersion of active material; this duplication of samples can be easily achieved with the combinatorial method. In addition to producing arrays containing 63 electrodes of different composition, this technique can be used to rapidly repeat results obtained for one type of electrode composition, thus allowing ease of determination of the scatter associated with the experimental method.

The SEM investigation of the high-throughput and conventionally prepared samples give an explanation of the electrode behavior during cycling, in that the existence of agglomerates of both conducting additive and active material may give rise to scatter in cycling performance. Further grinding of the powders used in the preparation of ink solutions, or compacting the electrode films to increase the inter-particle contacts could reduce this effect.

2.4.1 Further Work

Additional work in this area could include a study of the $LiMn_2O_4$/C/PVDF electrodes using impedance spectroscopy, as this may reveal more about the percolation of electronic conductivity and its frequency dependence. In addition the adaptation of the method to obtain a reliable direct conductivity measurement has been attempted and should be developed further. The increase of the diameter of the electrodes could lead to more accurate electrochemical measurements, as the larger quantity of material would reduce the systematic error associated with the handling of the ink suspensions. The degree to which changing the volume of material in each well affects the sample-to-sample reproducibility would depend on accuracy of the robot. The Multiprobe II is accurate to approximately ±2% (when dispensing 5 μL), this accuracy increases with the volume dispensed.

It would also be advantageous to study percolation effects in other lithium battery materials using this method as the development of the combinatorial method allows unknown systems to be rapidly characterised.

2.5 References

1. Spong, A.D., Vitins, G., and Owen, J.R. *Combinatorial Arrays and Parallel Screening for Positive Electrode Discovery*. in *IMLB 11*. 2002. Monteray, CA, Abstract No: 267.
2. Spong, A.D., Vitins, G., Guerin, S., Hayden, B.E., Russell, A.E., and Owen, J.R., *Journal of Power Sources*, 2003, **119**, p. 778-783.
3. Hanak, J.J., *Journal of Materials Science*, 1970, **5**, p. 964-971.
4. Mandal, S., Amarilla, J.M., Ibanez, J., and Rojo, J.M., *Journal of the Electrochemical Society*, 2001, **148**, (1), p. A24-A29.
5. *Durston Rolling Mills, Progress House, Hospital Hill, Waterside, Chesham, Bucks, HP5 1PJ, UK.*
6. Flandin, L., Prasse, T., Schueler, R., Schulte, K., Bauhofer, W., and Cavaille, J.Y., *Physical Review B*, 1999, **59**, (22), p. 14349-14355.
7. Le Gall, T., Reiman, K.H., Grossel, M.C., and Owen, J.R., *Journal of Power Sources*, 2003, **119**, p. 316-320.
8. Guerin, S., Hayden, B.E., Lee, C.E., Mormiche, C., Owen, J.R., Russell, A.E., Theobald, B., and Thompsett, D., *Journal of Combinatorial Chemistry*, 2004, **6**, (1), p. 149-158.
9. Hjelm, A.K. and Lindbergh, G., *Electrochimica Acta*, 2002, **47**, (11), p. 1747-1759.
10. Brown, M.A.C.S. and Jakeman, E., *British Journal of Applied Physics*, 1966, **17**, p. 1143-1148.

Chapter 3:
Solution Preparation of $LiFePO_4$ Materials: A Prerequisite for Combinatorial Synthesis

Chapter three focuses on the development of a new solution synthesis route to prepare lithium iron phosphate ($LiFePO_4$). This material is of great interest as a potential commercial material, as it has advantages of cost, non-toxicity and high theoretical capacity, which surpass current commercial materials [1]. However, this material is of low density and suffers from low intrinsic conductivity. These properties need to be improved before it can be considered as a viable commercial material. The development of a versatile solution synthesis route that can easily be adapted to allow the addition of dopants or additives would be an advantage, as it would lend itself to eventual automation. It has been suggested that the addition of dopants or additives may improve the conductivity [2]. In order to fully understand and optimise a system of many components, a combinatorial method of synthesis and screening has been developed.

3.1 Background and Objectives

The work in the following chapter is necessary step on the path to combinatorial discovery of new and potentially useful battery materials. At the outset of the work, no simple solution preparation routes had been reported for the preparation of the olivine phase of lithium iron phosphate ($LiFePO_4$). The potential of new useful materials based on doped or substituted $LiFePO_4$ has already been reported by Chiang *et al.*, in which it was demonstrated that a small change (< 1 atomic %) in material composition could result in a large change in properties (conductivity increase as high as 10^8 times) [2].

The combinatorial screening process outlined in chapter two, requires all precursors used in electrode preparations to be in the solution phase. It is sensible to suggest that minimising the number of processing steps would reduce the scatter associated with the electrochemical responses. Hence, a simple one-step deposition approach would be the most preferable synthesis type. It was also beneficial to devise a synthesis that could be carried out at low temperature, since this may offer increased choice of current collector and array design in the combinatorial synthesis phase.

The objectives of this chapter are described below:

- The development of a solution based synthesis of $LiFePO_4$ using sol-gel or soft chemistry techniques, using inexpensive and readily available precursors.

- The above synthesis should be undertaken at low temperature (< 700 °C) and should be a one-step process leading to well crystallised single-phase material.

- This route should be compatible with the automated electrode preparation technique described in chapter two, to allow substitution of other components, and hence, the preparation of arrays with compositional variation.

3.2 Experimental

$LiFePO_4$ powders were prepared using solid-state synthesis techniques and sol-gel methods. The materials were characterised using X-ray diffraction, SEM, EDX and electrochemical testing.

3.2.1 Solid-State Synthesis of $LiFePO_4$

Several possible reagents and synthesis routes were attempted before a viable synthesis route was developed. In early experiments, new synthesis routes were evaluated by solid-state reaction before solution synthesis was attempted. The constraints of the synthesis set out in section 3.1 limited the choice of precursors to those that dissolve in aqueous solution; therefore, nitrates and acetates were chosen as they fulfil the above criteria and they are readily available and inexpensive.

Initially, a test to determine the feasibility of synthesis was undertaken. In these experiments $LiFePO_4$ was prepared solid-state reaction from stoichiometeric quantities of lithium acetate ($LiCH_3COO.2H_2O$, *Fisher*), iron (III) nitrate ($Li(NO_3)_3$, *Avocado*), phosphoric acid (H_3PO_4, *Aldrich*) and sucrose ($C_{12}H_{22}O_{11}$) in the molar ratio 1:1:1:0.22 respectfully. The precursor powders were mixed together using a pestle and mortar. Because the iron (III) nitrate contains nine crystallisation water molecules, all powders were easily dissolved forming a highly concentrated homogeneous viscous gel. The viscous solution was heated to 70 °C for 2 hours to remove the water content. During this initial low temperature heating, the NO_3^- from the iron nitrate was observed to decompose to NO_2 (brown gas), and a yellow material formed. This product was reground for 2 minutes in a pestle and mortar and transferred to a tube furnace where it was heated to 700 °C for 10 h at a heating rate of 10 °C min^{-1} in an argon atmosphere. After 10 hours, the powder was removed from the furnace.

3.2.1.1 The Role of Sucrose

The use of sucrose in battery material synthesis is not new. It has been reported that sucrose can be used to coat the particles of $LiFePO_4$ with carbon after synthesis to increase electronic conductivity between the particles [3]. However, the solution precursor method the sucrose was primarily used as a reducing agent for conversion of Fe (III) to Fe (II). Moreover, it was subsequently found to act as a gelling agent, which is of critical importance to the solution synthesis described below. Sucrose allows the $LiFePO_4$ precursors to dry into a homogeneous glassy matrix and thus maintains the stoichiometry of the precursor material by inhibiting the segregation of different crystals of precursors during drying. In addition, it facilitates the reduction of Fe^{III} to Fe^{II}; and finally, it provides supporting carbon coating on the $LiFePO_4$ particles, enhancing the electronic conductivity of the particles.

3.2.2 Solution Synthesis of $LiFePO_4$

Lithium iron phosphate ($LiFePO_4$) was prepared from solution phase precursors using low temperature solution synthesis techniques. The olivine phase ($LiFePO_4$) was obtained using a 1:1:1 ratio of lithium acetate ($LiCH_3CO_2.2H_2O$, *Fisher*), Iron (III) nitrate ($Fe(NO_3)_3.9H_2O$, *Avocado*) and phosphoric acid (H_3PO_4, *Aldrich*). In addition, a 0.22 molar ratio of sucrose was added. Aqueous solutions of the reactants were prepared as follows, $LiCH_3CO_2$ (0.5M), $Fe(NO_3)_3$ (0.25M) and sucrose (0.5M). The concentration of phosphoric acid was 85% by weight in water. Precursor solutions containing the correct stoichiometric quantity of the reagents were prepared. The volume of each precursor solution was measured using a 100 mL measuring cylinder and placed in a 500 mL beaker. The solution was stirred and transferred to a water heated jacket cell connected to a water bath, where a constant temperature of 70 °C was applied until the water had evaporated.

Samples containing lithium acetate, iron nitrate and phosphoric acid, without sucrose were also prepared as precursor solutions and were heated to form solid precursor powders using the above method. The amount of sucrose used in the synthesis was varied between 0.1 and 1 in molar ratio with that of the other precursors.

The precursor material was placed in a quartz crucible and then transferred to a tube furnace (*Carbolite*) where it was heated for periods between 5-20 h, under argon (100 cm^3min^{-1}) at temperatures between 400 and 700 °C at a heating rate of 10 °C min^{-1}. The synthesis was also carried out in a 10% H_2 in argon atmosphere, as the H_2 was expected to provide additional reducing power to prevent the formation of iron (III) impurities. In addition to the above synthesis, the heating time, precursor ratio and carbon source were also varied.

3.2.2.1 Two Step Preparation for Enhanced Electrochemical Performance.

In addition to the one-step method developed primarily for combinatorial synthesis, work was undertaken to enhance the electrochemical performance of the materials by providing an additional conducting component. This was added to the already sintered product in the form of sucrose. It was determined in early experiments that the material prepared using the one-step method was not providing the expected electrochemical performance, as its maximum specific capacity was too low (~ 100 mA hg^{-1}) to be competitive with other synthesis methods, which typically achieve over 90% of the theoretical value (~160 $mAhg^{-1}$). The addition of sucrose should lead to an additional coating of the particles with sucrose and thus, increase the electronic conductivity between the particles. It is also possible that the second heat treatment with sucrose may improve the phase purity of the material, as it would be heated for an additional period. It is possible that some amorphous impurities (which are not observed by XRD) may exist after the first calcination and may be converted to the correct crystal phase. Regrinding after the first calcination may result in improving the homogeneity of the material thus aiding crystallisation.

In these experiments an additional amount of sucrose was added to the product of the first firing of $LiFePO_4/C$ prepared at 700 °C in Ar. For this purpose, the powder was soaked with 0.1 M sucrose solution to give 4.7 wt.% sucrose (2 wt.% carbon) of the $LiFePO_4/C$ weight. However, sucrose is partly lost with water by evaporation, and thus, the carbon residues were less than expected, as determined by TGA. The soaked

material was placed in alumina boat and heated to 700 °C with a rate of 20 °C min^{-1} in flowing Ar (300 mL min^{-1}) with a dwell period 3 h at 700 °C.

3.2.2.2 Preparation of Substituted $LiMPO_4$ by Solution Synthesis

The use of the solution method was tested in the preparation of other materials of the same crystal structure as $LiFePO_4$. It was hoped that the one-step solution synthesis route could be applied to materials containing Co, Ni, Mn, Cu and other transition metals leading to a generic method for the synthesis of phospho-olivines. This is particularly important in combinatorial synthesis, as solid solutions containing Fe, Ni, Co etc will be prepared on a combinatorial array. It is, therefore, important to know the structure and performance of the end members by synthesising them using more conventional methods.

The materials were prepared in a similar way to the one step synthesis of $LiFePO_4$. This procedure utilised solution precursors of lithium acetate, phosphorus acid, sucrose and metal nitrates as the source of the transition metal from 1.25 M solutions of Co, Ni, Mn and Cu acetate. A solution precursor was prepared using the same method as for $LIFePO_4$ by mixing all the aqueous components in a water heated jacket cell. This was kept at a constant temperature of 70 °C until the sample was sufficiently dry to remove to a crucible for heat treatment. The solid precursor material was heated at 700 for 10 h in Argon. It was not necessary to use an inert atmosphere of the synthesis of materials containing transition metals as a 2+ nitrate, as they are not oxidised to a 3+ state in oxygen. However, these materials must be formed in an inert atmosphere, as solid solutions will be prepared with an iron component, which is sensitive to oxidising conditions. These materials were characterised using XRD and electrochemical testing.

3.2.3 X-ray Powder Diffraction

X-ray diffraction was used to characterise solid materials prepared by the precipitation of aqueous solutions and solid-state reactions. A *Bruker D8* diffractometer equipped with a *Sol-x* detector was used in most measurements. However, some materials in

which fluorescence effects were not present were carried out on a *Siemens D5000* instrument. In these cases, the diffractometers utilise monochromatic X-rays (fixed wavelength) obtained from Cu K_α radiation, which impinge on the sample; diffracted X-rays are detected as a function of 2θ. X-ray patterns were collected for the 2θ between 15 and 50° at a scanning rate of 1.3° min^{-1}. These data were used for phase identification and were compared to a known pattern for the olivine phase of lithium iron phosphate. In addition to the synthesis products, precursor materials of varying composition were also examined by XRD.

There are four major components of an X-ray diffractometer, the power generator and power supply, the diffractometer itself, the data logging system and the water chiller. The arrangements of the components of the diffractometer are shown in Figure 3.1. Power is supplied to the X-ray tube by the generator and monochromatic X-rays are produced from a copper K_α source. The X-ray source and detector are housed within the goniometer, which is a mechanism, which allows for precise movement of the detector relative to the sample and X-ray source. The incident beam form the x-ray source impinges of the sample, where the planes of atoms in the sample diffract it. The Number of X-ray counts reaching the detector is logged as a function of the scanning angle 2θ. The intensity and angle of the observed reflections can then be used to identify the type of crystal structure present in the sample.

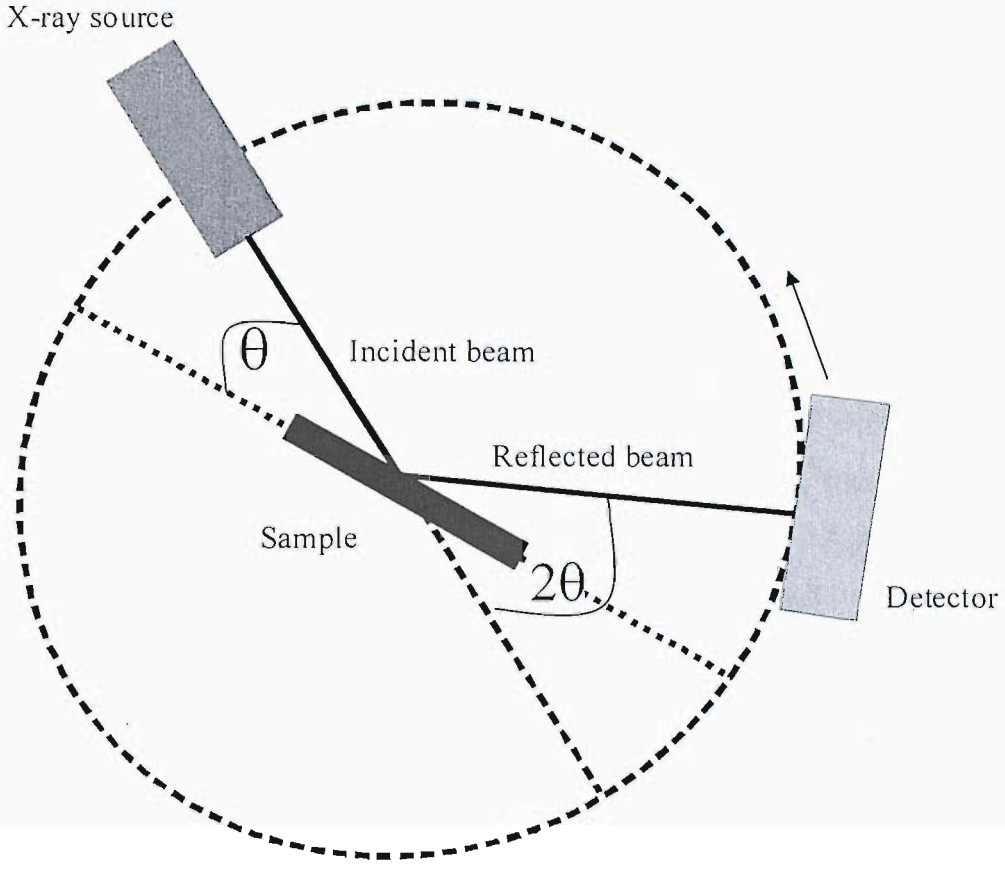

Figure 3.1 - Schematic representation of powder X-ray diffraction equipment [4].

3.2.4 Scanning Electron Microscopy and EDX Mapping

Samples of the powders containing the precursors of $LiFePO_4$ were studied using a scanning electron microscope (*Philips XL30-ESEM*) to investigate the relationship between their synthesis conditions, elemental composition and microstuctural features. Non-conductive precursor samples were observed in ESEM (wet-mode) and were observed using gaseous backscattering or secondary electron detectors. In addition to an investigation of the topography and surface features of the samples, an EDX mapping study was undertaken for the solid precursor powders with and without sucrose content. The aim of this study was to determine if the sucrose containing precursors were more homogeneous than those without sucrose. EDX maps were taken for iron, phosphorus and oxygen content and were then overlaid to form one EDX map. An accelerating voltage of 15.2 kV and a spot size of 5.7 μm were used. Electron micrographs were taken at an accelerating voltage between 10 and 15 kV using the secondary electron and backscattered electron detectors. These images gave a detailed indication of particle size as well as surface topography. EDX spot analysis was also undertaken, in which spectra were obtained for several 5 μm diameter spots.

3.2.5 Optical Microscopy

The optimum quantity of sucrose added to the precursor solutions was determined using an optical microscope (*Olympus BH-2*) equipped with a heating stage (*Ventacon, Winchester*). Samples were prepared differing only in the amount of sucrose added to the precursors. A 6 μL sample of each solution was transferred to a glass slide using a micropipette. The samples were heated to 70°C on the heating stage until a solid film formed. The films were examined for crystal formation during the drying process by observing their optical activity in polarised light. This allowed observation of the amount of crystallisation that occurred during solidification. Digital photographs were taken for each sample to determine how the sucrose content affected the amount of crystallisation observed. After examination, the samples were stored in a desicator.

3.2.6 *Electrochemical Testing*

The electrode materials were prepared as composites of three components, active material ($LiFePO_4$), conducting additive (acetylene black, *Shawinigan Black*, *Chevron*) and PTFE (Type: 6C-N, *Dupont*). The films were composed of 75 wt.% of active material, 15 wt.% of acetylene black and 10 wt.% PTFE. Films of approximately 0.1 mm in thickness were prepared by mixing the three constituents with a pestle and mortar. The materials were pressed into a lump and rolled into a film using a rolling mill *(Minimill, Durston)*. Pellets of diameter 1.1 cm were punched from each film using a cork borer. The mass and thickness of the pellets were measured and the pellets were dried for 12 hours under vacuum at 120 °C. The mass of the pellets was found to be in the range 13-17 mg, with a thickness of approximately 0.1 mm.

Electrochemical cells were assembled in an argon filled glove box (H_2O < 1 ppm, O_2 < 0.1 ppm, *MBraun*) using the pellets as positive electrodes in stainless steel cells. Metallic lithium was used as the negative (counter and reference) electrode and 1M $LiPF_6$ in EC/DMC: 1/1 by weight, *LP30, Merck*) as the electrolyte soaked into two glass separators (F type, *Whatman*, *Aldrich*). The cells were cycled galvanostatically using a multi-channel potentiostat (VMP, *Princeton Applied Research, Bio-logic Science Instruments*) at C/7 (with respect to the theoretical capacity) as a standard rate between 2 and 4.5 V *vs.* Li. In order to control and confirm good percolation of the conducting additive, the electronic conductivity of the electrode films was measured using the four-point probe method (see section 2.2.3)

3.2.7 *Analysis for Iron Content by TGA*

In the synthesis route described above, a quantity of carbon was added to the precursor materials as sucrose. It was expected that a small amount of carbon remained in the sintered material. This was useful, as it provided a conducting coating over the particles, and thus, aided in improving conductivity. In order to determine the amount of impurities (including carbon) remaining in a sample after heat treatment, a quantitative analysis of the material was conducted using thermogravametric analysis (TGA) in air.

Similarly Yang *et al.* have analysed $LiFePO_4$/C by TGA in oxygen at 500 °C [5]. In the present study samples (0.2 - 0.3 g) of $LiFePO_4$/C were fired for 10 to 15 minutes in air at 500-800 °C. The reaction was undertaken in an open crucible that was weighed before and after heat treatment. A propane gas flame was used as the heat source. The oxidation was judged to be complete when the sample powder looked uniformly red-orange after cooling. $LiFePO_{4.5}$ represents the fully oxidised material after heat treatment in air. It was expected that this material would form as it contains iron in its +3 state. The reaction resulted in the formation of a carbon-free oxidised material, effectively $LiFePO_{4.5}$ (see Equation 3.1).

$$2LiFePO_4 + C + 1\frac{1}{2}O_2 \rightarrow 2LiFePO_{4.5} + CO_2 \qquad \textbf{Equation 3.1}$$

From the weight difference between the initial $LiFePO_4$ and the oxidised material ($LiFePO_{4.5}$), the amount of carbon in the sample was calculated. A standard calculation is shown in Equation 3.2.

The mass of pure $LiFePO_4$ in the sample can be assumed to be:

$$m_{LiFePO4} = \frac{m_{LiFePO4.5}}{M_{LiFePO4.5}} \times M_{LiFePO4} \qquad \textbf{Equation 3.2}$$

Where,

$M_{LiFePO4}$ = 157.9 g mol^{-1}

$M_{LiFePO4.5}$ =165.9 g mol^{-1}

The weight fraction of $LiFePO_4$ in the sample is,

$$w_{LiFePO4} = \frac{m_{LiFePO4}}{m_{sample}} \qquad \textbf{Equation 3.3}$$

And the weight fraction of carbon remaining is the sample is assumed to be,

$$w_{carbon} = 1 - w_{LiFePO4} \qquad \textbf{Equation 3.4}$$

This method assumes that during the heating in air the total mass of material is converted to its oxidised form ($LiFePO_{4.5}$) and all the carbon in the sample is converted to CO_2. Also, it assumes that the amount of impurities in the sample consist of carbon, as any other impurities will be included in the mass of the active material after heating. The determination of remaining carbon in the sample allows more accurate calculations of specific capacity to be made. The validity of this method was confirmed by comparison with data from atomic absorption spectroscopy; both methods are in agreement. However, it is assumed that the material is 100 % pure phase $LiFePO_4$. If impurities exist in the sample, this will result in a reduction in the accuracy of the method.

3.2.8 Analysis of Iron Content in $LiFePO_4$ Samples by AAS

In addition to using TGA to calculate sample purity, some samples were tested by atomic absorption spectroscopy (AAS) to detect iron species in the sample. This was done to validate the assumption of Fe^{II} to Fe^{III} formation using the TGA method. $LiFePO_4$ synthesis products were characterised using atomic absorption spectrometry to determine purity of the sample, by estimating of the quantity of $LiFePO_4$ present. However, this method detects the amount all iron species in the sample. Therefore, some iron (III) impurities will be included in this measurement, which could lead to inaccuracies in the calculation of sample purity. Determination of the amount of $LiFePO_4$ is necessary, as it allows a more accurate value for the specific capacity of the material to be deduced. However, the amounts of crystalline iron (III) impurities are low, because the XRD experiments for most of the $LiFePO_4$ samples revealed a single-phase (olivine type) pattern. Hence, only amorphous impurities cannot be detected in the samples, for example residual carbon.

Atomic absorption spectroscopy experiments were undertaken using a *Perkin Elmer 2380 Flame Atomic Absorption Spectrometer*, using a Fe hollow cathode lamp

(I = 5μA). The samples were placed in an air acetylene flame and the intensity for each sample was displayed on the instrument. The instrument was calibrated to obtain reliable data, using 5 calibration solutions. Each solution contained Fe concentrations between 0 - 10 ppm. The standard iron compound used in these experiments was ferrous ammonium sulfate. Once the instrument was calibrated, test samples were added to the spectrometer and values of intensity for the samples were measured, which were proportional to the amount of iron species present in the material. These intensity values were recorded and the amount of iron species present in the samples was calculated. The calculated value for iron was assumed to be 100% $LiFePO_4$.

From the equation of the straight line in the calibration plot the concentration can be calculated as,

$$I = 24 \times C + 8.33 \qquad \textbf{Equation 3.5}$$

Where,

I = Measured intensity (arbitrary units)
C = Concentration (ppm)

Thus,

$$C = \frac{I - 8.33}{24} \qquad \textbf{Equation 3.6}$$

The samples were prepared such that the maximum concentration would be 10 ppm, as this was the optimum value for measurement for the instrument; this corresponds to 10 ppm being equal to a 100% pure sample. Therefore, the sample purity was calculated using Equation 3.7.

Sample Purity (%) = (measured intensity (ppm) / 10) 100 **Equation 3.7**

This method gives an accurate estimate of the amount of iron present in the $LiFePO_4$ samples. However, it assumes that all the iron in the sample is present as $LiFePO_4$. It does not take account of Fe (III) impurities, and therefore measures the total iron content regardless of its oxidation state or the type of compound that is present. This method gave results that were in good agreement with the TGA data. The values for iron content were used to calculate the amount of active mass present in the electrode films.

3.2.9 Composite Conductivity Measurements

The composite films that were used for electrochemical testing were measured for conductivity using a four-point method as described in section 2.2.3. Composite electrode films were prepared using different amounts of acetylene black and $LiFePO_4$ to observe the percolation of electronic conductivity in the samples. The specific conductivity values were plotted against wt.% of carbon.

3.3 Results and Discussion

3.3.1 X-ray Diffraction

Samples of $LiFePO_4$ were characterised using X-ray diffraction as described in section 3.2.3. This was undertaken to determine the phase purity of the materials. Samples varying in synthesis temperature, synthesis time and atmosphere of preparation, sucrose quantity and reducing agent type were examined. The graph in Figure 3.2 shows X-ray diffraction data obtained for compositionally identical samples calcined at 3 different temperatures, 700, 600, 500 and 400 °C. Examples of standard and theoretical diffraction patterns can be found in Appendix 2.

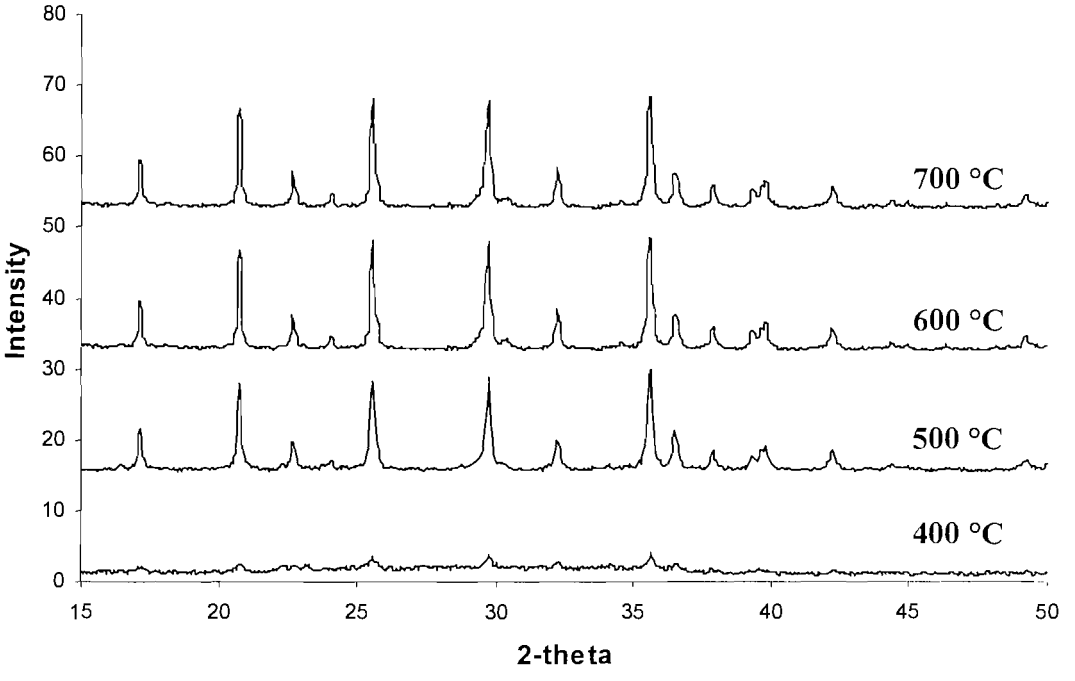

Figure 3.2 - X-ray diffraction patterns showing the effect of temperature on olivine $LiFePO_4$ phase formation for three compositionally identical samples (0.22 mol sucrose/Fe) calcined for 10 h in Ar.

It can be noted from the data in Figure 3.2 that the intensity of the diffraction reflections increases with the synthesis temperature. At 400 °C, it can be seen that evidence of a limited crystal structure is visible. However, the intensities of the 400 °C reflections are much lower relative to those of the 700 °C pattern. The pattern obtained for the 500 °C sample shows a well-developed crystal structure with reflection intensity approximately that of the 700 °C sample. This indicates that the temperature required to begin significant crystalline material formation is between 400 and 500 °C. This result is encouraging in that compared to existing reported synthesis routes [1, 3, 6-9] a temperature of 500 °C is required to form well crystallised material in a one step process, which is a significant improvement on existing methods. However, synthesis temperatures as high as 600 and 700 °C are required to form materials that give good electrochemical performance (see section 3.3.6). It should also be noted that the reflections associated with the 400 °C sample exhibit greater line broadening than the higher temperature samples. Indicating the crystal domain size is much smaller in the case of the low temperature samples.

The type of synthesis atmosphere was investigated to determine if the use of a reducing gas would improve sample purity and crystalinity. In samples prepared using 0-grade argon, a small amount of impurity (brown in colour) was observed on the surface of the grey/black powder after synthesis. The impurity was attributed to compounds containing Fe (III), which suggests that the reaction conditions are not sufficiently reducing. This may be due to an insufficient amount of sucrose, which served as the reducing agent, or due to oxidising species in the argon. Therefore, it was decided that samples would be prepared using 10 % H_2 in Ar gas. Figure 3.3 shows X-ray diffraction patterns of materials that were prepared under these conditions at three different temperatures.

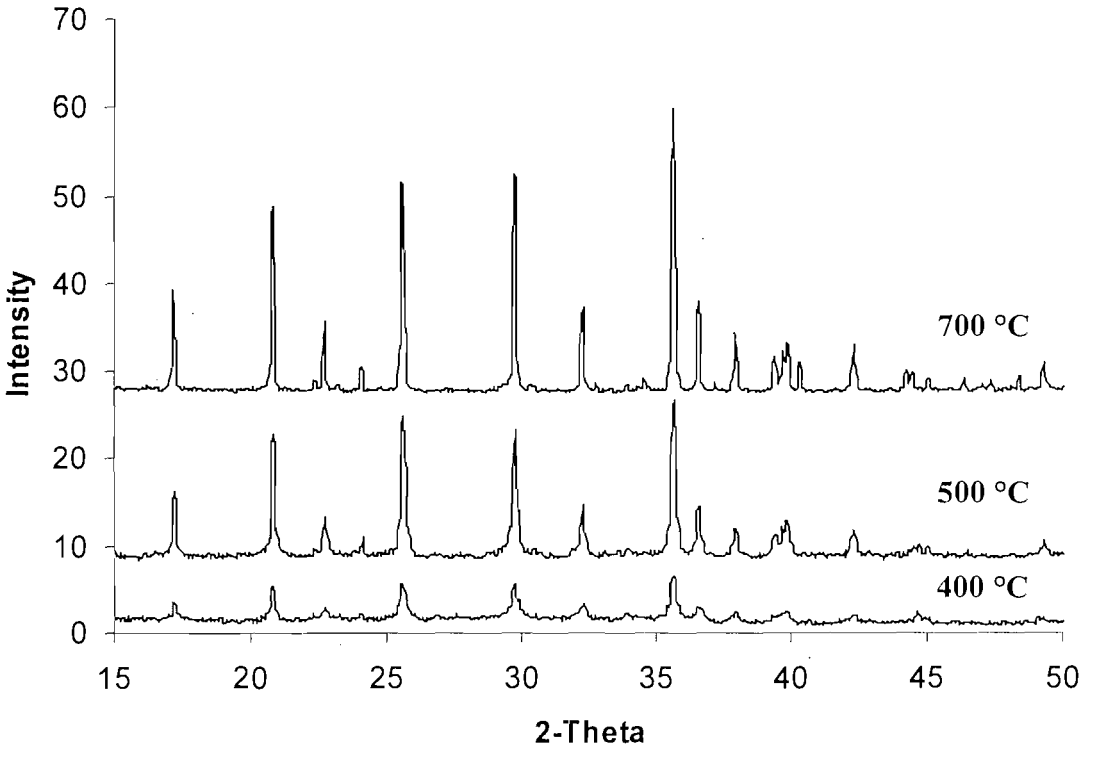

Figure 3.3 - X-ray diffraction patterns showing the effect of temperature on crystal phase formation for three compositionally identical samples (0.22 mol sucrose/Fe) calcined for 10 h under 10 % H_2 in Ar.

It can be seen that the use of hydrogen (reducing) gas has the effect of improving crystal phase formation at lower temperatures. The pattern for the 400 °C sample prepared using the 10% H_2 in Ar gas shows a higher overall intensity relative to the higher temperature samples than in the case of the 400 °C synthesised in zero-grade Ar. The presence of hydrogen would also appear to increase the amount of crystal phase formation at higher temperatures, as the pattern obtained for the 700 °C sample in hydrogen has higher overall intensity and reduced line broadening compared to the 500 °C sample.

It has been demonstrated that the presence of sucrose in the precursor material provides sufficient reducing power to form the olivine phase of $LiFePO_4$. The reducing

power of sucrose is provided by the 12 carbon atoms per formula unit, which remain after pyrolysis. This carbon is essentially similar to carbon black used as a conductive additive. In addition to the sucrose acting as the reducing agent for Fe (II) to Fe (III), the evidence in Figure 3.4 also suggests that the sucrose aids in the retention of compositional homogeneity of the precursors when in the solid phase. A possible explanation for this could be that sucrose acts as a solvent for the transition metal salts and other precursor materials when in the solid state. It was decided test this theory by preparing a precursor containing an identical amount of carbon in the form of acetylene black (Shawinigan, *Chevron Phillips Chemical Company*) as in the sucrose containing sample. The graph in Figure 3.4 shows the X-ray diffraction patterns for the sucrose and acetylene black containing materials.

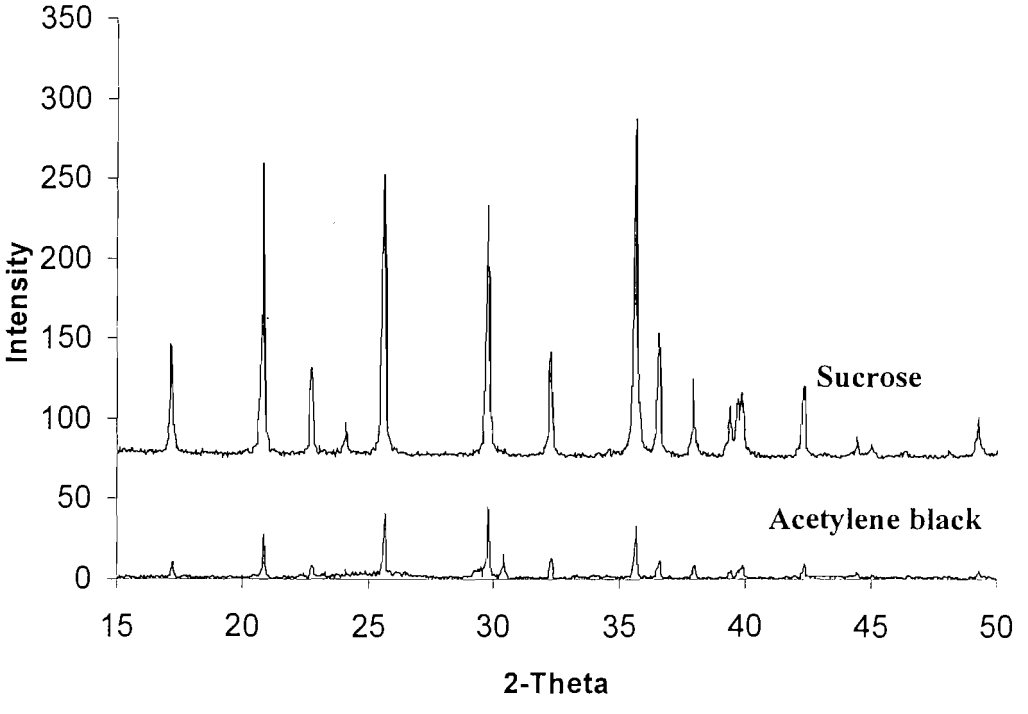

Figure 3.4 - X-ray diffraction patterns showing the effect of the type of reducing carbon used in synthesis. The samples were prepared at 700 °C for 10 h in 0-grade Ar. Electrochemical Data for this sample is given in Figure 3.26.

The data in Figure 3.4 show that the presence of sucrose leads to the development of a more crystalline material. It can be seen that the reflections in the $LiFePO_4$ pattern for the sucrose-containing sample are greater in intensity than those in the pattern for the sample prepared using the acetylene black as a reducing agent. The pattern for the material that was prepared using acetylene black indicates the presence of amorphous material because an elongated background can be seen around the reflections at 25 and 30°. This is indicative of a poorly developed crystal structure. It can also be seen that at $2\theta = 30.5°$ an impurity line exists and is evidence of poor homogeneity of the sample, as a significant amount of crystalline impurity phase is also formed. From this data, it can be concluded that the sucrose is required prior to calcination to maintain compositional homogeneity during the reaction.

X-ray diffraction was also used to characterise the precursor powders, with and without sucrose. This was undertaken to determine if crystal formation could be observed in samples without sucrose heated at low temperatures and to compare these with patterns of materials containing sucrose. The red pattern in Figure 3.5 shows evidence of crystal formation in the precursor. These phases were found to be $LiNO_3$ and $Fe(OH)(NO_3)_2$. This result gives clear evidence that crystal formation does occur in materials that do not contain sucrose. Further, it can be seen that the precursor containing 0.22 moles of sucrose/Fe, no crystal phases are visible in the dried pre-calcined material. Further, the material only begins to become crystalline at calcination temperatures between 330 - 400 °C, as the pattern for the sucrose-containing precursor shows no evidence of crystallinity until these temperatures are reached.

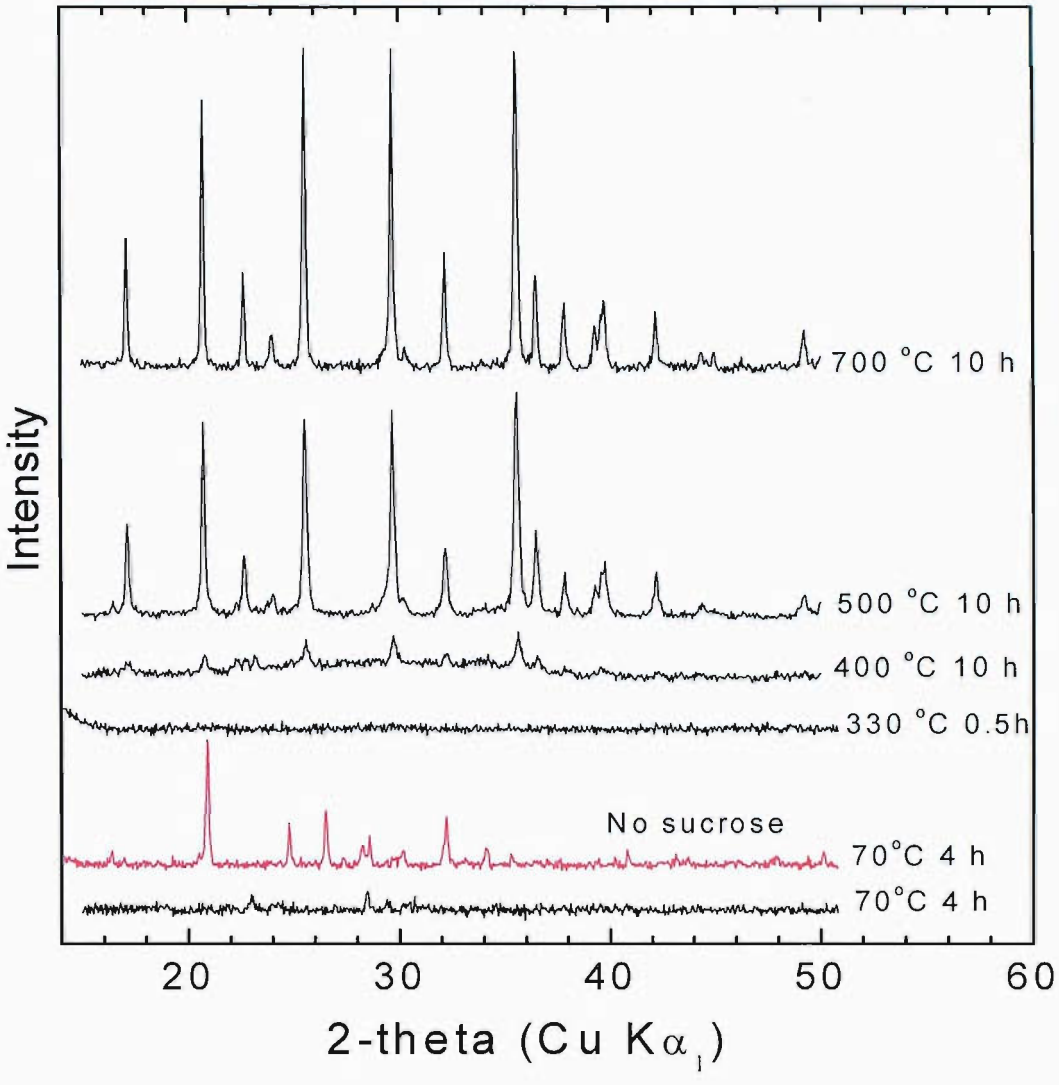

Figure 3.5 - X-ray diffraction of $LiFePO_4$ synthesis products compared to the precursor materials with and without sucrose.

3.3.2 *Optical Microscopy*

The importance of sucrose to the sample homogeneity was investigated using optical microscopy. Six samples were placed on a microscope heat stage and examined using an *Olympus BH-2* microscope under polarised light. The images of the heated solid films are shown in Figure 3.6. It is clear that as the sucrose ratio is increased above 0.22 moles (sucrose / Fe), the crystal growth is suppressed and a clear amorphous glassy material is formed. This may be due to the high viscosity of sucrose hindering crystallisation. Therefore, this should preserve the homogeneous distribution of the reactive species at the molecular level, and hence, should lead to the formation of a well-crystalised single-phase material, post calcination.

The materials that did not contain sucrose showed a large amount of crystal growth, whereas the sample containing 0.22 moles showed no crystal growth. For samples with the ratio between 0 and 0.22 a mixture of crystal domains and glassy behaviour was observed in some regions of the sample crystals, whereas in other areas crystallisation was suppressed. The amount of crystal growth decreased as the sucrose to iron molar ratio approached 0.22.

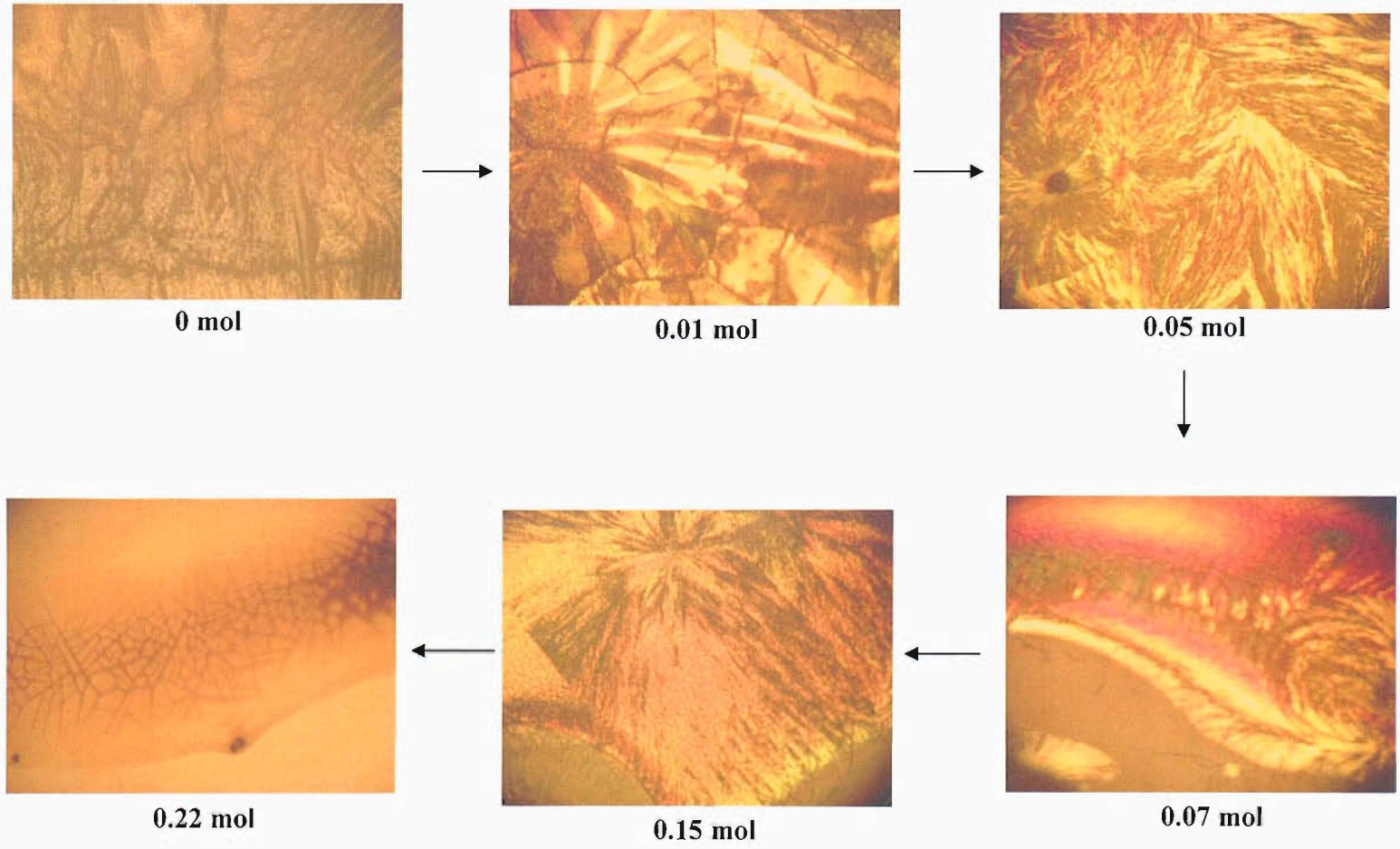

Figure 3.6 - Optical microscopy of $LiFePO_4$ precursor materials containing different amounts of sucrose.

3.3.3 Scanning Electron Microscopy

The effect of compositional segregation was investigated using scanning electron microscopy and EDX spectroscopy. The EDX maps in Figures 3.7 A and B are for two different areas of a precursor sample prepared without sucrose. These maps show areas on the surface of the samples that emitted X-rays with the characteristic energies of iron (green) phosphorus (dark blue) and oxygen (cyan). The presence of lithium could not be detected since it was outside of the range of the instrument. It can be seen in the figures that the three elements of interest are not uniformly spread across the sample. Large areas of phosphorus and iron (on the order of 20 μm in diameter) exist away from the areas containing iron. This is further evidence for the segregation of crystals of phosphate away from the crystals of iron nitrate as the solid phase was formed. The black areas represent the regions of the sample that did not produce X-rays, due to a lack of Fe, O or P containing material or recessed surface topography. By contrast, the EDX maps of the sample containing sucrose (0.22 molar ratios with respect to Fe) in Figures 3.8 A and B show a more uniform spread of the three elements across the area of sample.

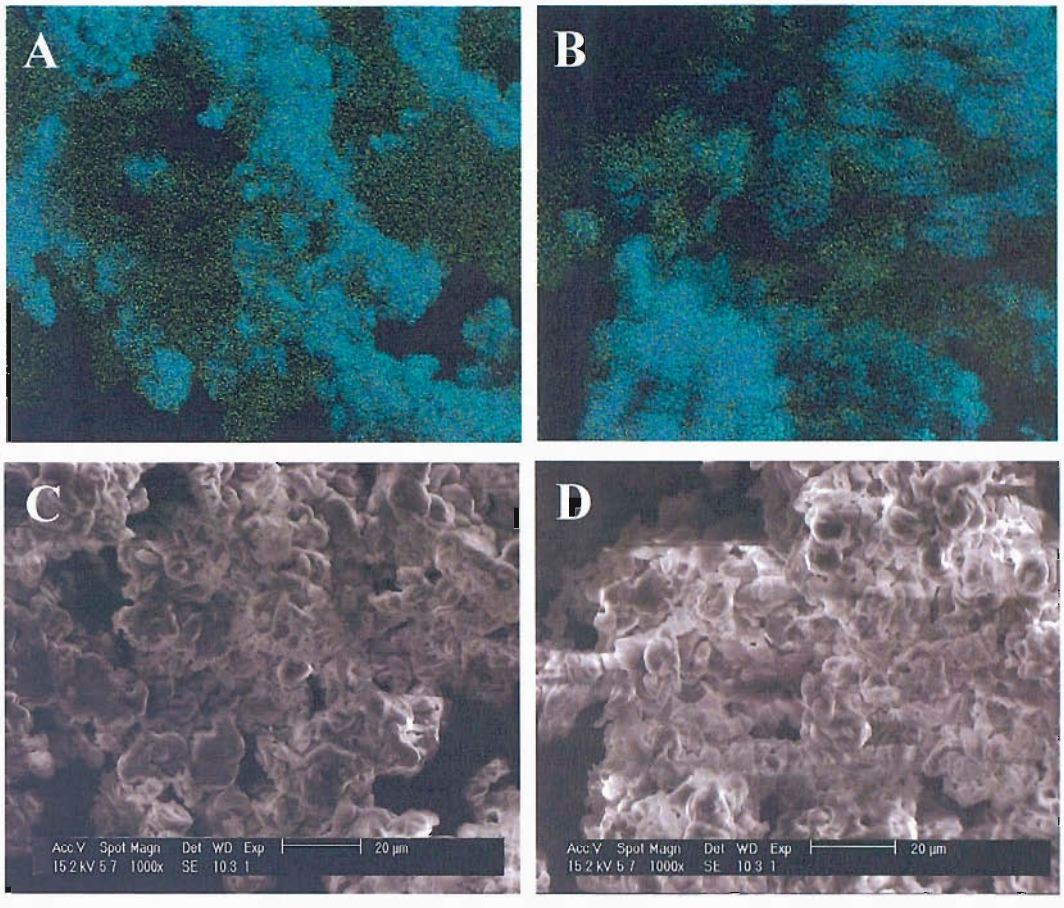

Figure 3.7-EDX mapping (A and B) and SEM images (C and D of precursor materials without sucrose. The EDX maps show regions of characteristic energy for iron (green), phosphorus (blue), oxygen (cyan).

The darker area between the highly homogeneous regions seen in Figure 3.8 B may be attributed to surface topography. The homogeneous distribution of precursors that is observed in the sample containing sucrose can also be seen in the optical microscopy data. This evidence supports the hypothesis that the presence of sucrose may suppress the formation of precursor crystals as the sample is heated, which would ordinarily separate as the material is dried. It is thought that the addition of sucrose to the precursors allows the compounds containing lithium, iron and phosphorus to remain immobile in a homogeneous glass phase and thus, inhibiting particle segregation on heating. This would suggest that if the distances between the reactive species were reduced (relative to that in a non-sucrose containing sample), as in a

homogenous glass, the diffusion distances would be reduced. Lower temperatures could then be used to obtain the pure crystalline phase.

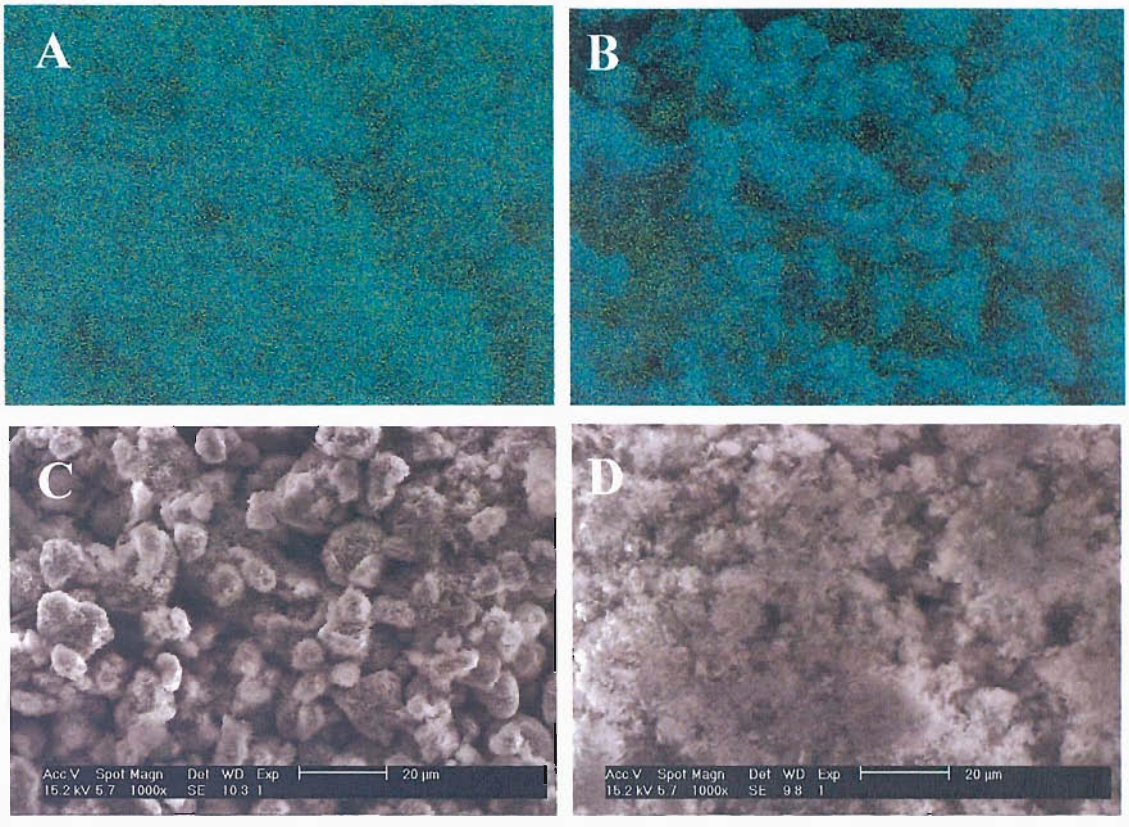

Figure 3.8 - EDX mapping (A and B) and SEM images (C and D) of precursor materials containing 0.22 moles of sucrose. The EDX maps show regions of characteristic energy for iron (green), phosphorus (blue), oxygen (cyan).

The SEM micrograph images (see Figures 3.7 and 3.8) indicate the differences in morphology between the non-sucrose and sucrose containing precursors. The sucrose containing samples (Figures 3.8 A and C) appear to have a surface coating that appear to be composed of finer particles. This may be evidence of a coating on the larger $LiFePO_4$ crystals. By contrast, the images of the surface of the non-sucrose containing samples appear sharper and the polycrystalline material can be clearly seen.

3.3.4 EDX Spot Analysis

Several spot areas (~5 μm) were studied in each sample (sucrose and non-sucrose samples) to determine if compositional differences were observed at different spots. The EDX site map is shown in Figure 3.9 and the data obtained for the eight spot areas is summarised in Table 3.1. EDX specta were collected at each of eight the spots that gave the measured intensity of the associated with elements found in the sample area *versus* their characteristic electron energy. Quantitative analysis was undertaken for each site to calculate the ratio of the elements present. An example of these spectra and the associated quantitative analysis is given in Figure 3.10.

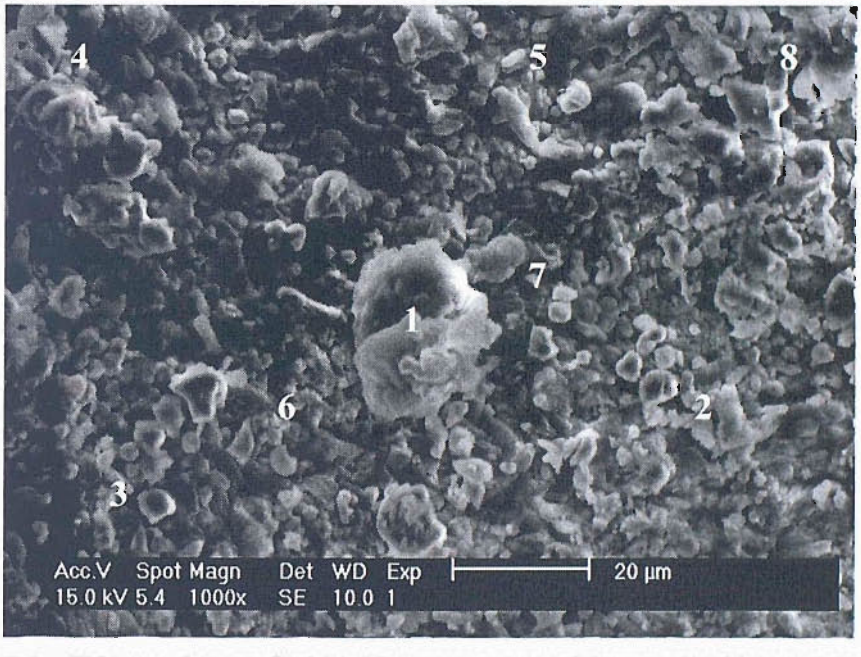

Figure 3.9 - EDX spot site map for $LiFePO_4$ precursor material prepared without sucrose. The numbers indicate the position of the spot for the data in Table 3.1.

Table 3.1 - Summary of EDX quantitative analysis data for the non-sucrose containing sample.

Spot	Element	Wt.%	At.%
1	N K	24.2	29.45
	O K	60.86	64.83
	P K	4.75	2.61
	FeK	10.19	3.11
P:Fe			
	P K	31.79	45.62
	FeK	68.20	54.37
2	N K	6.55	11.15
	O K	39.56	58.96
	P K	20.08	15.46
	FeK	33.81	14.43
P:Fe			
	P K	38.51	53.03
	FeK	61.49	46.97
3	N K	6.56	9.88
	O K	53.36	70.36
	P K	15.24	10.38
	FeK	24.85	9.39
P:Fe			
	P K	39.58	54.15
	FeK	60.42	45.85
4	N K	6.19	9.13
	O K	55.77	72.08
	P K	15.8	10.55
	FeK	22.25	8.24
P:Fe			
	P K	42.98	57.61
	FeK	57.02	42.39

Table 3.1 Continued.

5	N K	7.6	11.58
	O K	50.23	67.02
	P K	17.19	11.85
	FeK	24.98	9.55
P:Fe			
	P K	42.18	56.81
	FeK	57.82	43.19
6	N K	1.47	3.75
	O K	13.35	29.73
	P K	23.77	27.35
	FeK	61.4	39.17
P:Fe			
	P K	28.35	41.64
	FeK	71.65	58.36
7	N K	6.59	9.61
	O K	56.75	72.44
	P K	15.49	10.21
	FeK	21.16	7.74
P:Fe			
	P K	43.73	58.35
	FeK	56.27	41.65
8	N K	4.09	7.23
	O K	39.35	60.84
	P K	19.36	15.46
	FeK	37.2	16.48
P:Fe			
	P K	35.44	49.74
	FeK	64.56	50.26

Spot 1

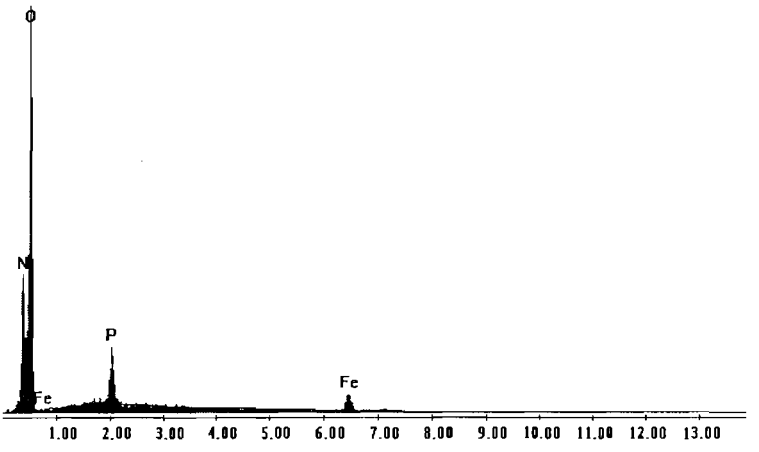

Element	Wt.%	At.%
N K	24.2	29.45
O K	60.86	64.83
P K	4.75	2.61
FeK	10.19	3.11
P:Fe		
P K	31.79	45.62
FeK	68.20	54.37

Figure 3.10 - EDX spectra and supporting quantitative elemental analysis for spot 1 (non-sucrose), the peak labels indicate the elements present in the sample.

It can be seen from the EDX data summarised in Table 3.1 that there is a large variation in the composition exists for the sample that does not contain sucrose. The amount of oxygen varies from 29.73 at.% at spot 6, to 64.8 at.% at spot 1. It is not likely that this is scatter associated with a random error in the measurement. This is because the sample containing sucrose, the oxygen atom percentage varies only between 52.6 and 54.5 at.%. It is clear that the sample is inhomogeneous in terms of composition at the distances required for the diffusion of species required to form the required material. This, therefore, suggests that reactions using such a precursor would require higher temperatures and further re-mixing steps than a well-mixed precursor.

Figure 3.11 shows the spots studied in the sucrose-containing sample. Only four sampling sites were studied in this case, because after three sites had been studied, it was determined that the composition was essentially identical at each site, therefore it was not necessary to explore additional sites.

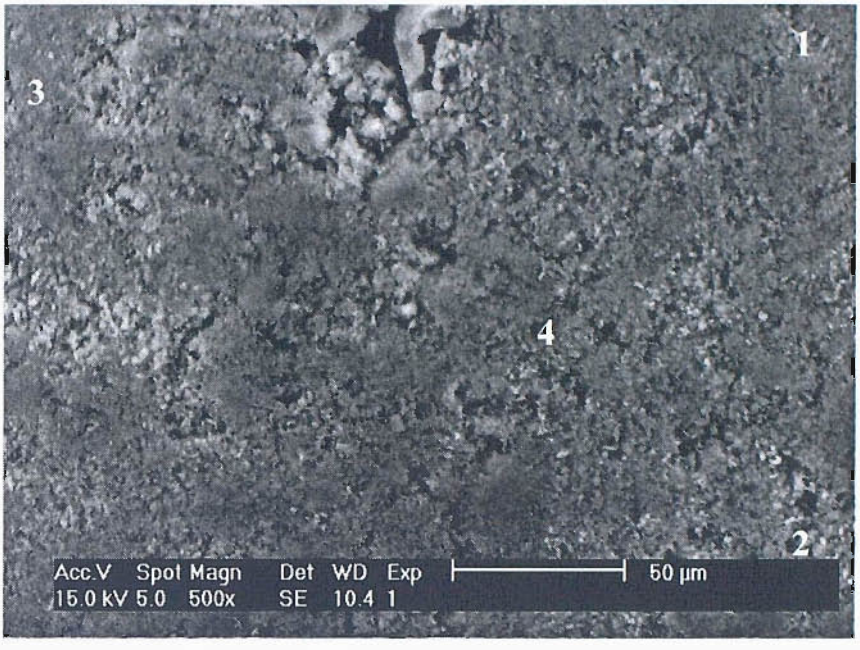

Figure 3.11 - EDX spot site map for a sample of $LiFePO_4$ precursor material containing as 0.22:1 molar ratio of sucrose to Fe. The numbers indicate the position of the spot for the graphs below A to D.

The EDX data summarised in Table 3.2 and Figure 3.12 shows that the intensity of the X-ray energies for the three elements are very similar in each of the four spots. An example of this is the value for the ratio of iron to phosphorus. The amount of iron varies only by approximately 2 At.% at all four spots, which is the approximate accuracy of the instrument. This result is therefore, further evidence to support the hypothesis that the presence of sucrose can suppress the segregation of the crystals in the precursor.

Table 3.2- Summary of EDX quantitative analysis data for the sucrose-containing sample.

Spot	Element	Wt.%	At.%
1	C K	9.45	17.21
	N K	2.71	4.24
	O K	39.65	54.24
	P K	17.25	12.19
	FeK	30.94	12.12
Fe:P			
	P K	35.53	49.84
	FeK	64.47	50.16
2	C K	9.99	18.49
	N K	2.08	3.31
	O K	37.81	52.55
	P K	17.83	12.8
	FeK	32.29	12.86
Fe:P			
	P K	37.4	51.85
	FeK	62.6	48.15
3	C K	8.11	15.3
	N K	2.43	3.93
	O K	37.96	53.8
	P K	18.6	13.62
	FeK	32.9	13.36
Fe:P			
	P K	37.13	51.58
	FeK	62.87	48.42
4	C K	10.78	18.87
	N K	3.06	4.59
	O K	41.42	54.42
	P K	17.46	10.05
	FeK	27.27	10.35
Fe:P			
	P K	39.03	49.26
	Fe K	60.97	50.74

Spot 1

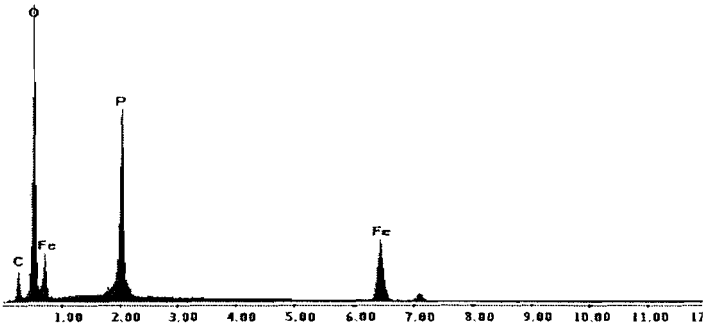

Element	Wt.%	At.%
C K	9.45	17.21
N K	2.71	4.24
O K	39.65	54.24
P K	17.25	12.19
FeK	30.94	12.12
P:Fe		
P K	35.53	49.84
FeK	64.47	50.16

Figure 3.12 - An example of an EDX spectrum and supporting quantitative elemental analysis for spot 1 for a sucrose containing precursor.

It can also be noted that the particle size for the non-sucrose containing precursor is larger than that for the sucrose-containing sample. Further, the surface of the sample is covered in a finer particulate material. It is possible that the reduced particle size may be a result of the transition metal salts dissolving into the sucrose matrix and being trapped within the network of smaller particles.

The bar graphs in Figures 3.13 and 3.14 show the relative proportions of iron and phosphorus in the non-sucrose and sucrose-containing samples as measured using EDX spectroscopy. In order for the sample to be considered homogeneous, the proportions of Fe and P at each site number should be 50:50 within acceptable experimental error. This would represent a precursor that would potentially yield 100 % conversion to $LiFePO_4$. It can be seen from Figure 3.13 that the non-sucrose containing precursor shows a large variation in this ratio between the sites, in some cases over 10 at.% in the amount of each component. This would clearly be very unfavourable to the formation of a pure phase material. In contrast, the sucrose-containing precursor shown in Figure 3.14 shows an equal value of iron and phosphorus (50:50) at each site and very little difference in the amount of phosphorus and iron at each of the sites (1 - 2 at.%). This small variation in the ratio of Fe:P is

possibly due to experimental error associated with the measurement, and thus, suggests there is no variation in composition of precursor samples containing sucrose.

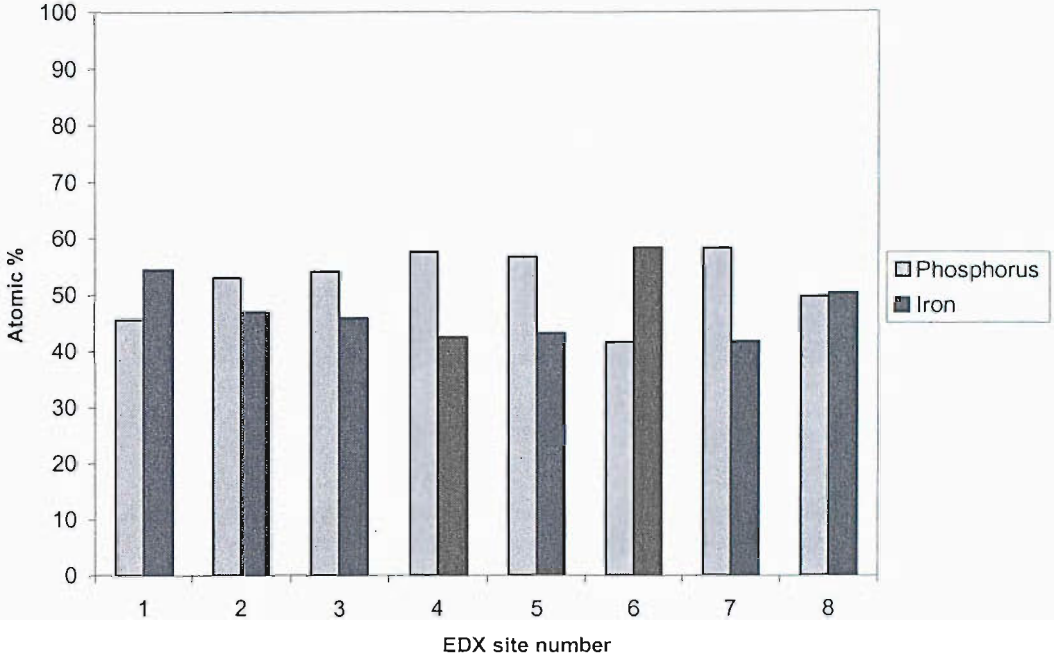

Figure 3.13 - A bar graph to show the relative percentages of phosphorus to iron in non-sucrose containing $LiFePO_4$ precursor samples, measured by EDX spectroscopy.

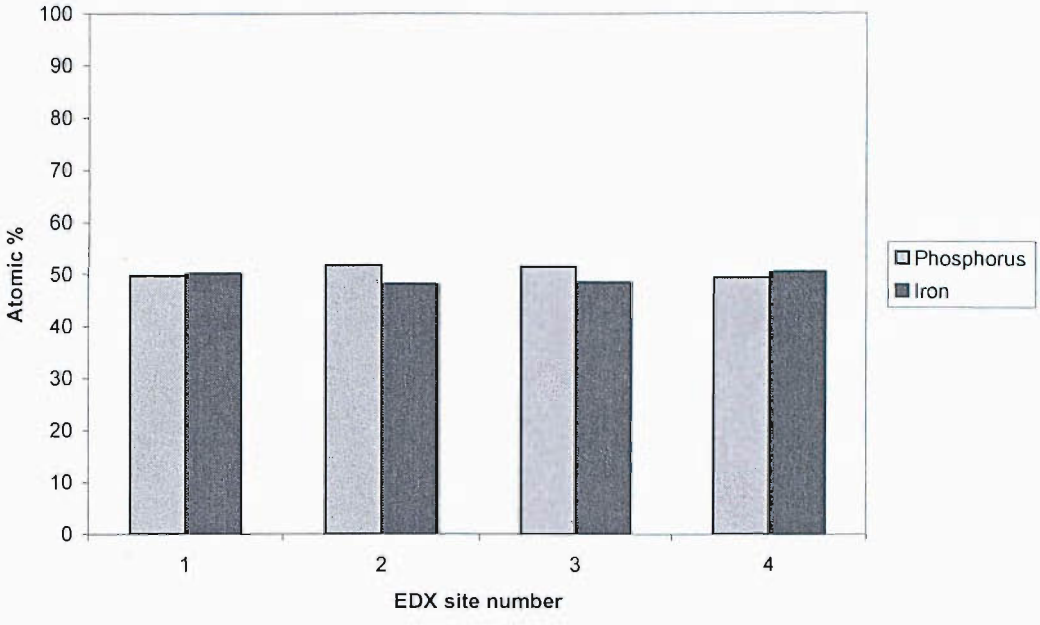

Figure 3.14 - A bar graph to show the relative percentages of phosphorus to iron in sucrose containing $LiFePO_4$ precursor samples, measured by EDX spectroscopy.

3.3.5 Electronic Conductivity

The conductivity of the composite films of $LiFePO_4$/C containing 5 wt.% PTFE was studied as described in section 3.2.9. Similar percolation behaviour was observed in these composites as seen in the $LiMn_2O_4$ composites. However, it was determined that the percolation behaviour was different in the amount of carbon required to reach the percolation threshold and also in the shape of the curve. A conductivity value of ~ 0.1 S cm^{-1} was measured for the peak conductivity for the $LiMn_2O_4$ films, using the two-point method, this value was reached at 5 wt.% of carbon. In the case of the $LiFePO_4$ composites ~ 10 wt.% carbon additives were required to reach the percolation threshold; the conductivity in this case was 1 S cm^{-1}. The shape of the curves also differed; the linear region (between 0 and 7.5 wt.% of carbon) was of a steeper gradient in the case of $LiMn_2O_4$ than in $LiFePO_4$ (see Figures 3.15 and 2.25). The $LiMn_2O_4$ materials were measured using the two-probe method, however the $LiFePO_4$ materials were tested using the four-probe method. It would appear that

when using $LiFePO_4$ active material, a larger amount of carbon is required to films with conductivities over the percolation threshold, than in the films made using $LiMn_2O_4$.

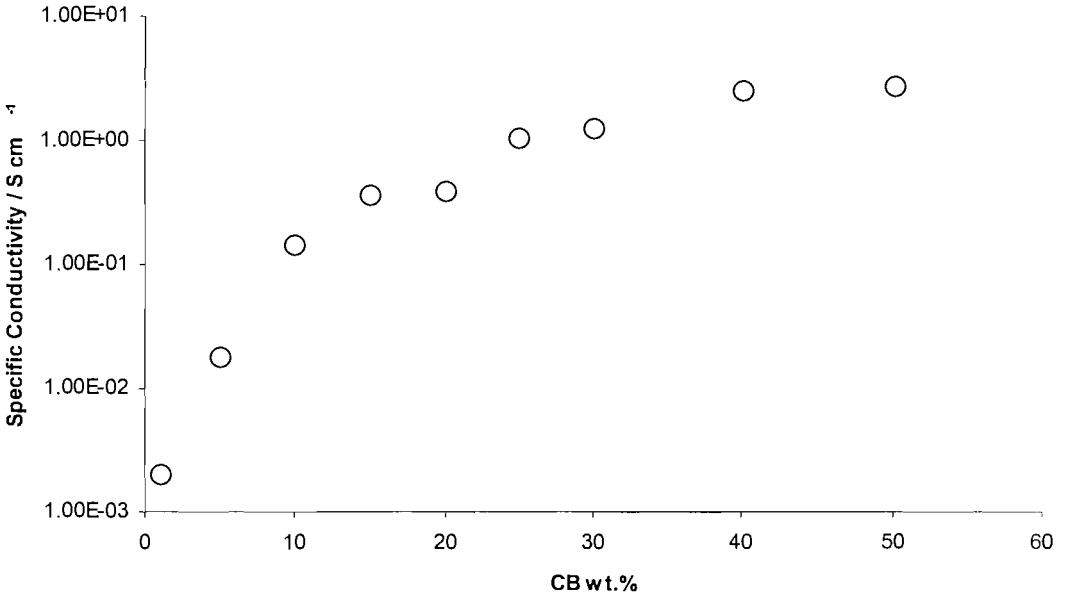

Figure 3.15 - Specific conductivity of $LiFePO_4$/C/PTFE composite films, measured using the four-point technique.

3.3.6 Electrochemical Testing

Electrode materials were tested using the methods described in section 3.2.6. The electrochemical cycling data for samples prepared using the one-step and two-step synthesis methods are shown in the following sections.

3.3.6.1 *One Step Synthesis of $LiFePO_4$*

Electrode materials were prepared and were tested using galavanostatic techniques as described in section 3.2.6. Figure 3.16 shows the charge-discharge behaviour of a

$LiFePO_4$/CB/PTFE electrode prepared under argon at 700 °C, using a 0.22:1 sucrose to Fe ratio. The specific capacity of this material is on average 105 mA h g^{-1} on charge and discharge. The first charge and discharge show a variation from the mean capacity values as irreversible capacity associated with parasitic side reactions contribute to the first charge. These reactions may occur due to the presence of some residual C-OH or C-H groups adsorbed on to the carbon, these groups may have remained from the pyrolyis of the sucrose. The extent to which this could contribute to the first charge will depend on the amount of these groups left after synthesis.

The cyclabity of the material is good over 20 cycles with little degradation on cycling. The agreement between charge and discharge value becomes greater as the material is cycled, thus, giving a good charge discharge balance. However, this material only exhibits 100 mA h g^{-1}, which is higher than can be achieved with the non-optimised material prepared by a solid state reaction, but less than the theoretical value of 170 mAh g^{-1}. Many groups have demonstrated close to 95% theoretical values for capacity of $LiFePO_4$. However, such reactions require a number of synthesis or processing to achieve high values of capacity (see section 1.4.3). The performance shown in Figure 3.16 was achieved in a single step, without further regrinding and additional treatment. It is well known, however, that the addition of carbon in the form of sucrose to $LiFePO_4$ materials after synthesis results in an increase in the specific conductivity of the material, due to a carbon coating on the surface of the material [10, 11].

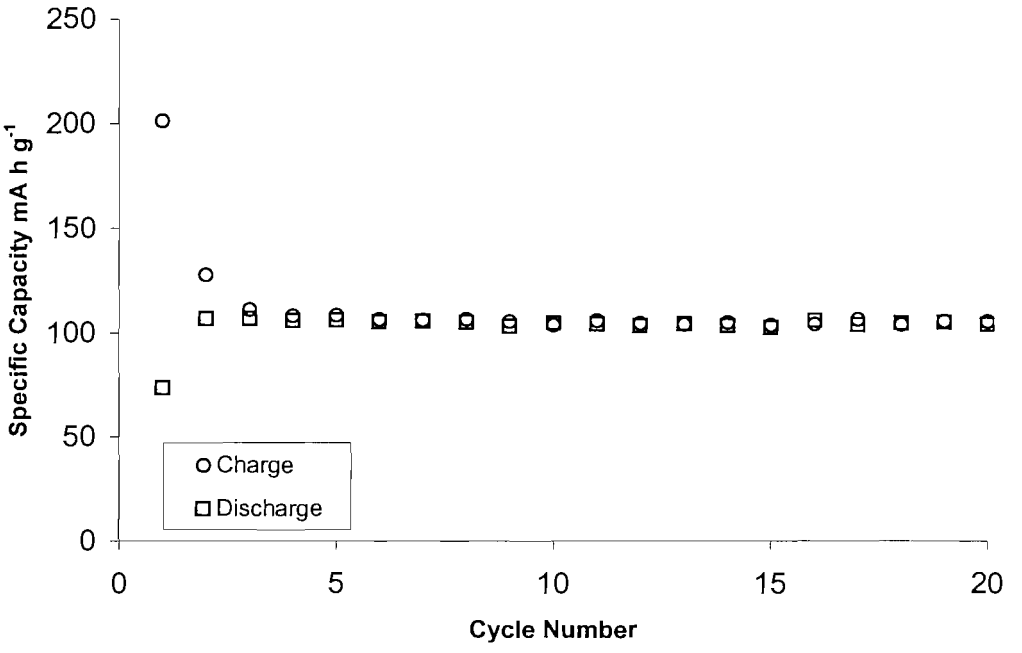

Figure 3.16 - Charge-discharge cycling for $LiFePO_4$ material prepared at 700 °C for 10 h, using 0.25:1 sucrose:Fe ratio in Ar.

The effect of synthesis temperature on electrochemical performance is shown in Figures 3.16-3.18. The performance of the material synthesised at 700 °C (Figure 3.16) shows good capacity (approximately 100 mAh g^{-1}) and the cyclablity is good with consistent capacity values up to 15 cycles. The material synthesised at 500 °C (Figure 3.17) shows lower capacity than the 700 °C sample, approximately 50-55 mA h g^{-1}. However, this material exhibits higher capacity than the sample prepared at 350 °C (Figure 3.18). The charging capacity in cycles 2 to 6 in the 500 °C sample appear to be higher than the discharges. Therefore, there is a large charge discharge imbalance in the cell. However, as the cycling proceeds, the charge and discharge cycles begin to become closer in value. The cyclablity of the 500 °C appears poorer than the cell cycled at 700 °C as it loses ~ 28 % of its initial capacity from the 2^{nd} cycle by the 15^{th} cycle.

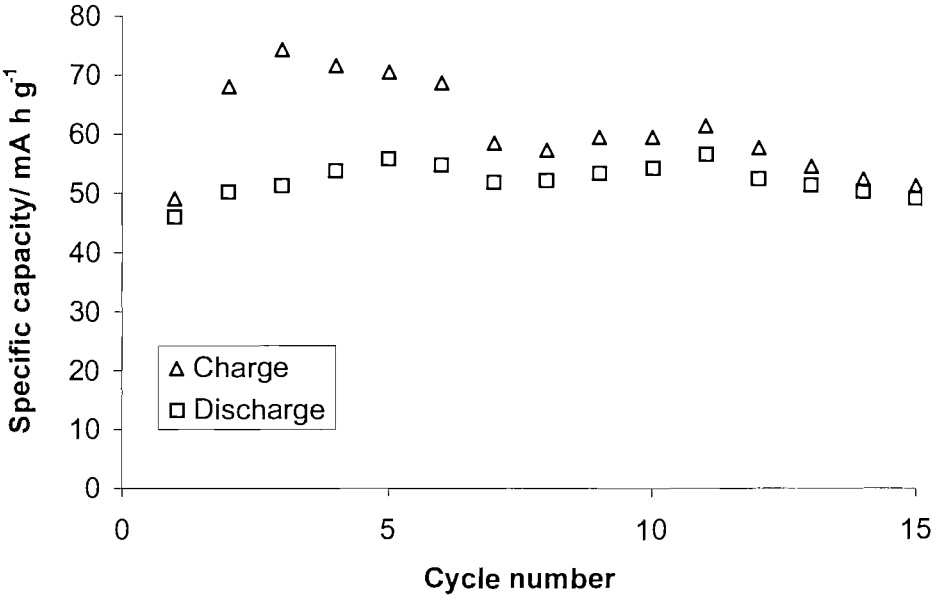

Figure 3.17 - Charge-discharge cycling for $LiFePO_4$ material prepared at 500 °C for 10 h, using 0.25:1 sucrose:Fe ratio in Ar.

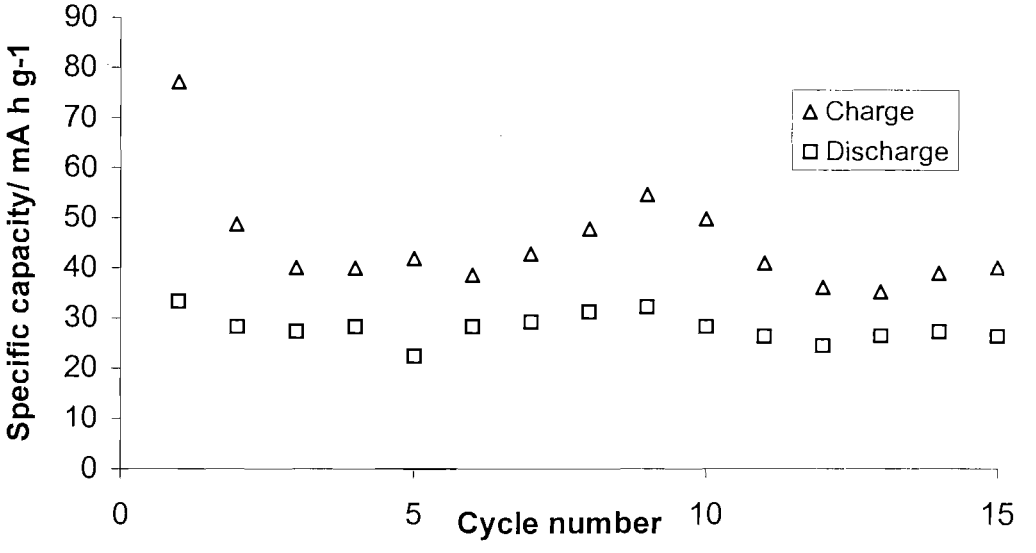

Figure 3.18 - Charge-discharge cycling for $LiFePO_4$ material prepared at 350 °C for 10 h, using 0.25:1 sucrose:Fe ratio in Ar.

The effect of increasing the carbon loading in the composite can be seen in Figures 3.19 - 3.21. Three carbon loadings were investigated 25 wt.% (Figure 3.19), 20 wt.% (Figure 3.20) and 10 wt.% (Figure 3.21). All three electrodes showed approximately the same values of capacity after the first charge (~ 100 – 110 mAhg1-1). These results suggest that all the electrodes contain a high enough carbon loading to utilise that full capacity available from the electrode material. The small variations in capacity may result from differences in the amount of active material present in the electrode and small difference in electrode conductivity and hence electrode kinetics.

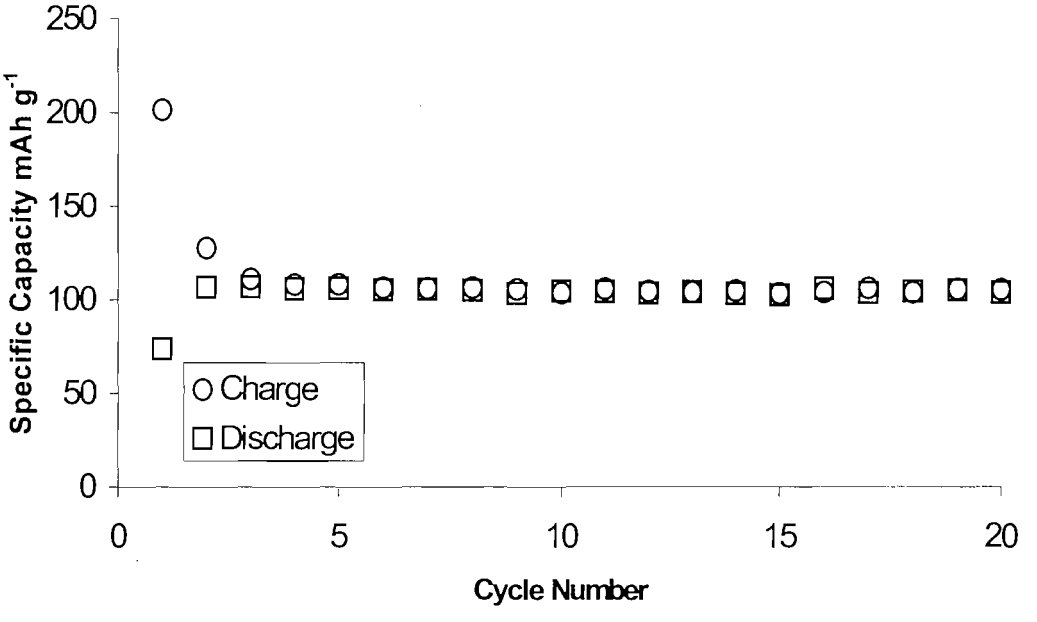

Figure 2.19 - Specific capacity *vs.* cycle number for a $LiFePO_4$ material prepared in 10% H_2 in Ar at 700 °C, for 10 h, with 0.25:1 sucrose to iron ratio. Electrode composition: 25wt% carbon black, 5 wt% PTFE 70 wt% $LiFePO_4$.

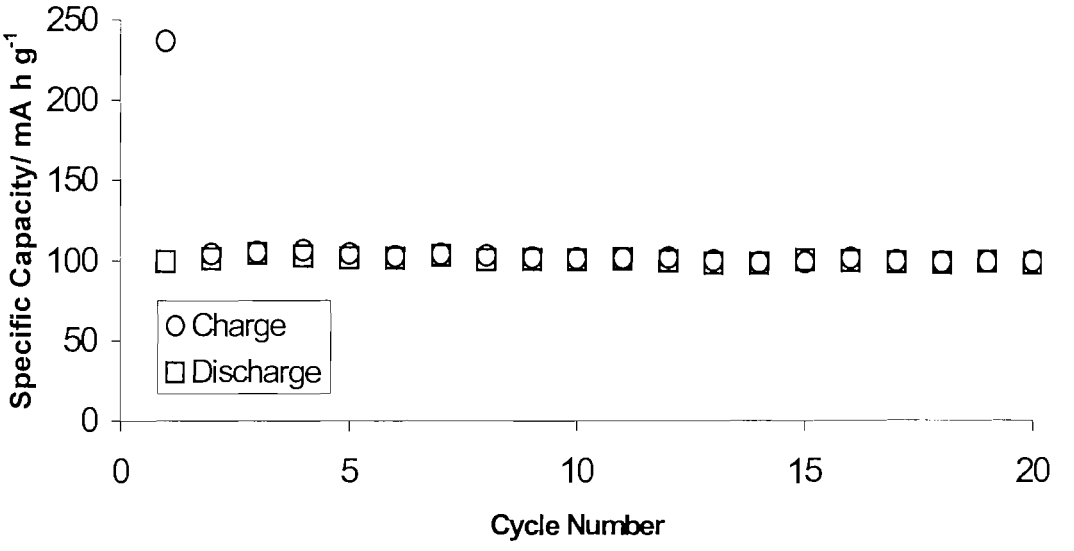

Figure 3.20 - Specific capacity *vs.* cycle number for a $LiFePO_4$ material prepared in 10% H_2 in Ar. Prepared at 700 °C, for 10 h, sucrose:Fe 0.25. Electrode composition: 20 wt.% of carbon black, 5 wt.% of PTFE, 75 wt.% of $LiFePO_4$.

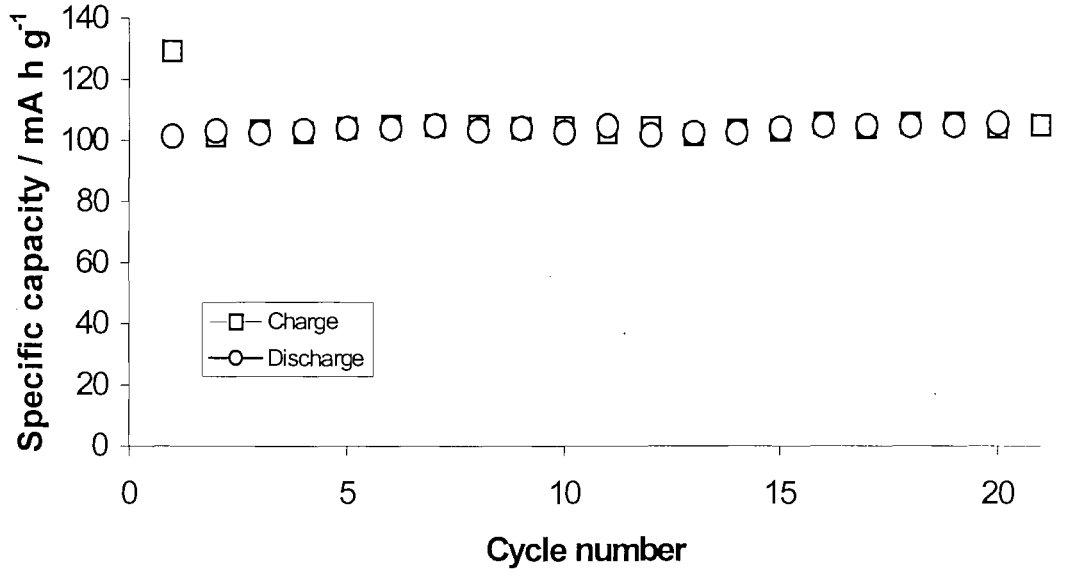

Figure 3.21 - Specific capacity *vs.* cycle number for a $LiFePO_4$ material prepared in 10% H_2 in Ar. at 700 °C for 10 h, sucrose:Fe 0.25. Electrode composition: 10 wt.% of carbon black, 5 wt.% of PTFE, 85 wt.% of $LiFePO_4$.

Figure 3.22 shows the electrochemical performance of the material prepared at 700 °C containing 10 wt.% carbon over a period of 15 cycles. It can be noted that the capacity on charge and discharge is well balanced and there is very little hysteresis on cycling. This suggests that the conductivity of the material is sufficient to an acceptable rate of electron transfer from the current collector to the active material.

The first charge is higher than the first discharge and subsequent cycles due to the irreversible capacity from reactive species on the surface of the electrode and in the electrolyte. This shows that the maximum specific capacity can be achieved at 10 wt% of carbon. This is in agreement with the conductivity measurements for the composites outlined in section 3.3.5.

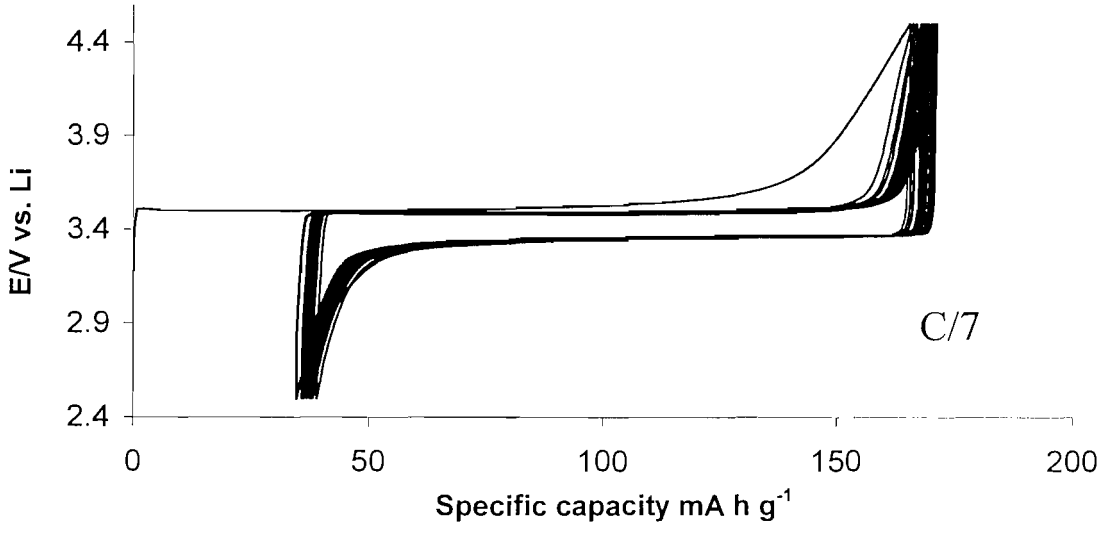

Figure 3.22 – Specific capacity *vs.* potential for an electrode prepared at 700 °C in 10 % H_2 in Ar for 15 cycles, 10 wt.% Carbon, 5 wt.% PTFE, 85 wt.% $LiFePO_4$.

The kinetics of the insertion reactions was investigated in samples prepared in different atmospheres. It is expected that the maximum specific capacity should be related to the cycling rate with a $(1/c)^{1/2}$ dependence, where c is the cycling rate assuming an electrode of infinite thickness. At high rates of cycling the capacity should be lower than that at low cycling rates. At an infinitely slow rate of cycling, the maximum capacity should be observed.

Figure 3.23 shows the specific capacity *vs.* cycling rate for the average of three charge/discharge cycles for a material prepared at 700 °C, for 10 h in 10% H_2 in argon. The data in Figure 3.23 shows that the specific capacity observed at a given cycling rate is proportional to the square route of the cycling rate. The gradient of the line is lower than for the sample prepared in argon (Figure 3.24) indicating a higher rate capability at elevated cycling rates for the samples prepared in hydrogen. The rate data for the electrode material prepared in H_2 shows over a 50 % reduction in capacity between the fastest and slowest cycling rates. In both cases the maximum capacity observed by extrapolation is approximately of 120 mAh g^{-1}.

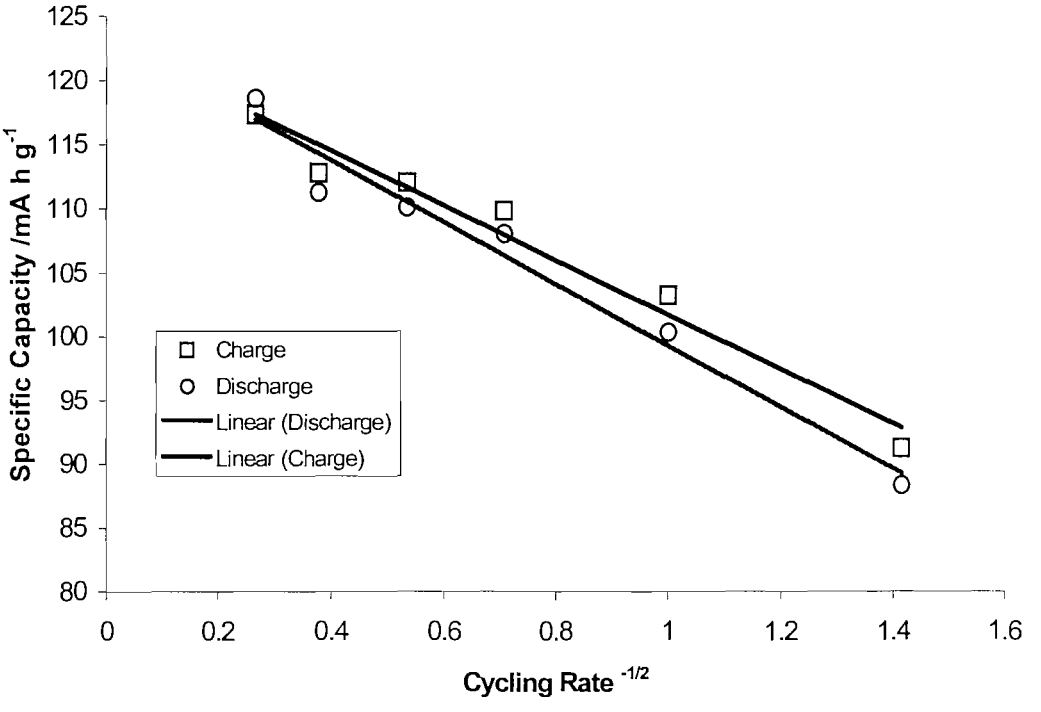

Figure 3.23 - Specific capacity *vs.* cycling rate for a $LiFePO_4$ electrode material prepared in a hydrogen atmosphere. The material was prepared at 700 °C, for 10 h, using a 0.25:1 ratio of sucrose to iron. The Electrode was prepared using 10 wt.% of carbon, 5 wt.% PTFE and 85 wt.% $LiFePO_4$.

Figures 3.24 and 3.25 report specific capacity *vs.* cycling rate for electrode material that was prepared in an argon atmosphere. Three charge and discharge cycles were obtained for each cycling rate. Figure 3.24 shows the relationship between cycling rate and specific capacity for an electrode material prepared at 700 °C in an argon atmosphere. It can be seen that the capacity falls more rapidly than in the case for the electrode composed of material prepared in argon than for the material prepared in H_2.

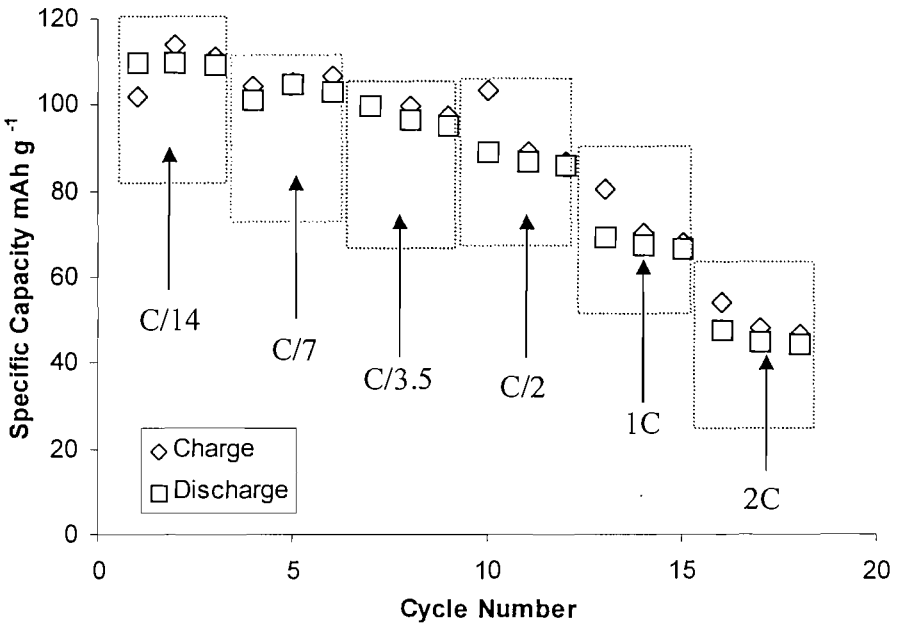

Figure 3.24 - Specific capacity *vs.* cycling rate for a $LiFePO_4$ electrode material prepared in an argon atmosphere at 700 °C for 10 using a 0.25:1 sucrose to iron ratio. Three charge discharge cycles were run for each cycling rate. Electrode was prepared using 10 wt.% of carbon, 5 wt.% PTFE and 85 wt.% $LiFePO_4$. Average values for each rate are shown in Figure 3.28.

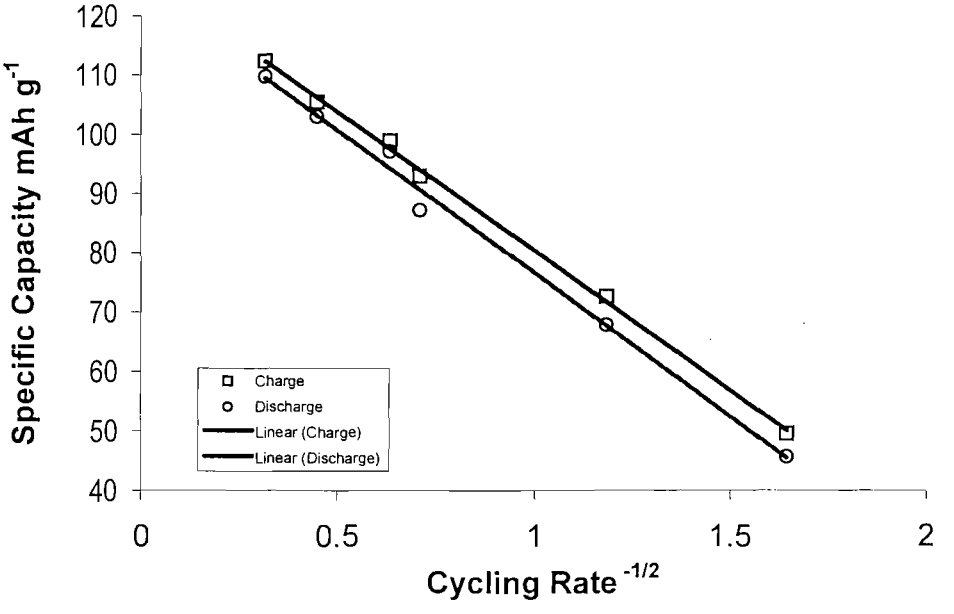

Figure 3.25 - Specific capacity *vs.* cycling rate for a $LiFePO_4$ electrode material prepared in an argon atmosphere at 700 °C, using a sucrose ratio of 0.25, calcined for 10 h.

The cycling data in Figures 3.23 and 3.25 show that the charge and discharge balance in the both electrodes is acceptable as the gradients of charge and discharge lines are almost identical for the cells for the materials prepared in argon and hydrogen. This indicates that the ratio of the capacity on charge and discharge are invariant regardless of the cycling rate, although the overall capacity decreases as the cycling rate increases.

The effect of using a different carbon source for the reducing agent was explained in section 3.3.1, in which a comparison between sucrose and carbon black one-step preparation routes was drawn between their X-ray diffraction patterns (see Figure 3.4). The sample used for this X-ray study was tested galvanostatically, it was found that this material had a much lower capacity than the sample prepared using sucrose (25 mAh g^{-1} *cf.* 105 mAh g^{-1}, for the sucrose containing sample) as shown in Figure 3.26. This low value of capacity is expected for a material prepared in such a way, as the poorly mixed precursor would require further regrinding and heating steps to achieve close to the values achieved using the one-step sucrose preparation method. The cycling data also shows poor capacity on cycling as a reduction of over 30% in capacity after 15 cycles.

It can be seen in Figure 3.26 that the use of carbon instead of sucrose in the precursor leads to the formation of low-purity materials (see XRD, Figure 3.4) with poor electrochemical performance. Figure 3.27 shows the specific capacity *vs.* potential for the 15 cycles. The first cycle gives much lower than expected performance for $LiFePO_4$, and subsequent cycling results in a rapid decrease in the capacity down to approximately 15 mAh g^{-1}. This value is around 100 mAh g^{-1} lower than that seen for the samples prepared using sucrose, which in contrast maintained good cyclablity over the 20 cycles that were recorded.

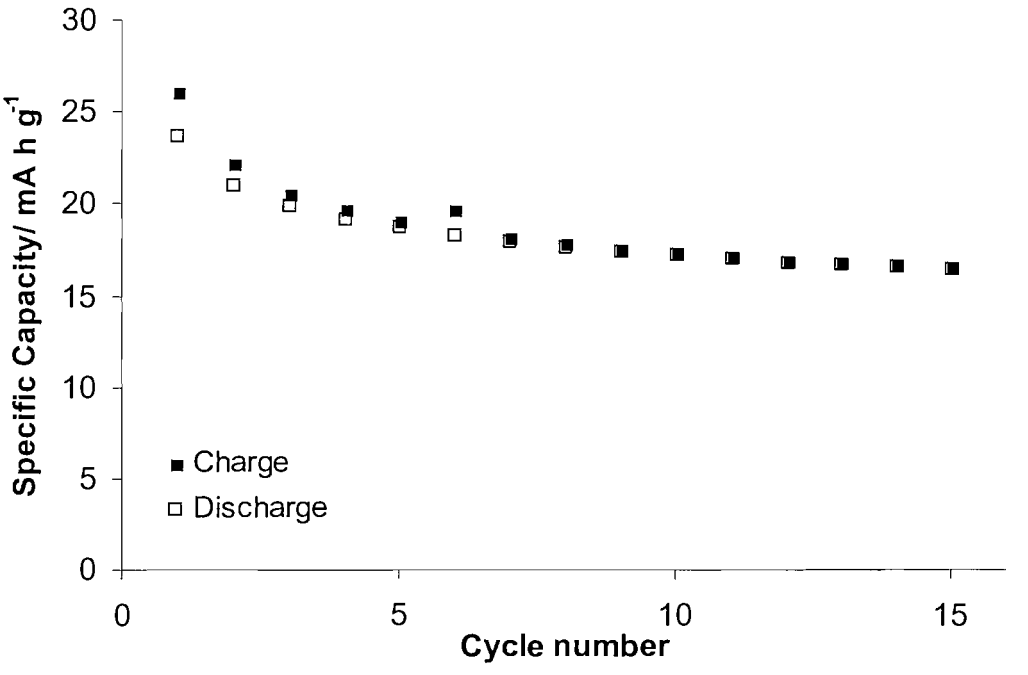

Figure 3.26 - Specific capacity *vs.* cycle number for $LiFePO_4$ prepared using a reducing carbon (AB) containing precursor.

Figure 3.26 shows the potential *vs.* specific capacity per cycle for the precursor prepared using acetylene black as a reducing agent. It can be noted that the capacity decreases on each cycle. The capacity values for this material are larger than that expected for activated carbon by approximately 10 mAh g^{-1}, indicating the formation of a small amount of active material and poor conductivity within the $LiFePO_4$ particles (agglomerates).

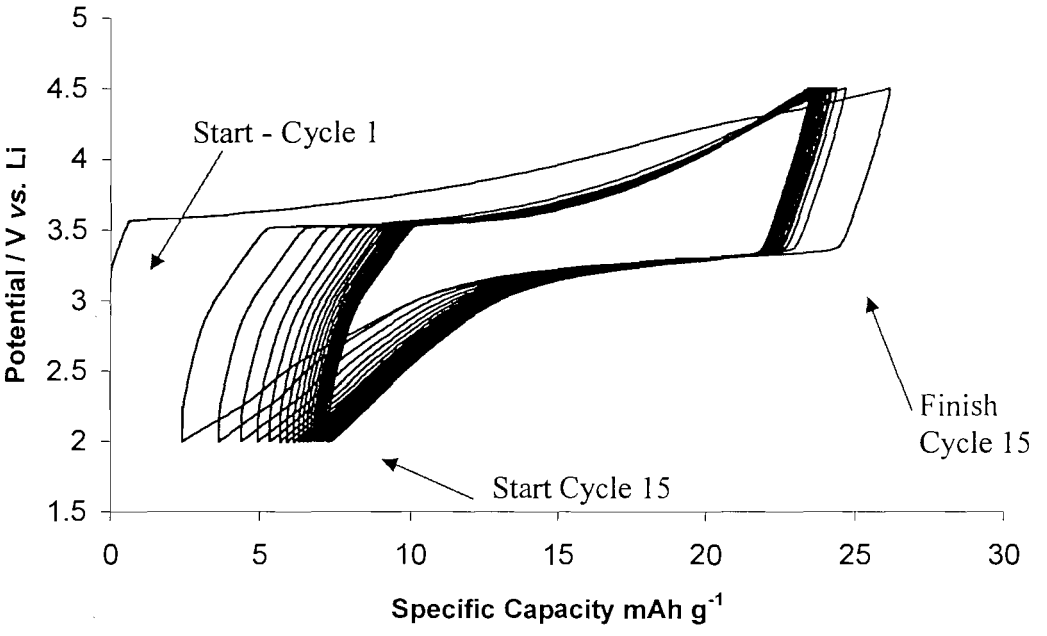

Figure 3.27 - Specific capacity *vs.* potential for $LiFePO_4$ prepared using a reducing carbon containing precursor, 700 °C, 0.22:1 carbon to iron ratio, in 0-grade argon.

3.3.6.2 Two Step Syntheses of $LiFePO_4$

The effect of the addition of a second impregnation of sucrose to the samples prepared using the solution synthesis route described in section 3.2.2.1, was to increase the specific capacity to within 90% of the theoretical value for $LiFePO_4$. Hence, a pure phase highly conductive material sufficient for good electrochemical performance can be prepared in a two-step process. From Figure 3.28, it can be indirectly deduced that the conductivity of the two-step material is higher than that of the material prepared using one-step method. This is because the two-step (2^{nd} sucrose impregnation) material exhibits higher specific capacity and reduced hysteresis on cycling. Whereas the samples prepared using the one-step method under identical synthesis conditions show lower capacities under the same cycling conditions. This suggest that the conventionally prepared electrode materials are not as conductive as those treated with a second sucrose impregnation. This route is highly conducive to a scale-up as it is a simple one-step calcination reaction in the first instance. The precursors are easily prepared using inexpensive solution based reagents and the preparation requires no grinding or processing step beyond a simple heating step to 70 °C and the calcination step at 700 °C. The additional step used to coat the particles with a second layer of carbon is required to make materials of high electrochemical performance. The materials prepared using the two step approach show similar performance to other $LiFePO_4$ materials prepared using more complex synthesis routes with many more processing steps [1, 3, 6, 7, 12].

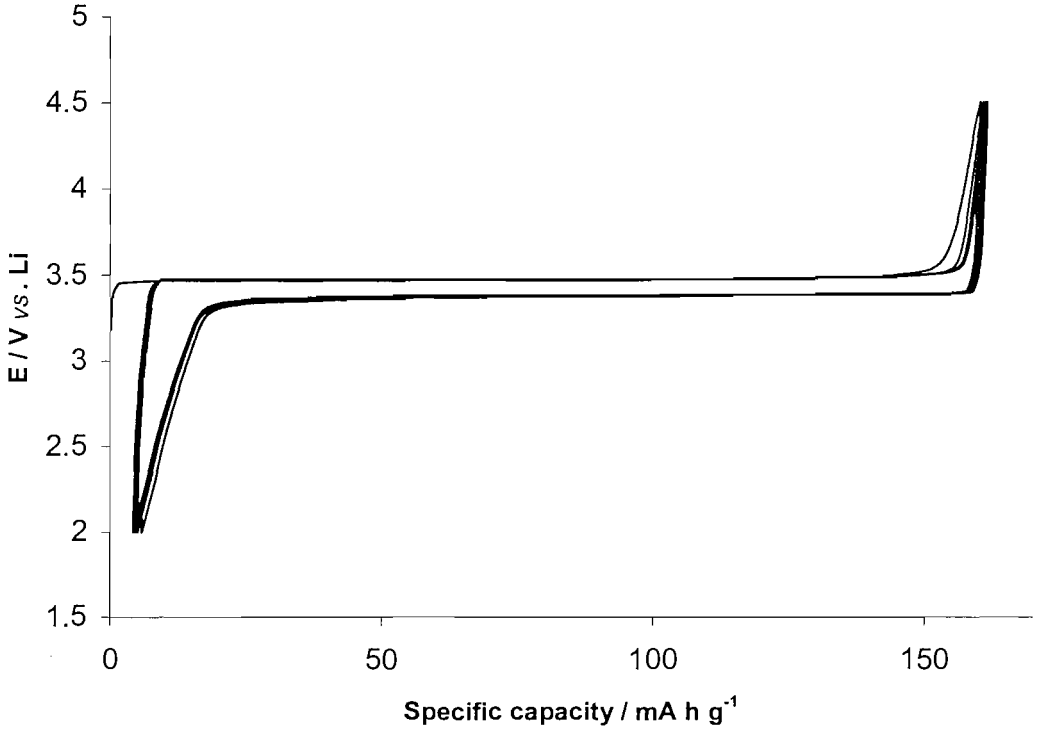

Figure 3.28 - Charge-discharge plots of $LiFePO_4$ material. Prepared at 700 °C using 0.22 moles of sucrose and second impregnation of 0.15 moles of sucrose to Fe.

It can be seen from Figure 3.28 that the electrochemical performance of the material that was subjected to a second carbon impregnation shows high specific capacity (~150 mA h g^{-1}) with little loss on cycling. There is little hysteresis observed indicating the lithium insertion/de-insertion reactions occur over a narrow potential window and are invariant during the cycling. It should be noted that the capacity of the first charge is higher than any subsequent cycles by approximately 5 mAh g^{-1}. This can be attributed to the irreversible capacity associated with parasitic side reaction within the electrolyte and non-redox active species adsorbed on the electrodes. It should be noted that the irreversible capacity on the first charge is much lower for the electrode treated with the second coating of carbon than the single step prepared materials. An explanation for this may be that the irreversible capacity may result from the oxidation of adsorbed species on the carbon remaining from the

pyrolyis of the sucrose. These adsorbed species could be C-H or C-OH groups. As the two-step prepared material had been heated twice, most of these groups may have been removed resulting in a lower irreversible capacity. Whereas the material that was heated once contained a larger amount of these groups and hence had a larger amount of irreversible capacity on the first charge.

3.4 Conclusion

A solution synthesis route has been developed for the preparation of $LiFePO_4$ utilising a novel sucrose solution precursor technique. The materials prepared at 700 °C showed high crystallinity when characterised using X-ray diffraction. Lower temperature samples showed some evidence of crystal phase formation as low as 400 °C. The synthesis technique was optimised for the amount of sucrose required to obtain phase pure, high purity materials with a low amount of residual carbon. It was found that the optimum performance and material properties occurred in samples containing a 0.25 ratio of sucrose to iron in the precursor.

Bulk samples of $LiFePO_4$ materials were prepared using a one-step synthesis technique. These materials were tested using galvaostatic cycling and it was found that high temperature samples (700 °C) achieved specific capacities between 100 and 115 mA h g^{-1}. Additional electrochemical tests were performed on samples that contained a second carbon impregnation using an additional 0.15 moles of sucrose. It was found that these materials had superior electrochemical properties than those with only a single carbon coating, giving 90 % of theoretical capacity at the C/7 rate (165 mA h g^{-1}). It is possible that the addition of the second sucrose impregnation results in the pyrolysis of carbon on the surface of the active material particles increasing their electronic conductivity and thus results in an increase in specific capacity.

It is clear that the presence of the sucrose in the precursor materials facilitates the formation of a homogeneous matrix. In this case all reagents were present in the required stoichiometry to form the pure phase material. Additional evidence for this effect comes from the XRD and EDX mapping studies, which indicate that the non-sucrose containing samples are in-homogeneous on the molecular diffusion scale. Such a sample would, therefore, require elevated temperatures for synthesis and may also require additional processing steps, such as regrinding and calcination.

The development of the new low temperature solution synthesis route for $LiFePO_4$ enables the study of this and related materials using high-throughput techniques. The benefit of using this solution technique is that composition spreads of

electrode materials can be prepared using existing combinatorial preparation methods utilising automated liquid handling techniques. This new method of synthesis will be coupled with the high-throughput techniques described in chapter two to enable the preparation of arrays of varying electrode composition to be studied.

3.4.1 Further Work.

After the successful preparation of $LiFePO_4$ using the solution preparation method, the technique was used to prepare some substituted materials such as $LiFe_{0.3}Ni_{0.35}Co_{0.5}PO_4$ (and other ternary mixed metal phosphates) and some other olivines such as $LiCoPO_4$, $LiNiPO_4$, however the characterisation of these materials was limited only to XRD. Additional work in this area could involve a detailed study of these materials by electrochemically testing many compositions using the conventional technique.

3.5 References

1. Padhi, A.K., Nanjundaswamy, K.S., and Goodenough, J.B., *Journal of the Electrochemical Society*, 1997, **144**, (4), p. 1188-1194.
2. Chung, S.Y., Bloking, J.T., and Chiang, Y.M., *Nature Materials*, 2002, **1**, (2), p. 123-128.
3. Franger, S., Le Cras, F., Bourbon, C., and Rouault, H., *Electrochemical and Solid State Letters*, 2002, **5**, (10), p. A231-A233.
4. Weller, M.T., *Inorganic Materials Chemistry*. 1994, Oxford: OUP. 13.
5. Yang, S.F., Song, Y.N., Zavalij, P.Y., and Whittingham, M.S., *Electrochemistry Communications*, 2002, **4**, (3), p. 239-244.
6. Andersson, A.S., Thomas, J.O., Kalska, B., and Haggstrom, L., *Electrochemical and Solid State Letters*, 2000, **3**, (2), p. 66-68.
7. Huang, H., Yin, S.C., and Nazar, L.F., *Electrochemical and Solid State Letters*, 2001, **4**, (10), p. A170-A172.
8. Takahashi, M., Tobishima, S., Takei, K., and Sakurai, Y., *Journal of Power Sources*, 2001, **97-8**, p. 508-511.
9. Yamada, A., Kudo, Y., and Liu, K.Y., *Journal of the Electrochemical Society*, 2001, **148**, (7), p. A747-A754.
10. Chen, Z.H. and Dahn, J.R., *Journal of the Electrochemical Society*, 2002, **149**, (9), p. A1184-A1189.
11. Doeff, M.M., Hu, Y.Q., McLarnon, F., and Kostecki, R., *Electrochemical and Solid State Letters*, 2003, **6**, (10), p. A207-A209.
12. Prosini, P.P., Carewska, M., Scaccia, S., Wisniewski, P., Passerini, S., and Pasquali, M., *Journal of the Electrochemical Society*, 2002, **149**, (7), p. A886-A890.

Chapter 4:
Combinatorial Screening of $LiMPO_4$ Compounds

The work presented in this chapter is effectively the fusion of the two previous chapters. It is focused on the attempts to expand the combinatorial technique into the area of battery material synthesis and screening. This was undertaken using the robot liquid handling techniques outlined in chapter two and the solution chemistry for $LiFePO_4$ synthesis that was outlined in chapter three. The aim of chapter four is to demonstrate how these two techniques have allowed compositionally diverse electrode materials to be synthesised and screened, using novel high-throughput methods.

4.1 Background and Objectives

In chapter three, it was outlined that a new one-step synthesis route to yield high purity $LiFePO_4$ material was achieved and could be adapted for use in combinatorial screening. The aim of the work presented in this chapter is to prepare and screen compounds of varying composition based on $LiFePO_4$. For example, materials such as $LiMnPO_4$ or $LiCoPO_4$ are known to have different electrochemical properties to those of $LiFePO_4$. For example, $LiCoPO_4$ shows lithium extraction at 4.8 V *vs.* Li [1].

A comprehensive study of the variation in composition between $LiFePO_4$ and $LiMnPO_4$ end members could be undertaken, which could give rise to some new useful, optimised materials. The ability to study compositional variations in multi-component systems is one of the great strengths of combinatorial materials science and the study of arrays composed of three or more components is now commonplace in composition spreads produced by *RF* sputtering [2]. Solution and sol-gel methods have been proved as very versatile methods in the preparation of materials from ceramics to battery materials [3]. These approaches have been commonly used to prepare pure materials [4] and solid solutions [5] and are ideal methods for use with high-throughput synthesis techniques, as the variations in composition can be easily achieved by adding different amounts of transition metal salts in the solution phase, metered using commercially available robot systems.

It has been demonstrated that substitution of transition metals leads an amalgam of material properties. An example of this is addition of Mn to Fe sites in to the olivine phase of $LiFePO_4$ leads to an increase of the redox potential for the M^{3+}/M^{2+} couple from 3.4 to 4.1 V *vs.* Li, allowing the maximum energy density to be achieved from

high voltage materials. It has also been demonstrated that the addition of Mn into $LiMPO_4$ type structures can increase the width of the 4 V redox plateaux, but also leads to a decrease in the total capacity [6].

The idea that doping battery materials can improve their physical properties has recently been considered for $LiFePO_4$ in work reported by Chaing and co-workers at MIT [7]. It has been suggested that doping of a small amount of zirconium on the lithium sites in olivine phase materials can increase the electronic conductivity of these materials by 10^8 S cm^{-1}. However, other groups did not confirm this effect until recently, and the explanation for the increase in conductivity observed in their samples was attributed to carbon residues from the alkoxide precursors used in the synthesis. The work of Herle *et al.* [8] is so far been the only published confirmation of this effect. However, it is suggested in this paper that the increase in conductivity can be attributed to the formation of contaminant metal phosphide phases coating the particles of $LiFePO_4$. The uncertainty in the results obtained by Chaing *et. al* prompted the study of these materials using the combinatorial technique. In addition to doping on the lithium sites, the combinatorial synthesis technique allows the preparation of many compositions of solid solutions of $LiFePO_4$ materials in which other transition metals can be substituted for iron, giving materials of the general formula, $LiFe_{1-x-y}Co_xNi_yPO_4$. Such a study was undertaken and sixty-three different compositions were prepared based on the above formula.

There have been many studies reported in the literature of the synthesis of two and even three component mixed metal oxides [9-11]. However in order to conduct a detailed systematic study of a three component mixed metal oxide, a combinatorial approach to synthesis should be undertaken. Recent developments in the area of lithium batteries have yielded potential new multi-component materials based on solid solutions of transition metal containing oxides and phosphates. An example is $LiNi_{0.82}Co_{0.18}O_2$ [12] in which nickel is included to reduce the cost of materials by reducing the amount of the more expensive cobalt while still retaining favourable capacity, voltage and rate capability offered by $LiCoO_2$. These materials have been commercialised by *Sanyo* and *Mitsubishi* [13] to provide improvements in terms of cost and capacity over that of

$LiCoO_2$. However, an increase in capacity results in a decrease in stability and thus, a compromise is reached due to the inclusion of nickel in the structure.

The importance of a one-step synthesis route to the preparation of materials for screening is paramount, as any regrinding or manipulation of the material itself during synthesis would result in possible damage to the films and complicate the screening process. For example the calculation of the active mass deposited on each electrode. It is also advantageous to prepare materials using a one-step short calcination step to increase the number of samples that can be screened using the high-throughput method.

The objectives of the fourth chapter are to link together the work undertaken in chapters two and three and use the combinatorial method to prepare and screen some novel material compositions. This will be a process of method optimisation and required the design and evaluation on new equipment, especially in terms of array preparation for X-ray diffraction and microscopy characterisation.

In addition, the objectives of chapter three are outlined below:

- To develop methodology and the infrastructure to enable the rapid preparation and screening of lithium battery materials prepared using solution based synthesis routes and to develop high-throughput methodologies for SEM/EDX and X-ray diffraction.

- The study of compositional variations of arrays based on $LiFePO_4$, substituting for Fe using other transition metals such as Mn, Co, Ni, and Mo.

- Substitution of $LiFePO_4$ using dopant species such as Zr, Nb, which have been reported to increase the conductivity of $LiFePO_4$ by eight orders of magnitude. The combinatorial technique can be use to separate the effects of two variables which may independently affect the conductivity of the samples.

4.2 Experimental

Electrode arrays were prepared using robotic liquid handling techniques outlined in chapter two. The arrays were prepared using automated liquid handling techniques from solution precursors and were calcined prior to screening. Arrays of varying composition and structure were prepared and screened using high-throughput electrochemical testing, XRD and SEM techniques.

4.2.1 Array Synthesis

Arrays of $LiMPO_4$ type materials were prepared using a similar automated method described in chapter two. The precursors used for the synthesis of these electrode materials were in the form of transition metal nitrates and acetates; these were used as they readily decompose to form NO_2 and CO_2 on heating leaving only the metal oxides in the precursor. The precursor materials used in the synthesis were $Fe(NO_3)_3$, $LiCH_3CO_2$, $Co(NO_3)_2$, $Ni(NO_3)_2$, H_3PO_4 and sucrose. In the doping experiments, $ZrO(NO_3)_2$ was used as the inorganic source of zirconium.

The solid precursors were dissolved in water to form precursor solutions of concentration 1.25 to 2.5 M. The concentrations are outlined in Table 4.1.

Table 4.1 - Concentration of solution precursors used in automated synthesis.

Solid Precursor	Concentration (mol dm^{-3})
$Fe(NO_3)_3$	1.25
$LiCH_3CO_2$	2.5
$Co(NO_3)_2$	1.25
$Ni(NO_3)_2$	1.25
H_3PO_4	85 wt. % in H_2O
$Zr(NO_3)$	2.5
Sucrose	1.0

In the synthesis of multi-component solid solutions such as $LiMn_xFe_yCo_zPO_4$, the total number of moles of transition metal M is equal to 1 per formula unit. The composition of the materials must take account of this and hence values of x, y and z must satisfy the equation $x + y + z = 1$, if the above synthesis is to be successful and lead to the formation of pure phase material. There is, therefore, a limit to the number of possible compositions, as the stoichimentry must be maintained.

In the case of transition metal doped $Li_{1-4x}M_xFePO_4$, the lithium is substituted by zirconium, niobium and other transition metals and should occur at the lithium sites. Using several precursors, samples of widely differing composition can be prepared on a single array. The direct synthesis of the $LiMPO_4$ arrays is outlined in Figure 4.1 and the experimental method is described below.

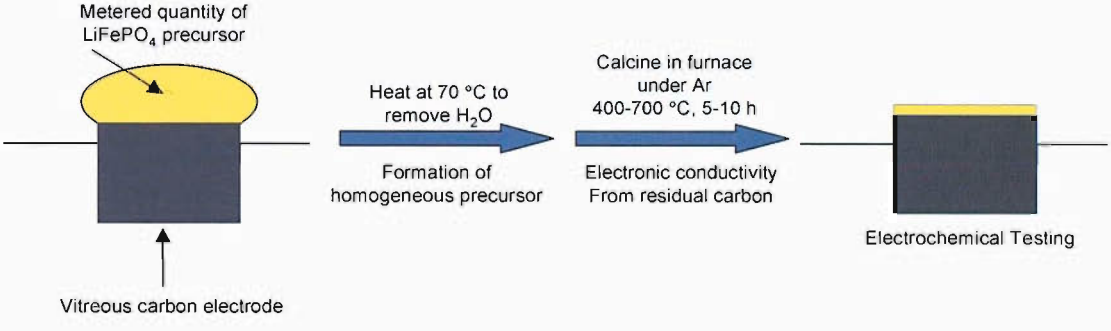

Figure 4.1 - Combinatorial one step synthesis of $LiMPO_4$ materials.

The precursor solutions were placed in 100 mL beakers on the deck of the robot, in set positions as required by the software. During the preparation, 64 stock solutions of varying composition were prepared in 2 mL capacity polypropylene sample vials using the precursors in differing amounts listed in an *Excel* spreadsheet. Examples of $LiFe_{1-x}Ni_xPO_4$ and $LiFe_{1-x}Co_{1-x}PO_4$ are shown in Figure 4.2 A and B respectfully. These values were calculated prior to preparation from the required ratios of the transition metals, the amount of dopant required and the amount of sucrose required. The sucrose

was added to facilitate the formation of a homogeneous glass and to provide additional conductivity additive.

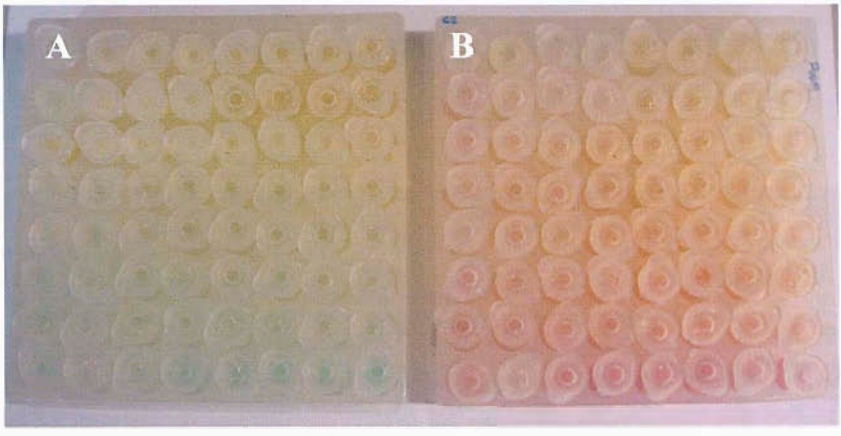

Figure 4.2 - Precursor solutions of A - $LiNi_xFe_{1-x}PO_4$, B - $LiCo_xFe_{1-x}PO_4$.

Typically a total of 500-1500 μL of solution was transferred to the vials; the preparation of the array of stock solutions took approximately 10-30 minutes depending on the number of precursors to be added and the number of steps in the preparation. After preparation, the vials were capped and the samples were homogenised by rotating the samples by hand, whilst in the array holder (combi-rack). In the synthesis of $LiFe_xMn_yCo_zPO_4$, it was found that the concentration of different transition metal salts was too high and some salts precipitated. Further, the addition of (~ 5 m moles) of nitric acid was enough to achieve the pH required to fully dissolve these salts in all sample solutions. The addition of nitric acid does not affect the overall stoichometry of the precursors, as during drying it decomposes to form NO_2. The arrays of stock solutions form libraries that can be kept sealed indefinitely and re-characterised at a later time, as only a few μL are required to perform electrochemical testing and X-Ray diffraction experiments.

Once the array stock solutions were prepared a small amount of each solution (1 - 10 μL) was transferred to the sample positions on the characterisation arrays. These were designed for electrochemical testing, XRD and SEM. The electrochemical testing

array is a 75x75 mm Macor® (machinable glass ceramic) array with 64 electrode positions into which fit 3 mm diameter by 6 mm long vitreous carbon rod electrodes (see Figure 4.3). This array is capable of being heated to over 1000 °C in argon and ~ 500 °C in air (the lower temperature is due to the oxidation of the carbon rod in air at temperatures exceeding 500 °C).

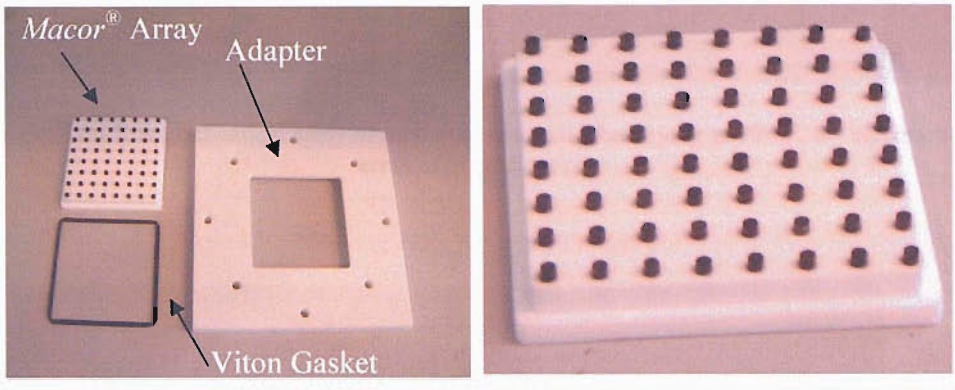

Figure 4.3 - Macor®/vitreous carbon electrochemical screening array.

The materials were deposited from the stock sample vials on to the electrode surface where they were dried in an oven at 70 °C. This produced a film of electrode precursor (see Figure 4.4). Once the material had dried on the electrode, additional deposition steps were undertaken (~ 5 μL), allowing thicker electrode films to be produced. Once the desired dry precursor film had been obtained, the Macor® array was transferred to a large bore (80 mm diameter) tube furnace (see Figure 4.5).

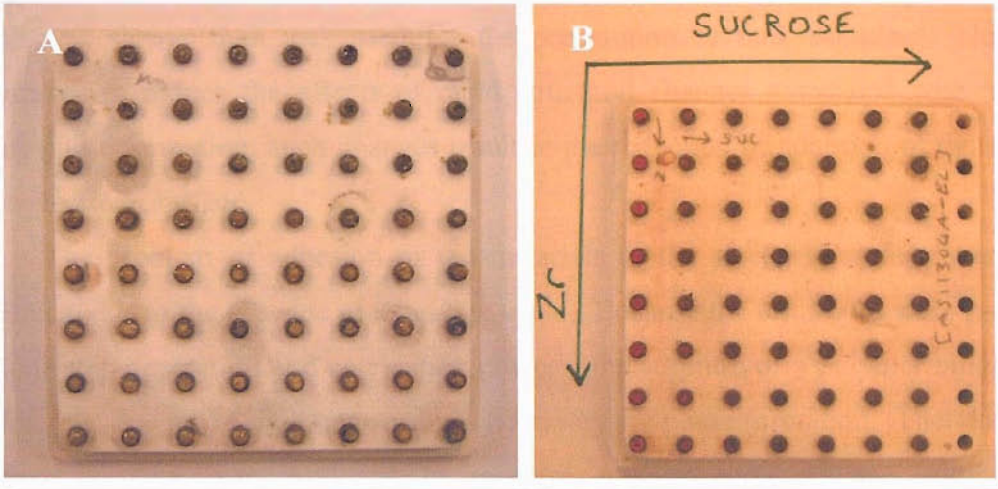

Figure 4.4 - A - Electrochemical array of precursor material after drying at 70 °C, B - electrochemical array after calcination.

Figure 4.5 - 80 mm large bore tube furnace for combinatorial synthesis.

During the calcination step, the array could be heated up to 500 °C in air, and at over 1000 °C under inert or reducing gas. The furnace uniform hot zone has the capacity for the heat treatment of up to three different arrays simultaneously under the same thermal conditions.

Typically the arrays were heated for 1-5 hours, this is less than in the bulk synthesis of $LiFePO_4$ samples, but is adequate since the amount of material to be synthesised is small (~0.1 mg per sample). A heating rate of 2 °C min^{-1} was used,

which was slower than was used for the preparation of bulk samples. This was undertaken to reduce the effects of rapid structural changes associated with heating during phase formation; such changes result in the reduction of adhesion of the sample to the electrode surface.

The problem of adhesion of the materials to the electrode surface was more significant due to the absence of a binding agent. Because the electrodes were prepared in a one step deposition and calcination process, the addition of a polymer binder was not feasible, due to the high temperatures necessary for phase formation. Therefore, the electrode surface was modified to increase the adhesion by the addition of hemispherical wells on the surface to act as containers for the materials. These wells were ground into the carbon rod using a *Black and Decker Wizard* grinding tool, and were typically ~ 2 mm in diameter. The solution was then dried into these wells and remained within them after calcination, with little movement of the material away from the electrode surface.

4.2.2 Electrochemical Screening

The *Macor®*/vitreous carbon electrochemical testing array was designed to fit into the standard electrochemical cell design, by aid of an adaptor to hold the synthesis array in place on the larger cell (see Figure 4.3). The electrochemical screening of the $LiMPO_4$ arrays was carried out using similar methods that were used for the screening of $LiMn_2O_4$/C/PVDF composites, in that the electrochemical techniques were essentially the same. Slow scan cyclic voltammetry was used to charge and discharge the electrodes at sweep rates between 0.01 and 1 mV s^{-1} and the potential sweep was provided by a single channel of the VMP multichannel potentiostat. The array was connected to a 63-channel current follower unit by which the currents for each channel were measured and the data was recorded using an in-house data-logging program. The current limits were set differently to those for the $LiMn_2O_4$/C/PVDF experiments, as the redox potential of the insertion reaction for $LiFePO_4$ occured at 3.5 V *vs.* Li. However, it would be expected that a shift in potential towards 4 V *vs.* Li could occur therefore the voltage limits were set between 3 and 4.5 V *vs.* Li. The data were treated using an

in-house designed analysis program '*The Analyser*', which can be used to rapidly identify the active samples, and look in detail at the electrochemical behaviour of the samples.

4.2.2.1 Calculation of Electrode Mass

The mass of each of the electrodes was calculated from the volume of the material that was deposited on the electrode. The number of moles of each component added was known prior to sample preparation and was used to calculate the volume of each material added to each sample well. Hence, the electrode mass was calculated to enable the calculation of specific capacity values. The mass of the electrodes was calculated using the following equations:

Number of moles of iron nitrate = number of moles of $LiFePO_4$

$$n_{LiFePO4} = C_{Fe(NO3)3} \times V_{Fe(NO3)3} \qquad \textbf{Equation 4.1}$$

So there are $n_{LiFePO4}$ moles in the total precursor sample volume V_{Prec}.
And the volume added to the electrode is V_{El}.

On each electrode there are n_{el} moles of material:

$$n_{el} = \frac{n_{LiFePO4}}{V_{Prec}} \times V_{El} \qquad \textbf{Equation 4.2}$$

The mass of $LiFePO_4$ on the electrode (m_{el}) can then be calculated from,

$$m_{el} = n_{el} \times 157 \qquad \textbf{Equation 4.3}$$

4.2.3 Optimisation of XRD and SEM Array Deposition Techniques

During this work much effort was directed at the development of the optimal deposition technique to prepare XRD and SEM arrays. It was found early in the project that a suitable inexpensive and disposable (one-use) substrate should be used to prepare libraries of materials that could be kept and re-characterised if necessary.

The preparation of an XRD or SEM array is similar in technique to the preparation of the electrochemical array. It differs in that the deposition is undertaken on a non-conducting substrate, such as an alumina tile or silica glass. In the early experiments, the arrays were prepared on silica glass of 150x150 mm, using $LiNi_xCo_{1-x}O_2$ as the material of study. This was used, as it could be easily prepared in air in a box furnace. This experiment was carried out prior to the arrival of a furnace of sufficient diameter to hold a 75x75 mm array within an inert atmosphere. The material was deposited on the surface of the silica glass as small spots containing 10 μL of solution. At this stage, no attempt was made to confine the spots using pre-cut wells or other methods. After deposition the array was placed in an oven at 70 °C to remove the water content and then transferred to the furnace in which it was heated to 500 °C. The result was the array shown below in Figure 4.6.

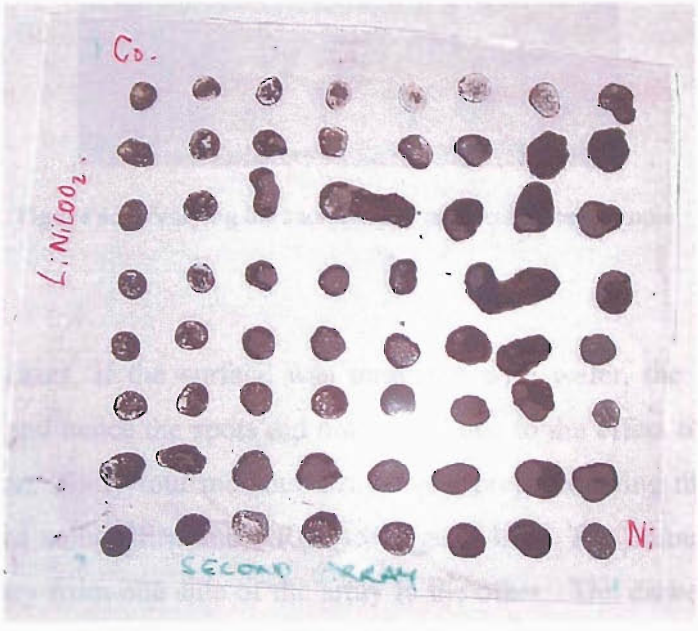

Figure 4.6 - $LiNi_xCo_{1-x}O_2$ array prepared on a silica glass substrate.

It was found that most spots tended to spread due to the breaking of surface tension and formed non-uniform films of ~ 0.01 mm in thickness. It was also evident that some of the spots merged with some closest neighbours leading to uncertain stoichiometeries in those samples. However, regardless of these difficulties, it was possible to obtain X-ray diffraction data for all samples in the array (see section 4.2.4).

The preparation of arrays based on composition spreads of $LiFePO_4$ type materials presented a more difficult challenge. These materials must be prepared at 700 °C in an inert atmosphere to obtain high capacity materials. Therefore, it was necessary to use a more thermally resistant material. Alumina tile was chosen, as it is inexpensive and can be heated to temperatures in excess of 1000 °C. Test samples were prepared using small pieces of alumina and between 0-10 μL of solution. 10 μL spots of different composition (sucrose loading) were placed on these sheets of approximately 100 x 20 mm. These were then placed in a 30 mm diameter tube furnace for heat treatment (see Figure 4.7).

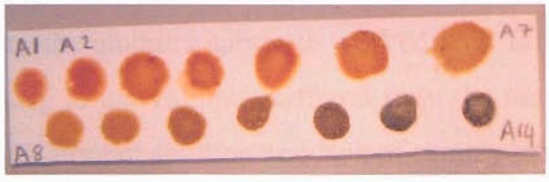

Figure 4.7 - Varying the sucrose ratio in precursor test sample.

In some cases, if the surface was untreated with water, the surface behaved hydrophobically and hence the spots did not spread due to the effect of the breaking of the surface tension. Sixty-four member arrays were prepared using this technique and were characterised using SEM and XRD (see Figure 4.8). The colour of the samples can be seen to vary from one side of the array to the other. The darker grey and black samples in the lower left are possibly due to the formation of iron (II) containing compounds, whereas the red and orange appearance of samples can be attributed to the formation of iron (III).

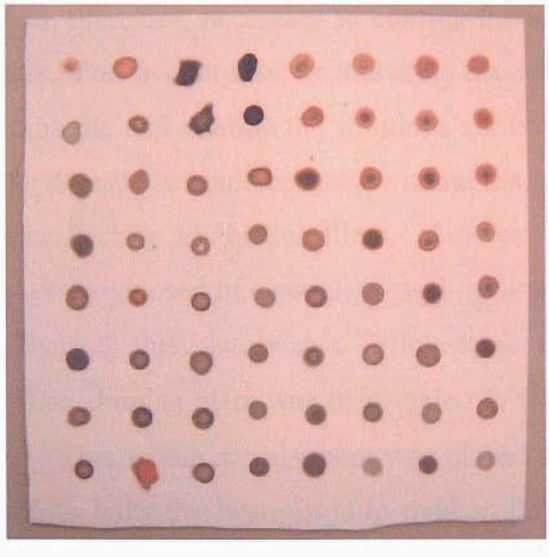

Figure 4.8 - $LiNi_xCo_{1-x}PO_4$ array prepared on alumina tile.

Deposition onto the alumina substrate worked well for small sample volumes, but arrays prepared using larger volumes suffered from the samples spreading into one another due to the larger amount solution and lack of sample confinement. It was found that after washing the surface of the array with water and then drying it the spots were more likely spread into one another. This made it difficult to reuse the alumina tiles to repeat an unsuccessful deposition. Therefore, the effect of adding a surfactant was investigated. Arrays with the surface treated using *Trition-X* surfactant were prepared. However this did not provide any benefit in terms of sample confinement. Moreover, successful arrays were prepared and tested using this technique and were screened using EDX, SEM and XRD. However, to keep the samples form merging in to one another, a very small amount (< 3 μL) of material was used. This led to difficulties in characterisation due to the presence of a high alumina background, and thus, XRD and EDX data suffered from a low signal to noise ratio, leading to inaccurate data. In addition, the iron containing samples suffered from fluorescence effects when studied by XRD, and hence, the overall intensity for the pattern was reduced further.

Increasing the sample thickness can alleviate the effect of low signal to noise ratio (both fluorescence and diffraction intensity are proportional to the amount of exposed sample). It was, therefore, necessary to confine the samples in wells or vials during the drying process. For this purpose, an 8x8 array deposition mask was designed to clamp over the alumina tile and confine the solutions above the sample positions on the tile. In this way, the deposition could proceed without the spreading of the samples and drying could occur, leading to thicker films. Figures 4.9 and 4.10 show the deposition array. This was composed of a stainless steel mask with 64 sample positions drilled into the plate. Beneath this plate was a Teflon mask, designed to confine the sample on to the tile. The alumina plate was then sealed to the Teflon® mask using a small amount of grease. This whole arrangement was placed on a stainless steel base plate, which contained four bolts that were used to tighten the array once the alumina substrate was inserted. After deposition and drying, the nuts were removed and the alumina tile, with its deposited samples was placed in the furnace.

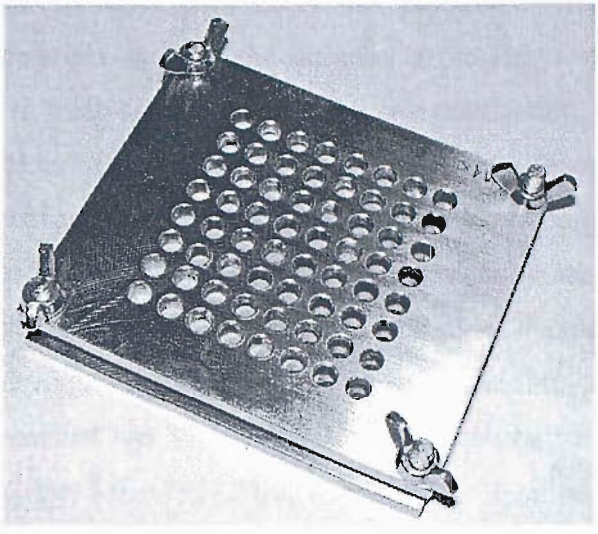

Figure 4.9 - Stainless steel deposition array.

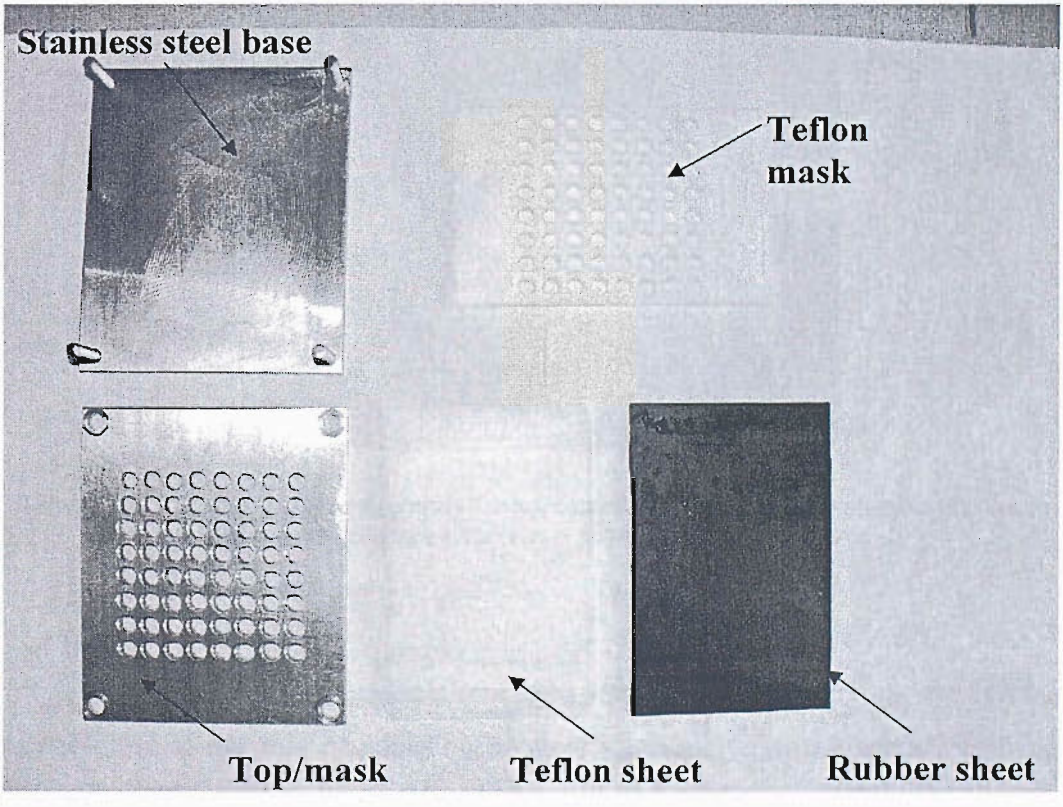

Figure 4.10 - Components of the stainless steel deposition array.

The use of the stainless steel array has produced mixed results. When depositing $LiFePO_4$ materials, most of the samples in the arrays were deposited with little problem leading to thick samples, useful for characterisation. However, in some cases (usually on the order of two or three samples per array), the samples stuck to the Teflon mask. This is not unexpected because the samples formed during heating often contained voids due to gas evolution leading to a low-density sticky material, which easily remained attached to the Teflon/grease. In the case of precursors that did not evolve gases while drying, the method worked well yielding arrays of precursor samples uniformly deposited and immobilised on the alumina tile (see Figure 4.11). This was found for arrays of $LiCo_xMn_{1-x}O_2$, prepared by a sol-gel process.

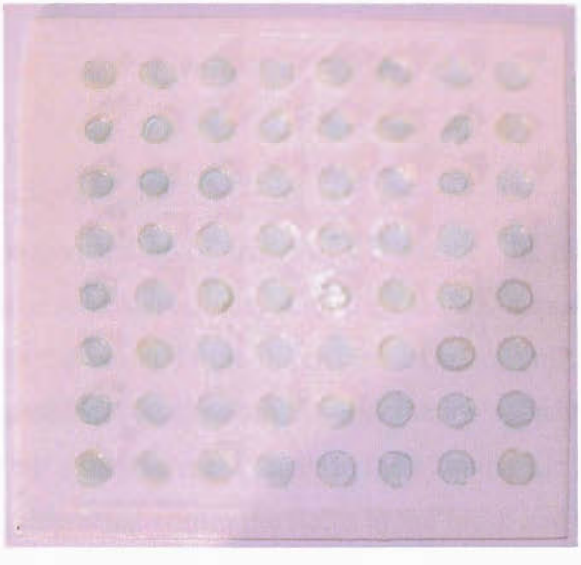

Figure 4.11 - $LiMn_xCo_{1-x}O_2$ array prepared using a stainless steel mask on an alumina tile, the array shows sol-gel prepared precursor material prior to calcination.

Even though most materials remained immobilised after drying, the calcination step resulted in the loss of adhesion of most materials from the surface causing the mixing of samples and loss of uniformity on the array (see Figure 4.12).

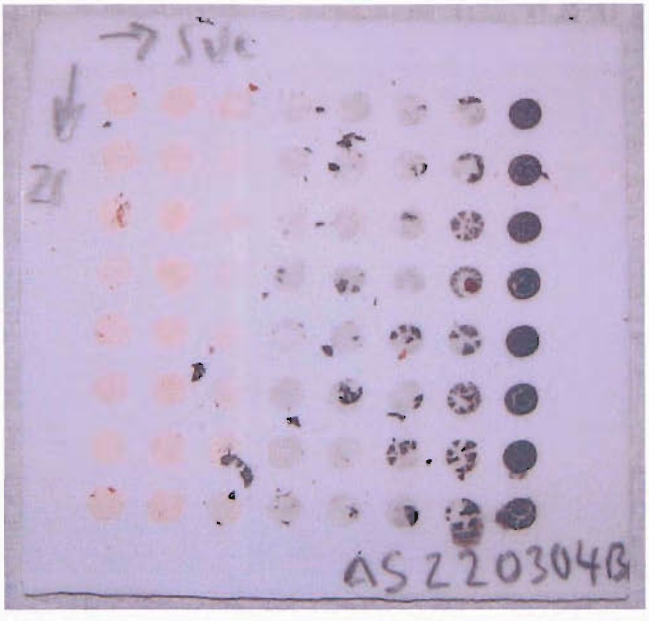

Figure 4.12 - An array prepared on an alumina tile after calcination. Resultant loss in adhesion has led to dislocation of samples

A technique using an adhesive mask was developed and used successfully by Lewis *et. al* [14] in the preparation of arrays of CO sensors. A number of these masks were obtained and tested for compatibility with the $LiMPO_4$ deposition method. It was found that these masks did result in the deposition of more uniform and thicker film; however, the sample problem of adhesion after calcination remained (see Figure 4.13). Figure 4.13 A shows the adhesive mask stuck to the alumina tile before removal. The sample solutions were deposited within the holes in the mask and then dried in an oven at 70 °C for 20 minutes. Figure 4.13 B shows adhesive mask in the process of being peeled off from the surface of the alumina tile leaving the dried precursor samples in place. Figure 4.13 C shows the alumina tile after the mask has been removed and Figure 4.13 D shows the alumina tile and samples after calcination at 700 °C in argon.

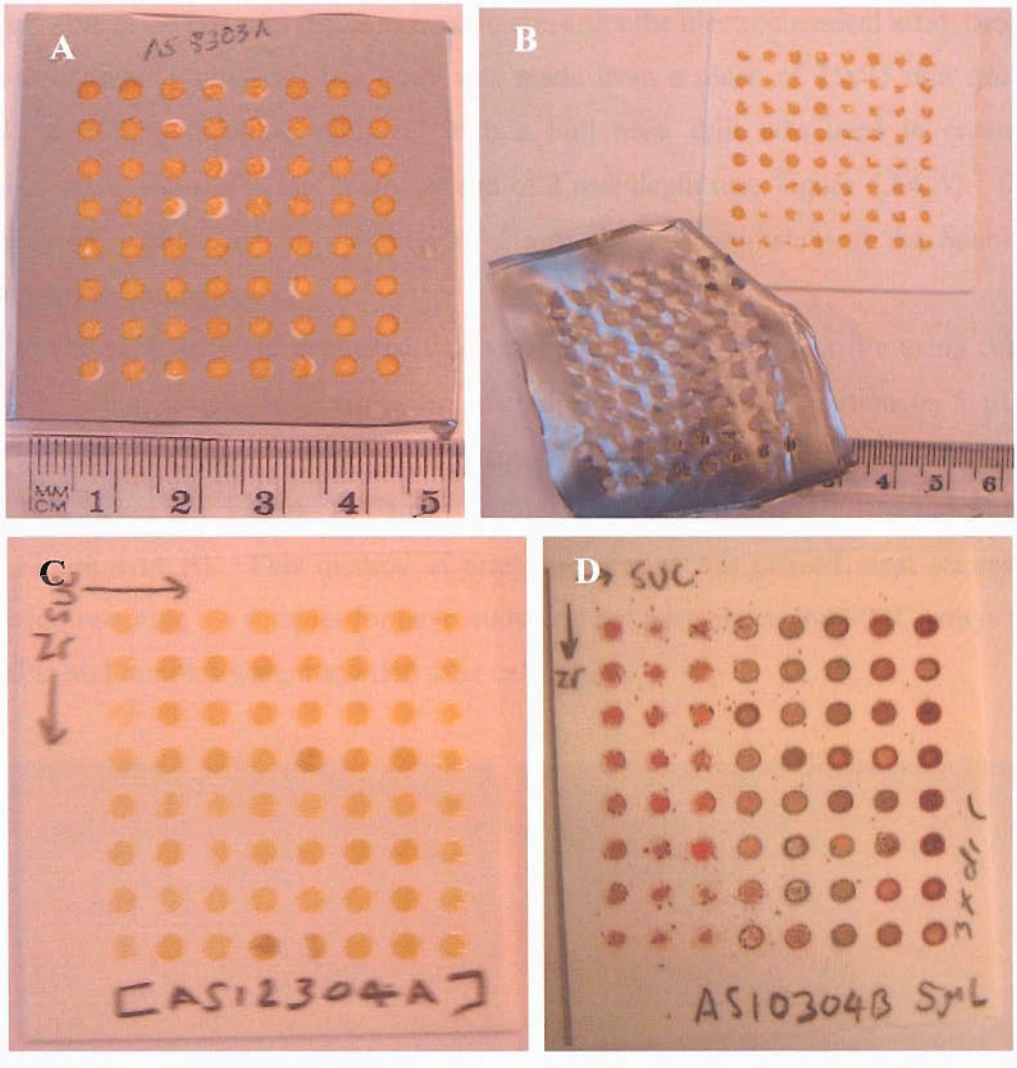

Figure 4.13 - Preparation of arrays using an adhesive mask to confine samples. A - Tile before mask removal, B- removal of the mask, C - an example of samples after the mask removal, D - an example of an array after calcinations shown loss of sample adhesion.

It was recognised that a method of confining the solutions and films must be built into the array itself. This presented problems in that the wells would need to be drilled into each new array. If these wells were to be one-use, the labour and costs involved would be too large. MGC or *Macor*® is the only ceramic material that can be easily manipulated using standard milling techniques and also tolerate the high temperature of the synthesis.

It was decided to design a re-usable array for XRD and SEM testing made from *Macor*®, the same material that was used to construct the electrochemical array used for high-throughput synthesis. The array was made from a piece of 75x75 mm *Macor*® block; a milling machine equipped with a bull nose drill was used to create 64 hemispherical wells of 4 mm diameter and of 2 mm depth (see Figure 4.14 A). These arrays were constructed by members of the mechanical workshop at the School of Chemistry in Southampton.

The samples were deposited in a similar way, as on alumina tile using robotic liquid handling techniques. However, after drying a second deposition (~ 5 μL) of solution was undertaken to increase the sample thickness to the height of the well and was undertaken to ensure a flatter visible surface for X-ray diffraction testing (see Figure 4.14 B). This method of array preparation has proved most successful; however, retaining the samples for later study was not possible, as the MGC arrays were reusable and samples were discarded after calcination.

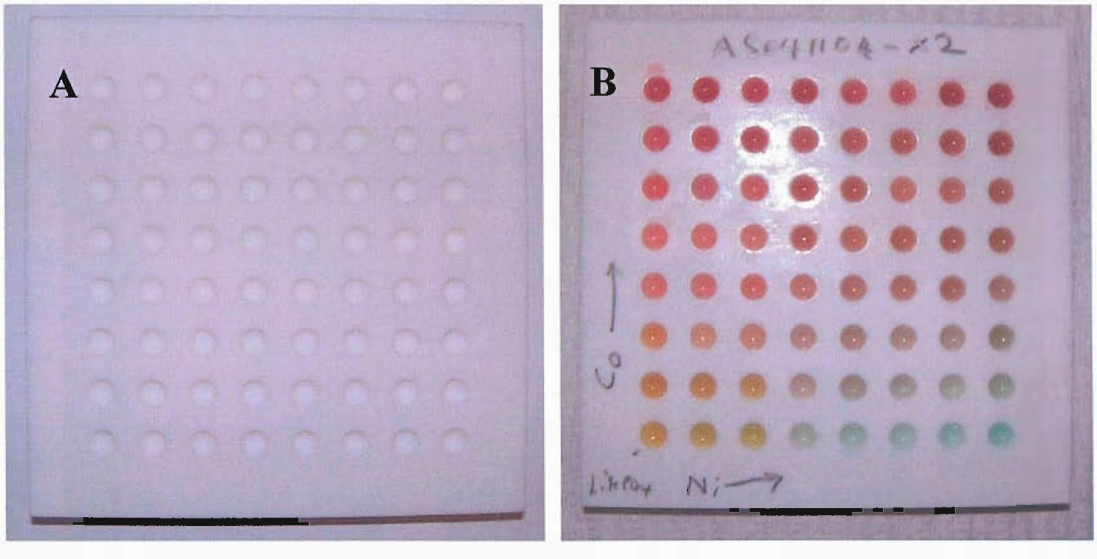

Figure 4.14 – A - Macor® array used for X-ray diffraction and SEM studies; B - composition spread of $LiFe_{1-x-y}Co_xNi_yPO_4$ solution precursors prepared on the Macor® array.

4.2.4 *X-Ray Diffraction of $LiMXO_4$ Arrays*

High throughput XRD methods were applied to the electrochemical materials prepared using the above method. XRD patterns were obtained for materials on a variety of substrates, alumina, silica glass and *Macor*® using a *Bruker AXS C2* diffractometer using Cu Kα radiation. The experimental set-up is detailed in Figure 4.15.

The *C2* is designed for the study of composition-spread arrays, as it has a movable *x*, *y*, *z* stage, enabling the X-ray source to be moved sequentially around the array and hence screen all samples. The *C2* is equipped with a *GADDS* detector that is capable of collecting data on the intensities of all angles of 2θ simultaneously. This enables samples to be screened in rapidly, and hence, a pattern can be obtained in 60-120 s for each sample.

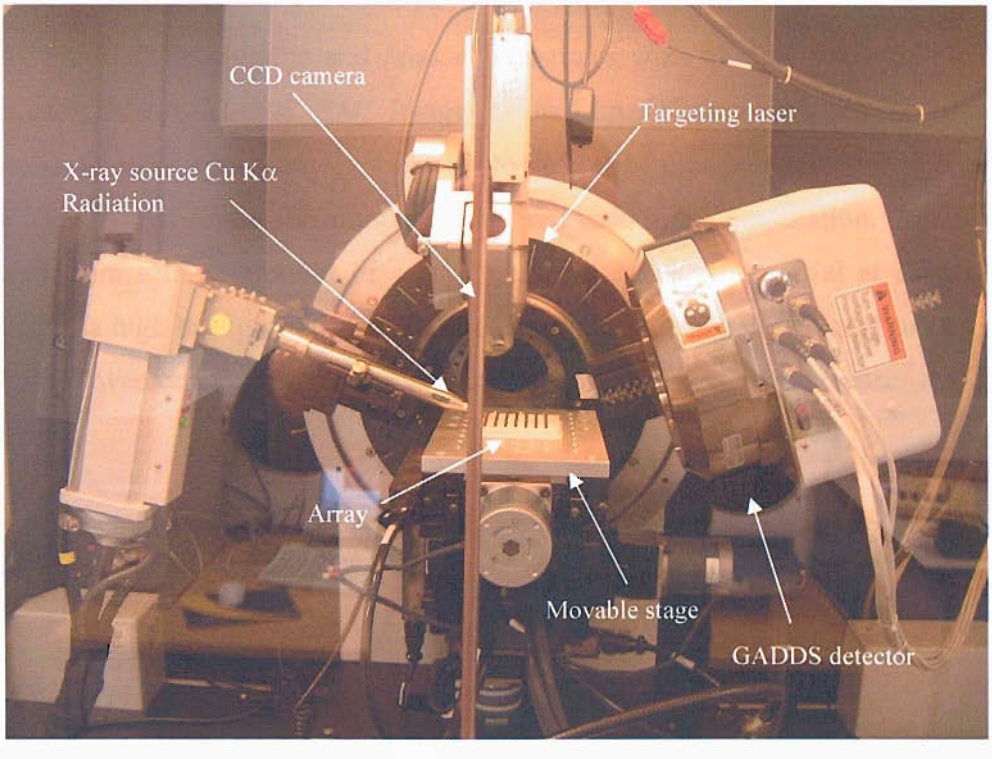

Figure 4.15 - High-throughput X-ray diffractometer.

The arrays are placed in the centre of the diffractometer moveable stage and values for the end member distances of x and y are programmed into the software manually. The program then calculates the distance between each sample and the distance it needs to move the stage to reach the first sample. The height of the sample stage is important in that it needs to be uniform for each sample if the patterns are to be compared objectively. The height is adjusted using a CCD camera and a targeting laser. However, variations in sample height of ± 2 mm can be allowed for by the automatic height adjustment of the sample stage by the software.

Measurements were taken by changing the angles of the X-ray source and the detectors relative to the base line. The size of these two angles will determine the values of 2θ obtained and the characterisation time in seconds is also set for each sample.

4.2.5 Scanning Electron Microscopy

Arrays prepared on alumina and *Macor*® substrates were observed using SEM in wet mode using *Philips XL-30ESEM*. Images of the film surface were taken for all samples in the array. EDX spot analysis was used to determine the composition of the samples; these were plotted *versus* the amount of material used in the preparation. Initial studies suffered from a large amount of scatter due to the lack of material at each site and resulted in a high background due to the substrate, and hence, low signal to noise ratio. This was overcome somewhat by using new techniques to increase the sample thickness.

4.3 Results and Discussion

Arrays of varying composition based on $LiFePO_4$ were tested using high-throughput electrochemical, XRD and SEM methods.

4.3.1 Electrochemical Testing of $LiMPO_4$ Arrays

4.3.1.1 $LiFe_{0.8}Mg_{0.2}PO_4$ and $LiFePO_4$

Electrochemical testing of materials based on $LiFePO_4$ was conducted. Initial experiments were undertaken on a small scale on one vitreous carbon electrode to determine the feasibility of the technique. The electrochemical behaviour of this material is shown in Figure 4.16.

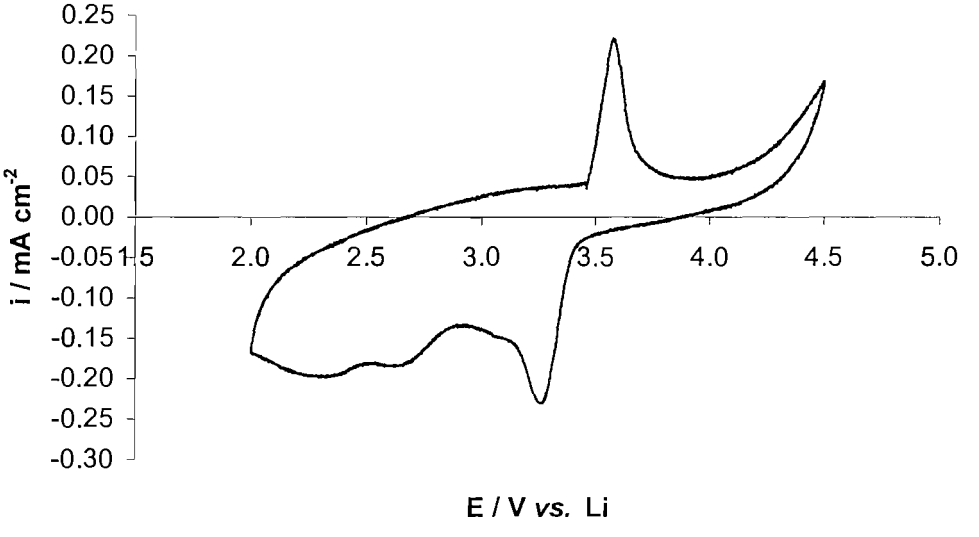

Figure 4.16 - First cycling of an $LiFePO_4$ electrode prepared on a 3 mm vitreous carbon substrate using the one-step deposition approach. The electrode was prepared at 700 °C, for 5 h in argon, using 0.25 molar ratio of sucrose to iron. The cell was cycled between 2 and 4.45 V *vs.* Li at a scan rate of 0.01 mV s^{-1}.

The expected performance is observed for the $LiFePO_4$ (olivine-type) material in that oxidation and reduction peaks attributed to the Fe^{2+}/Fe^{3+} couple are centred at 3.5 V *vs.* Li. However, it can be noted that there is a high reduction current between 2.0 and 3.2 V *vs.* Li. This is possibly due to the presence of non-redox active impurities or atmospheric moisture and may be due to poor sealing of the cell used in the experiment. This may also be due to the presence of some un-reacted precursor materials within the sample, which may be active in this region.

To test the method of automated preparation an array composed of 32 $LiFePO_4$ and 31 $LiFe_{0.8}Mg_{0.2}PO_4$ nominally identical samples were prepared from two aqueous stock solutions. This study enabled the observation of two compositionally different materials and allowed an evaluation of the technique to be undertaken by observing the scatter in the performance.

The rationale for the study of these two materials was the possibility of observation of the peak due to the formation of Fe^{4+} species during charging; this would show a change in the electrochemical response at higher potentials (~4 V *vs.* Li). It is hypothesised that the inclusion of electrochemically inert Mg^{2+} into the olivine structure could result in an increase in the number of oxygen atoms surrounding the iron atoms. The effect of this may be to reduce the potential of the Fe^{3+} to Fe^{4+} redox couple to within the stability window of the electrolyte.

Figure 4.17 shows the data obtained during the cycling experiment. The current values in the cyclic volatmmograms for the $LiFe_{0.8}Mg_{0.2}PO_4$ samples are higher than those obtained for the $LiFePO_4$ samples. No peaks are observed for the Fe^{3+}/Fe^{4+} redox couple in the Mg containing samples. However this is not unexpected since the redox power required to achieve this is possibly higher than is available during the experiment. At the outset of the experiment, it was not expected that the Mg containing electrodes would outperform the $LiFePO_4$ in terms of peak current and total charge. The experiment was conducted simply to observe some difference the materials. However, the larger currents for the Magnesium containing samples can be explained by the presence of a larger amount of residual carbon left over from the reduction of the iron. This carbon coats the particles of $LiFePO_4$, and thus, increases the effective conductivity, allowing the kinetics of the electrode transfer reaction to be increased,

thus increasing the current. There is greater residual carbon in the Mg containing samples because 0.2 moles less iron is present to be reduced than in the $LiFePO_4$ samples and hence, the carbon used in the reduction of these 0.2 moles of iron remains to form additional conducting additive.

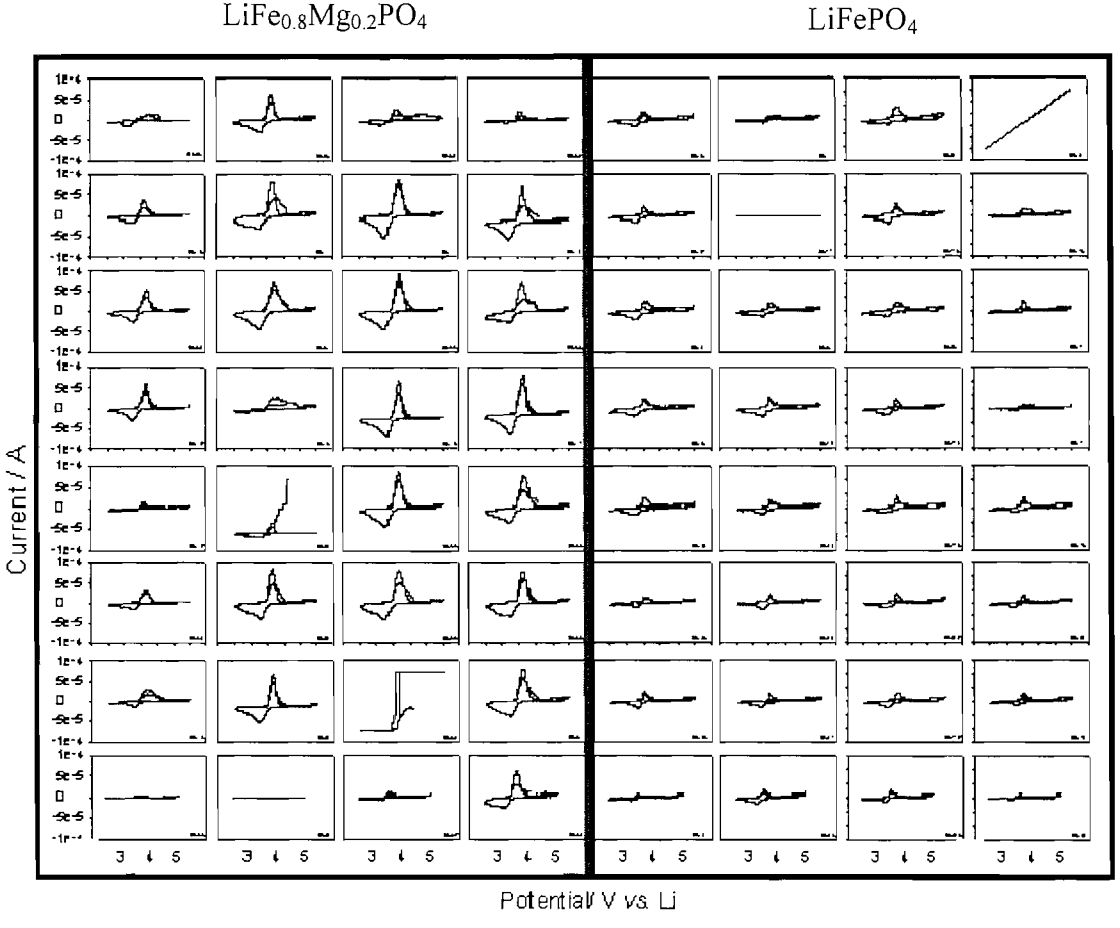

Figure 4.17 - Cyclic voltammetry of a 32 compositionally identical $LiFe_{0.8}Mg_{0.2}PO_4$ and 31 compositionally identical $LiFePO_4$ electrodes in an array. Electrodes were cycled between 2.5 and 4.5 V *vs.* Li, $v = 0.01$ mV s^{-1}. Array contained $LiFePO_4$ and $LiFe_{0.8}Mg_{0.2}PO_4$ precursors and 0.25:1 Sucrose to $LiFePO_4$ ratio. The array was heat treated at 700 C for 10 h in Ar in a tube furnace.

Figure 4.17 clearly shows the difference in electrochemical response between the types of materials. On the left hand side of the array ($LiFe_{0.8}Mg_{0.2}PO_4$), the peak currents are generally high. In contrast the response on the right hand side ($LiFePO_4$) is low. Based on these data, there would appear to be a contradiction in the response, because higher currents should be expected for a larger amount of active material. The $LiFe_{0.8}Mg_{0.2}PO_4$ samples contain less active material but the current response and the amount of charge stored is higher. This can be explained by the different quantity of carbon present in the two samples. In the $LiFe_{0.8}Mg_{0.2}PO_4$ materials, 0.2 moles of iron are replaced with magnesium in its 2+ form. In both materials the metal ions are in the 2+ state, but in the precursor material iron is in the 3+ state and magnesium exists in 2+ oxidation state. To form the olivine phase, the transition metal must be in the 2+ state and the presence of carbon from the pyrolysis of sucrose facilitates this reduction. This is because there is less iron to reduce Fe^{3+} to Fe^{2+}, as there is more residual carbon remaining in these samples. Because these materials were prepared with carbon residues around the percolation threshold, a small change in carbon loading will result in a large difference in current response.

Figure 4.18 shows the relationship between the peak current and the charge for each electrode in the above experiment. It can be seen that the $LiFePO_4$ electrodes are clustered in the lower left hand corner of the graph and most of the $LiFe_{0.8}Mg_{0.2}PO_4$ electrodes are clustered towards the top right. These data are normalised for mass by dividing by the charge because the peak current I_p of an electrode is proportional to the charge that can be stored. These are both dependent on the mass of active material present in the electrode. Hence the difference in the position of the points for the two types of electrode is a result of a difference in conductivity. This difference in conductivity between the two samples can be explained by the amount of residual carbon remaining in the materials after calcination. The $LiMg_{0.2}Fe_{0.8}PO_4$ material most probably contains a larger amount of residual carbon because there is less Fe (III) in the precursor that requires reduction to Fe (II). Although both the $LiMg_{0.2}Fe_{0.8}PO_4$ and the $LiFePO_4$ materials on the array were prepared with the same amount of sucrose, more of the carbon from the sucrose remains in the magnesium containing samples and

therefore, the magnesium containing material is more conductive and therefore gives rise to higher peak currents.

The scatter associated with the measurement of current for the two sample types was investigated by plotting the number of samples with a given charge *vs.* the charge (see Figure 4.19). This shows that a significantly larger number of $LiFe_{0.8}Mg_{0.2}PO_4$ electrodes exhibit higher values of charge relative to the $LiFePO_4$ samples. As described above, this may be the due to a difference the amount of carbon in of the samples, but is almost certainly a measure of the conductivity of the samples. The $LiFePO_4$ electrodes have a lower amount of carbon than the $LiFe_{0.8}Mg_{0.2}PO_4$ samples.

This is due to the larger amount of residual carbon in the samples containing magnesium. These results would suggest that such a level of carbon is above that of the percolation threshold, and hence, the probability of an adequate percolation network existing is higher in these samples. In the case of the $LiFePO_4$ electrodes, the probability of the electrode having a sufficient percolation network to enable the utilisation of the full capacity for each repeat sample is lower.

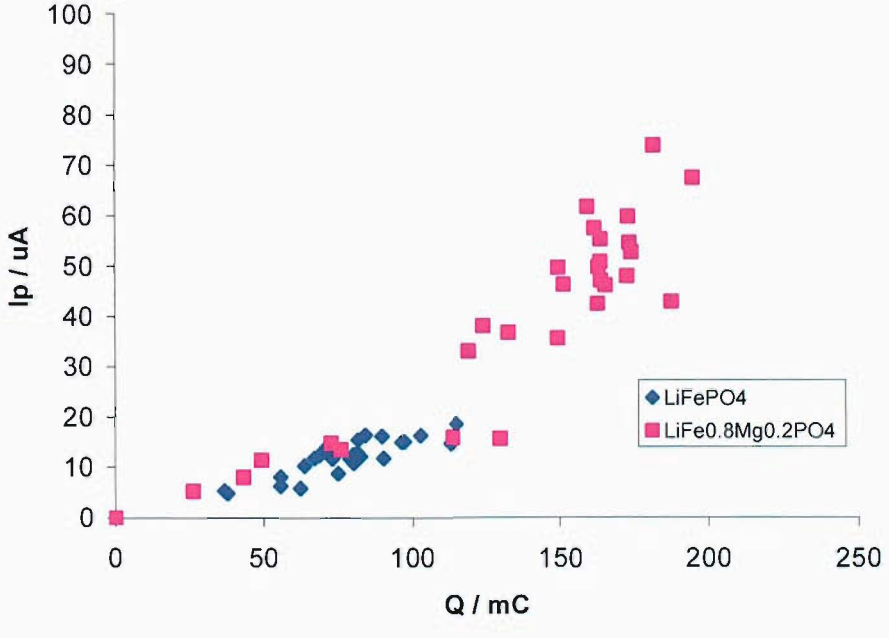

Figure 4.18 - Peak current *vs.* the total charge stored during the first cycle for $LiFePO_4$ and $LiFe_{0.8}Mg_{0.2}PO_4$ electrodes.

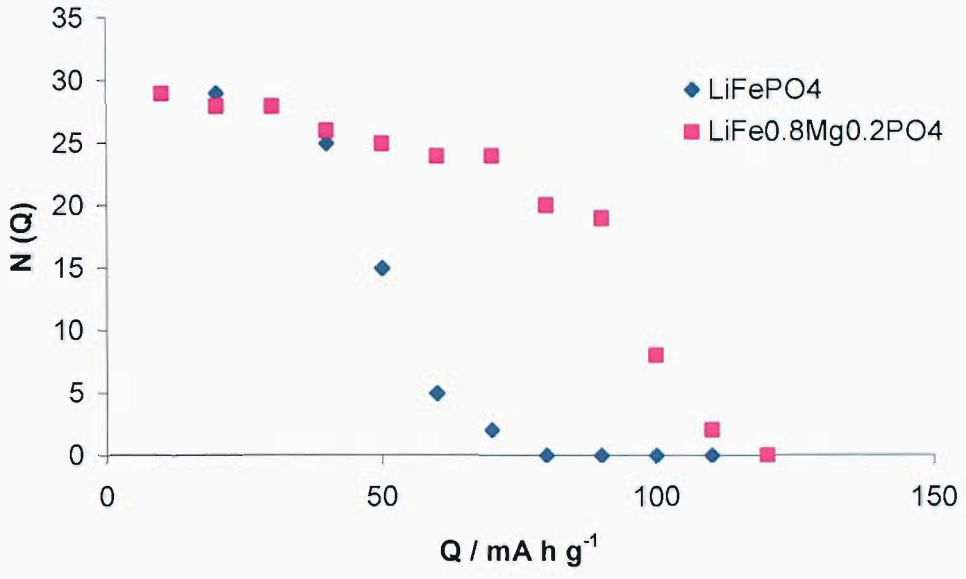

Figure 4.19 - A plot of the number of electrodes in the sample with charge Q *vs.* the charge Q.

Figure 4.20 and 4.21 show plots of the differentials of the above graphs *vs.* charge. These give an indication of the distribution of capacity amongst the samples for the $LiMg_{0.2}Fe_{0.8}PO_4$ and $LiFePO_4$ materials. The value on the *y*-axis is dN/dQ and is proportional to the number of samples (N) with a given charge (Q). The plot in Figure 4.20 shows a distribution for the number of samples with a given charge giving the mean value and the standard deviation. The mean charge is 80 mA h g^{-1} and is exhibited by the highest number of samples, where as a lower number of samples exhibit less than 80 mA h g^{-1} and likewise a similar number of samples show the highest capacity (between 80 and 140 mA h g^{-1}).

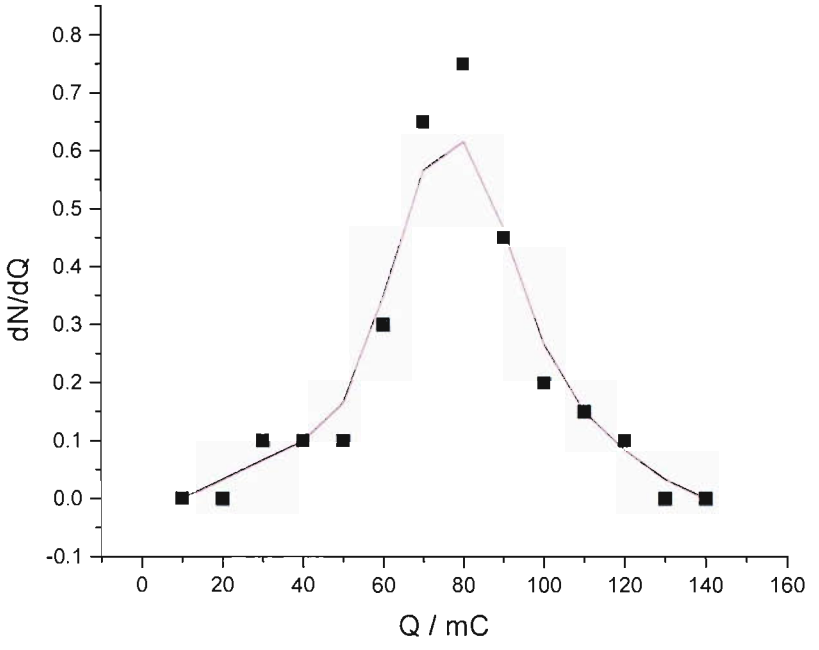

Figure 4.20 - The derivative of the number of samples with a given charge *Q vs.* the charge for all $LiFePO_4$ samples. The value *dN/dQ* is related to the population of samples with a given *Q*.

Figure 4.21 shows the distribution of the number of electrodes with a given charge for the $LiFe_{0.8}Mg_{0.2}PO_4$. This is similar to the plot shown in Figure 4.20 for the $LiFePO_4$ electrodes, however, the maximum in Figure 4.21 is shifted to the right relative to the peak in Figure 4.20. This is due to a larger number of electrodes exhibiting a higher charge due to the presence of a large amount of residual carbon.

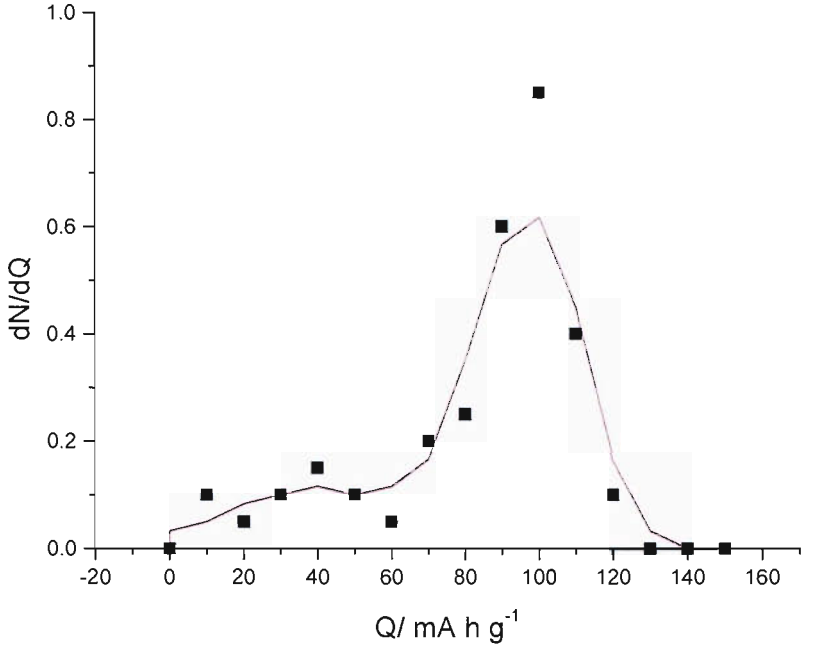

Figure 4.21 - The derivative of the number of samples with a given charge *Q vs.* the charge for all $LiFe_{0.8}Mg_{0.2}PO_4$. The value *dN/dQ* is related to the population of samples with a given *Q*.

4.3.1.2 $LiFePO_4$ and Sucrose

It was shown in chapter two that the quantity of sucrose present in the $LiFePO_4$ precursor had a large effect on phase formation and electrochemical performance. This was investigated using the high-throughput technique by preparing 64 stock solutions containing a graded amount of sucrose from 0 – 1 mol and this corresponded to an array of 64 electrodes with varying carbon loading. The array was electrochemically tested using slow-scan cyclic voltammetry at a scan rate of 0.1 mV s^{-1} between 2 and 4.5 V *vs.* Li. The results are shown in Figure 4.22).

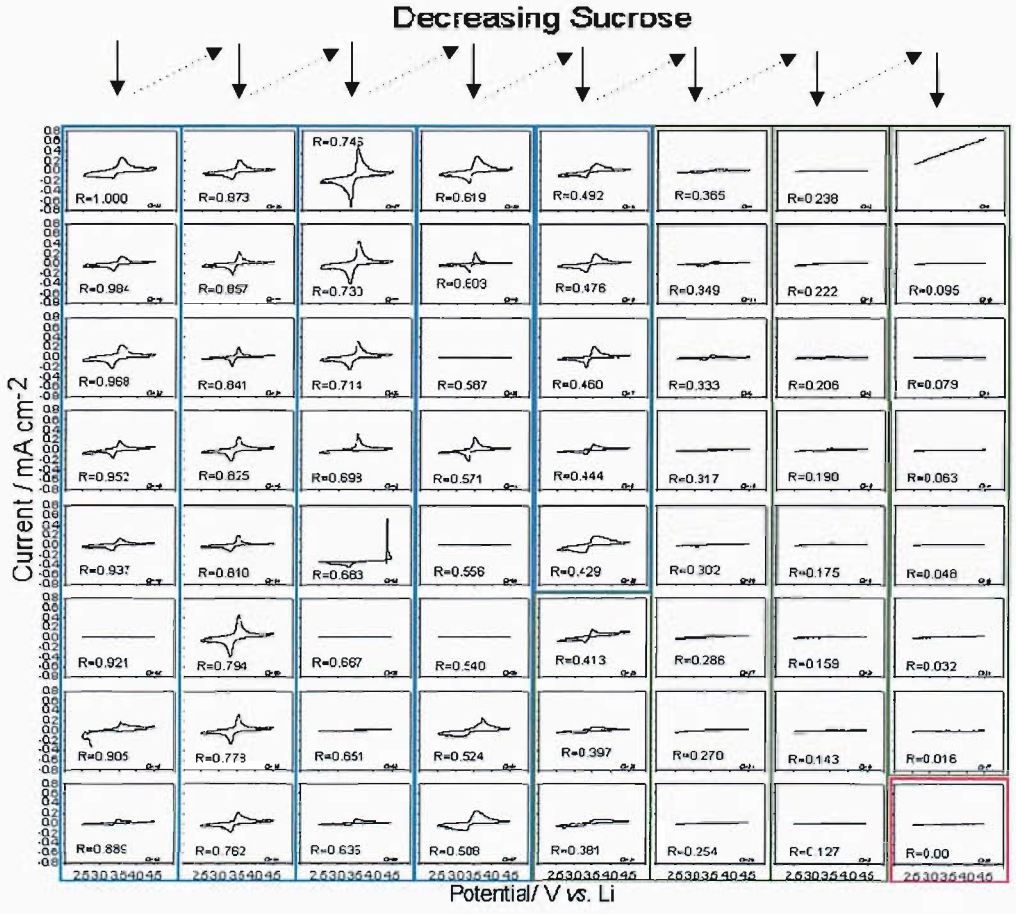

Figure 4.22 - Cyclic voltammerty of an array of $LiFePO_4$/C electrodes with a systematic variation in sucrose loading. $\nu = 0.1$ mVs^{-1}, $E = 2.5$ - 4.5 V *vs.* Li (molar ratio R is in the range 0-1).

The voltammograms are divided into three sections shown in blue, green and red. The voltammograms contained within the blue zone are electrodes containing high amounts of carbon in excess of the percolation threshold. These materials show higher currents than the electrodes in the green and red zones. The electrodes in the green coloured regions are those below the percolation threshold. They exhibit low currents and at some lower values of the sucrose to Fe ratio *(R)*, the material may not be in the correct phase. After synthesis of the array used in this experiment, it was observed that at low *R*-values the colour of the samples appeared red indicating Fe (III) impurities, and hence, XRD was conducted in addition to electrochemical testing to observe the point of phase formation. It can be noted from Figure 4.23 that the onset of percolation occurs around $R = 0.41$. It has been shown in chapter 2 that 0.2 moles of sucrose is required for phase formation, and hence, this would suggest 0.21 moles of sucrose are required to form sufficient conducting additive to give good electrochemical performance. The specific capacity of the samples was plotted versus the sucrose ratio and shown in Figure 4.23.

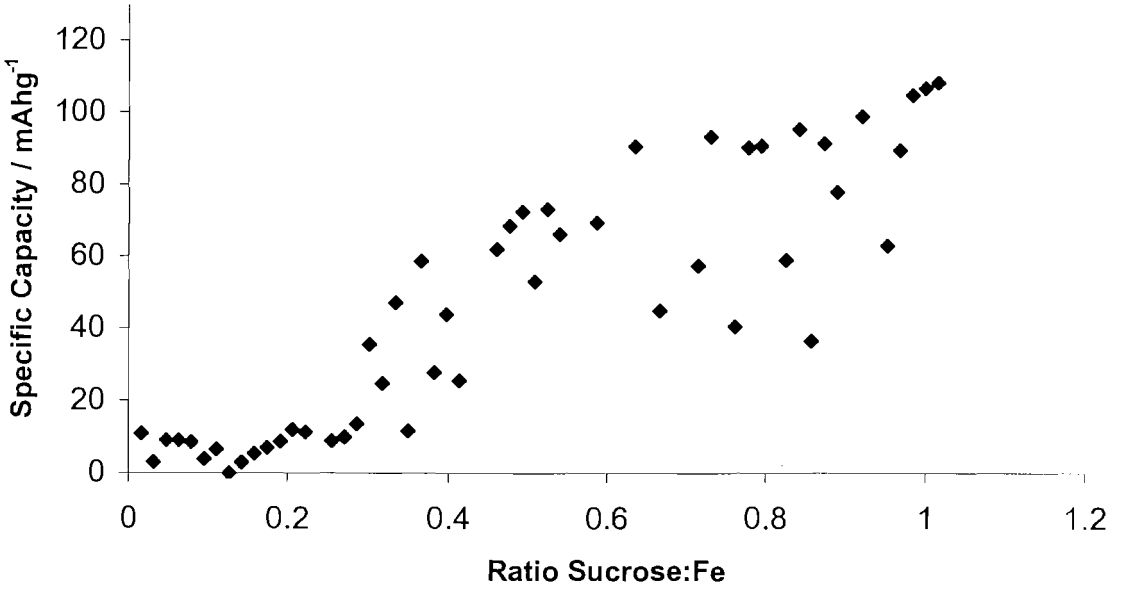

Figure 4.23 - Specific capacity of the first charge *vs.* sucrose: Fe ratio *(R)*.

It is clear that, at very low carbon loadings (0-0.3), low capacity values are observed. However, as the sucrose ratio is increased, the capacity values rise. There is some scatter in the region R = 0.3-0.95, but overall the data shows the expected percolation behaviour. Inaccuracies in preparation and loss of a small amount of material during calcination may be responsible for this scatter. It must be also noted that the maximum capacity observed for the array electrodes is lower than the theoretical capacity of $LiFePO_4$. This is due to the nature of the preparation route. Close to theoretical capacity values can be achieved with the aqueous solution preparation method, but this requires an addition calcination step with sucrose. However, because all electrodes in the array have been prepared under the same conditions, the high-throughput method may be used to compare the performance of materials relative to one another, rather than to give an absolute value for their performance.

4.1.3.3 $Li_{1-x}Zr_xFePO_4$ Arrays

Arrays of Zirconium doped $LiFePO_4$ were prepared to determine the effect of Zr on conductivity, and therefore, observed currents and capacity. This is in response to the work of Chaing *et al.* as described in Section 4.1. It was suggested that the increase in conductivity could be explained by the presence of carbon remaining from the alkoxide synthesis process, and not the Zr doping. It was, therefore, clear that these possible effects should be separated and investigated independently. This was achieved by placing them as variables on the two axis of a combinatorial array. An inorganic source of Zirconium [$ZrO(NO_3)_2$] was used and was added to the samples in increasing amounts along the y axis. The amount of sucrose was varied systematically along the x-axis; this gave eight different sucrose loadings and eight Zr doping levels plus all permutations of the two values.

The array of zirconium doped materials was tested electrochemically on an array of vitreous carbon electrodes by slow scan cyclic voltammetry using a scan rate of 0.1 mVs^{-1} and was cycled between 2 and 4.5 V *vs.* Li. The array of cyclic voltammograms is shown in Figure 4.24. The capacity stored in each of the electrodes during the second

charge was plotted as a function of composition on the x and y axes (see Figure 4.25). The electrodes with high capacity are shown in a red or orange colour, whereas electrodes with a small amount of capacity are shown in green and yellow.

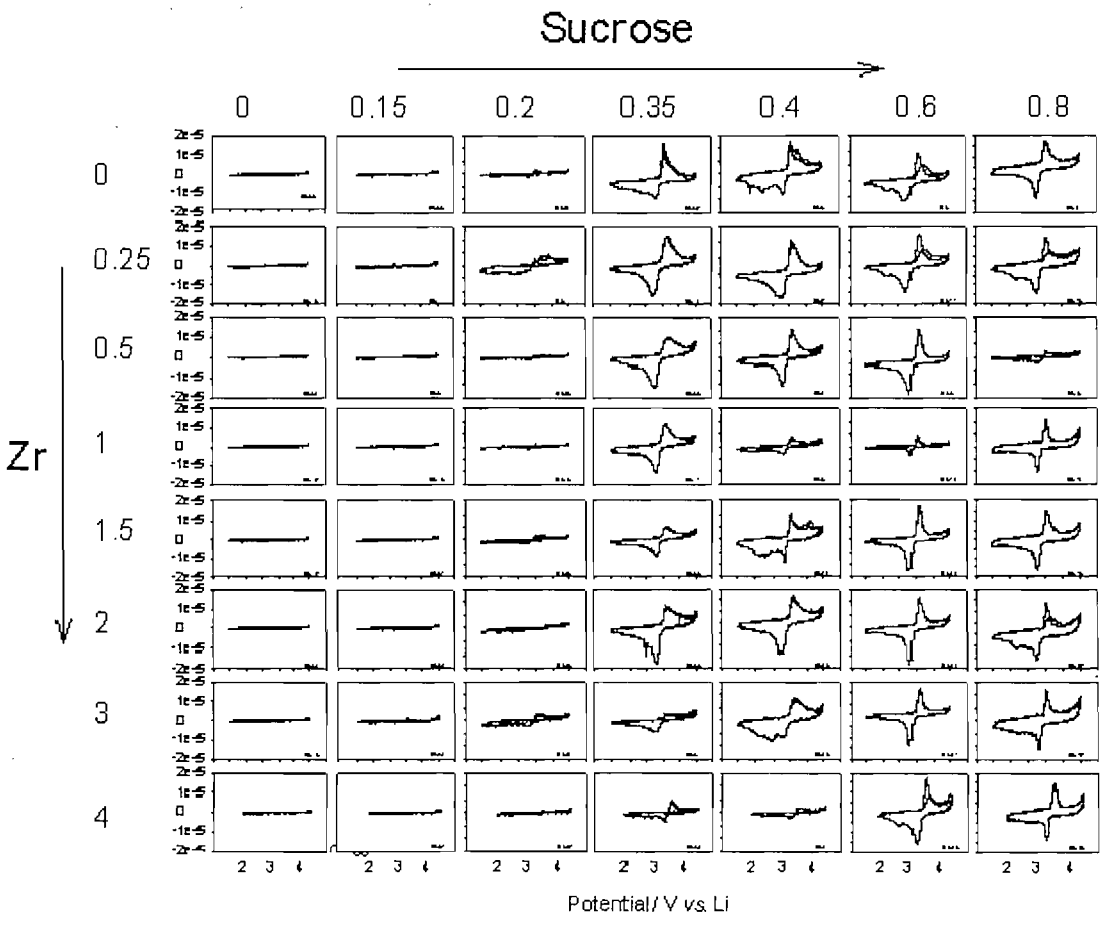

Figure 4.24 - Cyclic voltammetry of $Li_{1-x}Zr_xFePO_4$/C electrodes. $\nu = 0.1$ mV s^{-1}, E= 3-4.5 V *vs.* Li.

The data in Figures 4.16 and 4.17 suggests that, as adding sucrose increases the amount of carbon in the electrode, as there is a corresponding increase in the current and capacity values. This is the effect of developing a percolation network. As the amount of zirconium is increased, there is no evidence of a corresponding increase in conductivity. If the zirconium was to have the effect of increasing the conductivity, we should see an increase in current levels at electrodes under the percolation limit of 0.2 moles of sucrose. This effect should be seen most clearly in the behaviour of electrodes marked A, B and C. However, this is not observed and interestingly the addition of the zirconium appears to reduce the capacity of the electrodes labelled D, E and F. Moreover, this might still be scatter associated with inaccuracies in the amount of active material on the electrode.

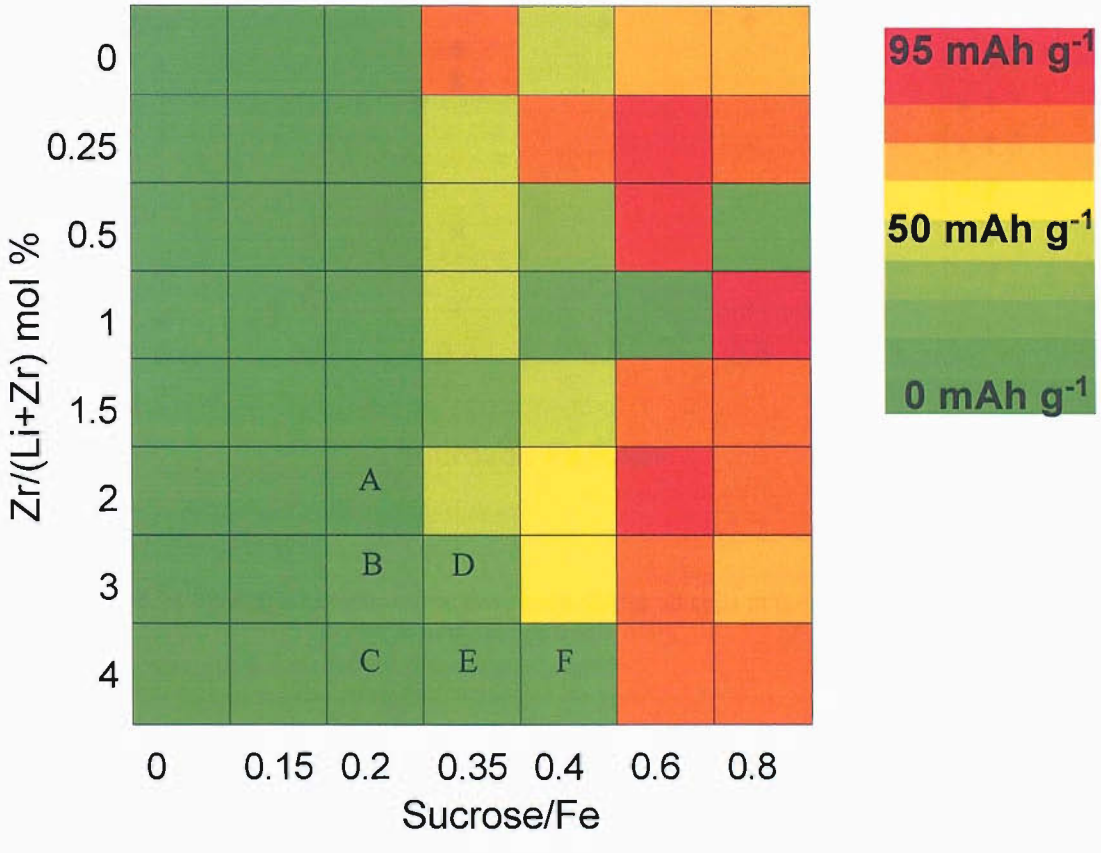

Figure 4.25 - Specific capacity mapping of first charge cycle for all electrodes in the array.

Figure 4.26 is a plot of sucrose content *vs.* specific capacity for each of the eight zirconium doping levels. This plot confirms the response seen in Figure 4.25 that there is no relationship between the zirconium doping level and the capacity. This therefore confirms, indirectly that the zirconium doping level does not have the effect of increasing the conductivity of the material. If doping the materials with zirconium had the effect of increasing the conductivity, then elevated capacity levels at low carbon loadings (< 0.2 mol sucrose) would be observed, but this is not the case. However the capacity of the zirconium-doped samples can be seen to increase as their carbon content is increased.

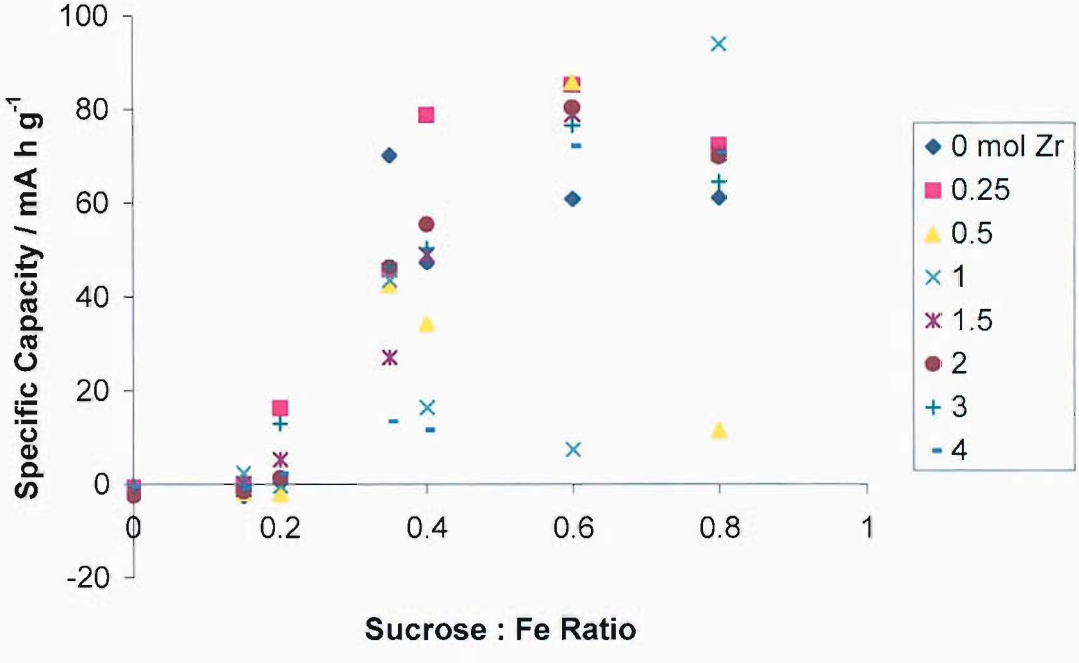

Figure 4.26 - Specific capacity *vs.* sucrose ratio *(R)* for all cells in the $Li_{1-x}Zr_xFePO_4/C$ (*R* is in the range 0 to 1 mol).

Figure 4.27 shows a plot of the ratio of the peak current versus the molar ratio of sucrose to iron (*R*). The calculated values for each electrode are shown as blue diamonds and the average values are shown by the purple squares. The data shows that, as the sucrose ratio is increased between 0 and 0.6 mol, the specific capacity increases linearly with *R*. However, the maximum I_p/Q ratio is

reached at R = 0.6 mol and the I_p/Q ratio drops as R is increased to 0.8 mol. As the ratio I_p/Q is normalised for the mass of material, it is a more direct measure of the conductivity of the material because the inaccuracy in the measurement of mass is eliminated. An explanation for the decrease in the I_p/Q ratio is that the materials containing 0.6 moles of sucrose have a sufficiently conducting carbon network, to access almost all of the active material particles, and thus, can access this charge. In the case of the material with R = 0.8, the carbon remaining from the pyrolysis of sucrose is greater than is required to form an adequate percolation network. The additional weight of carbon in the composite not redox active and does not contribute to the charge that can be stored.

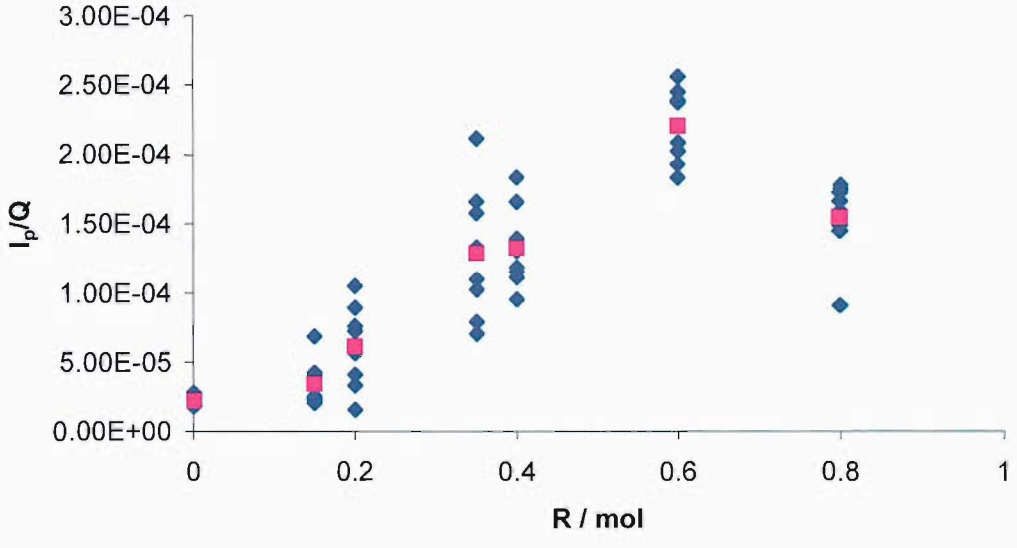

Figure 4.27 - The ratio of peak current to charge *(I_p/Q) vs.* the ratio of sucrose to iron (R).

4.3.1.4 Ternary Mixed Metal Phosphate – $LiCo_xNi_yFe_{1-x-y}PO_4$

A compositional spread of $LiFePO_4$ based materials containing three transition metals was prepared and tested. The samples were prepared as solid solutions of the general formula $LiCo_xNi_yFe_{1-x-y}PO_4$. The samples contained different proportion of Co, Ni and Fe added to the precursor material as solutions of

transition metal nitrates. The electrodes were prepared using the solution synthesis technique, which was developed for $LiFePO_4$. Iron was substituted for cobalt and nickel by varying the amount of iron, nickel and cobalt nitrate in the compositions that were prepared using an automated liquid handling system. The compositions of the samples prepared on the array are outlined in the ternary plot in Figure 4.28. The 64 compositions were chosen varying iron between 0 and 1 mole, cobalt between 0 and 0.5 moles and nickel between 0 and 0.5 moles.

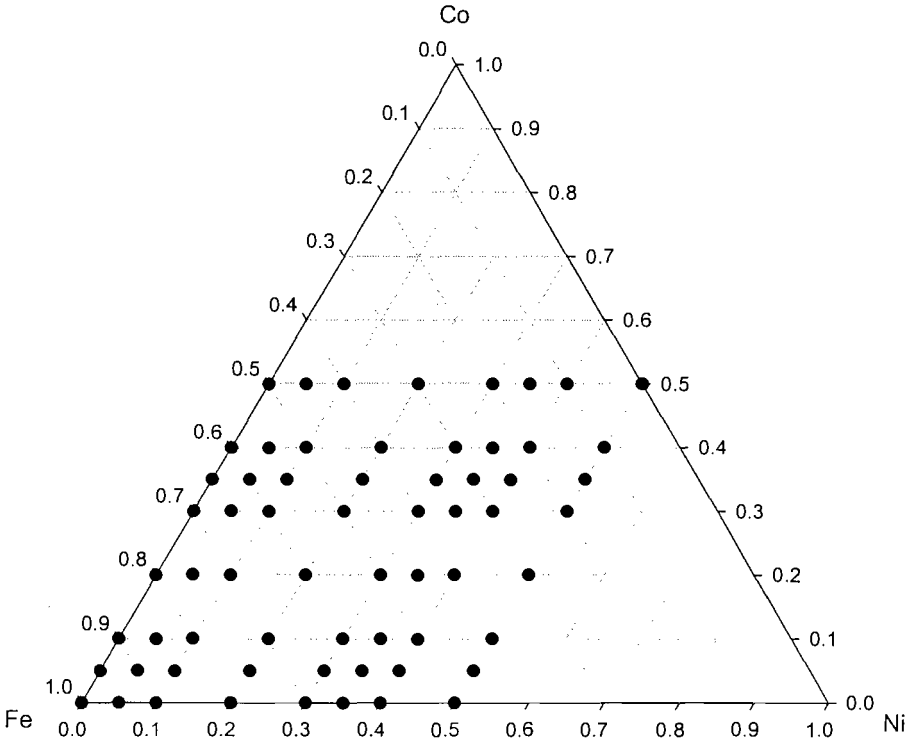

Figure 4.28 - Ternary plot of $LiNi_xCo_yFe_{1-x-y}PO_4$ compositions that were prepared using the high-throughput synthesis method.

Figure 4.29 shows cyclic voltammetry data for the composition spread of $LiNi_xCo_yFe_{1-x-y}PO_4$ materials outlined in Figure 4.28. It can be noted that the pure phase $LiFePO_4$ shown in red gives the best performance of the compositions surrounding it. However, it can be seen that a region of compositions with a larger current response exists, denoted by a green rectangle. In addition, the compositions containing a significant amount of nickel

(0.1 to 0.5 moles) and a low amount of cobalt (0 to 0.1 moles) give almost no response. This may be because the materials themselves do not exhibit redox capacity within the voltage region studied. This behaviour may also be the result of an unsuccessful synthesis, such that the materials were not formed on the electrodes and may also be due to poor contact between the active material particles, the carbon matrix and the current collector.

In chapter two (section 2.3 the randomisation of the sample locations was undertaken. The results of this study revealed that there did not appear to be a strong relationship between location and electrochemical performance. Therefore, it is more likely that the low response observed in the high nickel and low cobalt containing compositions is an effect of composition, conductivity or the result of problems with the sample preparation technique. It is also clear, that the compositions containing high amounts of cobalt showed a low response. However, it is unlikely that such large differences in performance could be the result of changing the composition by such a small amount.

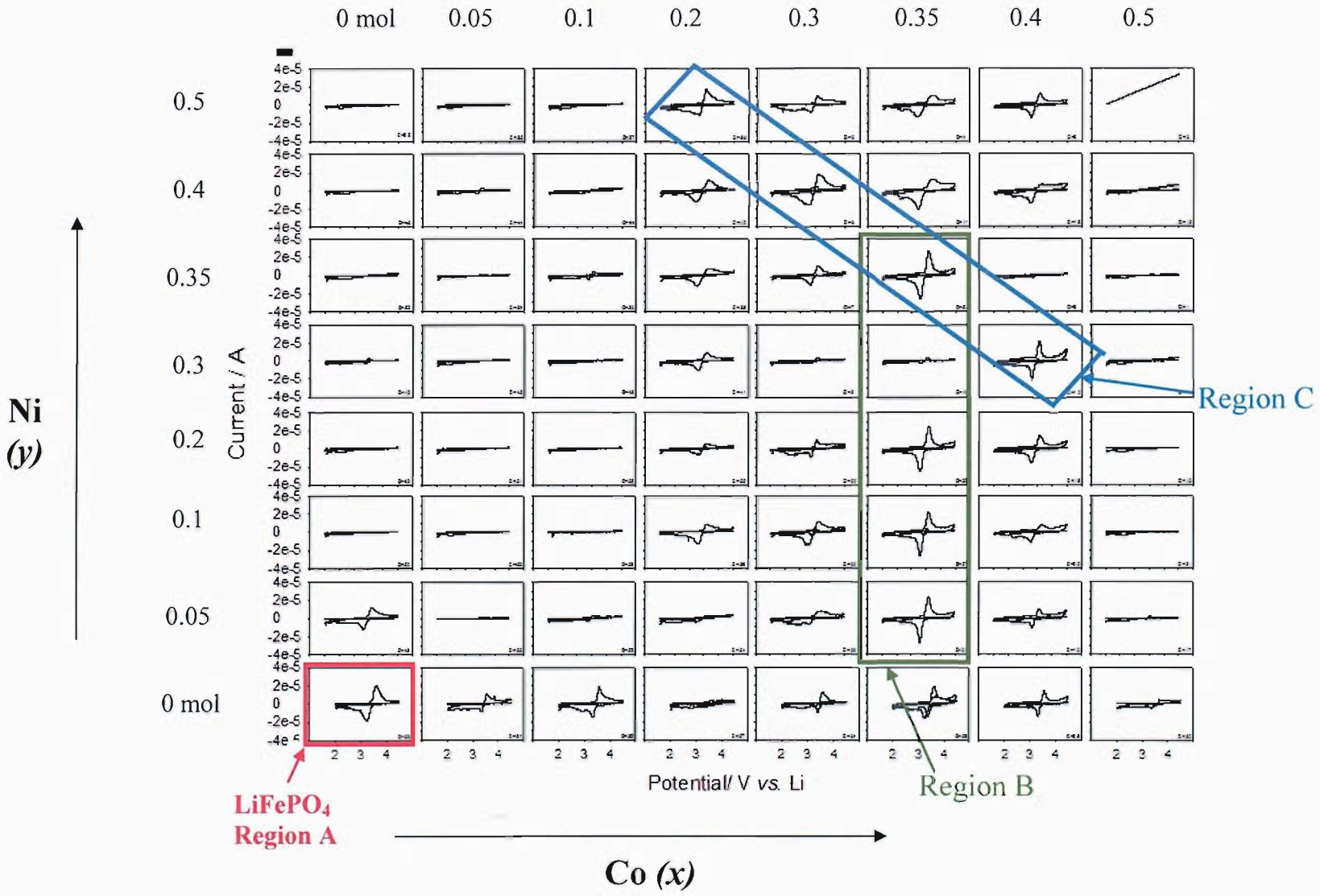

Figure 4.29 - Cyclic voltammetry of a $LiNi_xCo_yFe_{1-x-y}PO_4$ array, v = 0.01 mV s^{-1}, E = 2.5-4.5 V *vs.* Li.

It is possible that the changes in composition had the effect of changing the way the material interacted with the carbon matrix, and hence, resulted in a difference in electrochemical performance and inferred conductivity. However, behaviour demonstrates the benefit of combinatorial screening techniques, as they are capable of examining unknown systems rapidly and can lead to a number of new potential compositions with apparently superior performance. These compositions can then be prepared using traditional techniques and may lead to a new optimum composition. The data obtained from the array was treated and values for some figures of merit were obtained. These were the peak current on oxidation, the peak current on reduction and the total charge stored. The total charge has been quoted in coulombs because all compositions have approximately the same mass and the compounds are being screened relative to one another. These figure of merit values were plotted as a function of composition and are shown in the ternary plots in Figures 4.30 - 4.32.

Figure 4.30 is a plot of the peak current on oxidation as a function of composition. The three axes of the ternary give the proportion of iron, cobalt and nickel in each of the compositions, the current response is plotted as a colour on a fourth axis. Low current responses are shown in light green where as higher responses are shown in red.

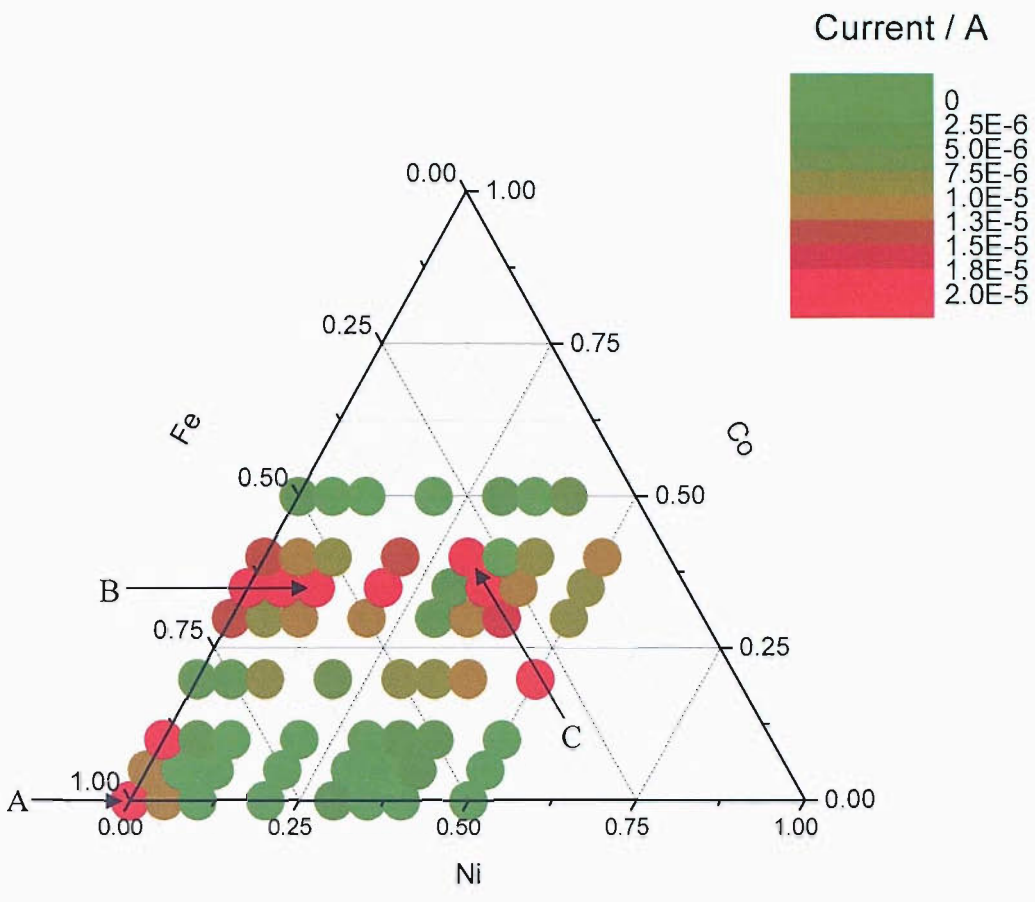

Figure 4.30 - Peak oxidation currents for the $LiMPO_4$ electrode compositions.

It can be seen that there are three main regions giving a high current response. Firstly a group of points in the bottom left portion of the plot denoted by the letter A. The first of these points represents $LiFePO_4$ with no substitution (at Fe = 1, Ni = 0 and Co = 0), the $LiFePO_4$ composition is denoted by a red rectangle in Figure 4.29. The second is a band extending left to right towards the top left of the plot denoted by the letter B. These points represent the compositions containing 0.35 moles of cobalt and show a particularly high response. The green box in Figure 4.29 also denotes these compositions. The third region of interest is a number of compositions extending diagonally from left to right noted as region C shown by the blue rectangle in Figure 4.29. There are also area of high current response in the composition between those noted by regions B and C. There are many reasons for these responses. It was expected that the composition containing only iron ($LiFePO_4$) material would give the highest current response and this is the case. However, the occurrence of very high current responses in substituted

materials was not expected. These responses are unlikely to be the result of a crystallographic effect, (*i.e.*, as a direct result of removing iron and replacing it with cobalt). However, it is more likely that the change in composition resulted in the materials having different morphologies that interacted with the carbon matrix such to increase or decrease the conductivity of the material. Evidence of the changing morphology with composition can be seen in section 4.3.3.

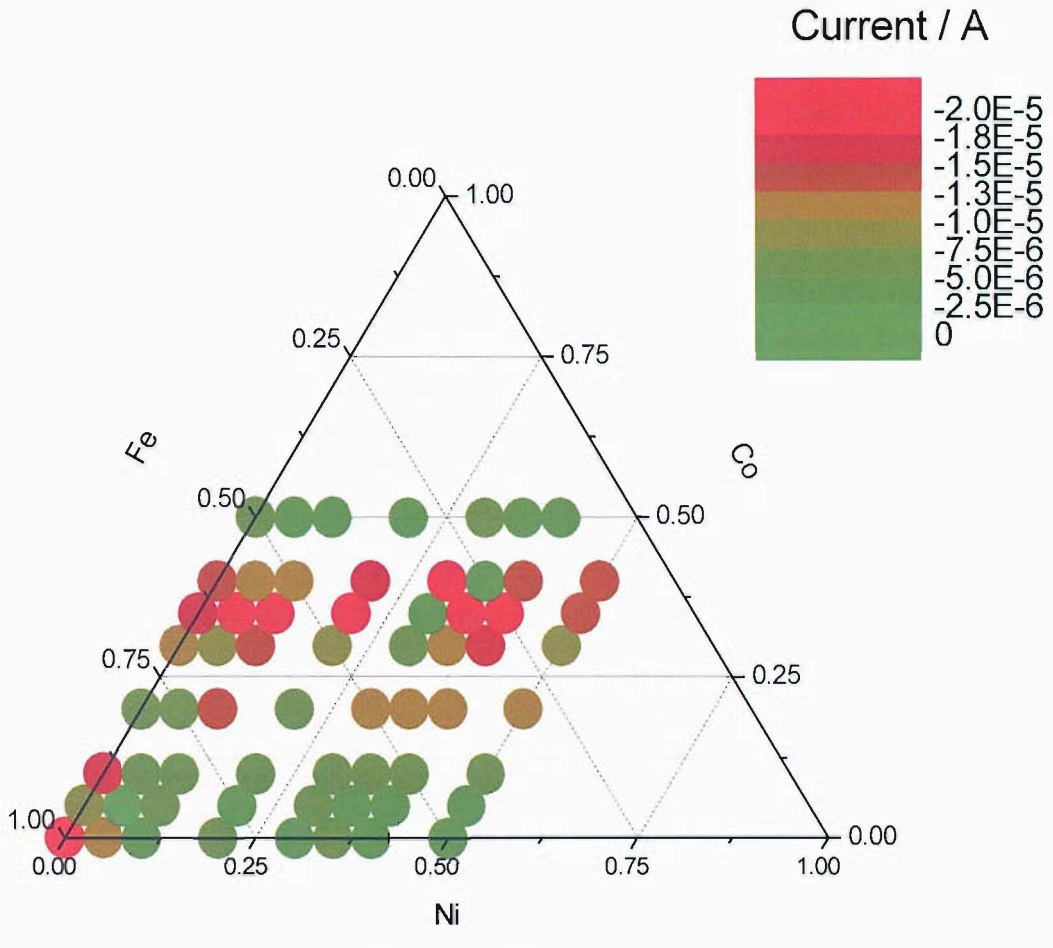

Figure 4.31 - Peak reduction currents for the $LiMPO_4$ electrode compositions.

The peak reduction currents for the $LiMPO_4$ compositions outlined in Figure 4.28 are shown in Figure 4.31. The data shows a similar pattern to that observed for the peak oxidation current (see Figure 4.30), indicating a good agreement between charge and discharge cycles. Again, the three main regions of high activity can be seen. It is possible that the substitution of $LiFePO_4$ with cobalt and nickel have resulted in materials that compare favourably in terms of performance with

$LiFePO_4$. In addition, a further investigation of these materials may lead to a better understanding of their properties such conductivity and cyclability. These areas require further study and methods are currently being developed to obtain a direct measurement of electronic conductivity of samples in a high-throughput experiment.

4.3.2 Combinatorial X-ray Diffraction

High-throughput XRD was conducted on arrays of lithium battery materials; the technique was applied to arrays of $LiNi_xCo_{1-x}O_2$ and $Li_{1-x}Zr_xFePO_4$. Initial experiments were conducted on an array of $LiNi_xCo_{1-x}O_2$. The X-ray pattern was not expected to differ between samples, due to the solid solution having the same crystal phase. This was conducted to test the method of combinatorial XRD as this material could be synthesised in air. The synthesis of the $LiNi_{1-x}Co_xO_2$ was easier to undertake with the equipment available at the time, as a sealed large bore tube furnace with an inert atmosphere was not required.

The patterns obtained for the $LiNi_{1-x}Co_xO_2$ material is shown in Figure 4.32. Solid solutions of $LiNi_{1-x}Co_xO_2$ were prepared by increasing the molar ratio of nickel to cobalt by 0.01moles per sample. For example the sample A1 is of LiCoO2 composition and sample H8 has composition $LiNi_{0.63}Co_{0.37}O_2$. It can be seen from the patterns in Figure 4.32 that the nickel substituted material maintains the same crystal structure as the pure $LiCoO_2$ material with two reflections in the region 2θ = 40-50 °. The 40 ° reflection relates to the 104 plane of the structure and is the most intense and the 50 ° reflection relates to the 105 plane of the rhombohedral structure of $LiNi_{1-x}Co_xO_2$ (R3m symmetry). Some samples produced patterns consisting of broad peaks indicating the presence of amorphous material, possibly the substrate on which the samples were prepared, silica glass.

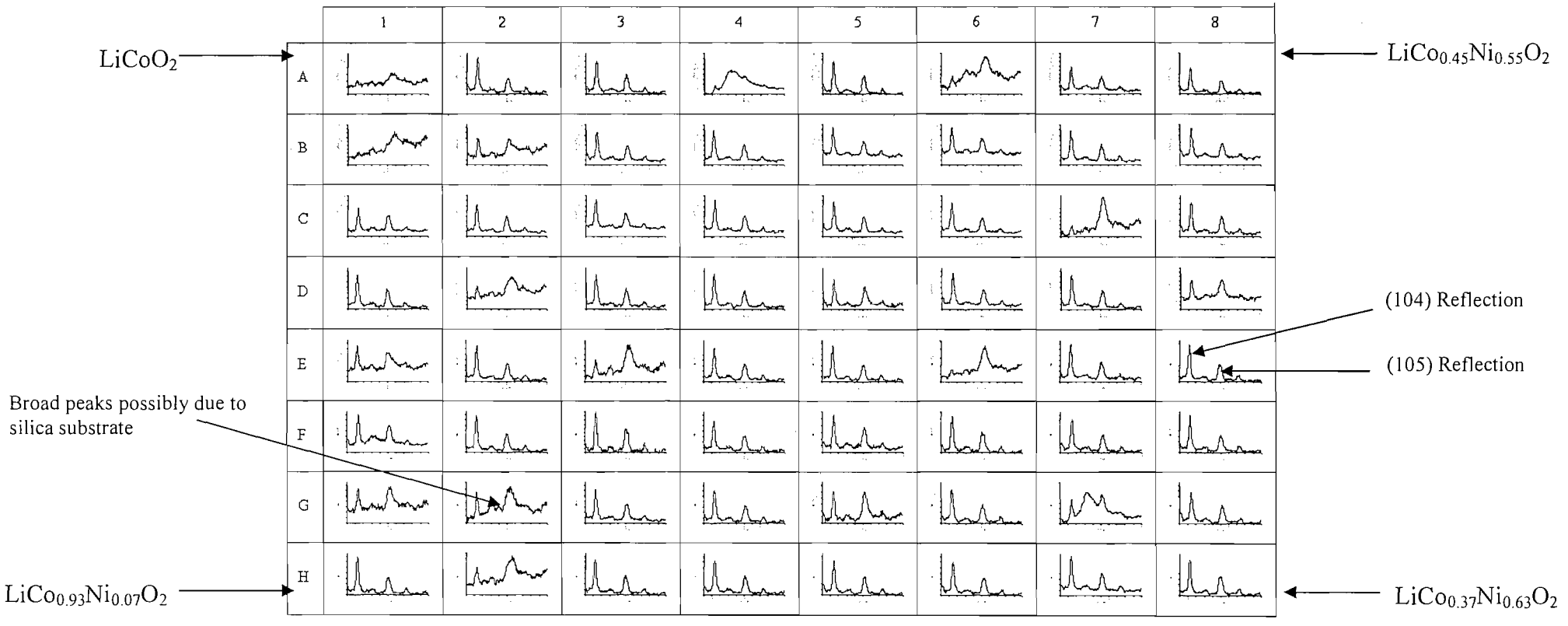

Figure 4.32 - Combinatorial XRD of $LiCo_xNi_{1-x}O_2$ compositions, 2θ = 40-50 °, Intensity is shown on the y-axis scale with 0 to 2000 arbitrary units. The composition was varied across the array by subsisting 0.1 moles on Ni for co in each sample. The first intense peak at 41° can be attributed to the (104) planes and the peak at 45° to the (105) plane.

Figure 4.32 shows high-throughput XRD data for $LiCo_xNi_{1-x}O_2$ compositions. There appears to be little scatter in these measurements, only 6 samples (A1, A4, A6, B1, G1 and H1) out of 64 gave showed abnormal behaviour. This was possibly due to a lack of material at the sample site, possibly the result of poor adhesion. These data were obtained from samples prepared on a silica glass substrate; hence, the presence of a high background is not likely. However, the data obtained are not of sufficient quality to undertake data analysis (*i.e.*, structural refinement). Moreover, the retention of the correct phase on the addition of Ni to the $LiCoO_2$ structure is evidence that the composition of the samples is as expected as all samples should exhibit a single phase in $LiCo_xNi_{1-x}O_2$ where $0 \geq x \geq 1$.

A similar experiment was undertaken using $Li_{1-x}Zr_xFePO_4$ materials; Figure 4.33 shows the XRD data obtained for this array. It can be seen that the overall intensity for most patterns is low; this is possibly due to the fluorescence effect, which increases the background level when collecting diffraction data, it may also be due to a lack of material at the sample site, due to poor adhesion to the substrate.

It can be noted from Figure 4.33 that samples containing low sucrose levels exhibit a different diffraction pattern from those containing larger amounts of sucrose. Figure 4.33 shows data only for 2θ = 30-40°, this is because few reflections were visible at other angles, possibly because they were too weak to be detected due to the effect of using a small amount of sample and the effects of fluorescence. The reflection observed at 2θ = 35 °, is the most intense reflection in the pattern observed for $LiFePO_4$ and corresponds to the (131) reflection for the olivine phase of $LiFePO_4$.

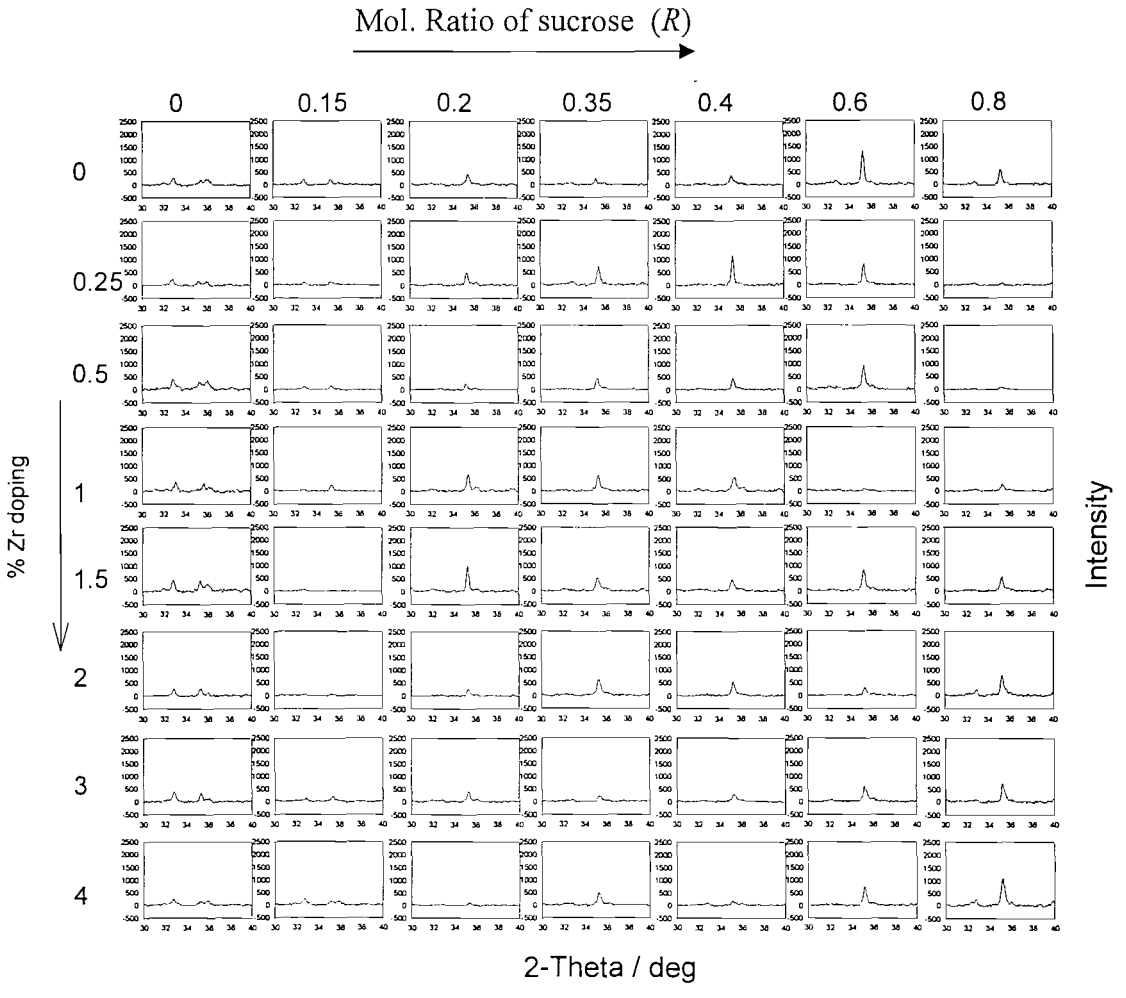

Figure 4.33 - High-throughput XRD of $Li_{1-x}Zr_xFePO_4$ materials. 2θ = 30-40 °.

It may, therefore, be assumed that this reflection peak is due to $LiFePO_4$ formation on the array. Figure 4.33 also shows evidence of another crystal phase with two visible reflections at $2\theta = 32$ and 37°. This observation is also quite reproducible and can be seen in the first column of the array, where the ratio of sucrose to iron (R) is zero. These reflections are possibly due to crystalline iron (III) oxides, as the samples were red in colour. In the second column, when $R = 0.15$, the intensity of these two reflections are lower in intensity than those observed in the first column, and in some samples, the $LiFePO_4$ reflection at 35 ° became visible. In the samples containing a molar ratio (R) of 0.2, the 35° reflections are intense and the $LiFePO_4$ becomes the dominant phase in most samples. As R is increased above 0.35, the reflection intensity becomes constant, indicating maximum conversion to $LiFePO_4$. This follows from the observation that over 0.2 moles of sucrose were required to form the correct phase; this appears to have been confirmed using the combinatorial XRD method. However, the electrochemical data for this array, shown in Figure 4.24 and described in section 4.3.1.2 shows only electrodes containing 0.35 moles of sucrose or greater are electrochemically active, even though the XRD data shows the olivine phase $LiFePO_4$ exists at 0.2 moles. This may be explained by the effect of percolation. Electrodes containing 0.2 moles of sucrose have sufficient reducing carbon to form the correct $LiFePO_4$ phase, but little excess carbon is present. Therefore, the electrodes have a carbon content below the percolation threshold for screening at the 0.1 mV s^{-1} rate.

4.3.3 Combinatorial SEM of $LiMPO_4$ Arrays

The variation in morphology of the calcined $LiMPO_4$ compositions was studied using scanning electron microscopy. Eight samples of varying iron, cobalt and nickel content were observed on a *Macor*® array designed for SEM, EDX and XRD experiments. The array of 64 different compositions was placed into the sample chamber of the SEM and each of the samples was observed using the gaseous secondary electron (GSE) detector. For each sample, an image was taken at 500 and 1000 times magnification. In addition, an EDX analysis was performed at 500 times magnification to determine the composition of the sample. This quantitative analysis of the EDX data was undertaken

for use in determining the accuracy of the sample preparation technique. A summary of the compositions investigated using the SEM is given in Table 4.2 and the micrographs for the compositions studied are shown Figures 4.34 to 4.41.

Table 4.2 – $LiMPO_4$ compositions studied using the SEM (after heat treatment at 700 °C).

Formula	Sample position on array	Figure
$LiFePO_4$	A1	4.34
$LiFe_{0.9}Ni_{0.05}Co_{0.05}PO_4$	B2	4.35
$LiFe_{0.8}Ni_{0.1}Co_{0.1}PO_4$	C3	4.36
$LiFe_{0.6}Ni_{0.2}Co_{0.2}PO_4$	D4	4.37
$LiFe_{0.4}Ni_{0.3}Co_{0.3}PO_4$	E5	4.38
$LiFe_{0.3}Ni_{0.35}Co_{0.35}PO_4$	F6	4.39
$LiFe_{0.2}Ni_{0.4}Co_{0.4}PO_4$	G7	4.40
$LiNi_{0.5}Co_{0.5}PO_4$	H8	4.41

It can be seen that the morphology of the olivine type ($LiMPO_4$) materials changes significantly as the composition is changed. Figure 4.34 is an image of un-substituted $LiFePO_4$. The surface of the material appears smooth and it is not possible to observe the individual particles. There does appear to be some surface features, but these are limited to indents and cracks on the surface. Figures 4.35 and 4.36 shows similar morphology for the $LiFe_{0.9}Ni_{0.05}Co_{0.05}PO_4$ and $LiFe_{0.8}Ni_{0.1}Co_{0.1}PO_4$ materials respectfully, indicating this small change in composition has little effect on the morphology of the materials. The surface of the material appears shiny and smooth with few surface features beyond cracks and raised areas in the material.

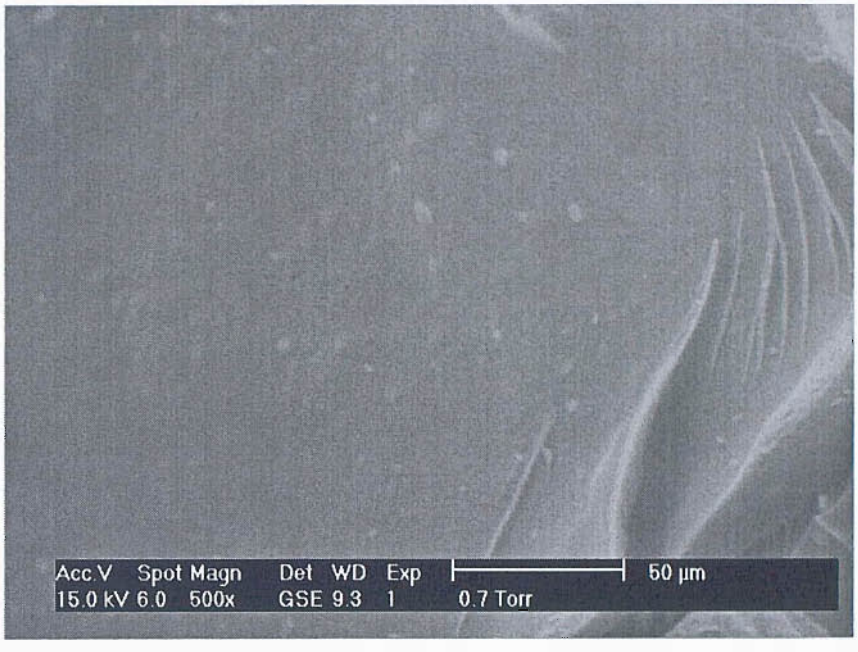

Figure 4.34 - An SEM micrograph of $LiFePO_4$ prepared on the high-throughput array – sample A1.

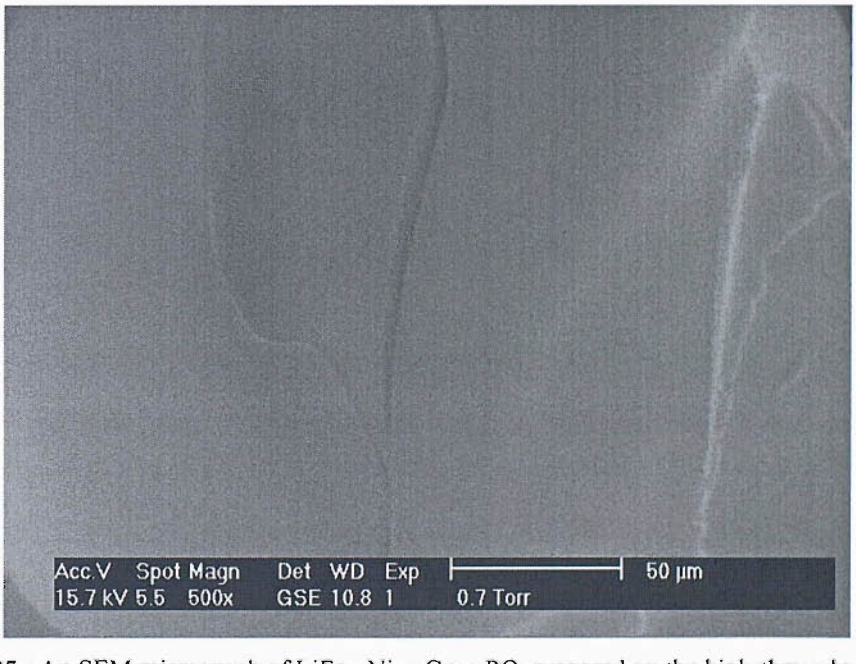

Figure 4.35 - An SEM micrograph of $LiFe_{0.9}Ni_{0.05}Co_{0.05}PO_4$ prepared on the high-throughput array – sample B2.

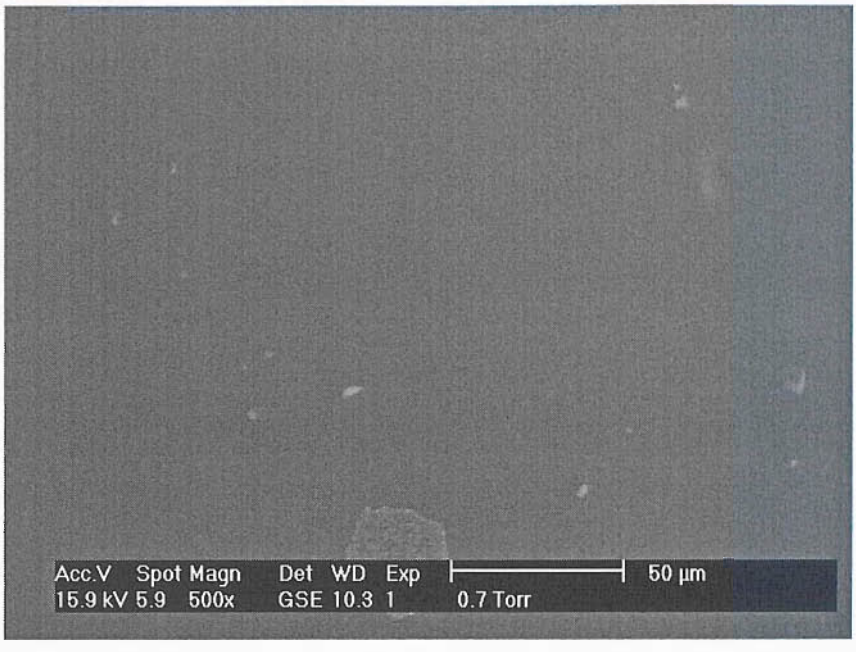

Figure 4.36 - An SEM micrograph of $LiFe_{0.8}Ni_{0.1}Co_{0.1}PO_4$ prepared on the high-throughput array – sample C3.

Figure 4.37 shows the micrograph obtained for the $LiFe_{0.6}Ni_{0.2}Co_{0.2}PO_4$ composition. The morphology of the material is clearly different from the previous three samples in that many more surface features are visible. Small pores in the surface can be on the order of around 1-5 microns and small particles can be seen on the surface of the material. The image in Figure 4.38 shows the morphology of the $LiFe_{0.4}Ni_{0.3}Co_{0.3}PO_4$ material is clearly different from the four previous samples. The surface is composed of much larger particles than those in Figure 4.37 and pores between the particles appear much larger and one would expect the density of this material to be lower than that of the previous samples (Figures 4.34 – 4.36). On the surface of the sample, larger particles are visible and have a smoother surface, which appears flatter, similar to that of the $LiFePO_4$ material.

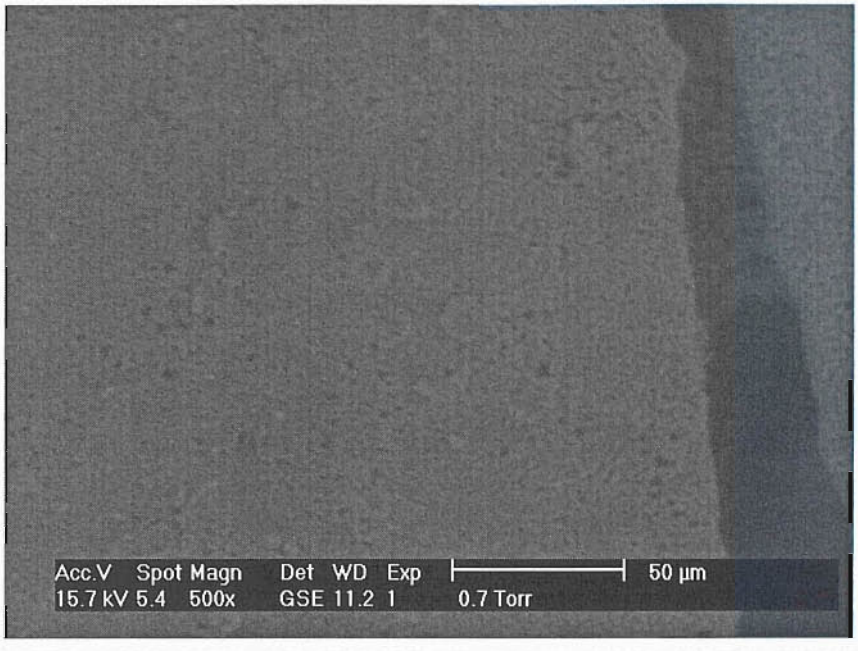

Figure 4. 37 - An SEM micrograph of $LiFe_{0.6}Ni_{0.2}Co_{0.2}PO_4$ prepared on the high-throughput array – sample D4.

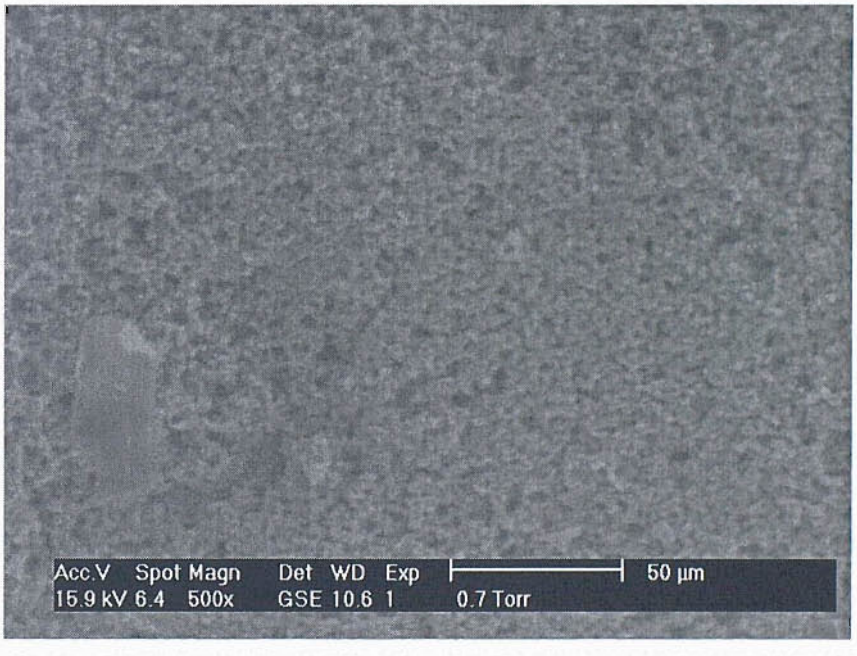

Figure 4.38 - An SEM micrograph of $LiFe_{0.4}Ni_{0.3}Co_{0.3}PO_4$ prepared on the high-throughput array – sample E5.

The morphology of the $LiFe_{0.3}Ni_{0.35}Co_{0.35}PO_4$ material shown in Figure 4.39 continues the same trend started by the previous two samples, in that the particle size is increasing. However, it appears that the particle size seen in Figure 4.39 is more uniform than in the previous materials. The particles at the surface of the $LiFe_{0.3}Ni_{0.35}Co_{0.35}PO_4$ material are approximately 3-5 microns in diameter and surface appears flat with no cracks or ledges. The trend of increasing particle size continues in Figure 4.40 for the material with the composition of $LiFe_{0.2}Ni_{0.4}Co_{0.4}PO_4$. In this material, the particle size reaches its largest for all the materials studied between 15 and 20 microns. The surface of the material appears uneven and the larger particles can be seen to protrude from the surface. The particle size distribution is also quite large with many small particles approximately 2 to 5 microns intermixed with the larger particles.

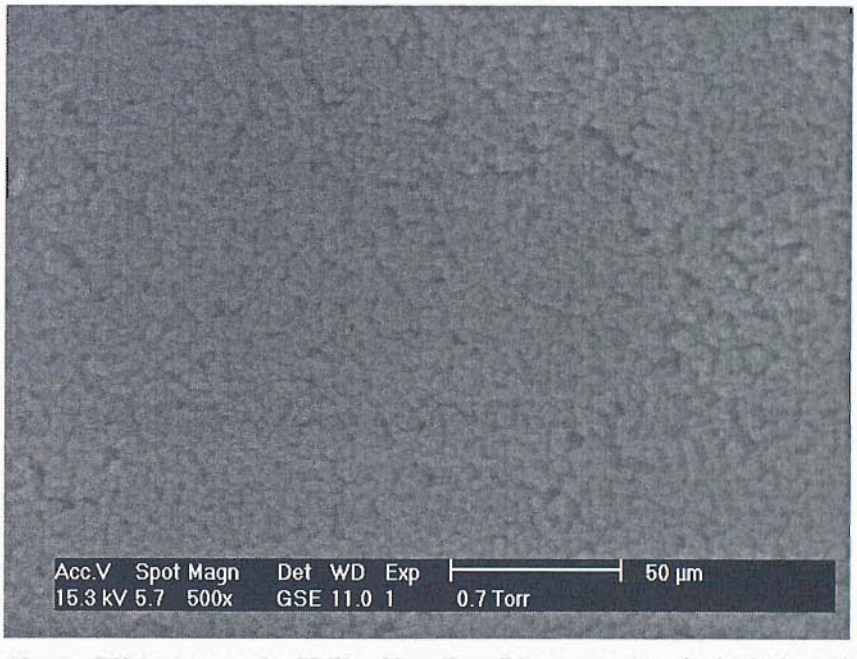

Figure 4.39 - An SEM micrograph of $LiFe_{0.3}Ni_{0.35}Co_{0.35}PO_4$ prepared on the high-throughput array – sample F6.

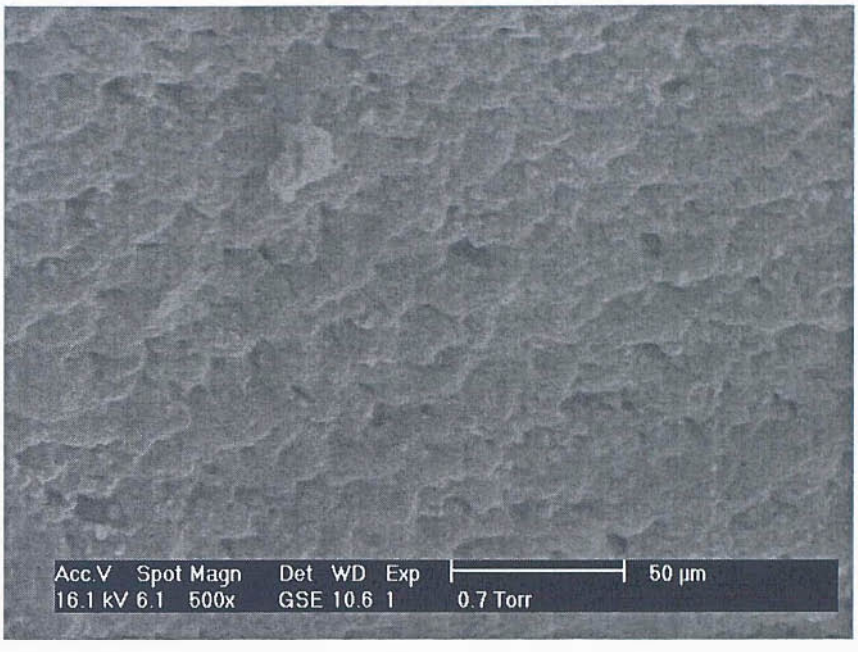

Figure 4.40 - An SEM micrograph of $LiFe_{0.2}Ni_{0.4}Co_{0.4}PO_4$ prepared on the high-throughput array – sample G7.

The morphology of the $LiNi_{0.5}Co_{0.5}PO_4$ material is shown in Figure 4.41. This composition of material was the only on the array that did not contain iron. The surface of the underlying material appears flat and featureless; however, there is evidence of large pores on the surface approximately 10-20 microns in diameter. In addition, there are many particles littering the surface ranging in size from 1 to 80 microns in size.

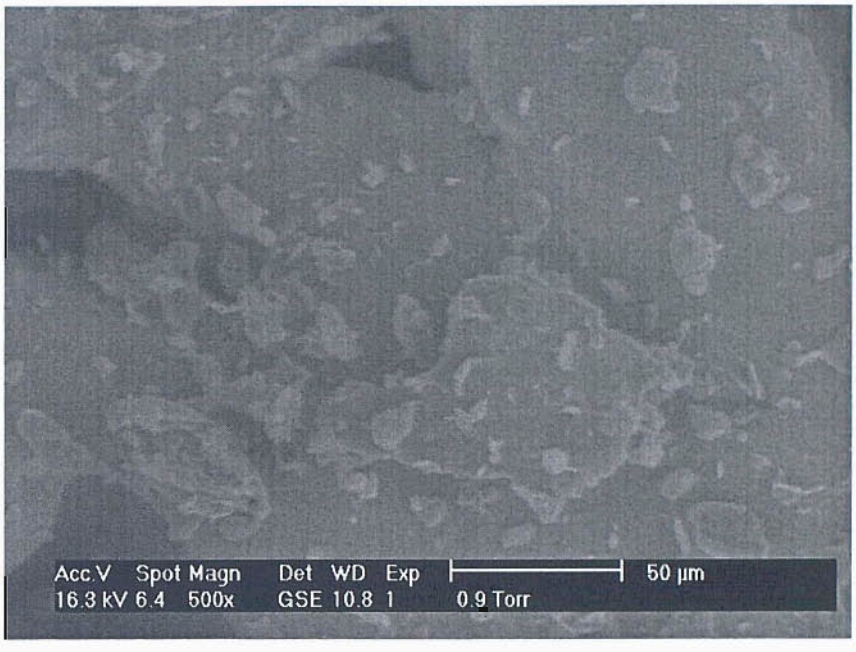

Figure 4.41- An SEM micrograph of $LiNi_{0.5}Co_{0.5}PO_4$ prepared on the high-throughput array – sample H8.

It is clear that as the composition of the $LiMPO_4$ material is varied, differences in sample morphology are observed. As the substitution in structure is increased, the particle size becomes larger. The largest particle size occurs when the ratio of iron cobalt and nickel are approximately 1:1:1. The particle size may increase because the highly substituted material is more disordered than an un-substituted material that contains only one transition metal. The large increase in particle size may aid in explaining the large currents observed for the high cobalt and nickel containing $LiMPO_4$ materials. The large particle size may facilitate a more favourable interaction between the active material and the conducting carbon that forms a matrix linking active material particles to the current collector. The larger particles in the high cobalt and nickel-doped materials may allow the carbon to mix more readily within its structure.

EDX spectra were obtained for each sample in a composition spread of $LiFe_{1-x-y}Co_xMn_yPO_4$ material. Quantitative analysis was performed on the data for the intensity of each of the elements present in the material. This experiment was also repeated for the $LiFe_{1-x-y}Co_xNi_yPO_4$ materials after further development of the sample preparation technique. The quantitative analysis data was used to plot the fraction of material calculated from the measured intensity by EDX *vs.* the fraction of each component added during synthesis. The two data sets shown below were obtained using two different preparation methods. The $LiFe_{1-x-y}Co_xMn_yPO_4$ samples were prepared on alumina tiles from approximately 5 μL of the solution precursor, whereas the $LiFe_{1-x-y}Co_xNi_yPO_4$ samples were prepared using the MGC synthesis array from approximately 20 μL of solution.

The graph in Figure 4.42 shows the normalised response for each of the three elements in the 64 samples. The general form of the plot is a straight line indicating that the added amount of each metal in the precursor can be detected as a similar value for atomic fraction by EDX. However there is a large amount of scatter probably due to the very thin sample spots and the low signal to noise ratio due to the small sample size and the presence of a large signal from the alumina.

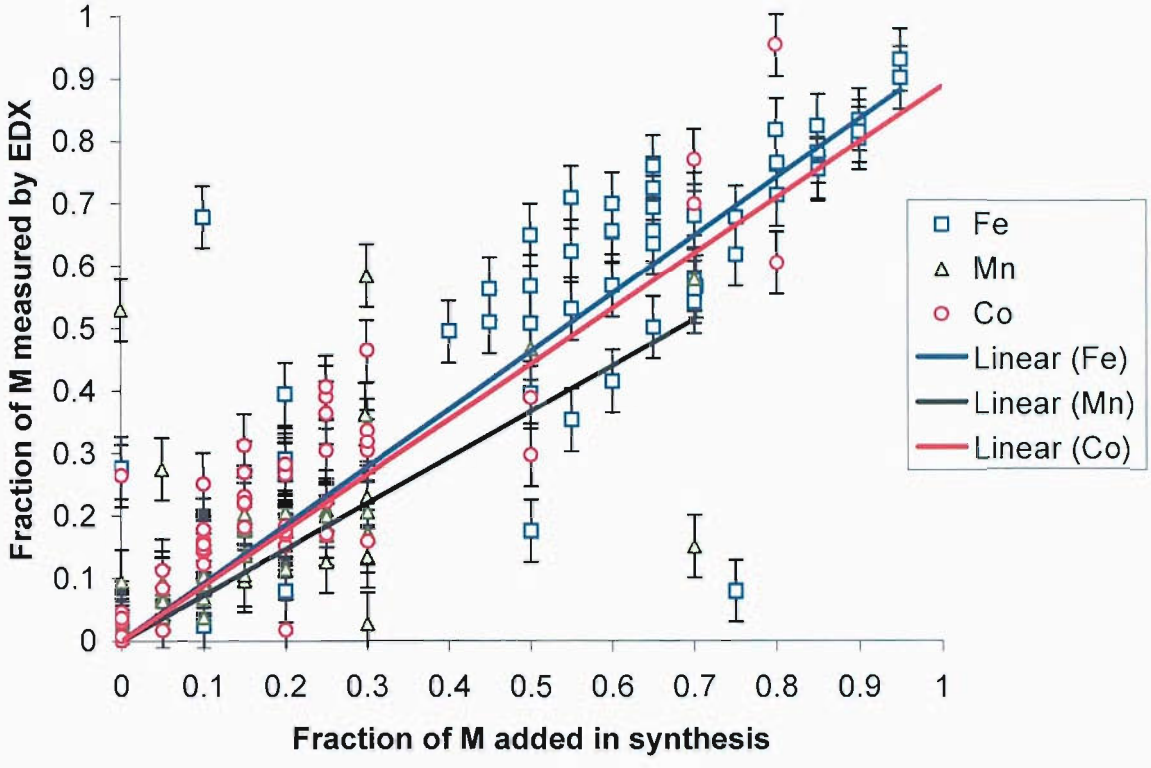

Figure 4.42 - Atomic fractions of the three transition metals in a mixed metal oxide array measured using EDX.

The method of screening $LiMPO_4$ material using EDX was improved by developing new arrays to increase the sample size in the hope of obtaining a more intense signal from the sample material. Figure 4.43 shows the plot of the fraction of each transition metal as calculated from the measured EDX intensity *versus* the fraction of material added during synthesis for $LiFe_{1-x-y}Co_xNi_yPO_4$.

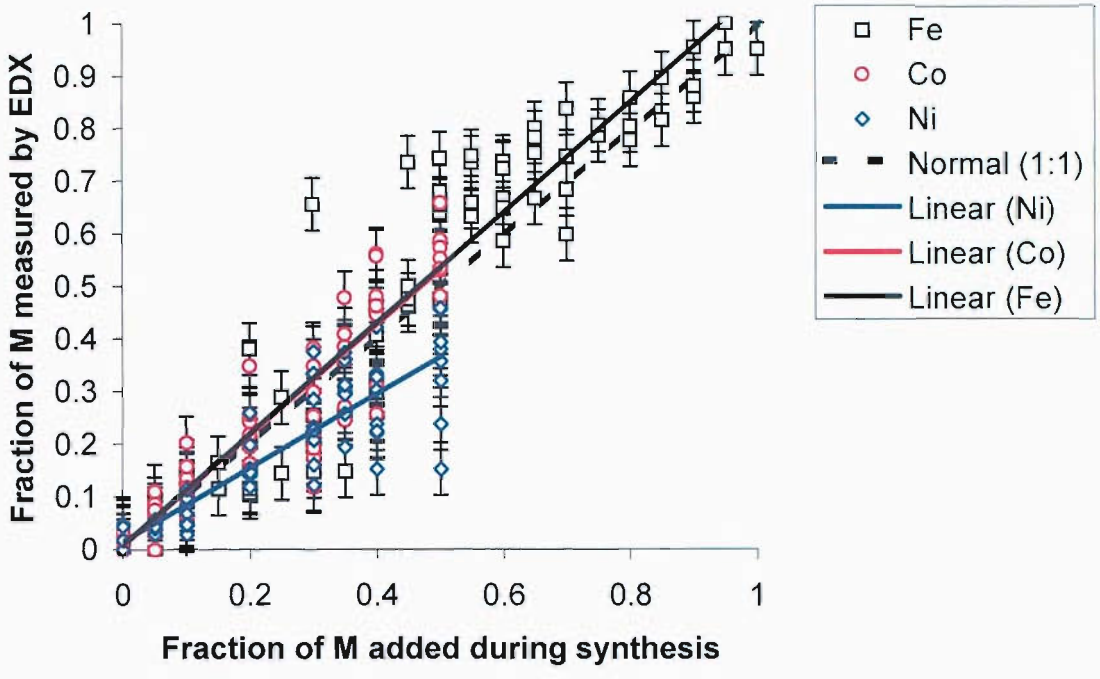

Figure 4.43 - Fraction of M measured using EDX *vs.* Fraction of M added during synthesis.

The data obtained using the MGC array contains less scatter than the data from the samples prepared on alumina tile. It is clear there has been an improvement in the signal to noise ratio. There is, however, some scatter in the values for the amount of nickel measured using EDX, which appear to be lower than expected. There is also scatter in the values obtained for the cobalt and iron fractions. However, the majority of the data points lie on the either side of the line of best fit and the majority are within the error limits of the technique. Plotting the data as a contour graph for each of the samples was considered however, it was decided that such a plot would not give a meaningful display of compositional data as the composition changes were made to discrete samples. The errors seen in the data sets shown in Figures 4.42 and 4.23 could be reduced by using thicker sample layers which would result in an improved signal to noise ratio.

4.5 Conclusion

High-throughput methods have been applied to the synthesis of multi-component arrays of electrode compositions. These arrays have been characterised using high-throughput and conventional techniques. It has been demonstrated that solution synthesis techniques used for bulk material preparation can be adapted for use in a combinatorial study. This included the doping and substitution of inorganic oxides and phosphates using automated solution based synthesis techniques producing varied compositional spreads. New methods of array characterisation have been developed and tested, including high-throughput X-ray diffraction, electrochemical screening and the development of a high-throughput method for composition confirmation using conventional EDX and SEM methods.

An investigation of the effect of doping $LiFePO_4$ with zirconium has been conducted using the combinatorial technique. This has enabled the effects of the Zr dopant and the conducting carbon to be studied simultaneously on the same array. It has been determined that zirconium has no effect on the specific capacity of the materials on the array. It is likely that the increased conductivity observed in Zr doped $LiFePO_4$ by Chaing *et al.* is the result of the presence of carbon residues that remained in the samples after synthesis.

Composition spreads of ternary mixed metal phosphates have been synthesised and screened using high-throughput techniques. $LiFe_{1-x-y}Co_xNi_yPO_4$ compositions were characterised using slow scan cyclic voltammetry and the peak current response was plotted as a function of the composition as a figure of merit (FOM). This revealed that some clusters of electrodes of a similar composition displayed higher current responses than the other electrodes. This would suggest that these electrodes might be composed of materials with superior electrochemical properties. It was suggested that these high current responses might be due to the way the materials were interacting with the carbon matrix formed by the pyrolyis of sucrose. This high current response is likely to be a result of enhanced conductivity of the composite and therefore is a percolation effect; however further electrochemical testing of these compositions is necessary to understand the nature of the enhanced performance.

The preparation of these new compositions has demonstrated the feasibility of high-throughput synthesis and screening to the discovery lithium battery materials. This method does require further development to enable it to be used as a tool for the rapid screening of new compounds and optimisation of systems.

4.5.1 Further Work

Further work on this area could include the study of additional ternary systems of mixed metal oxides and phosphates and the substitution of phosphorus in $LiFePO_4$ for non-metal elements, such as arsenic and silicon and substitution of oxygen for fluorine. A comprehensive study of electrolyte additives may prove a positive future direction. A systematic study of new compositions using impedance techniques may also prove a viable screen for these materials. The development of an experimental method for the direct measurement of conductivity would also be a useful rapid method of screening.

The electrochemical testing method does suffer from some scatter associated with the measurement of the current. It would therefore be advantageous to improve this technique to obtain increased reproducibility of the experimental data. This could be achieved by increasing the sample size from the 3 mm diameter disks up to round 5 to 7 mm in diameter. This would allow a larger amount of material to be deposited onto the electrode surface and hence this would reduce the error associated with the deposition technique. In addition the larger sample size would result in higher currents which itself would reduce the scatter.

4.6 References

1. Amine, K., Yasuda, H., and Yamachi, M., *Electrochemical and Solid State Letters*, 2000, **3**, (4), p. 178-179.
2. Hanak, J.J., *Journal of Materials Science*, 1970, **5**, p. 964-971.
3. Reuter, H., *Advanced Materials*, 1991, **3**, (5), p. 258-259.
4. Lu, C.H. and Saha, S.K., *Materials Science and Engineering B-Solid State Materials for Advanced Technology*, 2001, **79**, (3), p. 247-250.
5. Chang, S.H., Kang, S.G., and Jang, K.H., *Bulletin of the Korean Chemical Society*, 1997, **18**, (1), p. 61-65.
6. Yamada, A., Hosoya, M., Chung, S.C., Kudo, Y., Hinokuma, K., Liu, K.Y., and Nishi, Y., *Journal of Power Sources*, 2003, **119**, p. 232-238.
7. Chung, S.Y., Bloking, J.T., and Chiang, Y.M., *Nature Materials*, 2002, **1**, (2), p. 123-128.
8. Herle, P.S., Ellis, B., Coombs, N., and Nazar, L.F., *Nature Materials*, 2004, **3**, (3), p. 147-152.
9. Fey, G.T.K., Lu, C.Z., and Kumar, T.P., *Materials Chemistry and Physics*, 2003, **80**, (1), p. 309-318.
10. Hwang, B.J., Hu, S.G., and Santhanam, R., *Bulletin of Electrochemistry*, 2003, **19**, (5), p. 229-232.
11. Park, S.H., Park, K.S., Sun, Y.K., and Nahm, K.S., *Journal of the Electrochemical Society*, 2000, **147**, (6), p. 2116-2121.
12. Kim, K.M., Kim, J.C., Park, N.G., Ryu, K.S., and Chang, S.H., *Journal of Power Sources*, 2003, **123**, (1), p. 69-74.
13. Scrosati, B. and Vincent, C.A., *Modern Batteries: An Introduction to Electrochemical Power Sources*. 1997, London: Arnold. 233.

14. Lewis, M.J., *High-Throughput Development of Optical and Potentiometric Carbon Dioxide Sensors*, in *Department of Materials Engineering*. 2003, University of Wales: Swansea. p. 209.

Chapter 5:
Conclusions and Further Work

5.1 Conclusion

High-throughput methods have been developed for the screening of lithium battery positive electrode materials. It has been shown that these techniques can be used to rapidly prepare and screen many electrode compositions using robotic liquid handling techniques, multi-channel electrochemical testing equipment, high-throughput XRD and SEM methods. The technique was utilised to screen a well-known system, that of $LiMn_2O_4$/CB/PVDF to validate the experimental technique. The method was then applied to many unknown systems such as substituted and doped olivine materials, which may prove viable materials for commercialisation.

The initial validation experiments using $LiMn_2O_4$, acetylene black and PVDF showed that the expected behaviour observed for conventionally prepared cells could be replicated for the samples prepared using the high-throughput method. These experiments were repeated several times and the method was found to be an accurate screen for these materials. The high-throughput electrochemical techniques were used to accurately measure the current response of the 63 electrodes in the array and led to accurate observations of percolation behaviour of the $LiMn_2O_4$/C system.

It has been found that this method is a viable screening technique to compare the performance of cells relative to one another on the same array. However, it is impractical to compare results obtained form a single electrode using the combinatorial technique with those obtained from an electrode using conventional techniques. This is due to the scatter associated with results obtained using the high-throughput technique. However, when an average of several cells of the same composition is taken, it was found to be closer in value to the data obtained using the conventional methodologies. It was also found that some of the capacity values obtained for the electrode compositions were lower than expected. This may be due to a reduction in stack pressure in the combinatorial cells compared to the conventional cells. Another explanation is that the electrodes prepared using the high-throughput approach are uncompressed. This may result in a reduction in conductivity through the composite leading to lower capacity values. For this reason, generally lower capacity values are observed for cells using the combinatorial technique than for the conventional approach.

The reproducibility of the experimental technique was investigated for an array containing an identical amount of $LiMn_2O_4/C$ on all the electrodes in the array. This experiment showed that the specific capacity of approximately 90 % of electrodes on the array were within a 20 mAh g^{-1} window, and thus, validating method in terms of the reproducibility of the experiments.

After the initial validation test, the focus of the work was directed towards developing novel synthesis routes for battery materials that could be compatible with the combinatorial approach. These methods were sol-gel and solution type reactions that allowed for the easy change in composition of the materials on the array scale. This was done using doping and substitution for transition metals in the compounds. It was found that a versatile synthesis route using sucrose as a reducing and gelling agent could be developed using solution precursors that enabled the composition of the materials to changed by substituting and doping the materials with transition metals. $LiFePO_4$ materials of varying composition prepared under different synthesis conditions were prepared in quantities between 1 and 5 g per batch. The materials were characterised using galvanostatic cycling, X-ray diffraction and SEM/EDX. The characterisation experiments confirmed that a well crystallised, phase pure material could be obtained by heating the precursor at 700 °C using sucrose to iron ratio of 0.25. Synthesis was also conducted using reducing atmospheres during synthesis. However, this was found to have a negligible effect on crystal phase formation. Pure $LiFePO_4$ materials prepared using the optimum conditions were found to have specific capacity values around 68% of theoretical values (110 mAh g^{-1}). It was also found that adding a second carbon coating after the caclination step increased the practical specific capacity to 90 % of the theoretical value (155 mAh g^{-1})

The combination of these two experimental techniques was the focus of chapter four. With the design of the synthesis arrays, the combinatorial methodology was applied to high temperature synthesis of lithium battery materials. Robotic liquid handling techniques were used to prepare electrode precursor solutions that were deposited as droplets on the array. This allowed multi-component systems to be studied on a single array thus, allowing optimisation of synthesis conditions. Arrays containing

$LiFePO_4$ material and a varying sucrose ratio were used to confirm the conditions determined for the bulk preparation and both methods were in good agreement.

The use of the combinatorial screening method to investigate the behaviour of new systems was attempted with the study of the $Li_{1-4x}Zr_xFePO_4/C$ electrode compositions. Arrays of $LiFePO_4$ were prepared with varying carbon and Zr doping level. This was undertaken to separate the effect of the conductivity due to the carbon and possibly the zirconium. It was found that the Zr doping level had no effect on the capacity and thus the conclusion is that the inclusion of Zirconium within the $LiFePO_4$ structure does not result in enhanced capacity and hence, conductivity. This data also showed that the capacity increased as the sucrose to iron ratio was increased. This indicated that the electrochemical techniques were capable of measuring differences in the current response of these materials, and the conductivity of these materials could be inferred.

Ternary systems of substituted $LiFePO_4$ materials were prepared. These experiments demonstrated the ability of the combinatorial method to optimise complex systems very rapidly. Large composition spreads of materials were produced containing Mn, Fe, Ni and Co, Ni and Fe. These arrays were tested using cyclic voltammetry, XRD, SEM and EDX methods. However, the characterisation of these arrays was initially problematic. It was found that the substrates used for X-ray testing (disposable alumina tile) were unsuitable, as they did not allow the deposition of sufficiently thick samples. This coupled with the fluorescence effects due to iron and cobalt resulted in the XRD and EDX data from the samples being of low signal to noise ratio. A new reusable MGC array was designed. MGC can be easily manipulated using standard workshop milling tools thus, allowing deep wells to be drill to confine the material leading to the formation of thicker samples. This resulted in an improved signal to noise ratio for the EDX data. Electrode materials of the type $LiFe_{1-x-y}Co_xNi_yPO_4$ were tested electrochemically. These data revealed that certain clusters of compositions gave a higher current response than the majority of the other cells. This result suggests that the materials that registered a high current response might possess superior properties, such as elevated conductivity or charge storage capacity. These compositions require further study, but it has been postulated that the

elevated levels of current may be due to the way the active material interacts with the carbon matrix.

In summary, novel high-throughput method for the discovery of lithium battery materials has been developed and evaluated. The method yielded data that was in good agreement with the conventional testing methodologies outlined in chapter 2. It is clear that these methods and techniques must be developed further before the high-throughput method described in this thesis can be considered as a tool used routinely for materials discovery. However, the data and methodologies developed to date have allowed many new systems to be explored in a way that was not possible before. The study of the $LiFePO_4$/C/Zr system is such an example. The high-throughput method not only allowed the rapid preparation and screening of these materials, but also allowed the effects of the two variables, which were thought to be causing a single effect to be separated and observed independently. The rapid screening of compounds is a departure from conventional techniques, and some might argue that the conventional methodologies are more valid for testing materials. However, it is possible to use this technique as a probe to get a general understanding of a system, at which point the combinatorial methodologies may give way to the conventional testing techniques to characterise potential candidates which were identified using the high-throughput method.

5.2 Further Work

The value of combinatorial screening to the discovery of lithium battery materials has been demonstrated. However, there is still much work to be done on this area. The main areas for improvement should focus on reducing the amount of scatter in the measurement techniques and to therefore produce more reproducible data sets. The aim should be to reduce the scatter to such an extent that the technique is comparable with conventional methods in terms of reproducibility.

This work has only been concerned with the area of positive electrodes. A future combinatorial project could cover the study of negative electrodes, electrolyte additives and cell design. In addition, there remains much work to be done in the area

of positive electrodes. This work focused on the synthesis of a small number of possible compositions based on $LiFePO_4$, $LiMn_2O_4$ and $LiNi_xCo_{1-x}O_2$ materials. There are many other positive electrodes that are worthy of a combinatorial study. The investigation of the addition of other additives to the $LiFePO_4$ system may also be lead to some interesting findings.

The development of a method to effectively screen materials using high-throughput XRD was developed during this project, but has yet to be a routine procedure. The study of these positive electrodes using impedance spectroscopy and conductivity measurement technique would also be a useful extension to this work.

In addition to these new areas, further optimisation of the existing method must be undertaken. The scatter associated with the existing methodologies needs to be reduced, which would allow the technique to possibly evolve into a tool for materials scientists. This could be achieved by increasing the sample mass to reduce the inaccuracies associated with sample preparation and materials handling. The increased size of the samples would also lead to a higher current response, which would result in a higher signal to noise ratio in the electrochemical testing experiments.

During the high-throughput testing of the $LiMPO_4$ compositions, the adhesion of the electrode materials to the electrode surface after calcination was a problem. This was partially overcome by adding wells to the surface of the electrodes to confine the material. However, although this allowed characterisation to proceed and experimental data to be collected, it is still not an ideal method of electrode preparation. The solution to this problem may involve the design of a new electrochemical cell composed of deep wells, which may also serve as current collectors. In this way, the material is confined on the electrode surface, and thus, the scatter due to loss of electro-active material will be reduced.

Appendices

Appendix 1

Synthesis of Lithium Manganese Oxide ($LiMn_2O_4$).

$$\tfrac{1}{2}\, Li_2CO_3 + Mn_2O_3 \rightarrow LiMn_2O_4 + CO_2$$

Quantities

M (Li_2CO_3) = 73.89 $g.mol^{-1}$
M (Mn_2O_3) = 157.87 $g.mol^{-1}$
M $(LiMn_2O_4)$ = 180.81 $g.mol^{-1}$

Aim to produce 30g of lithium manganese oxide.

No of moles of $LiMn_2O_4$ =30/180.81 = 0.167 moles.

Mass of Mn_2O_4 required = 0.167 x 157.87
= **26.1938 g.**

Mass of Li_2CO_3 required = 0.5 x 0.167 x 73.89
= **6.1698 g**

Appendix 2

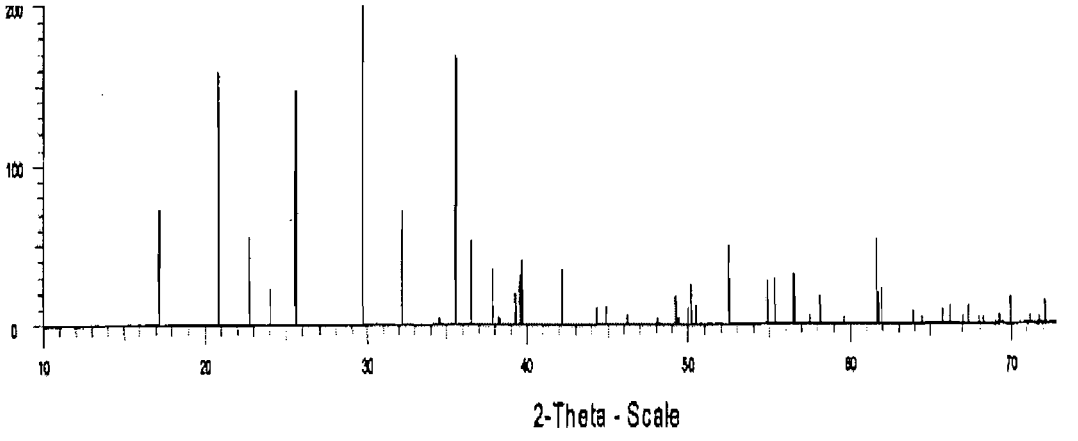

Theoretical X-ray diffraction pattern for olivine type $LiFePO_4$ [1].

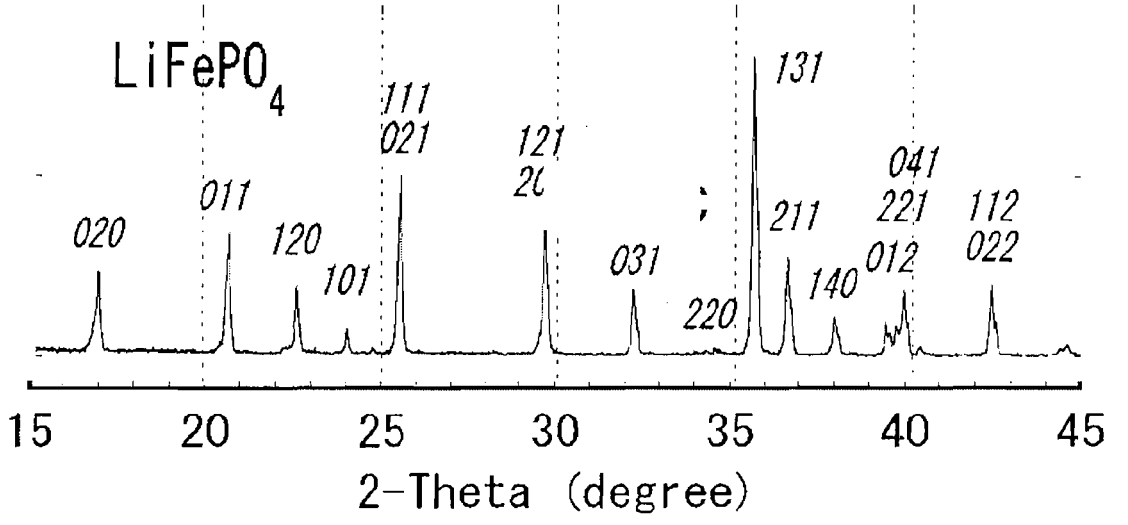

A standard XRD pattern for olivine type $LiFePO_4$. The numbers refer to the miller indices for each reflection [2].

1. Franger, S., F. Le Cras, C. Bourbon, and H. Rouault, Electrochemical and Solid State Letters, 2002. 5(10): p. A231-A233.

2. Yamada, A., S.C. Chung, and K. Hinokuma, Journal of the Electrochemical Society, 2001. 148(3): p. A224-A229.